



**HAL**  
open science

## A contemporary monograph on silicon cast irons microstructure - From atom scale to casting

Jacques Lacaze, Jon Sertucha, Manuel J Castro-Román

► **To cite this version:**

Jacques Lacaze, Jon Sertucha, Manuel J Castro-Román. A contemporary monograph on silicon cast irons microstructure - From atom scale to casting. 2024. hal-04447564

**HAL Id: hal-04447564**

**<https://hal.science/hal-04447564v1>**

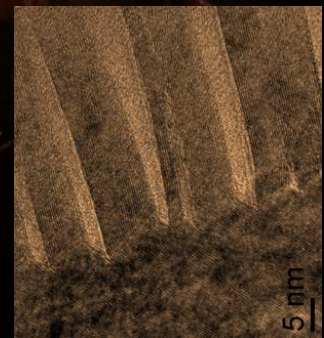
Submitted on 8 Feb 2024

**HAL** is a multi-disciplinary open access archive for the deposit and dissemination of scientific research documents, whether they are published or not. The documents may come from teaching and research institutions in France or abroad, or from public or private research centers.

L'archive ouverte pluridisciplinaire **HAL**, est destinée au dépôt et à la diffusion de documents scientifiques de niveau recherche, publiés ou non, émanant des établissements d'enseignement et de recherche français ou étrangers, des laboratoires publics ou privés.

JACQUES LACAZE, JON SERTUCHA  
MANUEL J. CASTRO-ROMÁN

From atom scale to casting  
**A CONTEMPORARY  
MONOGRAPH ON  
SILICON CAST IRONS  
MICROSTRUCTURE**



*February 2024*

*Free downloading from HAL*

*This monograph is expected to be of value to foundry engineers and master or PhD students, as well as researchers involved in the field of graphitic cast irons.*

*Our aim was to provide a comprehensive overview of the formation of the microstructure of **silicon cast irons** based on the works that the authors have carried out together or separately over many years.*

*This is an open access manuscript to be uploaded from the HAL website, France.*

*The first two editions were made available in November 2020 and April 2021 in a form that could have been considered a bit compact by the readers. The third edition was totally recast to appear as a usual textbook, and this 2024 edition brings a few small changes and some new references.*

\*\*\*\*\*

*Special thanks are due to Gérard Lesoult for comments on the first edition and the many suggestions he made for improving it. Fernando Landgra and Werner Menk kindly provided historical references.*

*Alain Hazotte and Steve Dawson contributed a lot to chapter 1, and Steve Dawson allowed us to use the text reproduced in appendix A. Insightful comments from Olivier Dezellus improved chapters 2 and 3.*

# Content

Foreword

Chapter 1 – Short introduction to cast irons

Chapter 2 – Fe-C-Si phase diagram and the carbon equivalent

Chapter 3 – Thermal analysis and solidification path

Chapter 4 – Nucleation of graphite – Inoculation

Chapter 5 – Primary graphite, crystallography and morphology

Chapter 6 – Two-phase growth in non-spheroidized melts. Austenite-graphite and austenite-cementite coupled eutectics.

Chapter 7 – Spheroidal graphite-austenite eutectic

Chapter 8 – Trace elements: graphite growth and degeneracy

Chapter 9 – Eutectoid transformations

Chapter 10 – Microstructure modelling

References

Glossary

Index of terms and physical properties

Appendices

Note: Authorisations for re-use of figures are listed on the last page.



# Foreword

This monograph finds its foundation in a simple fact: there is a paradigm with cast irons, which is that these alloys are produced and cast to shape since thousands of years but are amongst the most complicated metallic alloys when considering the formation of their microstructure by solidification and solid-state transformations. In turn, this complexity opens a wide range of possibilities for shaping their microstructure and engineering their service properties.

The first cast irons were mostly Fe-C alloys and as such solidified mainly in the metastable system, leading to hard and brittle parts that were heat treated for graphite precipitation to give malleable cast irons. The introduction of silicon into the melt increased the temperature difference between the stable and metastable systems, thus promoting the formation of graphite instead of cementite during solidification. This gave rise to the **silicon cast irons** that are the subject of this monograph.

With the advent of metallographic observations, it was realized that cast iron also often contained phosphides related to the origin of iron ores. A good control of the metallic charge allowed to improving the mechanical properties, in particular by ensuring a minimum strength before rupture under tensile stress. The essential step, however, was the discovery that it is possible to change the shape of graphite by transforming the interconnected lamellae into discrete spheroids. Cast irons thus became a material for safety parts and were no more restricted to construction. The late 1990s saw the industrial emergence of compacted graphite irons and austempered ductile cast irons.

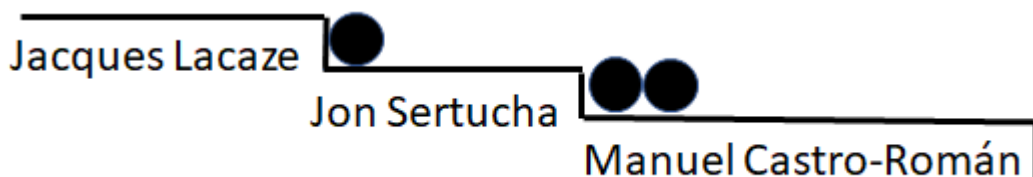
This **historical evolution** and the **research effort** during the first part of the 20th century are described in the extensive review carried out by Merchant in the 1960s [MER68]. At that time, there was an explosion of research on cast irons with the aim of describing and understanding the formation of graphite during solidification and, to a lesser extent, during heat treatment. As far as solidification is concerned, the review by Lux [LUX70a, LUX70b] of this research effort was an important step that already contained most of the questions and provisional answers that are still referenced in more recent works [STE05]. It is worth mentioning here Zhou's

comprehensive literature review on solidification of different types of cast iron [ZHO09, ZHO10, ZHO11].

This monograph is not intended to be an exhaustive review of the literature as those mentioned above, but rather to provide a coherent view of the formation of the microstructure of silicon cast irons. In fact, the authors felt it was very important to present how various aspects of microstructure formation could be related to each other using schemes based on known physical phenomena, and sometimes supported by ad hoc modelling. Consequently, the works that will be referenced first are those that contain information that has proven to be essential for the development of these schemes. Where appropriate, controversies will be mentioned with reference to the works where they are detailed, and emphasis will be on open questions.

All references are listed at the end of the monograph, where are also to be found a glossary of acronyms and unusual terms and an index of the parameters used in the equations and the values employed for physical quantities.

For more than 10 years, our work has certainly benefited from Azterlan's impetus and has greatly benefited from the dynamism of the European Cast Iron (ECI) group. The exchanges within this group, as well as the discussions and controversies that have taken place at its annual meetings have been renewed stimuli. We would like to thank the participants, both academics and industrialists, for their continued contribution to this group.



Jacques Lacaze  
Jon Sertucha  
Manuel Castro-Román

[Jacques.lacaze@toulouse-inp.fr](mailto:Jacques.lacaze@toulouse-inp.fr) - [jsertucha@azterlan.es](mailto:jsertucha@azterlan.es) -  
[manuel.castro@cinvestav.edu.mx](mailto:manuel.castro@cinvestav.edu.mx)

# Chapter 1 - Short introduction to cast irons<sup>1</sup>

Throughout history, cast iron is unique amongst metallic materials. No other metal can boast such a long history, together with such a wide diversity of variants, properties and applications. Arguably, no other material can claim to have such complexity. While the cast iron foundry routinely churns out myriad components, a supporting cast of researchers and engineers have ensured a choreography of carbon atoms that could make the busiest beehive look lethargic. We control the carbon atoms not with furnaces and wirefeeders, but with knowledge. This knowledge enables a material with a unique combination of design flexibility, mechanical properties, wear resistance, recyclability, low life cycle energy consumption, and low cost. And it will be with the continued pursuit of understanding and knowledge that tomorrow's researchers and engineers will ensure the continued growth of new material variants, with improved material properties and new applications. Cast iron: thousands of years of development and progress behind us; thousands of fascinating mysteries and opportunities ahead of us.

## 1.1 Cast irons at a glance

Cast irons are easy to shape materials whose properties have evolved over the years following technical and scientific improvements. As of 2018, cast irons represent 70% of the 110 Million tons of metals being cast each year in the world (10% for cast steels, 20% for aluminium and other alloys) [CEN19]. Cast irons are recyclable materials at low cost and with relatively limited pollution when compared to their present-day competitors. This is schematically illustrated in Fig. 1.1, where so-called grey cast irons are compared with cast steels and aluminium alloys in terms of price per MPa of Yield strength, vs. embodied energy (Fig. 1-a) and CO<sub>2</sub> footprint (Fig. 1.1-b). The latter two terms mean energy used and CO<sub>2</sub> emitted, respectively, for primary production, casting and recycling of 1 kg of alloy.

Even far before dollars were established as a universal reference, and far before aluminium could be thought of, cast irons were already quite attractive for several applications in agriculture, domestic applications and decoration. Cast irons are in fact historical materials that have appeared at the Iron Age when the temperature in the furnace for processing iron ore became high enough. It is thus of first interest to have a rapid look at the evolution of cast iron materials over the time until the modern era, this is rapidly done in the historical section to follow. As with all other materials, several important steps have been taken over the last two centuries in the processing of cast iron, in casting technology and in the cast iron itself; these are mentioned in the following sections.

---

<sup>1</sup> This chapter is based on the paper "Cast irons, an historically green material worthy of continuous research" [LAC21a]



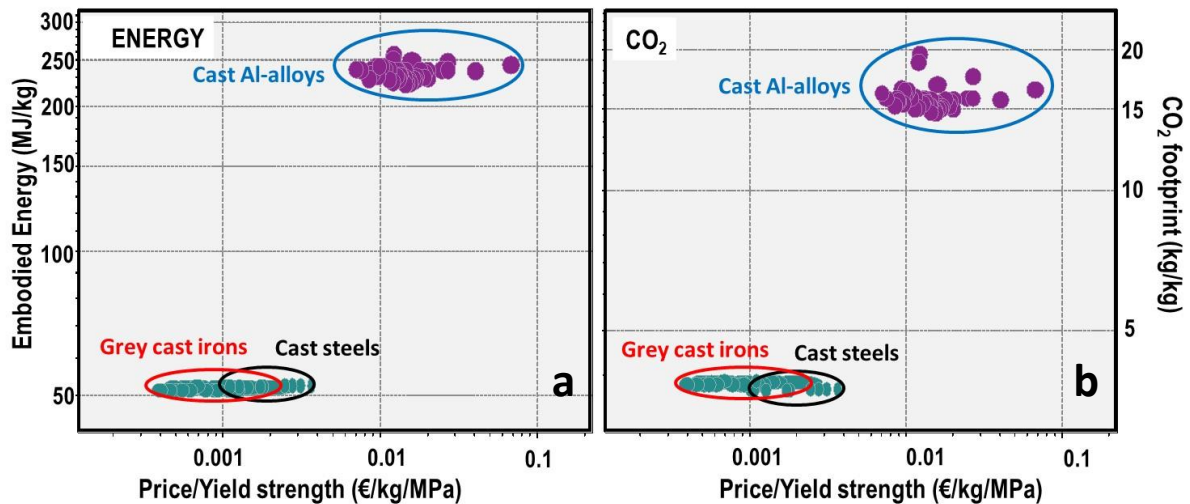


**Figure 1.1. Grey cast irons compared with cast steels and aluminium alloys in terms of price and environment impacts; x-axes concern the ratio between price and Yield strength, while y-axes concern estimations of energy used (a) and equivalent CO<sub>2</sub> emissions (b) for the primary production, casting and recycling of one kg of alloy. Data from [GRA20].**

Nowadays, cast irons are a family of materials as depicted in Fig. 1.2. Two main branches can be defined depending on the carbon-rich phase, which can be either cementite and other carbides or graphite. Alloys within this former branch, also called white cast irons for the colour of the rupture surface, have good wear properties and good heat and corrosion resistance when alloyed, but they are brittle. This branch is however a minor part of the family and most of the current production consists of grey (or graphitic) cast irons in which the carbon-rich phase is graphite giving a dark contrast to rupture surfaces. The vast majority of these irons are based on Fe-C-Si alloys and thus could be called silicon cast irons. These irons are the focus of this work. Ni-resist graphitic cast irons are heat and corrosion resistant, while very high-Si alloys are corrosion resistant. Behind the sorting in Fig. 1.2 is a continuous evolution of cast iron alloys and their processing, as described in the section "Main Steps".

The properties of silicon cast irons are determined by their microstructure after the two following phase transformations: 1) solidification during which the graphite shape is determined; and 2) solid-state transformation of the Fe-rich matrix in ferrite or pearlite. With low levels of Ni and Mo, silicon cast iron can be austenitized (austempered) and then transformed at 300-450°C to give a matrix of ausferrite. This material is called austempered ductile iron (ADI) and has very high mechanical properties. The present market share and the associated concerns are presented in a section dedicated to production and concerns. These concerns are associated to on-going laboratory researches and are challenging, in particular because of the increasing demands for weight reduction and increased loading together with an ever-increasing number of recycling loops compounding the effect of trace elements on the parameters controlling the microstructure. Some of the up-to-date challenges are discussed in a last section.

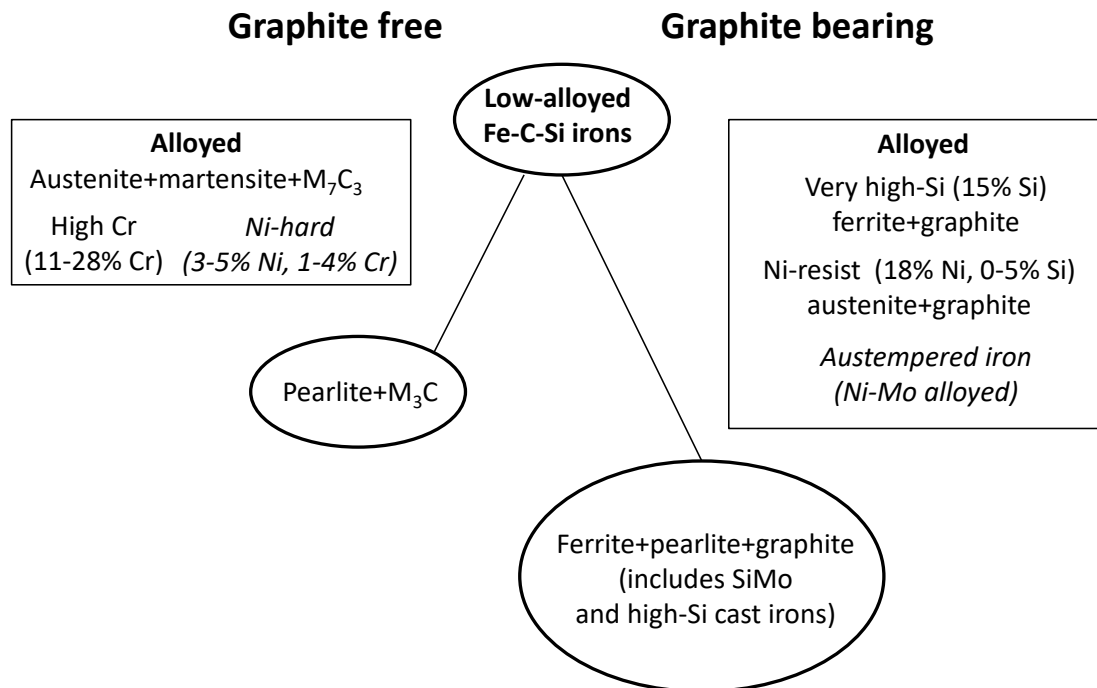


**Figure 1.2. The cast iron family with the basic microstructures indicated. They are all obtained in the as-cast state, except those appearing in italics that are subjected to specific heat-treatment (after Elliott [ELL88] and Stefanescu [STE17a]).**

### 1.2 A very brief history (inspired by [Appendix A](#))

Legend reports that, "approximately 4,000 years BC, scientists and sages commissioned the first iron cupolas. These early metallurgists placed a curious metal-like substance, which we now know as iron ore, in the hollow of a burnt out tree trunk. The charred inner surface of the trunk provided fuel for the fires and thermal insulation, while random holes that burned through the trunk allowed the ambient winds to enter and feed the charcoal. With the right combination of wind, rich ores and extra charcoal, the charge was reduced to a metallic iron sponge that could be rolled, using rocks, into decorative beads. It was 6000 years ago, and iron was more highly valued than gold." [DAW01]

This is more or less what historical works describe which locate the very start of iron history in Anatolia (Armenia) or Mesopotamia (Iran) [COZ00, STE17a], or else China [TAN10]. It is worth noting that independent development in sub-Saharan Africa at the same time was postulated and is now well documented [COZ17, ROB18]. A short but comprehensive presentation of the beginning of iron ore processing, and of the parallel development of iron and cast irons, has been published by Le Coze [COZ00]. Production techniques and raw materials were gradually refined as the Iron Age evolved. Iron implements and weapons began to appear in approximately 3000 BC, and the comparatively advanced technique of hardening iron weapons by heat treatment was known to the Greeks by about 1000 BC.

As the temperature of the furnaces was progressively increased and reached 970°C (Fe-C-P eutectic), 1154°C (Fe-C eutectic) and above, some liquid may have formed which was certainly mixed with scoriae. Increasing further the temperature slightly above 1200°C allowed reaching the FeO-fayalite or fayalite-SiO<sub>2</sub> eutectic, meaning the dross and scoriae became partly liquid and could be separated more easily from the iron loupe. In most production

locations, this carbon enriched liquid iron – the ancestor of cast irons - was eliminated except in China where the first crafts, tools and weapons made of cast irons date back to 600-500 BC [TAN10, STE17a]. This means that it was early understood that the furnaces could be conducted either to give "wrought" iron for further refining by hammering to give steel, or to give carbon-rich iron liquid that was suitable for casting. In this latter case, adding minerals (clay, shells, ...) changed the scoriae into a slag protecting the metallic liquid and thus keeping its casting ability while more of the charge was melting. It is probable that some silicon dissolved in the liquid, in an amount that increased with the temperature, and that it was early understood that solidification with fast cooling rates resulted in brittle components while slower cooling yielded enough ductility to keep the cast parts in one piece when handling them. This historic development of cast irons in China contrasts with the fact that cast irons became recognized in Europe only during the 14<sup>th</sup> century AD.

Cast iron was such an "easy" material to process that it soon allowed gigantism. This applies to the use of cast iron that was selected to erect impressive sculptures such as the Cangzhou lion in Fig. 1.3 or the famous pagoda in the Yuquan temple. With some delay, the same happened in Europe with the 35 km of cast iron pipes and other components that were installed during the second part of the 17<sup>th</sup> century to bring water to the dozens of jets in the garden of the Versailles castle [VER1665] so as to satisfy the egocentrism and megalomania of one single human being.



**Figure 1.3. Iron lion of Cangzhou, 953 AD.**

The development of cast iron followed the progress of iron processing which is nowadays known in detail with the evolution in Europe of the Catalan forges to larger and larger blast furnaces. The state of the art at the beginning of the 19<sup>th</sup> century has been described by Karsten [KAR1816], including a detailed description of the work by de Réaumur at the beginning of the 18<sup>th</sup> century on the solid-state heat treatment of cast irons to give malleable cast irons and cemented iron. The two routes for making steel, i.e. the direct reduction through

a pasty state that gave "wrought" iron and remelting and oxidizing of cast iron, were both used until the development of the Bessemer's converter. Although the metallurgy was not understood, and Bessemer wrongly concluded that air was fuel as many before him [COZ17], the breakthrough was realised and steelmaking could leap from kilograms per day to tonnes per hour. This is only with the publication of the first Fe-C phase diagram at the very end of the 19<sup>th</sup> century that it was clearly understood that "wrought" iron, steel and cast irons belong to the same family.

Iron ore processing used huge amounts of charcoal so that optimizing it became a necessity certainly very early, and this implied increasing the maximum furnace temperature. To achieve this, blast furnaces have become increasingly taller with better and better control of the air blown onto the charge. In the early 18<sup>th</sup>, charcoal started to be replaced by coke for its better mechanical properties with the drawback of adding sulphur to the melt. For later processing, the liquid cast iron could be tapped into a trough made in the sand floor of the foundry and flowed into impressions made by the foundryman's foot on either side of the trough. Because the orientation of the foot-sized ingots along the trough resembled piglets feeding at a sow, the small ingots became known as pig iron.

Even though cast iron metallurgy was not yet mastered, casting technology was already in an advanced stage. This is illustrated with Berlin iron (fer de Berlin) jewellery that came in fashion during the early 1800's when Prussia needed to finance their war against Napoleon. The Prussians were asked to turn in their gold jewellery to raise funds for the war and were given iron jewellery in return. Berlin iron was sand-cast and then lacquered black. Many such pieces can be found in museums in Continental Europe, but also in Brazil where the fashion was exported at the same time the country built its first blast furnaces; see Fig. 1.4.



**Figure 1.4. Brazilian cast iron necklace following the fashion known as Berlin iron, early 19<sup>th</sup> century [ARA21].**

At the same time, cupolas and other kinds of furnaces for melting and processing irons and steels developed. In present days, blast furnaces define facilities providing pig iron for immediate use, particularly in integrated steel mills. Cupolas, in contrast, were designed for manufacturing stocks of cast iron to be processed later. They evolved along the time and became the most usual means to melt the charge in foundries. Today, high volume foundries

use a combination of cupola and electric induction furnaces to melt the iron. The melting costs of both techniques are similar, but the cupola has a productivity advantage. Large cupola furnaces can melt more than 100 tonnes per hour from a single furnace while the largest induction furnaces can only produce approximately 30 tonnes per hour. Despite the productivity advantages, the cupola will eventually be relegated to the history books. In Europe, the cupola will likely be phased out by 2050 as part of the Net Zero European Green Deal. Good for the environment, but potentially devastating for the European foundries who must continue to face international competition.

### **1.3 The main steps during the modern era (Anthropocene)**

Being optimistic, scientific and technical understandings are intermixed with industrial progresses, though these latter may often be leading for economic concerns. As for iron and steel, this was put in an historical perspective by Le Coze who stressed the technical evolution between 400 BC and 1400 AD in contrast to the explosive and parallel scientific and technical changes since then [COZ00]. The advent of chemical analysis, microscopic observations and other metallographic tools such as X-rays supported the improvements of materials properties.

Until the 19<sup>th</sup> century, the composition of the cast parts was given by that of the iron ore [WIT59] and also, though not understood at that time, by the minerals added to generate the slag. The importance of the slag composition for limiting iron loss (as FeO) and to remove sulphur from the coke and phosphorus from the ore has developed progressively, mostly in the 20<sup>th</sup> century. Slag is most generally described by its basicity which is the ratio of basic oxides (CaO, MnO, FeO, Na<sub>2</sub>O) over acid oxides (SiO<sub>2</sub>, P<sub>2</sub>O<sub>5</sub>). By controlling the composition of the slag and the temperature at the metal/slag interface, it is possible nowadays to get out of the blast furnace a cast iron with the desired silicon content. Beyond the cast iron industry, modern steelmakers have taken slag science to new heights, leading to the expression: “take care of the slag and the iron will take care of itself”.

Until the mid of the 20<sup>th</sup> century, the main concern was low ductility and associated moderate tensile strength because of the lamellar shape of graphite, see the bottom-left micrograph in Fig. 1.5. In the 1940s, following earlier attempts in Germany, Morrough and Williams in England and Millis and co-workers in America sought a way to ball graphite. The British (at BCIRA) found that additions of less than 0.1% cerium were sufficient to cause the graphite to grow in the form of individual spheroids instead of flakes. The Americans (at Inco) found that additions of approximately 0.05% magnesium would do the same thing. The Inco magnesium process eventually won the battle on technical grounds and the annual worldwide production of spheroidal graphite (aka nodular graphite or ductile) iron (SGI) has since grown to more than 25 million tonnes.

The modification of the graphite shape from flakes to nodules had a profound affect on the properties and the market potential of cast iron. In comparison to grey iron, the tensile strength tripled, the stiffness increased by 50% and ductility or elongation changed from nearly 0% to more than 5%, and up to more than 25% with a ferritic matrix. This quantum step in cast iron technology is illustrated in Fig. 1.5 for the case of cast iron pipes manufactured by the Pont-à-Mousson company that was created in the mid of the 19<sup>th</sup> century. This figure presents the parallel evolution of the elongation at rupture and of the microstructure of the cast irons. The

microstructure at the turn of the 20<sup>th</sup> century was certainly much alike that of Versailles' pipes that is illustrated here. Brittleness of cast iron parts was a concern, not only because of the lamellar shape of graphite, but also because the parts contained large precipitates of eutectic cementite and some phosphides. The treatment of the melt or the selection of iron ores allowed halving the phosphorus content and thus suppressed phosphides. At about the same time was introduced the centrifugal process in which the melt is poured in a water-cooled and rotating metallic die. This led to a significant refining of the microstructure of lamellar graphite irons (LGI), in particular by shortening the graphite lamellae. The dramatic change in the 1950 is due to the switch to SGI instead of LGI.

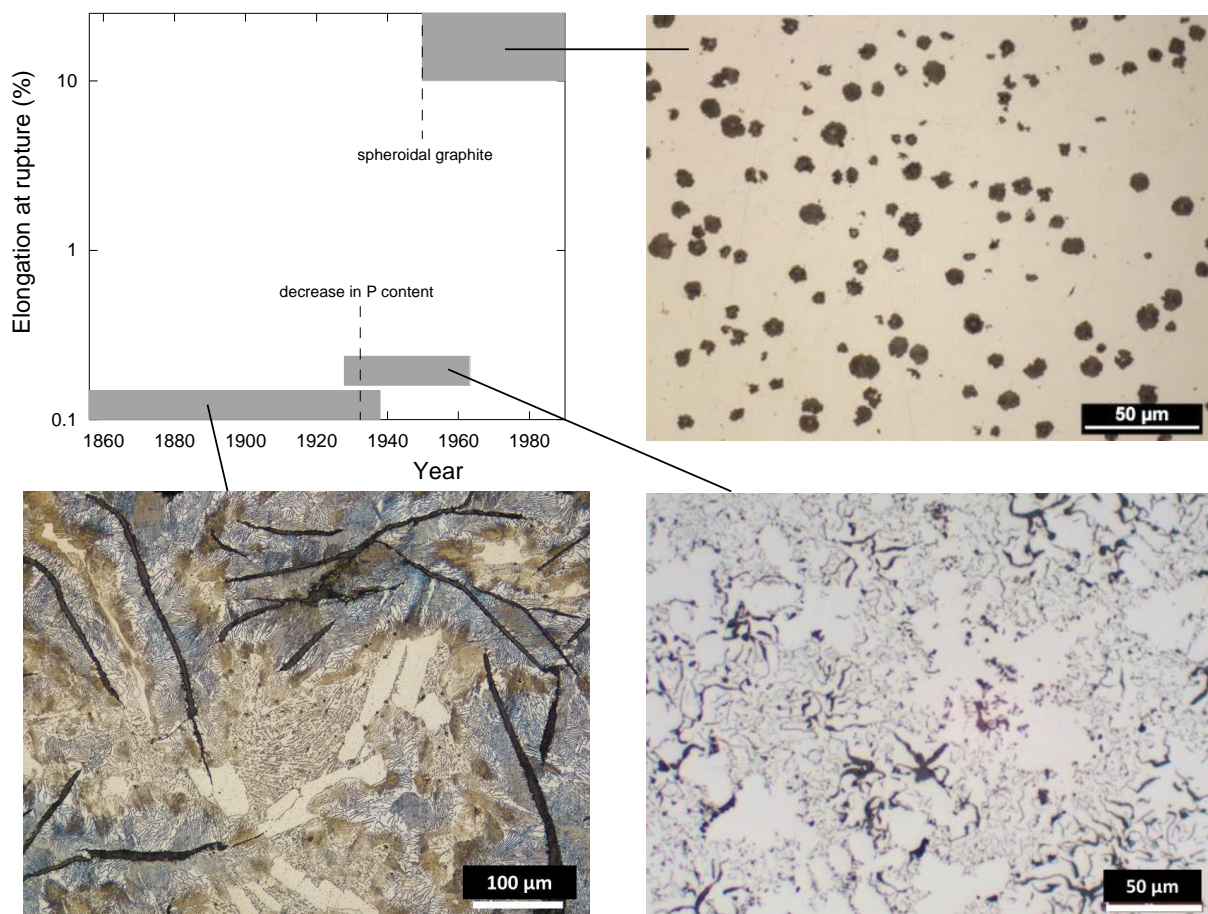


**Figure 1.5. Evolution of the elongation at rupture of cast iron used for water pipes (adapted from Lesoult et al. [LES84]) and of their microstructure. Graphite appears in dark contrast in the micrographs. The samples were etched so as to reveal the constitution of the matrix, which is pearlite in the historical material (with some coarse eutectic cementite) and ferrite in the two centrifugally cast pipes. Note that centrifugally cast LGI and SGI are both heat treated for full graphitization just after casting.**

Millis et al. also received a patent in 1949 for a grey iron having improved properties because graphite assumed a more compact shape than usual flakes. The compact graphite shape was achieved by adding a controlled amount of magnesium, and such irons became later known as compacted graphite irons (CGI). Interestingly, the patent was applied for in 1948 on the same day as Millis' more famous ductile iron patent, and the two patents were

granted on the same day in 1949, with US patent number US2485760 for SGI and US2485761 for CGI. CGI has better mechanical properties than LGI and is much less prone to microporosity than SGI. Critically, for modern engine applications, CGI also has higher thermal conductivity than ductile iron. However, it was only in the 1960s that it was found interesting to purposely generate this intermediate graphite form, see the review by Nechtelberger et al. [NEC82]. CGI has thus been in use for a long time but this was only for niche applications until the development of a proper thermal analysis control of melt preparation just before casting. The first series production of CGI engine for passenger vehicles was launched by Audi in 1999 and since the beginning of the 21<sup>st</sup> century CGI is breaking the market of automotive engines and components, though not yet appearing as such in production trends that differentiate data only considering LGI, SGI and malleable irons [STE19a].

Nowadays, graphite is industrially spheroidized by simultaneous addition of magnesium and **rare earths (RE)**. In contrast, there are several ways to generate compacted graphite as reviewed by Nechtelberger et al. [NEC82]. However, the most usual is by limited additions of Mg and RE when compared to SGI. Fig. 1.6 shows the change in graphite nodularity as function of Mg content [DAW02], with indication of the domains and typical examples of graphite shape for LGI, CGI and SGI. Note that the nodularity was set negative for lamellar graphite to emphasize that the industrial nodularity scale is defined for compacted and spheroidal graphite and not for lamellar graphite for which letters (A-E) are used to differentiate the various shapes [DAW03]. The evolution of ultimate tensile stress (UTS) with nodularity for 85-100% pearlitic cast irons is also illustrated.

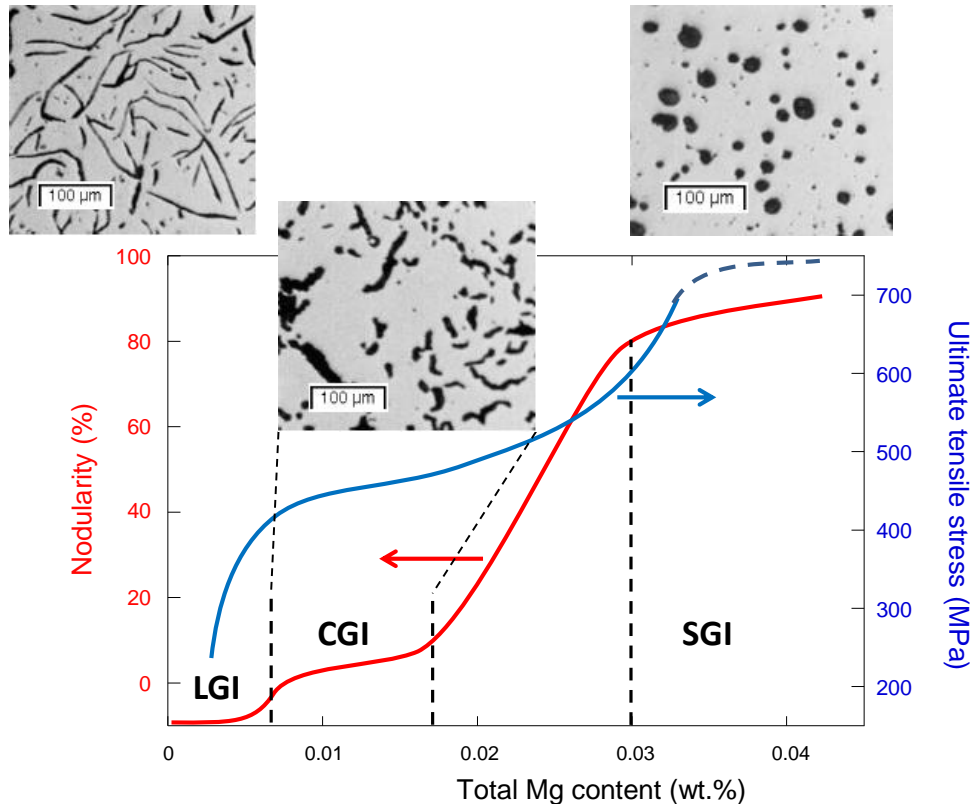


**Figure 1.6. Evolution of graphite shape and UTS (pearlitic matrix) with Mg content, illustrated for a base iron sulphur content of 0.013% [DAW02].**

The composition of most of the silicon cast irons is selected on the basis of the graphite shape as illustrated with Fig. 1.7 adapted from Elliott [ELL88]. This graph shows the projection of the iron-rich corner of the Fe-C-Si diagram with the solubility limit of carbon in austenite (at eutectic temperature) that defines the lower limit of the cast irons domain. The upper limit is at carbon contents slightly larger than the eutectic line. White cast irons are low-silicon hypo-eutectic alloys and are more and more replaced by high-Cr cast irons for wear properties. Their use is mostly limited to manufacture malleable irons by heat-treatment. LGI is mostly hypoeutectic, with the austenite dendrite network guaranteeing a minimum rupture elongation. If LGI could be made with higher carbon content, the industry would do it to maximise thermal conductivity. But there is a need to restrict the carbon content to ensure (i) that the graphite doesn't cause brittleness, and (ii) that there is enough austenite to carry the load and compensate for the ill-effects of the graphite. CGI and SGI are near-eutectic alloys for minimizing microporosity.

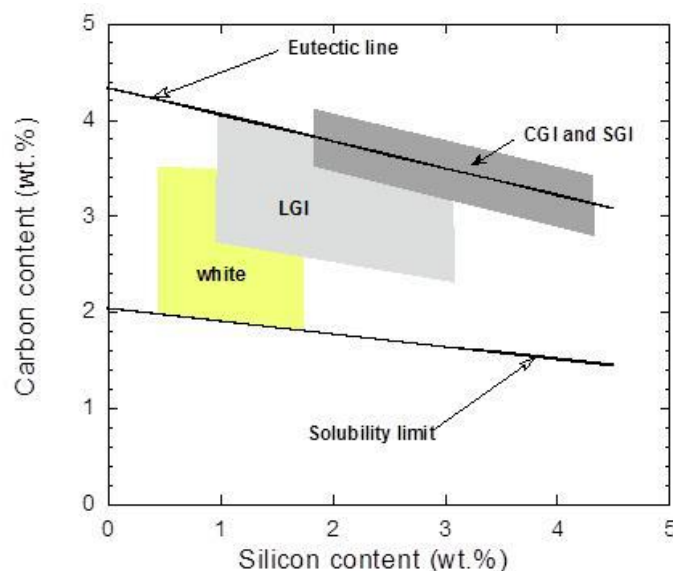


**Figure 1.7. Carbon and silicon composition ranges of silicon cast irons (adapted from Elliott [ELL88]).**

The trend for higher silicon content for SGI and CGI started in the early 1980s with the development of the so-called SiMo cast iron for exhaust manifolds. Higher Si content raises the eutectoid temperature and thus increases the maximum service temperature while Mo is added as it gives rise to a network of eutectic carbides that improve creep properties. However, as exhaust temperatures continue to rise to satisfy emissions requirements, SiMo exhaust manifolds and turbocharger housings are being widely replaced by stainless steels that do not incur a phase transformation. These higher temperature capabilities outweigh the fact that oxide scales are generally better adhering on cast irons than on steels.

Since the 2000s, high-silicon SGI has developed as the yield stress and ultimate tensile stress are linearly increasing with Si concentration because of partial ordering of the ferritic matrix. Mechanical properties similar to pearlitic irons may thus be obtained with the advantage of decreasing tool wear during machining because the matrix is more homogeneous. More generally, there is a wealth of research for improving mechanical properties of the matrix of



cast irons. Amongst the many possibilities that have been considered, austempered cast irons are slowly showing great industrial potentialities.

**1.4 An overview of present cast iron production and concerns**

Cast irons are found in pipes, machinery, railway, automotive and energy industries, as well as in cooking and ornaments in public areas, etc. Fig. 1.8 differentiates the market share for SGI (about 25 million tonnes per year) and LGI (about 50 million tonnes per year) based on the 2018 USA data [AFS19] that are certainly representative of the world market.

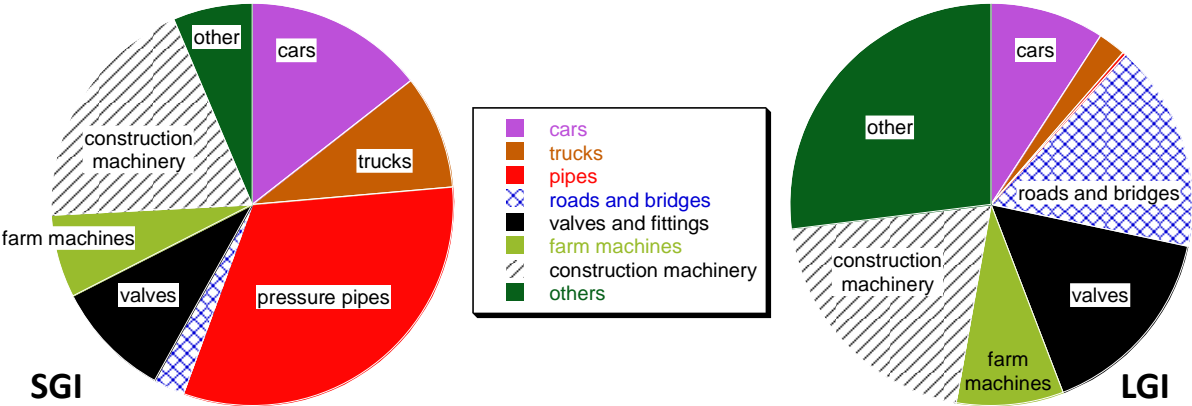


**Figure 1.8. Market distribution in USA in 2018 for SGI (to the left) and LGI (to the right) [AFS19]. CGI data is included in the LGI data, as the primary application for CGI is cylinder blocks and heads.**

After the short panic the COVID-19 pandemic created in 2020, things appear to run again following the same steps as before. In particular, there is no more any question on the fact that the demand for goods transportation must be met, which led to the development of gigantic cargos that require corresponding engines (Fig. 1.9). These engines are run with high-sulphur oils that pollute air to an incredible level, but significant development is ongoing in this field as well, with low-sulphur fuel mandated since 2020, longer-stroke engines that provide efficiency improvements by reducing rpm, and the likely introduction of ammonia as an alternate fuel in the near-term. Stronger cast irons are required to ensure that this demand can be satisfied with more efficient engines and with decreased pollution.

As in the on-road sector, where the peak firing pressure in heavy duty commercial vehicle engines has increased from approximately 200 bar in 2010 to 250 bar today (as for 2021) to provide higher thermal efficiency and lower emissions, the peak firing pressure in large marine engines is also increasing. Over the past ten years, grey iron piston rings have been replaced by CGI rings to contain the higher thermal and mechanical loads and today, many of the largest cylinder liners, measuring up to four metres in length and 15 tonnes per piece, are being converted from grey iron to CGI. This is an excellent example of cast iron research contributing directly to environmental improvements.



**Figure 1.9. A large ship engine (Wärtsilä X62 engine). The steps on the left side can be used for an estimate of the scale. (<https://www.wartsila.com/media/news/08-01-2015-wartsila-x62-engine-now-fully-approved-and-available-to-the-market>).**

In the introduction, we abruptly stated that cast irons are ‘green’ materials with respect to others cast alloys (cf. Fig. 1.1). This is certainly not all the truth. Similar to other engineering materials, the production of cast irons has steadily increased since the 19<sup>th</sup> century, with the associated increase of environment impacts (pollution, energy and primary resource consumption, green-house gas -mostly CO<sub>2</sub>- emissions, ...) to reach an overall level that has become unacceptable. However, sustained efforts have long been made to decrease pollution from fumes during melt preparation (both blast furnaces and other foundry furnaces). Because the cupola will be banned in Europe in 2050, the full circle – from only blast furnaces and cupolas to only electric – will be closed in about two centuries.

More recently, fine and complete life cycle analyses (LCA) have been carried out, which trace the environment impacts at different steps of the whole extraction and production process (see for instance [MIT17, JOL17, JHA17, SAL19, STE19b] and an example in Fig. 1.10). These tedious works are necessary guides for still reducing energy consumption and CO<sub>2</sub> footprint of casting industry. Recyclability is also a positive point for cast irons. The percentage of recycled and downcycled material in the total worldwide supply of grey cast irons has reached about 70%, compared to less than 50% for cast steels or Al-alloys [GRA20]. Finally, a particular feature of aluminium and cast iron castings is the use of huge amounts of sand, with green sands that may be recycled while sands that have been chemically bound cannot. It is noted that the gravity sand casting of passenger vehicle aluminium cylinder blocks uses approximately four times more chemically bonded sand than an equivalent cast iron cylinder block.

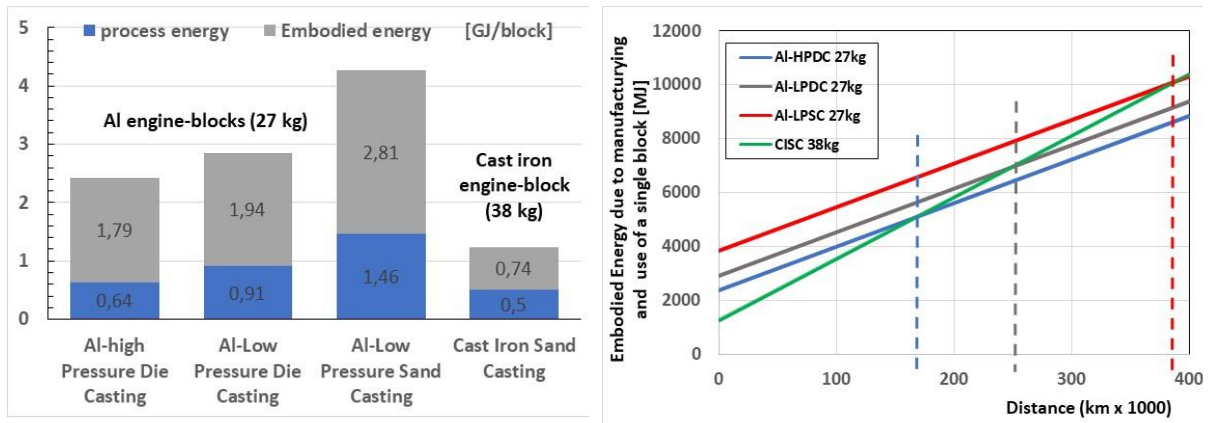


**Figure 1.10. a) Energy for manufacturing a 1.6 L diesel engine block made of cast iron (38 kg) or Al alloy (27 kg); b) Total (manufacturing + use) energy as a function of driving distance for the same engine block in an automotive vehicle of 1200 kg with an average consumption of 7 L/100 km; vertical dotted lines mark break-even distances between cast iron and Al-alloy produced by different casting processes; the average life of such a vehicle is approximately 220 000 km. (adapted from [SAL19]).**

Stronger materials, like CGI, also reduce the weight of conventional LGI components, contributing to the environment by reducing the melting demand. If CGI reduces the weight of a grey iron cylinder block by 15%, the saving corresponds to 7,500 tonnes per year of castings and 10,000 tonnes per year of liquid metal for every one million 50 kg cylinder blocks. In turn, this saving corresponds to a reduction of 100 MJ of energy for electric melting and 500 tonnes of CO<sub>2</sub> per year. In transportation industry, the weakest point of cast irons is clearly their high density, which evidently suggests to substitute them by lighter materials, as Al-alloys or even Mg alloys. However, this solution needs to be validated for each component, since the gain in energy consumed (or CO<sub>2</sub> generated) during service can not always counterbalance the excess of energy used for the production of lighter alloy (cf. Fig. 1.1 and Fig. 1.10-a). As an example, Fig. 10-b (from [SAL19]) shows that the break-even distance for paying back the substitution of cast iron by Al-alloy in a given engine block is similar or even longer than the service life of the vehicle.

While considerable attention is given to the electrification of passenger vehicles, the market penetration to date – and the likely development over the next decade – is not as rapid as most media reports suggest. The pie charts to the right of Fig. 1.11 show passenger car sales in 2020 for Europe, the US and China according to fuel, namely petrol, diesel, hybrid, electrified (plug-in hybrids plus battery electric vehicles) and alternate fuel (propane, natural gas, etc). Globally, passenger vehicle electrification in 2020 was less than 10% and, as shown in Fig. 1.11, global sales are expected to be approximately 30% in 2030. Many of these vehicles will be hybrids, also containing an internal combustion engine. On the commercial vehicle side, there is no foreseeable alternative to the diesel engine for long-haul heavy duty goods transport and there is a widespread consensus in the industry that the diesel engine will dominate until at least 2040. Even if the transformation to electrification becomes complete, the internal combustion engine will remain on global road for decades after production stops. Clearly, there is a need for continued research in cast iron to make the internal combustion as environmentally effective as possible.

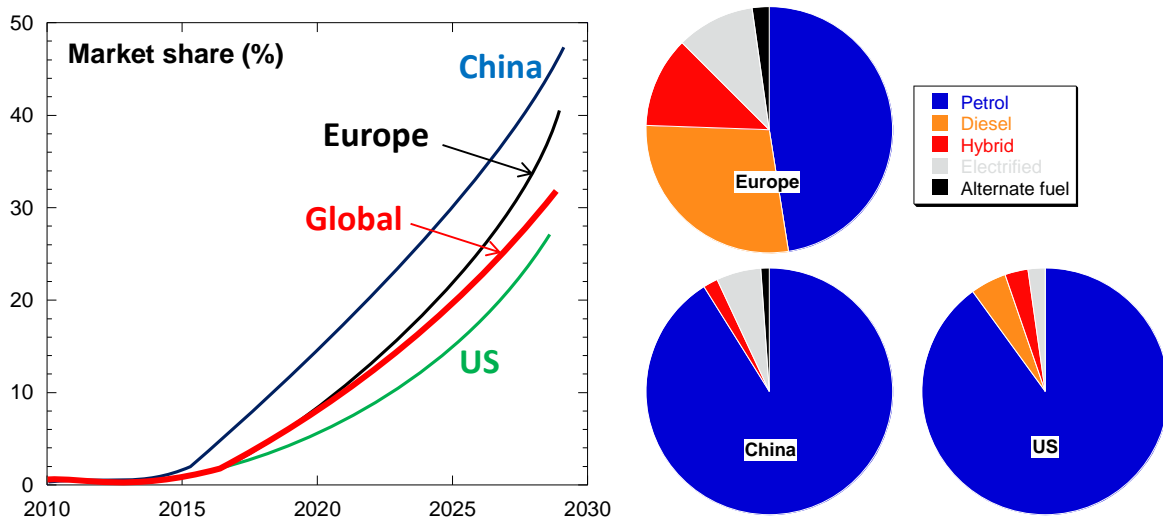


**Figure 1.11. Penetration of electrically charged vehicles is poised to remain below 50% for at least the next decade (adapted from Automotive News, 17 May 2021). The pie charts show passenger car sales in 2020 for Europe, the US and China according to fuel.**

### 1.5 Future outlook: a material worthy of further research

At the end of the 20<sup>th</sup> century, progress in metallurgy has benefited from the development of computers and small-scale analytical methods. Computer capabilities have been first used for developing simulation tools for describing the successive processes of melt preparation, filling and casting, and several commercial software packages are nowadays available. Another important application is in the control of melt preparation just before pouring that makes use of thermal analysis with dedicated rapid curve analysis so that a green or red light is provided prior to casting, enabling the foundry to adjust the iron and to ensure that only good iron is poured. However, the most exciting advances for metallurgists are the capabilities of modern apparatus to investigate matter at small-scale, going down to atom scale as with the so-called Atomic Resolution Microscopes. This certainly opens ways to improve the understanding of microstructure formation in cast irons.

In general, it is desirable for lowering the costs to use cast iron parts in their as-cast state, which means avoiding heat-treatments. This implies that the graphite shape and the matrix constitution that were sought for are obtained, which may be challenging in parts having complex shapes. As a matter of fact, the shape of graphite is highly sensitive to small changes in both melt preparation and cooling rate. Furthermore, changes brought about by these factors are closely inter-related; see Fig. 1.12. After standard preparation, a cast iron melt yields flake graphite, while a full or partial spheroidizing treatment after desulphurisation is used to get spheroidal or compacted graphite, respectively. However, in a casting with various section thicknesses, the graphite shape depends on the local cooling rate. The following changes can be noticed as the cooling rate increases:

- Lamellar graphite to undercooled graphite.
- Compacted graphite with low nodularity to nearly or fully spheroidal graphite.
- Irregular spheroidal graphite to well-rounded one.

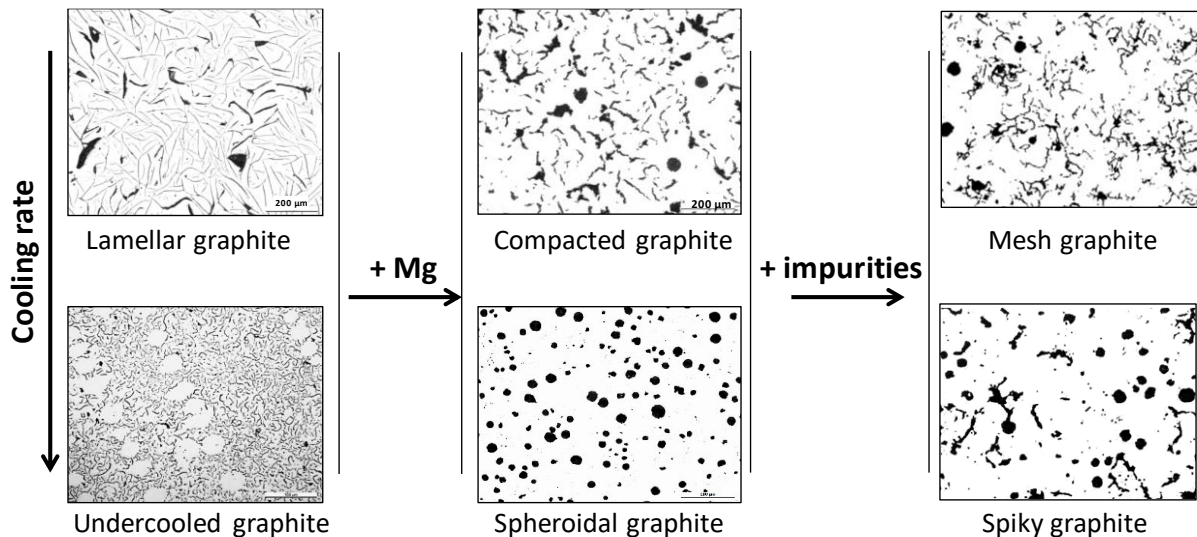


**Figure 1.12. The interplay between chemical and cooling rate routes.**

Inoculation helps controlling graphite shape, e.g. avoiding undercooled graphite in LGI that would conduct to a ferritic matrix while fully pearlitic LGI are preferred for mechanical properties. Furthermore, obtaining a fully graphitic SGI upon casting definitely relies on appropriate inoculation of the melt for avoiding the formation of metastable eutectic. Understanding the bases of the formation of graphite nuclei [SKA93, LOP98] has allowed defining new inoculant compositions in particular to fight against fading and thus against porosity in SGI. This is an area of fierce competition on an industrial point of view, and of sharp stimulation for scientists. The main concern is understanding early precipitation and growth of graphite, in particular in relation with the presence of additives in the inoculants. Recent results on hypereutectic alloys strongly suggest that both primary and eutectic growth of graphite needs a significant undercooling to proceed, and that this undercooling depends on melt chemistry [CAS20]. This should lead to revisit thermal analysis records as well as modelling approach of cast iron solidification.

The additives mentioned above are elements prone to react with oxygen, sulphur and nitrogen to precipitate compounds that are active in the process on graphite nuclei formation. However, at the same time, many of these elements also affect graphite shape and are then seen as impurities leading to graphite “degeneracy” - i.e. the development of unwanted graphite forms – when present in the melt at a level above a critical limit that may be so low that these so-called poisoning elements can often be classified as trace elements. These degeneracies are illustrated in Fig. 1.12 with mesh and spiky graphite in the case of SGI, but the phenomenon is also known for LGI and CGI. While the role of these impurities have been described since a long time as can be seen in several reviews [SAW68, JAV95], understanding how they actually proceed to induce graphite degeneracy is still in its infancy [LAC22a]. In practice, rare earths are used to fight the deleterious effects of trace elements, but again very little has yet been made to describe the kinetics of the very many precipitation and dissolution processes behind rare earths additions [LEK09, LEK18].

The precise mechanism of the action of the spheroidizers is still unknown, or more precisely, still controversial. The first effect of magnesium and rare earths has long been associated to their high affinity with oxygen and sulphur, i.e. considering that change in graphite shape is

controlled by tightening oxygen and sulphur as oxy-sulphides. Subramanian et al. [SUB82] therefore suggested associating the different forms of graphite with the thermodynamic activity of residual oxygen and sulphur. The presence of some residual magnesium and RE dissolved in the liquid of a melt dedicated to SGI and CGI appears however essential for achieving the desired graphite shape with the associated challenge of understanding the exact way these elements interact with graphite.

In the same way as for graphite shape, the constitution of the matrix in the as-cast state depends both on the chemical composition and on the cooling rate, with a strong effect of graphite fineness. Increased inoculation in SGI and decrease of graphite size in LGI eases the transformation of the matrix in the stable system, i.e., increases the amount of ferrite. On the other hand, increased cooling rate favours the transformation in the metastable system with precipitation of pearlite. Adding Sn and Sb is used industrially to avoid the formation of ferrite, with the risk of graphite degeneracy if added at too high levels. It is thus usual to add also Mn and Cu which are less potent for pearlite formation but are also easier to tolerate when considering the avoidance of deleterious graphite shapes. An important feature of the eutectoid transformation is the effect of microsegregations that are issued from the solidification step. While they can be easily described [EIK20a, EIK20b], their mastering for controlling the eutectoid transformation has not yet given the expected results. Microsegregation is also a concern for achieving controlled austempering of ADI parts as well as for mastering so-called dual-phase microstructures. Here, it is worth noting that recent works have demonstrated that 1-3 wt.% Al added to a silicon cast iron inverses silicon segregation [MUH15, FRA19]. This finding may soon be exploited to decrease microsegregation and thus improve matrix properties of cast irons.

Improvements of melt and casting processes as well as mastering of microstructure formation are triggered by the need for better service properties within a framework of competition between materials. For dynamic properties, and in particular in the case of SGI, it is not only the matrix constitution that is important but also the casting defects such as porosity. Some progress has been made in describing porosity formation [KWE20] though still not accounting for the mechanical effect due to graphite bulging that has long been recognized but has rarely been accounted for [LES09]. Also, the mechanical behaviour of cast iron is intrinsically elasto-visco-plastic with a strong effect of damage which has led to a wealth of complex modelling approaches that are hardly introduced in foundry software packages. Ad hoc models fitted to experimental overall mechanical behaviours are often preferred. Fatigue properties are also of importance, especially for thin wall castings whose surface quality could be improved by use of dedicated sands, see Fig. 1.13.

Beyond the metallurgy itself, significant improvements continue to be introduced to the mechanical engineering side of the foundry. Over the last 25 years, complex components like cylinder blocks and heads have progressively evolved from green sand casting to fully-enclosed core packages. In parallel, minimum wall thickness for passenger vehicle cylinder blocks has decreased from 4.5 mm (+/- 1.0 mm) to the current state-of-the-art of 2.7 mm (+/- 0.5 mm). And the development has not stopped. Until recently, 3D sand printing was preserved for rapid prototyping, but many series production foundries are now embracing additive manufacturing for the production of highly complex cores. Without draft angles, these complex

cores can add to weight reduction and eliminate costly – and energy consuming – post processing of the castings.

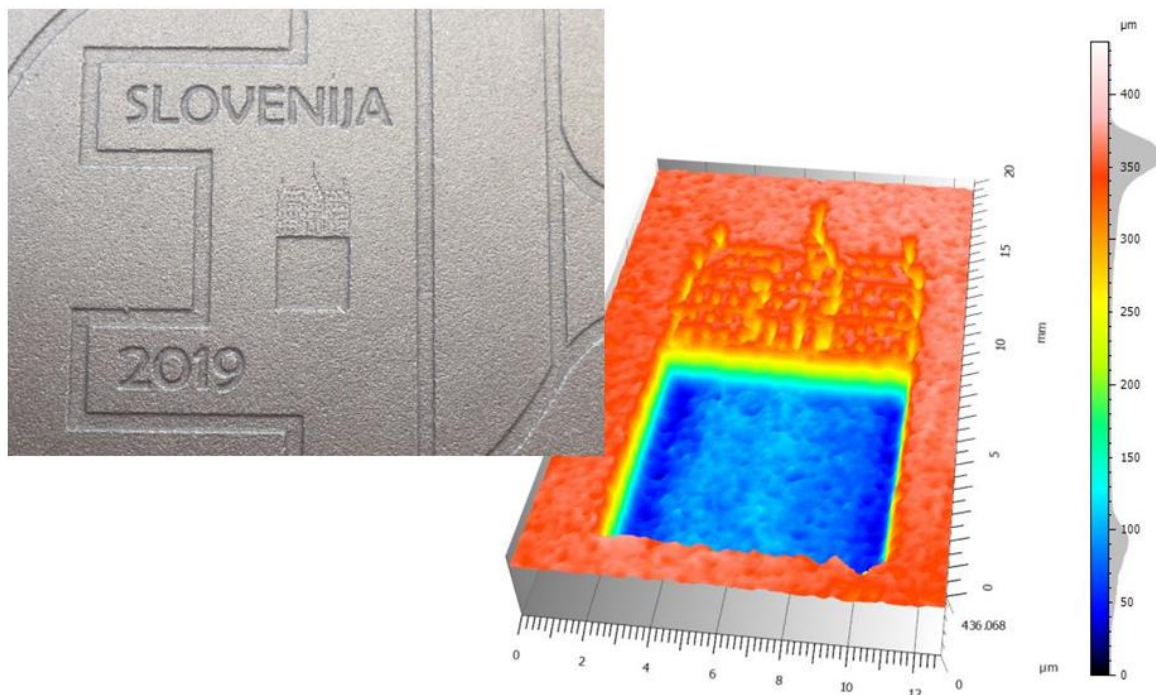


**Figure 1.13. The photograph on the left shows the central part of a medal cast by the lost wax process, with the square in the centre being one cm<sup>2</sup> in size. The colour map on the right shows the surface roughness in the very centre of the medal (see the scale to the right), with the water basin in front of the castle (courtesy Sandrine Duluard, CIRIMAT).**

### 1.6 Time to go in

We continue to judge the iron foundry by its grey walls, despite the significant progress in cleaning up the dust, see Fig. 1.14. The real image should be the atoms, not the walls. Cast iron is the first composite material, and it remains one of the most versatile composites available today from a technical point of view, and one of the most fascinating from a scientific point of view. In the future, iron foundries will produce castings with different graphite shapes in different areas of the component to optimise specific properties where they are needed. While the iron foundry world may struggle for image, our present-day ability to control alloy additions to within 10 grams per tonne will soon seem rudimentary. The real iron-age is just beginning and the next iron will build its own legend.

To go in and support this expected evolution, we need first to have a basic knowledge of the relevant phase diagrams (Chapter 2) and of the solidification step as observed daily with thermal analysis (Chapter 3). We could then follow the chronological order of nucleation of graphite and the related inoculation of the melt (Chapter 4), or select to proceed directly to primary growth of graphite (Chapter 5). The eutectic transformation is discussed in two successive chapters, Chapter 6 for the case of flake graphite and for white eutectic, and Chapter 7 for spheroidal graphite mainly, but in which eutectics with chunky graphite and compacted graphite are also mentioned. Chapter 8 is dedicated to various effects of impurities and trace elements on the expected graphite shape. Here and there, solid-state

transformations will have been mentioned which are more specifically considered in Chapter 9. Throughout these chapters, reference is made to modelling and some answers to the questions that modelling might address are presented in Chapter 10.



**Figure 1.14. View from above of the pouring of cast iron in a modern and clean sand-mould semi-automatic line (credit: Sakthi foundry, Portugal).**





# Chapter 2 – The Fe-C-Si phase diagram and carbon equivalent

The microstructure of a foundry alloy depends on its entire history, from the preparation of the cast iron for casting and solidification, to cooling and eventual heat treatment, and finally to the service conditions. During this process, a number of phase transformations take place, which are key steps in describing and understanding how the microstructure was built and evolves. Each of these transformations takes place with its own thermodynamic driving force which can, in most cases, be appropriately expressed by reference to the equilibrium phase diagram. Two equilibrium systems are to be considered, the stable system in which the carbon-rich phase is graphite and the metastable system in which it is cementite. The two corresponding equilibrium phase diagrams are presented in this chapter.

## 2.1 The Fe-C isopleth sections

In most textbooks, silicon cast irons are differentiated from carbon steels as being Fe-C based alloys with a carbon content higher than 2.0 wt.%. This value refers to the maximum solubility of carbon in austenite in the binary Fe-C system and relates to the **stable eutectic**, i.e. to the reaction liquid (L)→austenite ( $\gamma$ )+graphite at 1154°C. The part of this stable Fe-C diagram that corresponds to the eutectic is shown with bold lines in Fig. 2.1-a. It is also seen in Fig. 2.1-a that the **metastable** eutectic liquid (L)→austenite ( $\gamma$ )+cementite ( $\text{Fe}_3\text{C}$ ) lies only a few degrees below the stable one in the binary system, at 1148°C.

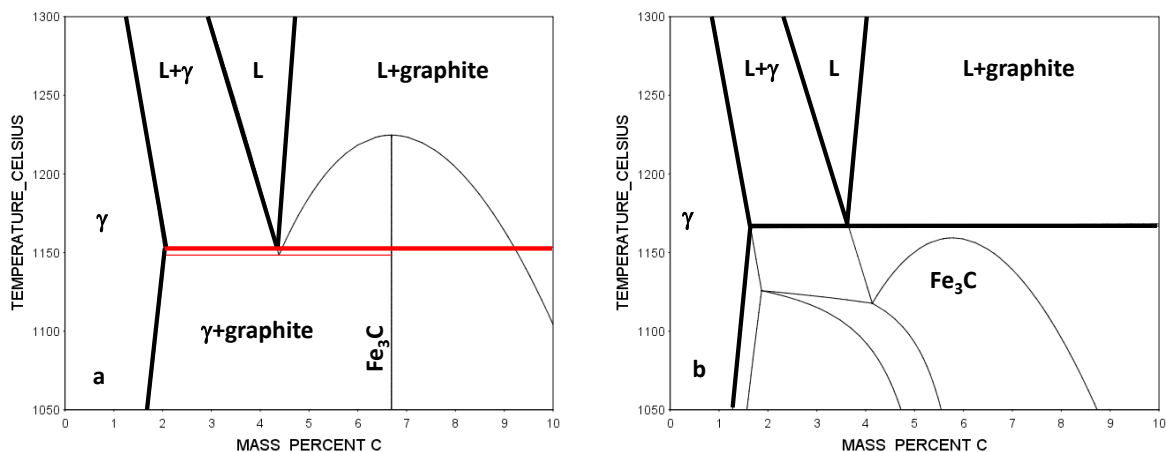


**Figure 2.1. Binary Fe-C phase diagram (a) and Fe-C isopleth section of the Fe-C-Si phase diagram at 2.5 wt.% Si (b). Bold lines are for the stable system, thin lines for the metastable one [TCFE8].**

Fortunately, adding silicon to the melt increases significantly the temperature difference between the stable and metastable systems as illustrated with the section of the Fe-C-Si phase diagram at 2.5 wt.% Si in Fig. 2.1-b. Such a section is called a Fe-C **isopleth section** of the phase diagram. The two graphs in Fig. 2.1 were calculated using the **TCFe8** database and all calculations performed similarly will be referenced [TCFE8] from now on. This chapter is

concerned only with the solidification range while the domain relevant for solid-state transformations will be dealt with in Chapter 9.

Isopleth Fe-C sections are essential in the metallurgy of silicon cast irons because these alloys can be described as behaving like pseudo-binary Fe-C alloys. In practice, this statement means that the segregation of silicon and other alloying elements during solidification is not pronounced, i.e. the composition of the liquid can be considered to remain in the same isopleth section: only the carbon content changes during solidification while the content of other elements remains unchanged. To know the equilibrium temperatures (austenite liquidus, graphite liquidus, stable and metastable eutectics) and the corresponding carbon contents, it is therefore sufficient to have access to the relevant Fe-C isopleth section.

Nowadays, the calculation of Fe-C isopleth sections can be performed using thermodynamic software packages with appropriate databases. However, if one considers a limited range of silicon contents, a simple and fairly accurate description of the phase diagram can be achieved using linear relationships as described in the following section. This has the great advantage of easily showing how to define the so-called carbon equivalent, CE, and the carbon equivalent austenite liquidus, CEL, which will be introduced in a later section where their difference will be evidenced.

## 2.2 Linear relations for describing the Fe-C-Si phase diagram

Comparing the binary Fe-C phase diagram and the isopleth section in Fig. 2.1, it is seen that the austenite liquidus,  $T_L^y$ , and graphite liquidus,  $T_L^g$ , appear straight in both of them. Further, the two austenite liquidus, on a one hand, and the two graphite liquidus, on the other hand, are nearly parallel to each other. This strongly suggests that these liquidus could be represented by planes in the Fe-C-Si system, see Fig. 2.2, and this has been found to apply for silicon contents in the range 0-3 wt.%.

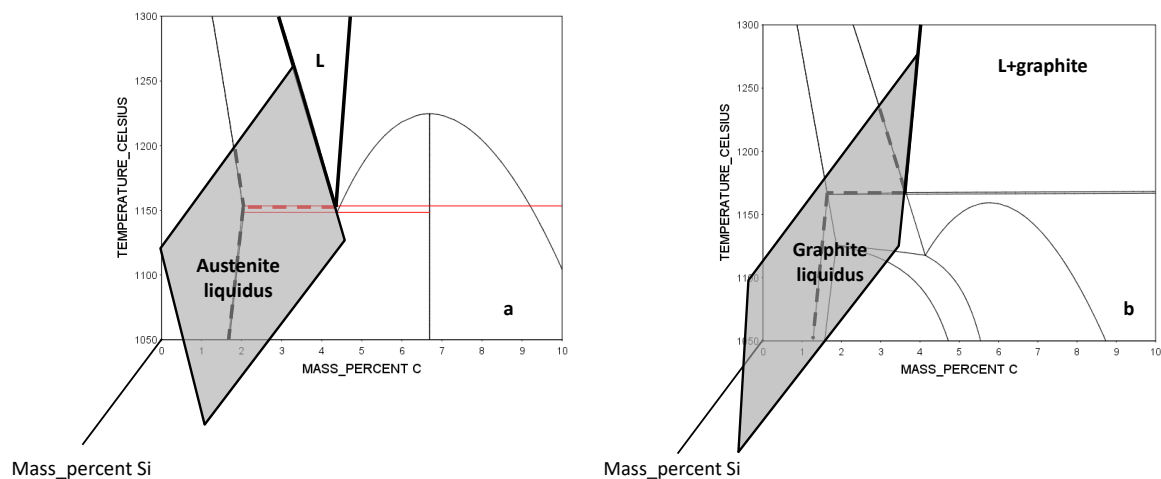


**Figure 2.2. Representation with planes of the austenite and graphite liquidus in the Fe-C-Si system, for silicon content lower than 3 wt.%.**

Such a representation corresponds to simple linear relation between temperature and composition (carbon and silicon contents):

$$T_L^\gamma = T_0^\gamma + m_C^\gamma \cdot w_C + m_{Si}^\gamma \cdot w_{Si} \quad (2.1)$$

$$T_L^g = T_0^g + m_C^g \cdot w_C + m_{Si}^g \cdot w_{Si} \quad (2.1')$$

in which  $T_0^\gamma$  and  $T_0^g$  are constants,  $m_i^\gamma$  and  $m_i^g$  are the liquidus slopes relative to element  $i$  for austenite and graphite, respectively, and  $w_i$  is the content in element  $i$  of the alloy (wt.%).

The constants in Eq. (2.1) and (2.1') were evaluated using: 1) The assessment of the Fe-C system [GUS85] for which the stable eutectic is given by the invariant point (4.34 wt.% C; 1154°C); 2) The slope of the austenite and graphite liquidus assessed by Heine [HEI95]; 3) A point along the eutectic line in the assessed Fe-C-Si phase diagram [LAC91]. The above equations could thus be expressed as follows, where the temperature is given in Celsius:

$$T_L^\gamma = 1576.3 - 97.3 \cdot w_C - 23.0 \cdot w_{Si} \quad (2.2)$$

$$T_L^g = -534.7 + 389.1 \cdot w_C + 113.2 \cdot w_{Si} \quad (2.2')$$

The reliability of the linear approximation of the liquidus surfaces could be confirmed by comparing the values calculated with Eq. (2.2) and (2.2') to those obtained from the TCFE8 database. This is illustrated in Fig. 2.3 for silicon contents of 0, 1, 2 and 3 wt.%.

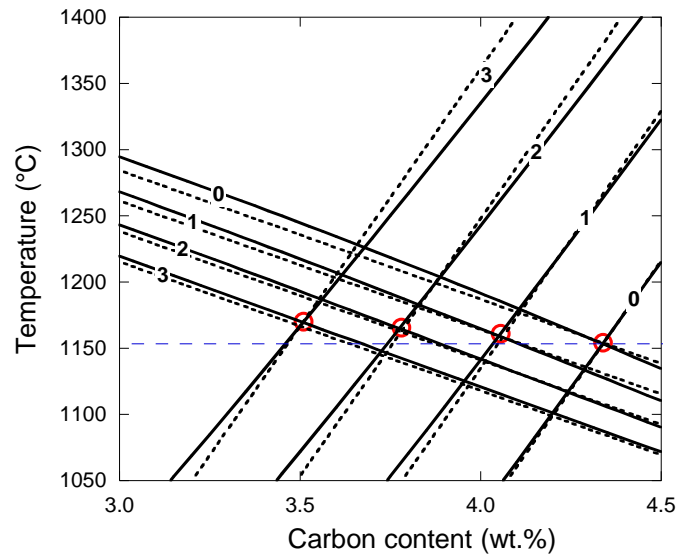


**Figure 2.3. Comparison of the austenite and graphite liquidus given by Eq. (2.2) and (2.2') (dashed lines) with those calculated with the TCFE8 database (solid lines). The numbers along the curves refer to the amount of silicon (0 to 3 wt.%), with the open red circles showing the eutectic point for each silicon content and the dashed horizontal line indicating the temperature of the binary Fe-C eutectic (0 wt.% silicon)**

The intersection of the two planes describing the austenite and graphite liquidus corresponds to the eutectic trough. By equating Eq. (2.1) and (2.1'), one thus gets the carbon content along the stable eutectic trough,  $w_C^{eut}$ :

$$w_C^{eut} = 4.34 - \frac{(m_{Si}^g - m_{Si}^\gamma) \cdot w_{Si}}{m_C^g - m_C^\gamma} \quad (2.3)$$

$$w_C^{eut} = 4.34 - 0.28 \cdot w_{Si} \quad (2.3')$$

The corresponding eutectic temperature,  $T_{EUT}$ , is obtained by inserting  $w_C^{eut}$  in the  $T_L^\gamma$  (or  $T_L^g$ ) expression:

$$T_{EUT} = 1154.02 + \left( m_{Si}^\gamma + 97.3 \cdot \frac{m_{Si}^g - m_{Si}^\gamma}{m_C^g - m_C^\gamma} \right) \cdot w_{Si} \quad (2.4)$$

$$T_{EUT} = 1154.02 + 4.246 \cdot w_{Si} \quad (2.4')$$

### 2.3 Extension to multi-component alloys

In the composition range of usual silicon cast irons, namely for silicon content lower than 3 wt.% as in section 2.2, and for low level of other alloying additions, the austenite liquidus,  $T_L^\gamma$ , and graphite liquidus,  $T_L^g$ , can certainly be represented by the following extended linear relationships of alloy composition:

$$T_L^\gamma = T_0^\gamma + m_C^\gamma \cdot w_C + \sum_i m_i^\gamma \cdot w_i \quad (2.5)$$

$$T_L^g = T_0^g + m_C^g \cdot w_C + \sum_i m_i^g \cdot w_i \quad (2.5')$$

where  $i$  is for any alloying element other than carbon.

The constants and the slope for carbon and silicon take the same values than those given above. To estimate the other  $m_i^\gamma$  and  $m_i^g$  values, points were selected in the assessed Fe-C-i phase diagrams that are listed in Table 2.1 where are also indicated the values of the austenite and graphite liquidus slopes that could be calculated with these data (see [REG20] for more details). The expressions thus derived are expected to be valid for silicon contents up to 3 wt.% and for any other alloying element up to 1 wt.%.

**Table 2.1 - Data used to characterize the effect of third elements on the binary Fe-C stable system**

i species	solid phases in equilibrium with liquid	$w_C$	$w_i$	T (°C)	$m_i^\gamma$	$m_i^g$
Cr	austenite, graphite and cementite	4.2	4.30	1156	-2.71	13.14
Cu	austenite and graphite	4.0	3.7	1172	-4.08	40.62
Mn	austenite, graphite and cementite	4.32	3.0	1139	-5.66	-2.40
Mo	austenite and graphite	5.0	12.6	1350	-10.3	-4.84
Ni	austenite and graphite	3.8	10.0	1128	-7.86	18.41
P	austenite, cementite and Fe <sub>3</sub> P	2.2	7.1	954	-57.8	89.6
Si	austenite and graphite	3.78	2.0	1162.5	-23.0	113.2

The intersection of the two hyper-planes describing the austenite and graphite liquidus corresponds to the eutectic trough. By equating the two equations (2.5) and (2.5'), one thus gets the carbon content along the stable eutectic trough,  $w_C^{\text{eut}}$ :

$$w_C^{\text{eut}} = 4.34 - \frac{\sum_i (m_i^g - m_i^\gamma) \cdot w_i}{m_C^g - m_C^\gamma} \quad (2.6)$$

The corresponding eutectic temperature,  $T_{\text{EUT}}$ , is obtained by inserting  $w_C^{\text{eut}}$  in the  $T_L^\gamma$  (or  $T_L^g$ ) expression:

$$T_{\text{EUT}} = 1154.02 + \sum_i \left( m_i^\gamma + 97.3 \cdot \frac{m_i^g - m_i^\gamma}{m_C^g - m_C^\gamma} \right) \cdot w_i \quad (2.7)$$

$$T_{\text{EUT}} (\text{°C}) = 1154.02 + 0.46 \cdot w_{\text{Cr}} + 4.86 \cdot w_{\text{Cu}} - 5.00 \cdot w_{\text{Mn}} - 9.21 \cdot w_{\text{Mo}} - 2.60 \cdot w_{\text{Ni}} - 28.31 \cdot w_{\text{P}} + 4.246 \cdot w_{\text{Si}} \quad (2.7')$$

## 2.4 The carbon equivalent

The isopleth Fe-C sections as the one shown in Fig. 2.1-b are all similar to the Fe-C diagram in Fig. 2.1-a, with only a shift of the stable eutectic point to lower carbon content and higher temperature as silicon is increased. This led defining the carbon equivalent CE of a cast iron that indicates if an alloy is to the right or to the left of the stable eutectic point in the isopleth section. From the expression of  $w_C^{\text{eut}}$  in Eq. (2.6), one can express the carbon equivalent, CE, of an alloy as:

$$\text{CE} = w_C + \frac{\sum_i (m_i^g - m_i^\gamma) \cdot w_i}{m_C^g - m_C^\gamma} \quad (2.8)$$

With the data in Table 2.1, this writes:

$$\text{CE}_{99} (\text{wt.}\%) = w_C + 0.033 \cdot w_{\text{Cr}} + 0.092 \cdot w_{\text{Cu}} + 0.007 \cdot w_{\text{Mn}} + 0.011 \cdot w_{\text{Mo}} + 0.054 \cdot w_{\text{Ni}} + 0.303 \cdot w_{\text{P}} + 0.280 \cdot w_{\text{Si}} \quad (2.9)$$

It should be stressed that this expression is based on relatively recent assessed values for equilibrium, and in particular the reference carbon content for the eutectic is 4.34 wt.%. The corresponding equilibrium eutectic line in the Fe-C-Si system has been plotted in Fig. 2.4 with a bold line. Alloys located above, resp. below, the line will be hypereutectic, resp. hypoeutectic, according to the equilibrium phase diagram.

In the various editions of the ASM handbook on cast iron, emphasis is put on the older work by Neumann [NEU68] who made a review of the experimental information to evaluate the change in solubility of carbon in Fe-C-i melt due to alloying with I, with the carbon content in the binary Fe-C system at 4.26 wt.%. This author also provided thermodynamic evaluation for nearly the whole periodic table that compared well with reported experimental values, though calculations were done at the very high temperature of 1550°C using data for steel. Limited to the same elements as above, the following experimental carbon equivalent expression,  $\text{CE}_{\text{ASM}}$ , was obtained:

$$CE_{ASM} \text{ (wt.\%)} = w_C - 0.064 \cdot w_{Cr} + 0.076 \cdot w_{Cu} - 0.028 \cdot w_{Mn} - 0.014 \cdot w_{Mo} + 0.051 \cdot w_{Ni} + 0.3331 \cdot w_P + 0.310 \cdot w_{Si} \quad (2.10)$$

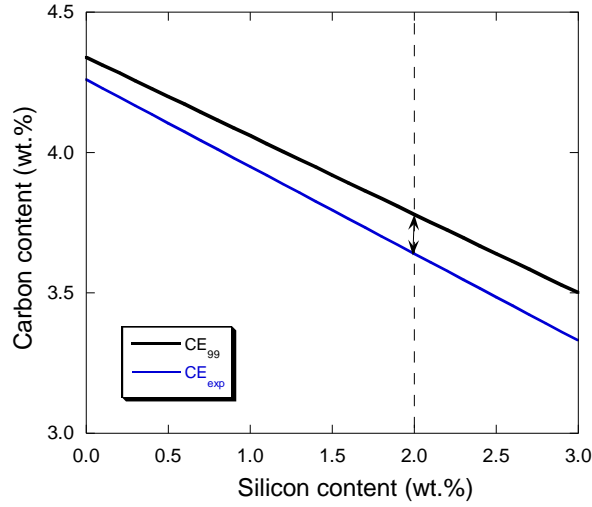


**Figure 2.4. Projection on the composition plane ( $w_C$ ,  $w_{Si}$ ) of the austenite-graphite eutectic line of the Fe-C-Si system according to  $CE_{99}$  and  $CE_{ASM}$  expressions.**

In both expressions of the carbon equivalent, it is quite noticeable that the prevalent terms are those for silicon and phosphorus, which means that for usual modern cast irons with low level of phosphorus and other alloying elements, the difference between the two expressions depends on the value of the carbon content of the binary Fe-C eutectic and of the silicon content. This difference is illustrated in Fig. 2.4 and amounts to 0.04 wt.% C for a cast iron at 2 wt.% Si. Other expressions have been reported in the literature with silicon coefficients smaller than that in Eq. (2.10) and closer to that in  $CE_{99}$ .

According to Eq. (2.8), the coefficient for element  $i$  in the CE expression is given by  $(m_i^g - m_i^\gamma)/(m_C^g - m_C^\gamma)$ . The sign and values of the coefficients in  $CE_{99}$  and  $CE_{ASM}$  agree for graphitising elements (Cu, Ni, P and Si) but not for carbide former elements (Cr, Mn and Mo). The reason is certainly to be found in the fact that the values of  $m_i^g$  and  $m_i^\gamma$  are both small for these three latter elements (see Table 2.1), and thus certainly sensitive to small inaccuracies in the data used for either or both of the CE expressions given above.

Eq. (2.5) may be rewritten as follows:

$$T_L^\gamma = T_0^\gamma + m_C^\gamma \cdot w_C + \sum_i m_i^\gamma \cdot w_i = T_0^\gamma + m_C^\gamma \cdot \left( w_C + \sum_i \frac{m_i^\gamma}{m_C^\gamma} \cdot w_i \right) = T_0^\gamma + m_C^\gamma \cdot CEL \quad (2.11)$$

in which CEL is called the carbon equivalent austenite liquidus.

Limited to silicon, and using the data for  $CE_{99}$ , the CEL writes:

$$CEL = w_C + 0.236 \cdot w_{Si} \quad (2.12)$$

The silicon coefficient in CEL is not far but lower than that in  $CE_{99}$ , which may be the reason these two quantities, CE and CEL, are sometimes confused. Comparison of the expressions in (2.8) and (2.11) demonstrates they are not the same quantities, and this is one of the great advantages of the above linear description of the Fe-C-Si phase diagram to demonstrate this.

## 2.5 The Fe-C-Si phase diagram at higher silicon contents

Since the 1980s, high silicon cast irons have been developed for which the above linear description of the Fe-C-Si phase diagram becomes inaccurate. A second order polynomial description of the austenite and graphite liquidus could possibly be developed but this does not appear to have been done. In all practicality, it is thus recommended to calculate Fe-C isopleth sections using a thermodynamic software package and a relevant database. Insofar as the database used can be trusted, this has the great advantage of allowing alloying elements (Cu, Cr, Mn, Ni, etc.) and impurities or trace elements (Mg, O, S, etc.) to be correctly taken into account in the calculation of Fe-C isopleth sections. Examples of such calculations will appear here and there in the following chapters while the description below is limited to the effect of silicon as the main alloying element of silicon cast irons.

The stable eutectic in the Fe-C phase diagram is a so-called invariant point that gives rise to a monovariant eutectic line in the Fe-C-Si ternary system. Fig. 2.5-a shows the projection on the  $(w_C, w_{Si})$  plane of the stable liquidus in the Fe corner, with this eutectic line starting at the binary point e and the peritectic line (liquid+ferrite- $\alpha$ →austenite- $\gamma$ ) at the binary point p. These two (mono-variant) lines intersect at the invariant ternary point E at about 7 wt.% Si (liquid→ $\alpha$ + $\gamma$ +graphite). Note that Fe-C-Si eutectic alloys with a Si content higher than this value would solidify with ferrite as Fe-rich phase instead of austenite.

The same applies in the metastable system, i.e. the binary invariant eutectic Fe-Fe<sub>3</sub>C gives rise to a monovariant line in the ternary system. In Fig. 2.5-b both the stable and metastable eutectic lines are plotted in the  $(w_C, w_{Si})$  plane with a reduced Si scale compared to Fig. 2.5-a. It is seen that the carbon content of the eutectic decreases significantly with added silicon in the stable system, but much less in the metastable system. Hence, the distance between the two eutectic lines in terms of carbon content increases with the silicon content. This relates to the increase in the temperature difference between the two eutectics that is illustrated in Fig. 2.6 by projection of the diagram on the  $(w_{Si}, T)$  plane.

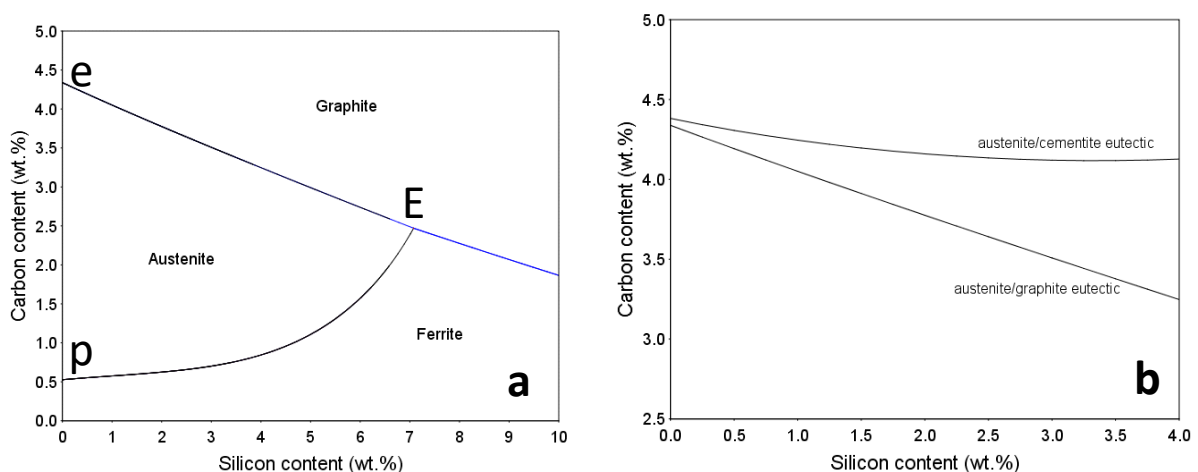


**Figure 2.5. a: projection of the stable liquidus of the Fe-C-Si system.  
b: projection of the stable and metastable eutectic lines on the  $(w_C, w_{Si})$  plane  
in the Fe corner [TCFE8].**



The maximum of the stable eutectic of 1172°C at about 5.5 wt.% Si is due to a slight curving of the austenite and graphite liquidus surfaces. The metastable eutectic goes to a minimum at about 1074.4°C for 4.5 wt.% Si where a third solid phase appears which is a Fe-C-Si silico-carbide, namely  $\text{Fe}_8\text{Si}_2\text{C}_3$  in the database used for the calculations in Fig. 2.6. The dashed horizontal line refers to the invariant eutectic (liquid $\rightarrow$ austenite+ $\text{Fe}_3\text{C}$ + $\text{Fe}_8\text{Si}_2\text{C}_3$ ) of the metastable system for silicon contents above 4.5 wt%, for which, however, no experimental results seem to exist.

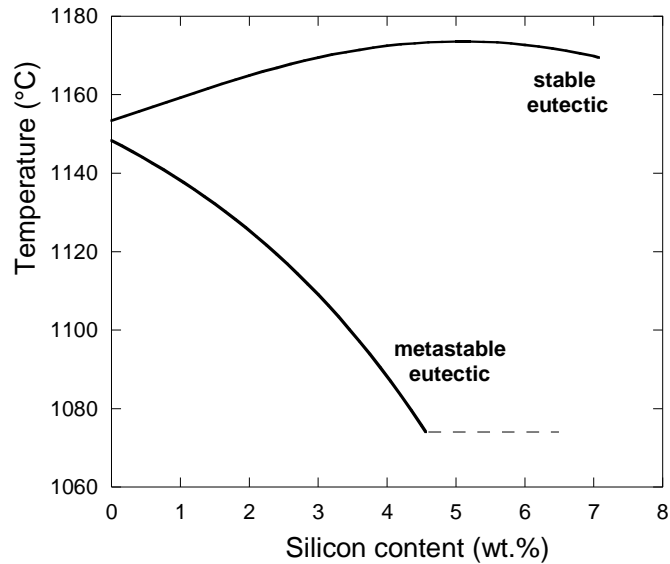


**Figure 2.6. Change in temperature of the stable and metastable eutectics as function of Si content [TCFE8].**

As a matter of fact, measuring the effect of silicon on the equilibrium temperature of the metastable eutectic is not a simple task because it is more and more difficult to reach as higher and higher amounts of silicon are added. Oldfield and Humphreys [OLD62a] developed a method consisting in casting in the same mould cylindrical bars of different diameters so as to achieve a large range of cooling rates. Each bar was equipped with a thermocouple in its centre that allowed the temperature of the thermal arrest associated with the metastable eutectic to be measured. These values were then extrapolated to a zero cooling rate to give an estimate of the equilibrium metastable eutectic. In a recent work [REG22], it was suggested to be given as:

$$T_{EW} = 1148 - 12.23 \cdot w_{\text{Si}} \quad (2.13)$$

Owing to the finite cooling rate of the thermal analysis cups, the metastable arrest takes place at a temperature  $T_{EW}^{\text{cup}}$  lower than that given by Eq. (2.13). Comparison of data from different sources [REG22] showed that it follows closely the following relation proposed by Heine [HEI95] that is valid for silicon content lower than 3 wt.%:

$$T_{EW}^{\text{cup}} = 1140.8 - 12.6 \cdot w_{\text{Si}} \quad (2.14)$$

Eq. (2.14) is drawn in Fig. 2.7 as a dotted line and can be compared to the TCFE8 curve (solid line) from Fig. 2.6. To account for the undercooling for the metastable eutectic growth,

this latter curve shifted by 8°C has also be plotted with a dashed curve that obeys the following relation [REG22]:

$$T_{EW}^{cup} = 1139.6 - 7.16 \cdot w_{Si} - 1.94 \cdot w_{Si}^2 \quad (2.15)$$

This figure also shows recent results on cast irons with up to 3.9 wt.% Si that confirm the curvature of the temperature along the metastable eutectic trough. The use of these relations (2.14) and (2.15) for estimating the silicon content of an alloy by means of thermal analysis will be presented in Chapter 3.

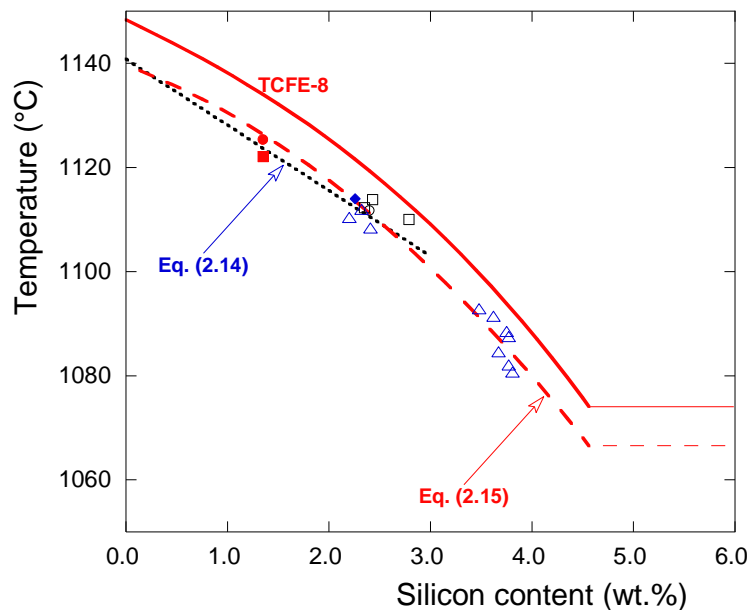


**Figure 2.7. Effect of silicon content on the metastable eutectic temperature. Symbols represent experimental values evaluated by thermal analysis.**

## 2.6 Summary

A linear description of the austenite and graphite liquidus in the Fe-C-Si system has been derived for the range of compositions related to cast irons with less than 3 wt.% silicon, and extended to account for a number of alloying elements at level up to 1 wt.%. From this description, it is straightforward to express the eutectic composition in the stable system, the carbon equivalent CE and the so-called carbon equivalent austenite liquidus CEL as functions of the composition with parameters linked to the characteristics of the austenite and graphite liquidus. This approach presents the interest to show in why and how CE and CEL values differ.

With the current development of high-silicon cast irons, the linear approach of the austenite and graphite liquidus is no more valid. It could certainly be possible to replace the linear terms describing the effect of silicon by second order polynomials for accounting of the curving of the liquidus surfaces in the Fe-C-Si system. However, it appears more appropriate and effective to rely on the development of thermodynamic databases for the calculation of the isopleth sections and of other characteristics of the phase diagrams that are needed.

Some emphasis has been put in this chapter on the co-existence of the stable and metastable systems because of the risk of changing from stable to metastable solidification. In most cases, the resulting **mottled** structure, i.e. a mixture of microstructures of the two

eutectics as the one illustrated in Fig. 2.8, is unwanted. However, this transition is used in the manufacturing of centrifugally cast iron pipes as a mottled microstructure eases the extraction of the tubes from the die because the white eutectic shrinks significantly upon solidification while the stable eutectic does not. The pipes are later shortly heat-treated in the austenite field – typically at 950°C - for full graphitisation.

In this chapter, only the upper temperature range of the diagrams has been presented as this is what is needed for dealing with solidification. The low temperature range corresponding to the stable and metastable eutectoid transformations will be presented in Chapter 9 that deals with solid-state transformations.

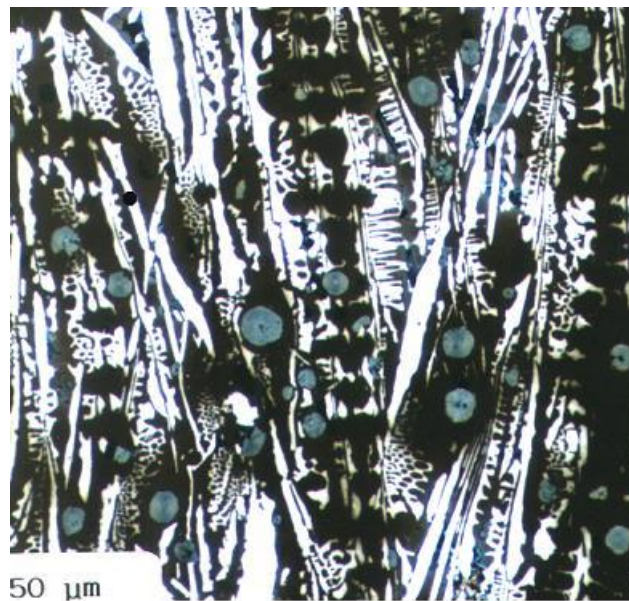


**Figure 2.8. SGI with a mottled structure.**

# Chapter 3 – Thermal analysis and solidification path

**Thermal analysis (TA)** is used in foundries for control of melt preparation before pouring, but can as well be seen as a suitable means for studying solidification and solid-state transformations. This chapter is dedicated to solidification while solid-state transformations are dealt with in Chapter 9. In many respects, phase transformations in cast irons can be described by considering that they are pseudo-binary Fe-C alloys, which means that qualitative and quantitative features may be obtained from information given by the appropriate **Fe-C isopleth section** such as the one in Fig. 3.1-a for a silicon content of 2.5 wt.%. This view is adopted in this monograph, though the necessity of accounting for alloying elements in a more precise way will be mentioned here and there when appropriate. Equilibrium solidification will first be considered as a useful introduction before describing features of actual thermal records and of the associated solidification steps for hypo- and hyper-eutectic alloys. It will be seen that the analysis of cooling records of quasi-eutectic (hypo- or hyper-eutectic) alloys can be a difficult task and recent ideas that are under development (as of 2022) will be presented. Note that no distinction will be made in the present chapter between LGI, CGI or SGI, because "reading" of the TA records does not depend on the type of cast iron under investigation.

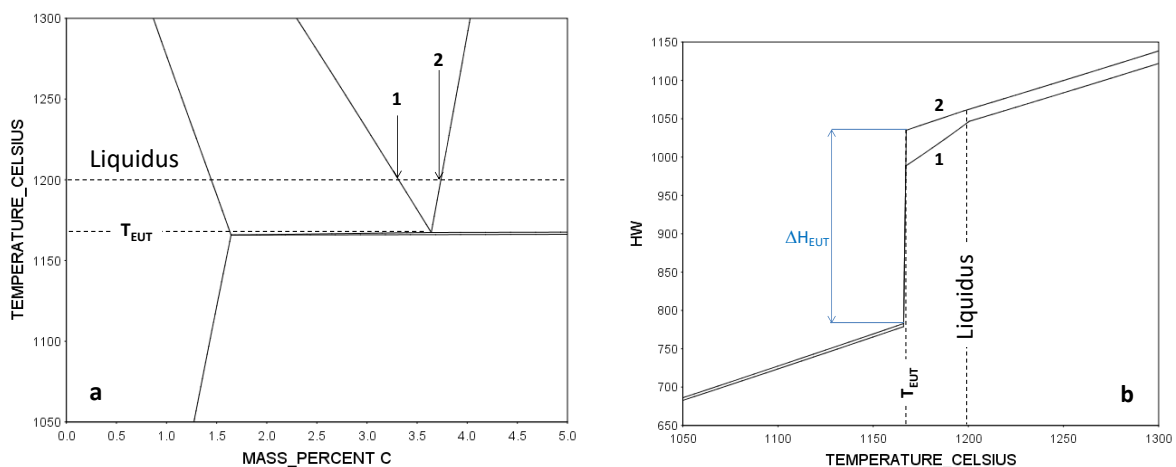


**Figure 3.1. (a) Fe-C isopleth section of the stable phase diagram at 2.5 wt.% Si with indicated an hypo-eutectic (1) and an hyper-eutectic (2) alloy, both alloys having a liquidus of 1200°C [TCFE8]. (b) Evolution with temperature of the enthalpy HW (J.g<sup>-1</sup>) of these alloys for equilibrium solidification [TCFE8].**

## 3.1 Equilibrium solidification

Equilibrium solidification assumes that there is no delay in nucleation and growth of the solid phases to precipitate, i.e. no undercooling, and furthermore sufficient time is given for these phases to be chemically homogeneous at any time during solidification. An hypo-eutectic (1) and an hyper-eutectic (2) alloy with both a liquidus temperature at 1200°C are located in

Fig. 3.1-a. Upon cooling from a temperature at which the material is liquid, the equilibrium **solidification path** of these alloys consists successively of:

- **Primary precipitation** of austenite (alloy 1) or graphite (alloy 2), starting at the liquidus temperature and continuing along the corresponding liquidus line as the temperature decreases. At any temperature, the liquid composition is given by the liquidus line and the fraction of primary phase by the lever rule applied to carbon; see Eq. (10.6) to (10.8) in Chapter 10.
- **Eutectic transformation** of the remaining liquid occurs (liquid→austenite+graphite) when the eutectic temperature,  $T_{EUT}$ , is reached. Note that the invariant eutectic of the binary Fe-C system is now changed to a monovariant one because of Si addition so that there is a very narrow eutectic temperature interval. In practice one defines the eutectic temperature  $T_{EUT}$  as the upper value of this interval.

Fig. 3.1-b shows the **change in enthalpy** of the two materials during equilibrium solidification. Primary precipitation leads to significant latent heat release for alloy 1 while the amount of primary graphite is too small for alloy 2 to lead to any thermal effect. The abrupt change at nearly constant temperature represents the **latent heat** of the eutectic transformation,  $\Delta H_{EUT}$ . Note that the total solidification enthalpy change is nevertheless quite similar for both alloys.

### 3.2 Principles of "ideal" Thermal Analysis (solidification of small casting)

Solidification never takes place at equilibrium because both nucleation and growth of solid phases require undercooling, i.e. a **driving force**. Recording the cooling curves as function of time, denoted  $T(t)$  in the following, is the most usual way to investigating alloy solidification. In aluminium and cast iron industries, this has led to the development of **thermal analysis (TA)** for melt control. The method is based on pouring and solidifying a sample small enough to solidify in a couple of minutes but large enough to be representative of casting solidification. Thermal cups as the one shown in Fig. 3.2-a have dimensions of the order of a few centimetres.

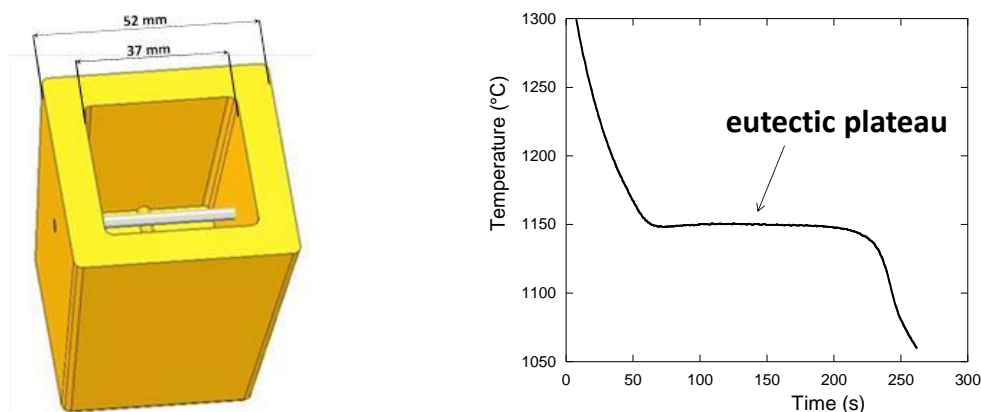


**Figure 3.2. (a) Schematic of a cup for thermal analysis with the thermocouple in the centre. (b) Typical TA cooling curve  $T(t)$  showing a single thermal arrest, the eutectic plateau.**

The TA record in Fig. 3.2-b shows one single thermal arrest which is typically associated to eutectic solidification without primary deposition. When analysing such a thermal record, it

is implicitly considered that the temperature of the metal in the cup is homogeneous at any time during cooling and solidification. With this assumption of ideality, cooling and solidification of small castings such as TA cups could be described and simulated quite satisfactorily using the following heat-balance:

$$A \cdot q = \rho \cdot V \cdot C_p \cdot \frac{dT}{dt} - \Delta H \cdot \frac{dV^S}{dt} \quad (3.1)$$

where  $q$  is the density of the heat flux exchanged by the metal with the mould ( $q < 0$  for usual casting conditions),  $V$  and  $A$  are the volume of the casting and its outer surface, respectively,  $V/A$  being the thermal modulus,  $\rho$  and  $C_p$  are the density and the heat capacity (per unit mass) of the metal, respectively,  $T$  is the sample temperature,  $\Delta H$  is the latent heat of melting per unit volume ( $> 0$ ),  $V^S$  is the solidified volume and  $t$  is time. Both the density and the heat capacity are weighted averages of the values for liquid and solid that are updated at each calculation step.

Assuming a fully eutectic structure consisting of  $N_V$  eutectic spherical cells having the same radius  $R$  at time  $t$ , the change in the solidified volume during growth of the existing nuclei writes  $dV^S/dt = 4\pi N_V \cdot R^2 \cdot dR/dt$ . It will be further assumed that the growth of individual eutectic entities may be written  $dR/dt = \alpha_{EUT} \cdot (\Delta T_{EUT})^n$ , where  $\Delta T_{EUT} = T_{EUT} - T$  is the eutectic undercooling and  $n$  is of the order of 1 or 2, see Chapter 6. During the eutectic plateau, the temperature is nearly constant leaving:

$$A \cdot q = -\Delta H \cdot N_V \cdot R^2 \cdot \alpha_{EUT} \cdot (\Delta T_{EUT})^n \quad (3.2)$$

which may be written as:

$$\Delta T_{EUT} = \left( \frac{-A \cdot q}{\Delta H \cdot N_V \cdot R^2 \cdot \alpha_{EUT}} \right)^{1/n} \quad (3.2')$$

Hence, increasing heat extraction rate ( $q$ ) does increase eutectic undercooling while increase in the number of eutectic entities  $N_V$ , e.g. by inoculation, does decrease it. These opposite actions are represented in the plot of  $N_V$  versus  $\Delta T_{EUT}$  in Fig. 3.3.

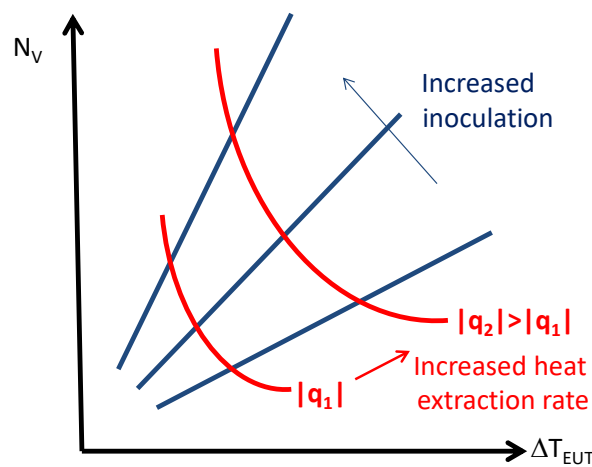


**Figure 3.3. Relation between number of eutectic entities,  $N_V$ , and undercooling of the eutectic plateau,  $\Delta T_{EUT}$ , depending on heat extraction  $q$  (red cuves) and inoculation (blue lines).**

### 3.2.1. Solidification of hypo-eutectic alloys

Consider an hypo-eutectic alloy having the composition pointed with the vertical arrow (1) in Fig. 3.4-a. Though unrealistic, it is of interest to first consider the case of equilibrium solidification, further assuming there is no thermal gradient in the cup. As the temperature decreases from the pouring temperature, the austenite liquidus  $T_L^\gamma$  is eventually reached. With further decrease in temperature, growth of austenite gives rise to a slope change in the  $T(t)$  curve until the eutectic temperature is reached where graphite becomes stable. At that temperature and under equilibrium, the stable eutectic reaction proceeds at  $T_{EUT}$  which is considered as an invariant temperature. The curve labelled 1 in Fig. 3.4-b shows the corresponding temperature evolution with time.

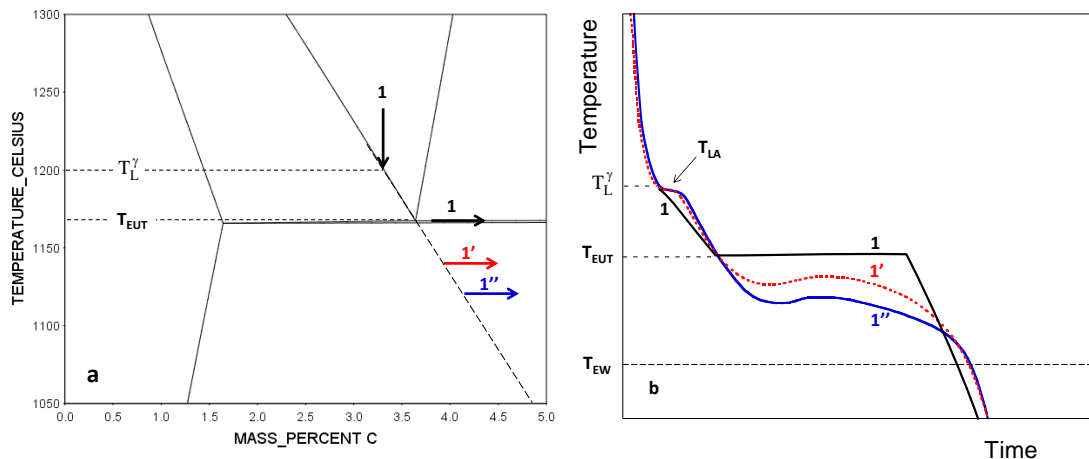


**Figure 3.4. (a) Solidification path of an hypo-eutectic alloy in the related Fe-C isopleth section. (b) Cooling curves,  $T(t)$ , associated with the solidification paths 1 (equilibrium), 1' and 1''.**

On an actual record such as curves 1' and 1'' in Fig. 3.4-b, the formation of austenite leads to a smooth thermal arrest noted  $T_{LA}$ . It is generally not recalescent, which means that austenite does not appear by nucleation and growth in the liquid but rather grows from the surface of the TA cup towards the centre as will be discussed later in this chapter. With further cooling, austenite continues growing alone until the eutectic temperature is reached. However, nucleation of graphite needs a high undercooling (driving force), see Chapter 4, which leads to the fact that the melt undercools significantly below the eutectic temperature before the bulk eutectic reaction sets up. During this stage, it is considered that austenite continues growing along the **metastable extrapolation** of the austenite liquidus which is shown with an interrupted line in Fig. 3.4-a. When the number of graphite particles has increased enough, the bulk eutectic reaction takes place and the temperature may rise because of rapid latent heat release, this is the so-called **recalescence** that shows up in curves 1' and 1'' in Fig. 3.4-b. The  $T(t)$  curve then shows a plateau with a maximum temperature being the result of a balance between heat extraction rate and latent heat release due to eutectic growth. As seen with Eq. (3.2') this balance is directly related to the **eutectic undercooling**  $\Delta T_{EUT} = (T_{EUT} - T)$  which is often used to express the driving force for eutectic growth. During this stage, the temperature must remain below the stable eutectic temperature given by the phase diagram. However, this reference temperature may be affected by **microsegregation**, particularly of substitutional elements (Si, Cr, Cu, etc.), see Chapter 10.

In Fig. 3.4-b, the two curves labelled 1' and 1'' differ by the temperature at which the bulk eutectic reaction takes place, i.e. when the number of graphite nuclei has increased enough. If, instead, the number of graphite nuclei and thus of eutectic entities remains too low, the temperature of the metal decreases further and eventually falls below the metastable eutectic temperature  $T_{EW}$ . Once cementite has nucleated, the cementite plates and ledeburite rapidly invade the still unsolidified liquid, as their growth rate is high in comparison to any of the graphitic eutectic, see Chapter 6 and [Appendix B](#).

### 3.2.2 Solidification of hyper-eutectic alloys

The case of hyper-eutectic alloys is illustrated with Fig. 3.5. **Under equilibrium**, precipitation of primary graphite starts when the liquidus temperature  $T_L^g$  is reached but it does not lead to any significant signal on the thermal record as previously emphasized, see Fig. 3.1-b. The equilibrium solidification path first follows the graphite liquidus until the eutectic temperature is reached when a simple flat eutectic plateau labelled 2 in Fig. 3.5-b takes place.

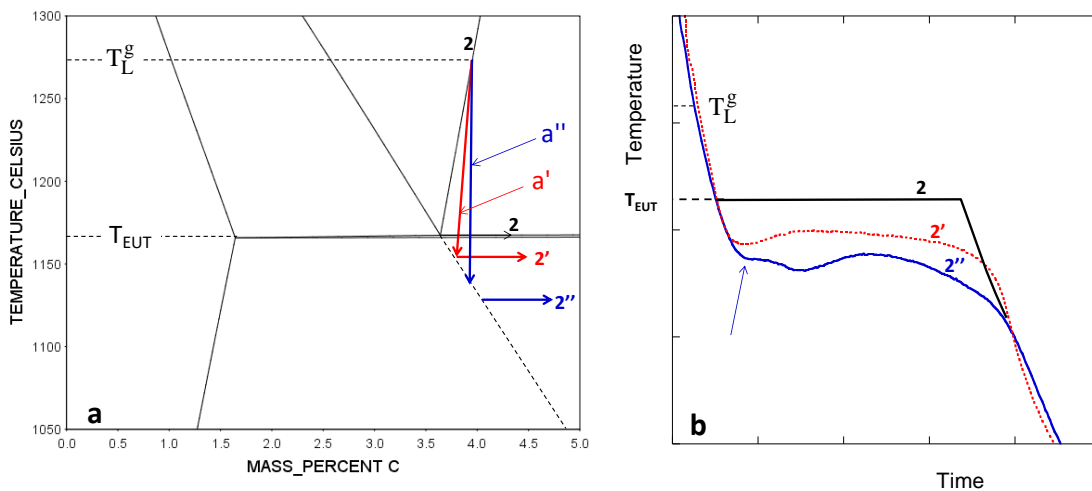


**Figure 3.5. Solidification path of an hyper-eutectic alloy in the related Fe-C isopleth section. (b) Cooling curves,  $T(t)$ , associated with the solidification paths 2 (equilibrium), 2' and 2''.**

In reality, both nucleation and growth of graphite are kinetically limited so that the carbon content of the liquid remains higher than the equilibrium liquidus value: accordingly, the solidification path during primary deposition lies below the graphite liquidus as indicated with the arrows labelled a' and a'' in Fig. 3.5-a. With decreasing temperature, the solidification path will eventually hit the metastable extrapolation of the austenite liquidus somewhere below  $T_{EUT}$ . It will be considered in this section that austenite nucleates and grows with little undercooling, this will be discussed in a later section. In case enough graphite particles nucleated during the primary stage (curve a'), austenite precipitates and bulk eutectic solidification takes place without delay leading to a eutectic plateau labelled 2' in Fig. 3.5-b. If, however, the nucleation of the primary graphite particles has been insufficient (curve a''), austenite forms in the same way when the austenite liquidus extrapolation is reached, but further cooling is required for more graphite particles to nucleate and for bulk eutectic to occur. The curve labelled 2'' shows thus an arrest associated with austenite formation (blue arrow) and a eutectic plateau with a



minimum temperature at lower temperature. During recalescence in case 2", the temperature can rise above the austenite arrest but should stay below  $T_{EUT}$  as for hypoeutectic alloys.

Fig. 3.5 calls for further remarks. The first is that decreasing the cooling rate or increasing graphite nucleation kinetics is expected to move the lines labelled "a" to the left, i.e. austenite will appear at increasing temperature though remaining below  $T_{EUT}$ . A second remark is that, according to usual practice, curves 2' and 2" would be said characteristic of an eutectic and hypo-eutectic alloy, respectively. This contradiction – or inconsistency – is discussed further later in this Chapter. Finally, a first small thermal arrest associated to primary precipitation of graphite has been reported for alloys with  $CE > 4.60$  wt.% (with CE calculated as  $w_C + w_{Si}/3$ ) [CHA74, CHA75]. Analysis and modelling of these latter results have been carried out [CAS20] which allowed differentiating mildly and strongly hypereutectic alloys and suggested that both nucleation and growth of graphite requires some significant undercooling to proceed, see section 3.8 later in this chapter.

### 3.3 Thermal analysis nomenclature

Analysis of cooling records is first based on the evaluation of a few characteristic temperatures. Unfortunately, not only the name given to these temperatures, but also the way to estimate them, vary significantly in the literature with the use of the first and second, or even higher, time derivatives. It is thus important to detail the used procedure when reporting thermal analysis results. Fig.3.6 illustrates the case of a hypoeutectic alloy which starts solidifying with appearance of austenite at a temperature denoted  $T_{LA}$  (or  $T_{AL}$ ). In most cases, the arrest is not-recalescent and shows up on the  $dT/dt$  curve by a local maximum which is used to estimate it (downwards black arrow). However, this maximum in  $dT/dt$  does not always appear and may be replaced by a faint slope change whose start may be somewhere in the greyed area. On the plot, it is seen that this may lead to an uncertainty of about  $5^\circ\text{C}$  on the evaluation of  $T_{LA}$ .

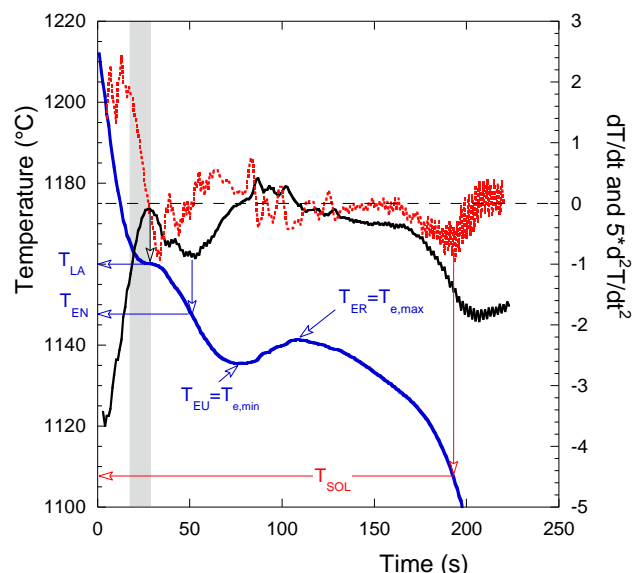


**Figure 3.6. Example of a TA cooling curve  $T(t)$  with the definition of characteristic temperatures. The first (black curve) and second (red curve) time derivatives have also been drawn after smoothing with a mobile average of 5 points for  $dT/dt$  and 10 points for  $d^2T/dt^2$ .**

In between the liquidus and the eutectic plateau, the cooling curve shows a curvature change corresponding to a minimum on the  $dT/dt$  curve (see the downward blue arrow). The corresponding temperature is sometimes reported as the temperature for the initiation of the eutectic,  $T_{EN}$ , meaning that growth of eutectic entities starts even though they are not numerous enough (or the undercooling is not high enough) for bulk eutectic reaction and associated plateau.

An ambiguity however shows up if the alloy is mildly hypereutectic. The cooling curve will present the same shape but the arrest noted  $T_{LA}$  should correspond to the formation of austenite while precipitation of graphite is thought possible: such an arrest should thus be named  $T_{EN}$  according to the above remark. Recent results suggest not to do so, i.e., to keep the name  $T_{LA}$  for an arrest such as that seen in Fig. 3.6 even if the alloy is hypereutectic, see section 3.8. As a matter of fact, this choice allows also to distinguish cases where two successive and similar arrests are recorded as illustrated with Fig. 3.7-a. While the first arrest must correspond to the formation of austenite, and thus be denoted  $T_{LA}$ , the second arrest is thought to rely with the beginning of a eutectic reaction and could be denoted  $T_{EN}$ . This intermediate arrest occurred because not enough eutectic entities were developing at this  $T_{EN}$  temperature, and further cooling was required before the eutectic plateau appeared.

In most cases, the eutectic plateau is simply characterized by reading directly on the curves the minimum temperature before recalescence,  $T_{e,min}$  (or  $T_{EU}$ ) and maximum temperature after recalescence,  $T_{e,max}$  (or  $T_{ER}$ ). In case there is no recalescence, these two temperatures merge in one single characteristic temperature to be evaluated at the maximum of the  $dT/dt$  curve. Finally, the temperature for the end of solidification,  $T_{sol}$ , is estimated as corresponding to the minimum of the  $dT/dt$  curve or better of the second derivative  $d^2T/dt^2$ , see the downward red arrow in Fig. 3.6.

In strongly hypereutectic alloys, an arrest corresponding to precipitation of graphite and denoted  $T_{LG}$  is sometimes observed, that appears as a slope change or sometimes as an arrest with recalescence. An example with slope change is presented in Fig. 3.7-b.

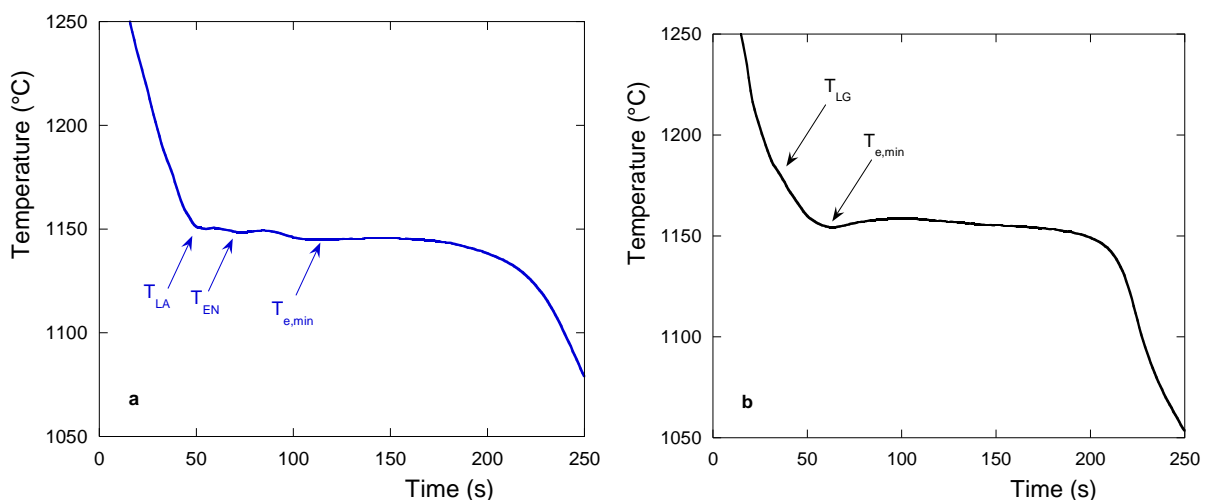


**Figure 3.7. Example of a TA record showing two similar pre-eutectic arrests (a) and a slope change associated to graphite precipitation (b) [REG21].**

### 3.4 Determination of CEL values

One of the important use of TA is the evaluation of the carbon equivalent austenite liquidus, CEL, that has been introduced in chapter 2. For a production that ensures nearly constant silicon content in the melt, evaluating the CEL by measuring the austenite liquidus arrest  $T_{LA}$  is a means to control the carbon content, i.e., the position of the alloy with respect to the eutectic composition. As emphasized in Chapter 2, the eutectic composition corresponds to a value 4.34 wt.% of the carbon equivalent:  $CE=4.34$  wt.%. Inserting Eq. (2.8) in Eq. (2.12), one gets the following relation between CEL and CE:

$$CEL = CE + \sum_i \left[ \frac{m_i^\gamma}{m_C^\gamma} - \frac{m_i^g - m_i^\gamma}{m_C^g - m_C^\gamma} \right] \cdot w_i \quad (3.3)$$

Limited to silicon and phosphorus, and with the values listed in Table 2.1, one gets:

$$CEL = CE - 0.044 \cdot w_{Si} + 0.29 \cdot w_P \quad (3.3')$$

in which it is noticeable that the phosphorus coefficient is large and of positive sign. For an alloy with 2 wt.% Si and 0.02 wt.% P, the eutectic composition according to the phase diagram is achieved for  $CE=4.34$  wt.% that corresponds to a CEL value of 4.26 wt.%.

It has been seen in the preceding sections that the arrest associated with the formation of austenite is not a simple slope change on the cooling curve and that its value can be underestimated. To get a better idea of the capability of TA for CEL estimation, it is thus of interest to look at series of  $T_{LA}$  values as function of carbon content at given silicon content. There are a few such series in the literature amongst which values reported by Moore [MOO72] for two levels of silicon, 1 and 3 wt.%. These results are plotted in Fig. 3.8 by selecting only data related to those alloys with phosphorus content equal to or lower than 0.02 wt.%.

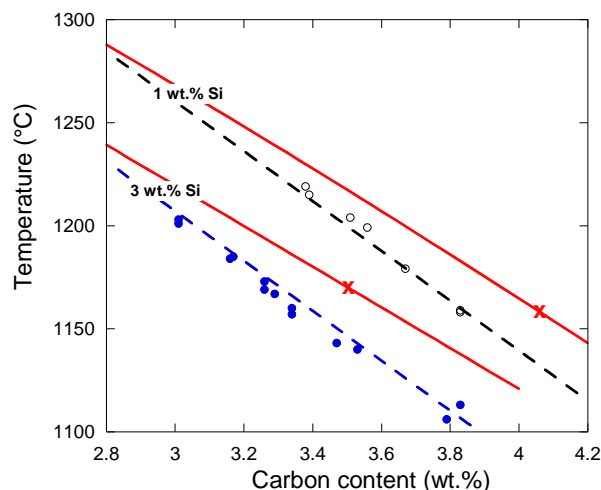


**Figure 3.8.  $T_{LA}$  results from Moore [MOO72] for alloys with 1 and 3 wt.% Si,  $P \leq 0.02$  wt.%. Solid lines represent the calculated austenite liquidus [TCFE8] and the crosses show the location of the stable eutectic point for each silicon content. The dashed lines are best fit lines estimated by Moore, Eq. (3.4').**

In the figure, the results are compared to the calculated austenite liquidus [TCFE8] and very similar lines would have been found using Eq. (2.2). It is thus seen that the experimental

values of the austenite liquidus are significantly lower than the calculated equilibrium values. However, the results show a reasonably linear evolution with the carbon content which suggests that they could be described using a relationship such as:

$$T_{LA} = T_{LA}^0 + a_C^{\gamma,exp} \cdot w_C + a_{Si}^{\gamma,exp} \cdot w_{Si} = T_{LA}^0 + a_C^{\gamma,exp} \cdot \left( w_C + \frac{a_{Si}^{\gamma,exp}}{a_C^{\gamma,exp}} \cdot w_{Si} \right) \quad (3.4)$$

where  $T_{LA}^0$  is a constant,  $a_C^{\gamma,exp}$  and  $a_{Si}^{\gamma,exp}$  the experimental slopes of  $T_{LA}$  with respect to carbon and silicon, respectively. Moore evaluated these three parameters for giving the best fit to his experimental results and obtained:

$$T_{LA} = 1650 - 121 \cdot (w_C + 0.22 \cdot w_{Si}) \quad (3.4')$$

This relation is represented with the dashed lines in Fig. 3.8. Several similar expressions for  $T_{LA}$  have been proposed based on series of TA records for various carbon and silicon (up to 3 wt.%) contents. Some of these expressions are listed in Table 3.1 where it is seen that most of them show a composition dependence expressed as  $CEL=(w_C+0.25w_{Si}+0.5w_P)$ . The liquidus expression derived in Chapter 2 is given for comparison in the last line of Table 3.1 where it is seen that the silicon and phosphorus coefficients agree fairly well with the experimental estimates. As expected and already pointed out by Heine [HEI95], it can be verified that all experimental curves lay below the equilibrium austenite liquidus  $T_L^{\gamma}$ , meaning that austenite appears and/or grows with some undercooling.

**Table 3.1. Various expressions from the literature for the austenite arrest,  $T_{LA}$ , as function of the main elements, carbon and silicon, and for some of them phosphorus and magnesium. The carbon equivalent austenite liquidus CEL appears between brackets.**

Type of melt	Equation	reference
Base iron	$1609.4-108.72 \cdot (w_C+0.22 \cdot w_{Si})$	[CHA74]
NiMg treated iron	$1608.3-107.4 \cdot (w_C+0.25 \cdot w_{Si}-0.69 \cdot w_{Mg})$	[CHA75]
Base iron	$1569.0-97.3 \cdot (w_C+0.25 \cdot w_{Si})$	[HEI95]
Deoxidised iron	$1594.4-102.2 \cdot (w_C+0.25w_{Si}+0.5w_P)$	
Super-heated iron	$1550.0-92.06 \cdot (w_C+0.25 \cdot w_{Si}+0.5 \cdot w_P)$	
	$1669-124 \cdot (w_C+0.25 \cdot w_{Si}+0.5 \cdot w_P)$	Humphreys, cited in [STE15]
Heraus – Electronite	$1623.6-112.36 \cdot (w_C+0.25 \cdot w_{Si}+0.5 \cdot w_P)$	[PERRE]
Phase diagram	$1576.3-97.3 \cdot (w_C+0.236 \cdot w_{Si}+0.59 \cdot w_P)$	$T_L^{\gamma}$ , Eq. (2.2)

It is noticeable that the set of equations in Table 3.1 shows a difference between the various experimental relations that increases from about 10°C at  $CEL=4$  wt.% to 20°C at  $CEL=4.30$  wt.%. From his compilation of previous works dating back the 1960s and 1970s, Heine [HEI95] analysed this sensitivity of  $T_{LA}$  estimates as related to melt processing, namely an effect of the melt oxygen content and of superheating. This analysis has been accepted by other authors as reviewed by Stefanescu [STE15] and shows that a deoxidised iron has higher  $T_{LA}$  value than a base iron, while an iron which has been super-heated before pouring has a lower  $T_{LA}$  value. Stefanescu [STE15] suggests that the increase in  $T_{LA}$  with oxygen is associated with a decrease of carbon activity, which is equivalent to a decrease in carbon content of the melt

thus raising the austenite liquidus. Similarly, super-heating would decrease the nucleation potential of the austenite in the melt.

If we now consider that the  $T_{LA}$  arrest is in most cases not recalescent as seen in Fig. 3.4, the above analysis implies that melt processing affects nucleation of austenite at the surface of the TA cup. Further, the scatter between  $T_{LA}$  estimates may be due also partly to the fact that the austenite undercooling depends on the TA cup which has been used as an increased cooling rate leads to an increased undercooling [CHA74]. In other words, a full understanding of the  $T_{LA}$  arrest would need an approach that accounts for nucleation of austenite at the TA cup walls and for its growth from the surface to the thermocouple junction at the centre where the arrest is recorded. It appears that such an approach has not yet been done but it will be seen in section 3.7 that it would have significant consequences on the reading of TA records.

In practice, it may be expected that the conditions for nucleation and growth of austenite are reproducible within a foundry using always the same procedure for melt preparation and TA analysis. Thus, each foundry could make dedicated trials so as to determine the constants to insert in Eq. (3.4) for CEL determination by TA.

**3.5 Determination of carbon and silicon contents by thermal analysis**

The basic principles of using thermal analysis (TA) to evaluate the carbon and silicon contents in cast irons date back to the 1960s and were presented in detailed works by Moore [MOO72] and Heine [HEI77]. The actual possibility of doing so is illustrated with Fig. 3.9-a that shows the isopleth Fe-C section at 2.0 wt.% Si of the Fe-C-Si phase diagram. In this figure, both the stable and metastable eutectics are shown that are located at the intersection of the austenite liquidus with the graphite and cementite ( $Fe_3C$ ) liquidus, respectively. Using 0.005-0.01 wt.% Bi [HEI77] or about the same amount of Te as most often preferred, graphite growth is hindered thus suppressing eutectic solidification in the stable system which then proceeds in the metastable system.

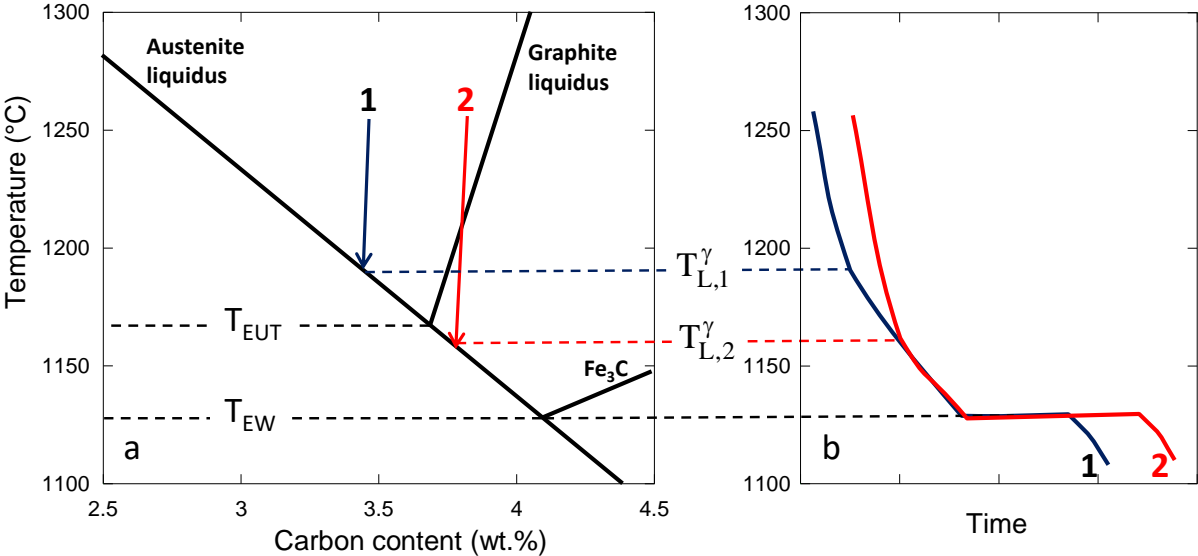


**Figure 3.9. a: Isopleth Fe-C section at 2 wt.% Si of the Fe-C-Si phase diagram showing both the stable eutectic at  $T_{EUT}$  and the metastable eutectic at  $T_{EW}$ . b: Thermal records corresponding to "equilibrium" solidification of alloys #1 and #2 in a.**

In this metastable system, the "equilibrium" solidification consists in two steps: i) precipitation of primary austenite starting at temperatures indicated as  $T_{L,1}^{\gamma}$  and  $T_{L,2}^{\gamma}$  for alloys #1 and #2, respectively; ii) solidification completion with the austenite-cementite eutectic processing at the same  $T_{EW}$  temperature for both alloys. The corresponding "equilibrium" TA records are schematically drawn in Fig. 3.9-b where the start of austenite precipitation is marked with a slope change while the eutectic corresponds to the plateau at  $T_{EW}$ .

However, because of the austenite undercooling just mentioned and because of the undercooling of the metastable eutectic described in Chapter 2, the results should be located along the bold dashed lines in Fig. 3.10 that relate to  $T_{LA}$  and  $T_{EW}^{cup}$ . In all practicality, the silicon content of the alloy is evaluated from the temperature of the metastable eutectic,  $T_{EW}^{cup}$ , either using Eq. (2.14) for silicon content lower than 3 wt.% or Eq. (2.15) for silicon content lower than 4.5 wt.%, that is, respectively:

$$w_{Si} = -\frac{1140.8 - T_{e,min}}{12.6} \quad \text{for } w_{Si} < 3 \text{ wt.}\% \quad (3.5)$$

$$w_{Si} = 0.718 \cdot \sqrt{1146.21 - T_{e,min}} - 1.845 \quad \text{for } w_{Si} < 4.5 \text{ wt.}\% \quad (3.5')$$

where  $T_{e,min}$  is the minimum temperature of the plateau associated with the metastable eutectic. Examples of valid records for estimation of the metastable eutectic temperature are given elsewhere [REG22].

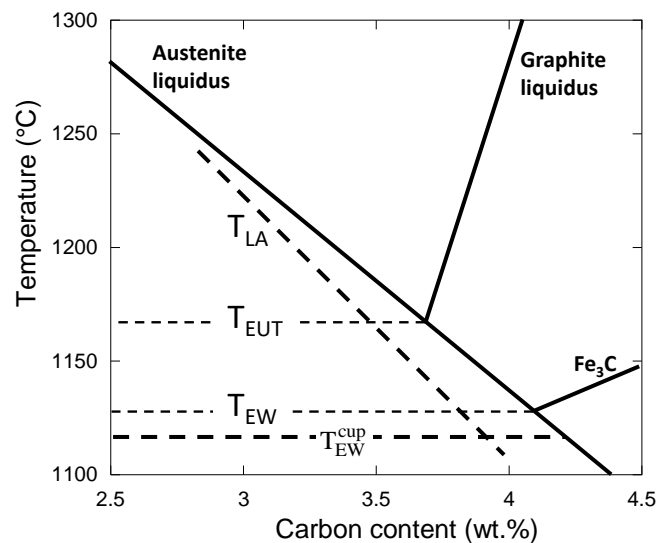


**Figure 3.10. Isopleth Fe-C section at 2 wt.% Si of the Fe-C-Si phase diagram showing both the stable eutectic at  $T_{EUT}$  and the metastable eutectic at  $T_{EW}$  as well as the reference curves  $T_{LA}$  and  $T_{EW}^{cup}$  for the undercooled transformations.**

There is not much detailed information in the literature on the reproducibility of  $T_{EW}^{cup}$  estimates. Setting a small uncertainty of  $\pm 2.5^\circ\text{C}$  on  $T_{e,min}$  values converts to a relatively large uncertainty of  $\pm 0.2$  wt.% silicon by virtue of Eq. (3.5). This contrasts with the reasonable uncertainty of about  $\pm 0.05$  wt.% on the CEL value that is associated with an uncertainty of  $\pm 5^\circ\text{C}$  on the  $T_{LA}$  estimate by virtue of Eq. (3.4'). Note that the large uncertainty on the silicon estimate makes the evaluation of the carbon content through the CEL expression, Eq. (2.12), of little interest.

In parallel to the development of TA for checking cast iron melts before pouring them, many studies have been devoted to use such small casting for getting a better understanding of cast iron solidification. Their results bring some light on the thermal field in the TA cups (section 3.6) and its consequences on austenite undercooling for hypoeutectic compositions (section 3.7). This latter section together with analysis of graphite undercooling in strongly hypereutectic alloys (section 3.8) will finally lead to discuss the difficulty in asserting solidification of near-eutectic or mildly hypereutectic cast irons.

### 3.6 Thermal gradients in small-scale castings

Mampaey carried out quenching experiments at different times during the solidification of 38 mm diameter cylinders, studying LGIs and SGIs [MAM83] and then CGIs [MAM00]. Fig. 3.11-a illustrates three successive stages in the solidification of an LGI with a metallographic section of the cylinder on which the quenched liquid appears white. It can be seen that as time progresses, a solid shell develops on the outer surface, then becomes fully solid and thickens towards the centre of the cylinder. The micrograph in Fig. 3.11-b shows the solid shell at an intermediate solidification time, with the quenched liquid on the right side of the image. The solid fraction in the centre of the casting is 20-40% when the shell becomes fully solid, the exact amount depending on the CE value of the cast alloy.

Mampaey reported that the mushy zone remains extended for a much longer time in the case of SGIs, meaning that the complete solidification of the outer shell occurs when the solid fraction in the centre has already reached 50-80% depending on the CE and the level of inoculation. Finally, CGIs behave like SGIs at the beginning of cylinder solidification, and develop an extensive mushy zone, but follow the evolution of LGIs during the second part of their solidification.

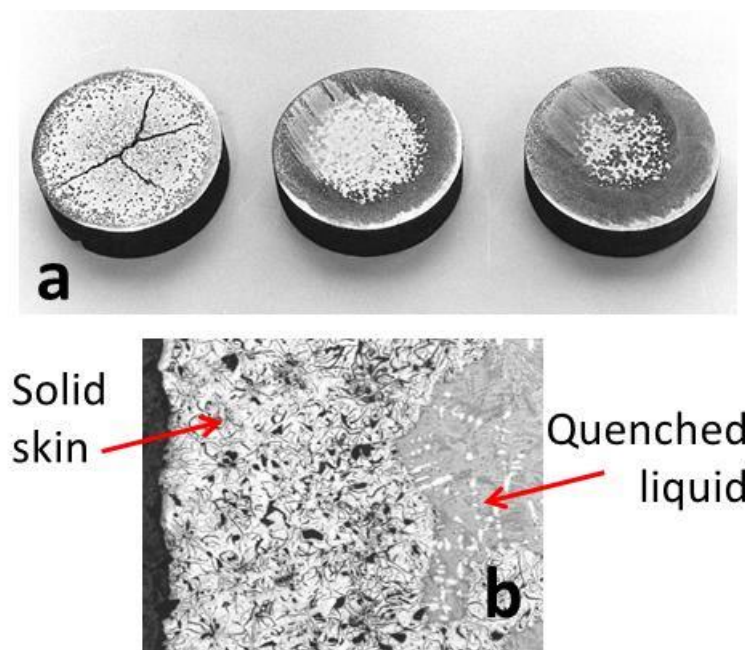


**Figure 3.11. (a) Metallographic section of a cylinder 38 mm in diameter quenched at various times during solidification of a LGI. (b) Micrograph of the outer fully solidified shell (Courtesy F. Mampaey).**

It is clear that a temperature difference must exist between the surface and centre of a casting. A few works have been devoted to the so-called Fourier thermal analysis of solidification of castings which applies to simple cylindrical geometry [FRA97, DIO04]. This analysis allows accounting for radial temperature gradient and may be supported by recording the temperature at two locations, typically at the centre and nearer to the surface of the casting. Examples of such records are reproduced in Fig. 3.12-a [FRA97] for a 40 mm in diameter cylinder cast in sand mould and solidifying within 200 seconds as TA cups do. The cylinders were equipped with two thermocouples, one at the centre and the other 12 mm away from it. It is seen that, at any time during solidification, the calculated temperature difference between these two locations is between 10°C and 20°C, while experimentally temperature differences appear only during solidification. In these records, austenite formation appeared as a simple slope change which [FRA97] could reproduce using a dendrite growth model accounting for nucleation and growth undercooling, see below and Chapter 10.

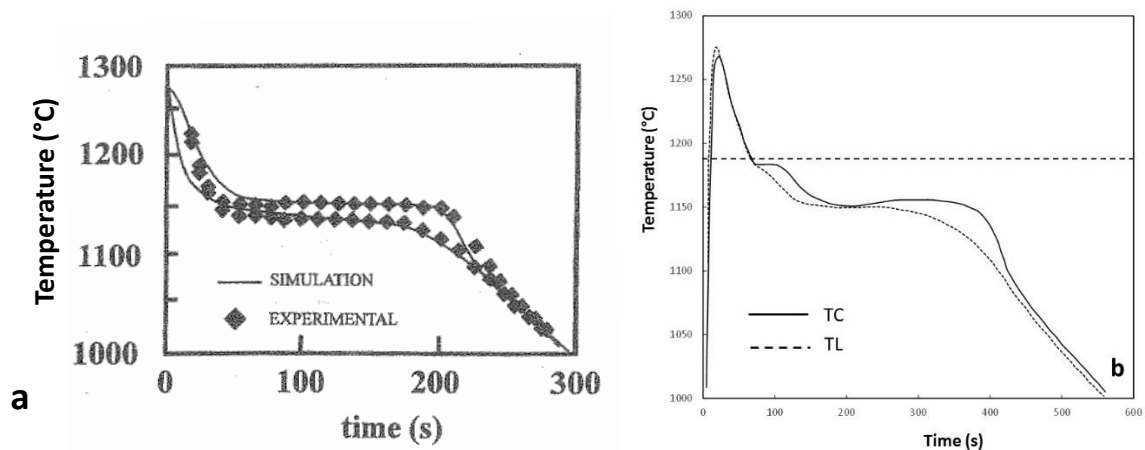


**Figure 3.12. Comparison of cooling curves recorded in the centre of a small LGI sand casting and closer to the surface. (a) 40 mm in diameter cylinder with thermocouples located at the centre and at 12 mm from the centre [FRA97]; (b) Small-sized cylinder cast in sand with one thermocouple at the centre (TC) and the other at mid-radius (TL) (adapted from [DIO04]).**

Dioszegi and Svensson [DIO05] investigated the solidification of cylinders 5 cm in diameter solidifying in 600-700 seconds. They recorded the temperature evolution at the centre TC and at mid-radius TL of the cylinders as illustrated in Fig. 3.12-b. As in Fig. 3.12-a, it is seen that the temperature in the liquid is homogenized, with differences between the two records appearing only once solidification has started. In Fig. 3.12-b, the difference in the shape of the two arrests associated to primary austenite is striking, with mostly a simple slope change at the location TL while a pseudo-plateau showed up at the location TC. While the solidification front progresses towards the centre, the temperature gradient in the liquid certainly decreases, leading eventually to this extended austenite liquidus arrest at the centre of the casting. The arrest at TC sometimes presented a very small recalescence which could be indicative that new austenite grains nucleated at the centre of the castings, but this was apparently never the case at location TL. The horizontal dashed line in Fig. 3.12-b shows the austenite liquidus calculated at 1188.9°C using the data in Table 2.1 for the composition indicated by the authors.



(3.45 C, 2.02 Si, 0.68 Mn, 0.114 Cr, 0.259 Cu, wt.%). It evidences the significant undercooling of austenite in both TL and TC locations.

### 3.7 Growth undercooling of austenite

Whichever austenite develops as a dendritic array from the wall of the TA cup or by repeated nucleation of new grains in the liquid, its growth is dictated by the inwards move of the isotherms. According to TA records as those in Fig. 3.7, the solidification front of austenite needs about 50 seconds to reach the centre of the cup, thus corresponding to an average growth rate of 350  $\mu\text{m/s}$  for a TA cup shown in Fig. 3.2-a. During growth of austenite, there is redistribution of solutes between austenite and liquid, in particular around the dendrite tips. In the growth direction of these dendrite tips, there is some build-up of solutes that increases with the growth rate because being controlled by diffusion in the liquid around the tip. This shift of the liquid composition at the dendrite tips gives rise to a so-called tip undercooling, i.e., a temperature difference between the nominal austenite liquidus of the alloy and the actual growth temperature of austenite dendrites. This can be described as indicated in Chapter 10 and was applied to Fe-C-Si alloys with 2.26 wt.% Si and 2.7-3.7 wt.% C [REG22] for analysing results by Alagarsamy et al. [ALA84].

Fig. 3.13-a shows the result of these calculations as tip undercooling versus growth rate for 2.7 and 3.7 wt.% C. The vertical dashed line indicates the average rate of move of the isotherms estimated above and it is thus seen that the predicted austenite tip undercooling is of the order of 10°C. Further, this undercooling is higher the higher the carbon content, though the effect of 1 wt.% carbon is only of about 2°C. These predictions have been compared in Fig. 3.13-b to the  $T_{LA}$  measurements by Alagarsamy et al. [ALA84] with which they compare quite well except for the near-eutectic alloy at 3.7 wt.% carbon that shows a significantly higher undercooling.

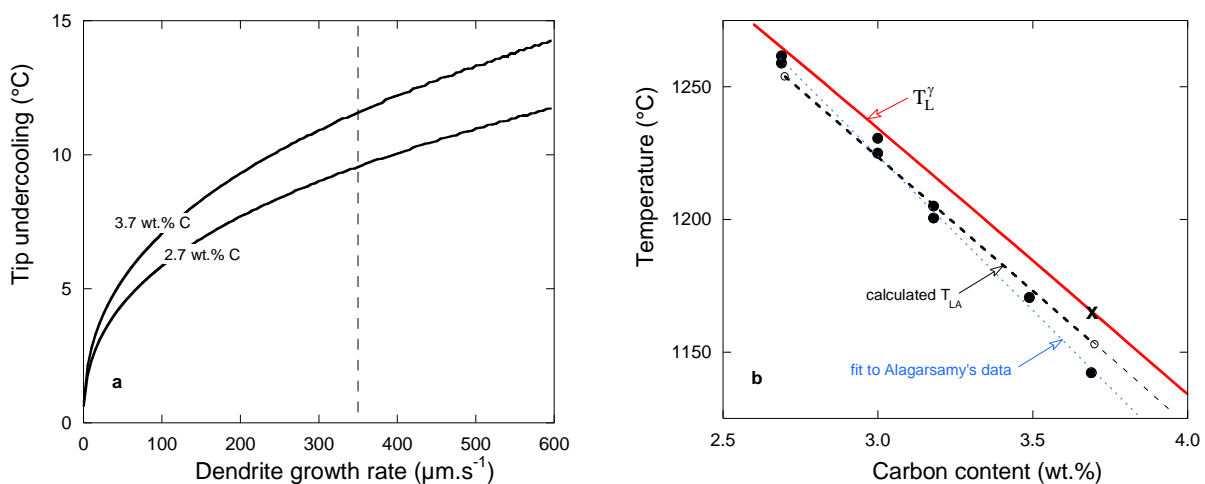


**Figure 3.13. (a) Calculated tip undercooling of dendritic austenite for Fe-C alloys with 2.7 and 3.7 wt.% carbon. (b)  $T_{LA}$  results from Alagarsamy et al. [ALA84] for alloys with 2.26 wt.% Si and 0.7 wt.% Mn, with carbon content in the range 2.7 to 3.7 wt.%. The solid line shows the liquidus calculated with TCFE-8 and the cross locates the stable eutectic. The dashed line connects the  $T_{LA}$  values calculated considering tip undercooling of austenite dendrites for 2.7 and 3.7 wt.% carbon, and the dotted line is the best fit through the experimental data.**

The 2.26 wt.% Si content of the series of alloys studied by Alagarsamy et al. locate them in between the two series showed in Fig. 3.8. It is thus seen that these latter gave higher austenite undercooling and it could not be settled if this is due to a difference in the size of the TA cups or in the way  $T_{LA}$  was evaluated. However, it is of great interest to note that the results in Fig. 3.8 show exactly the same trends as those in Fig. 3.13-b: 1) the austenite undercooling increases with carbon content for hypoeutectic alloys; 2) the undercooling for near eutectic and hypereutectic alloys is significantly larger.

What is noticeable with the results in Fig. 3.8 and 3.13-b is that the temperature associated to  $T_{LA}$  for the near-eutectic hypoeutectic alloys is lower than the equilibrium eutectic temperature. This is schematized on the Fe-C isopleth section in Fig. 3.14 where the open circle shows the nominal carbon content of a slightly hypoeutectic alloy. The double arrow along the austenite liquidus illustrates the shift of the carbon content associated to the carbon build-up in the liquid at the dendrite tips, and the horizontal arrow points to the related  $T_{LA}$  temperature that is below the stable eutectic temperature,  $T_{EUT}$ .

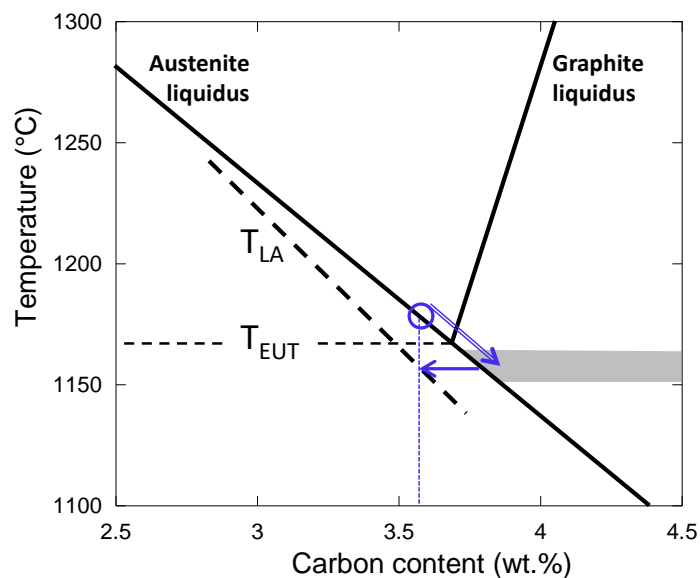


**Figure 3.14. Fe-C isopleth at 2 wt.% Si showing the shift to higher carbon content in the liquid at the dendrite tips (double arrow) and its relation to austenite undercooling (horizontal arrow). The nominal carbon content of the considered alloy is represented with the open circle. The greyed area shows a range of possible eutectic growth temperatures.**

Fig. 3.14 thus suggests that  $T_{LA}$  values lower than  $T_{EUT}$  can be associated with growth of the stable eutectic and not only austenite. In fact, in experiments with non-inoculated near-eutectic or hypereutectic alloys, it is common to observe a grey rim on the outer part of the TA samples with a white or mottled structure in the centre. Alagarsamy et al. [ALA84] did effectively report that their sample at 3.7 wt.% carbon had a large grey rim. It is thus easy to consider that the solidification front during the formation of this rim consisted of an array of austenite dendrites and of austenite/graphite eutectic proceeding together from the surface to the centre of the TA cup. As the temperature of the liquid in the cup is rapidly homogenized (see the experimental curves in Fig. 3.12), the non-recalescent  $T_{LA}$  thermal arrest recorded in

the centre of the cup is at the same or at a lower temperature than the temperature of the solidification front of the rim.

During the growth of the rim, the dendrite tips may have been slightly ahead of the graphite eutectic front if their tip temperature was slightly higher, but may as well have been at the same temperature depending on the growth conditions of the graphite eutectic. The greyed area in Fig. 3.14 shows the possible range of stable eutectic growth temperature. If the actual growth temperature of the stable eutectic is in the low range of this area, austenite dendrites may grow slightly ahead and a  $T_{LA}$  arrest may be recorded. On the contrary, if the eutectic growth temperature is in the upper range of the greyed zone, the austenite dendrites will be engulfed by the eutectic front in which case this is a eutectic arrest that will be detected. If the number of eutectic entities at the solidification front is low, the arrest will be alike a  $T_{LA}$  arrest and further cooling can drive the melt below the metastable eutectic temperature as in the case of Alagarsamy experiments. However, if the nucleation of eutectic entities is prolific, the TA record will show a eutectic plateau with no primary arrest. The above description explains why the  $T_{LA}$  arrest sometimes disappears in near-eutectic (either hypo- or hyper-eutectic) alloys as pointed out a long time ago by Chaudhari et al. [CHA74, CHA75].

Fig. 3.14 illustrates a further practical consequence of austenite undercooling when considering again the slightly hypoeutectic alloy represented with the open disc. In the case the alloy is conveniently inoculated, the stable eutectic may proceed at a temperature higher (upper range of the grey zone) than that at which austenite dendrites would grow accounting for tip undercooling. In such a case, there will be no  $T_{LA}$  arrest recorded during TA analysis and the alloy will be considered as eutectic. The schematic in Fig. 3.14 shows that this will lead to an apparent eutectic composition that is lower than the true stable eutectic composition. In other words, there is a shift of the apparent eutectic composition to lower carbon content that might explain why the carbon equivalent of the eutectic is most often set at 4.26 wt.% while the assessed phase diagram value is 4.34 wt.% [GUS85].

### 3.8 Growth undercooling of graphite

Fig. 3.7-b showed that a thermal arrest can sometimes be recorded in strongly hypereutectic alloys, related to the formation of primary graphite precipitates. Re-analysis of literature data and our own series of results showed that this arrest is located at a significant undercooling below the equilibrium graphite liquidus [CAS20]. Furthermore, it was observed that the undercooling is higher for SGI than for LGI, thus demonstrating that the arrest is also dependent on graphite growth and that the spheroidizing treatment slows it down significantly. These results are shown in Fig. 3.15-a where LG stands for lamellar graphite and SG for spheroidal graphite, with the double arrow showing how is defined the growth undercooling of graphite. Note that the horizontal axis uses the CE content instead of the usual carbon content.

What was then observed is that all alloys having a high enough carbon content show the same temperature for the arrest related to the formation of austenite. In Fig. 3.15-b, these alloys are the strongly hypereutectic alloys at the right of the greyed area, i.e., with a nominal carbon content higher than  $w_{C,1}$ . This observation implies that these strongly hyper-eutectic alloys all show the same solidification path during primary precipitation of graphite which is represented with the arrow in Fig. 3.15-b. This solidification path parallels the dashed lines in

Fig. 3.15-a and is located at very high undercooling with respect to the graphite liquidus, namely about 60°C for LG and 110°C for SG. Though it seems quite normal that the growth undercooling for a faceted phase as graphite is much higher than for the non-faceted austenite in similar cooling conditions, the similarity of the solidification path during graphite precipitation for alloys with different carbon contents could only be explained by modelling growth of primary spheroidal graphite precipitates; see Chapter 10.<sup>2</sup>

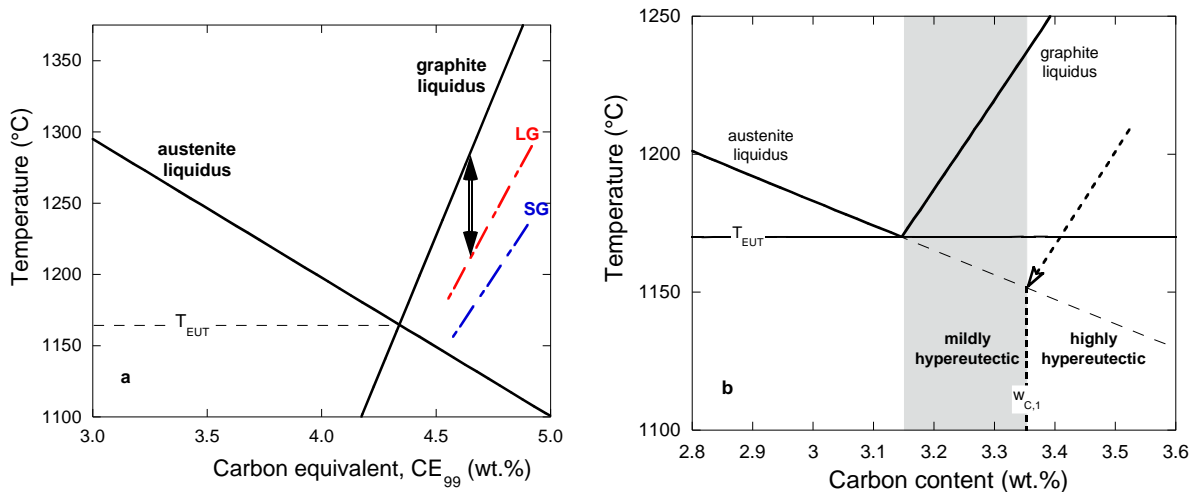


**Figure 3.15. (a) Isopleth Fe-CE section with the dot-dashed lines representing the locus of the thermal arrest of primary graphite for LGI and SGI [CAS20]; (b) Isopleth Fe-C section showing the solidification path for primary precipitation of graphite in strongly hypereutectic cast irons.**

The consequence of this analysis is that primary precipitation of graphite cannot be observed in mildly hypoeutectic alloys because the undercooling with respect to the graphite liquidus is too small. For these alloys, austenite appears first during cooling with a  $T_{LA}$  arrest leading to carbon enrichment of the remaining liquid until its content is high enough for graphite growth. Once graphite has appeared, the eutectic reaction can take place. As seen in the previous section for hypoeutectic alloys, it may happen that the austenite dendrites got engulfed in the eutectic front growing from the walls so that the first arrest would correspond to eutectic growth. It means that a  $T_{LA}$  arrest can be observed or not for mildly hypereutectic alloy in agreement with observations by Chaudhari et al. and others [CAS20].

<sup>2</sup> Unless sometimes stated, the amount of magnesium added for spheroidizing the melt is far too low for having any significant effect on the austenite or graphite liquidus. This can be verified using the TCFE8 database that allows calculation of the effect of Mg when added at trace level. It is thus predicted that addition of 0.05 wt.% Mg does decrease by 0.36°C (i.e. 7.2 °C/wt.%) the austenite liquidus and increases the graphite liquidus by 0.5°C (i.e. 10°C/wt.%). In other terms, the same graphite liquidus applies for LGI and SGI as depicted in Fig. 3.15. The relative positioning of the dashed lines is therefore indicative of an effect of magnesium on graphite growth. It is worth noting also that the very small effect of magnesium on the liquidus implies no measurable effect of magnesium on the equilibrium eutectic valley.

### 3.9 SUMMARY

In this chapter, solidification of small samples has been described for introducing the main steps of the solidification path of hypo- and hyper-eutectic silicon cast irons in relation with the characteristics of the equilibrium phase diagram. In the first part of the chapter, cups used for thermal analysis have been considered as such small samples with a homogeneous temperature at any time during their cooling. The discrepancies between the characteristic temperatures given by thermal analysis and the equilibrium temperatures indicated by the phase diagram have been emphasized and described as undercooling due to either or both nucleation and growth of the solid phases.

These discrepancies impair an accurate determination of the CEL value that is used in the foundry practice. However, reasonable estimate could be obtained if the melting and casting procedures are made reproducible in the foundry wishing to use thermal analysis for CEL control of hypoeutectic alloys. In that case, a linear relation between the  $T_{AL}$  and CEL values can be derived that has the same form as the linearized austenite liquidus but with coefficients that account for the discrepancies.

For the determination of both CEL of near eutectic and mildly hypereutectic alloys, it is necessary that growth of any graphite is properly and totally hindered. If this is not the case, the start of growth of graphitic eutectic entities can interfere with the growth of austenite, in particular if the outer part of the sample solidifies in the stable system.

Though not considered in this chapter, it is worth mentioning that the possibilities of thermal analysis have been extended to predicting graphite shape, effectiveness of inoculation and tendency to porosity formation as reviewed several times (e.g. [STE15]). Also, inverse calculations of solidification kinetics have been carried out for one thermocouple [FRE75a, EKP81, BAR97] and two thermocouples [FRA97, BAR97, DIO04, DIO05] configurations for checking the appropriateness of assumed nucleation and growth laws for the description of microstructure formation.

# Chapter 4 - Nucleation of graphite – Inoculation

Refining the microstructure by inoculation is always necessary as part of the mechanical performance of the shaped materials depends on it. Similarly, inoculation in LGI and SGI castings is crucial to avoid a mottled structure when reducing the wall thickness of the casting. The understanding of inoculation uses classical nucleation theory as an essential guide in the search for inoculation performance. Thus, the essential foundations of homogeneous and heterogeneous nucleation phenomena are first given. Their application to casting is then presented, which will illustrate the complexity of nucleation phenomena in industrial processes. It will be seen that the detailed mechanisms are too complex to be elucidated quantitatively, so that ad'hoc heuristic laws are used.

Many of the data used in this chapter concern the inoculation of spheroidal graphite iron associated with the nucleation of graphite spheroids. Indeed, spheroidal graphite is unique in providing microstructural evidence of the heterogeneous nature of graphite nucleation, while also being a valuable aid to finding and studying nucleation substrates.

## 4.1 Homogeneous nucleation: the critical nucleus

The framework of classical nucleation theory allows us to seek to understand inoculation and to organise the knowledge gained to improve it. This theory is based on four key concepts:

- a. Thermodynamic equilibrium of small solid particles inside the liquid.
- b. Probability of the appearance and growth of small solid particles, called nuclei.
- c. Kinetics of adhesion of atoms from the metastable phase – here the liquid - to the nuclei.
- d. Nucleation of the stable phase on other solid phases, also called substrates.

The high surface/volume ratio inherent in forming a small volume of solid inside a metastable phase implies the need to consider interfacial energy in the energy balance. The free energy,  $\Delta G_r$ , of a small sphere is thus given by:

$$\Delta G_r = -4/3 \cdot \pi r^3 \Delta G_m + 4\pi r^2 \sigma \quad (4.1)$$

where  $r$  is the sphere's radius,  $\Delta G_m$  is the standard energy of melting per volume and  $\sigma$  is the solid/liquid interface energy.

Sigma is always positive, and  $\Delta G_m$  is positive at temperatures below the melting temperature,  $T_m$ , of a pure element or below the liquidus temperature of an alloy. In the present case, this is the graphite liquidus that is to be considered when dealing with graphite nucleation. Note that the need to compensate for interfacial energy for the solid to nucleate could also be considered as a free energy barrier to nucleation.

Fig. 4.1 illustrates the evolution versus  $r$  of the two terms in the right hand side of Eq. (4.1) and of their sum,  $\Delta G_r$ . The value of the critical radius,  $r^*$ , beyond which  $\Delta G_r$  begins to decrease

with the growth of the sphere, is obtained from the differentiation of Eq. (4.1), which gives the so-called Gibbs-Thomson's equation:

$$r^* = \frac{2\sigma}{\Delta G_m}; \quad \text{when} \quad \frac{d\Delta G_r}{dr} = 0 \quad (4.2)$$

Considering the following approximation valid close to  $T_m$  (in Kelvin):

$$\Delta G_m = \Delta H_m - \frac{T_K \cdot \Delta H_m}{T_m} \quad (4.3)$$

where  $T_K$  is the temperature in Kelvin and  $\Delta H_m$  is the enthalpy of melting per volume; then the critical radius is given as:

$$r^* = \frac{2\sigma T_m}{\Delta H_m} \cdot \frac{1}{\Delta T} \quad (4.4)$$

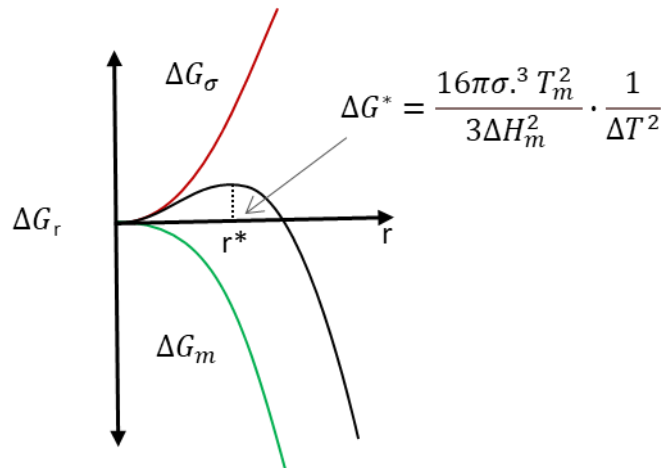
and

$$\Delta G_r^* = \frac{16\pi\sigma^3(T_m)^2}{3(\Delta H_m)^2} \cdot \frac{1}{\Delta T^2} \quad (4.5)$$

where  $\Delta T = T_m - T_K$  is the undercooling corresponding to the formation of the solid phase and  $\Delta G_r^*$  the free energy of the nucleus of size  $r^*$ .

In Eq. (4.1) and (4.3), the free energy and the enthalpy should be given per mole to be strictly conservative. For simplicity, and to better show the involved physical concept, their expression per volume has been adopted here. In doing that, it is considered that molar volume is constant even in such a small atomic aggregate.

**Figure 4.1. Free energy barrier,  $\Delta G^*$ , to nucleus formation at a given  $\Delta T$ .  $\Delta G_r$  is the free energy of the sphere of radius  $r$ ,  $\Delta G_\sigma$  and  $\Delta G_m$  are the interfacial free energy and standard energy of melting, respectively. The solid line is the sum of  $\Delta G_\sigma$  and  $\Delta G_m$ .**



Interfacial energy is essential for phase transformation in metals and metallic alloys at small scale phenomena, such as Ostwald ripening, the curvature effect on nucleation as well as growth shapes. This so-called capillary effect is described by appropriate application of the Gibbs-Thomson equation, Eq. (4.2). For the case of nucleation, Eq. (4.4) gives the relationship between the radius of a solid sphere with  $\Delta T$  at the equilibrium of driving forces for solidification and melting back [KUR98]. By inserting typical values for pure metals in Eq. (4.4),  $\Delta T$  is

calculated as less than 1 K and about 40 K for a sphere with 1 μm or 0.01 μm radius, respectively. That shows that capillarity becomes important below a micron-scale or so for metals.

#### 4.2 Homogeneous nucleation: kinetics

The classical theory of nucleation is based on the concept of discontinuous phase fluctuations from Volmer and Weber, also called structural fluctuations [CIN00]. These fluctuations lead to the spontaneous presence of  $N_r$  embryos of the solid phase inside the liquid phase according to Eq. (4.6a), where  $N$  is the total number of atoms in the system and  $k$  is the Boltzmann's constant. Due to the exponential nature of Eq. (4.6a), tiny embryos are numerous, while large ones are scarce. Figure 4.2 shows a diagram of such a distribution of embryos,  $N_r$ , at a given temperature.

$$\begin{aligned}
 \text{a) } N_r &= N \cdot \exp\left(-\frac{\Delta G_r}{k \cdot T_K}\right) \\
 \text{b) } N^* &= N \cdot \exp\left(-\frac{\Delta G_r^*}{k \cdot T_K}\right) \\
 \text{c) } N^* &= N \cdot \exp\left(-\frac{16 \cdot \pi \cdot \sigma^3 \cdot (T_m)^2}{3 \cdot (\Delta H_m)^2 \cdot \Delta T^2} \cdot \frac{1}{k \cdot T_K}\right)
 \end{aligned}
 \tag{4.6}$$

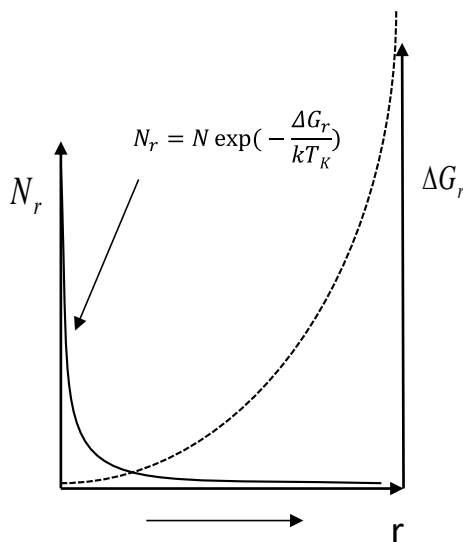


Figure 4.2. Scheme of the number of embryos as a function of their size  $r$ , at a given  $T$  or  $\Delta T$ .

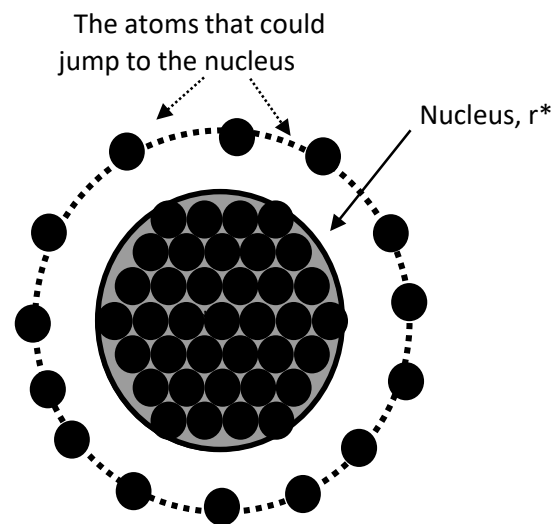


Figure 4.3. Graphical representation of the addition of atoms to the solid from the liquid.

Homogeneous nucleation occurs when the probability of forming a nucleus of critical radius  $r^*$  becomes sufficiently high. The number  $N^*$  of nuclei of size  $r^*$  with the structure of the solid into a metastable liquid, is then given by Eq. (4.6b), or by Eq. (4.6c) by virtue of Eq. (4.5).

It is essential to note in Eq. (4.6b) that  **$N^*$  exponentially increases when  $\Delta G^*$  decreases, i.e., when  $\Delta T$  increases**. When undercooling is high enough to ensure the presence of a few nuclei of critical size  $r^*$  in a small volume, for example one  $\text{cm}^3$ , then nucleation can proceed. Next, the nuclei grow by atom jumps from liquid to the solid across the phase boundary; see Fig. 4.3. The probability that these jumps occur,  $J_s$ , is represented by Eq. (4.7), where the



energy barrier for the jumps is estimated as the activation energy for atom diffusion in the liquid,  $\Delta G_d$ .

$$J_s = A \cdot \exp\left(-\frac{\Delta G_d}{kT_K}\right) \quad (4.7)$$

In this expression, A depends on geometrical considerations related to the distribution of atoms of a metastable phase in contact with the nucleus.

Finally, the nucleation rate, I, is expressed as the product of  $N^*$  and  $J_s$ :

$$I = A \cdot \exp\left(-\frac{\Delta G_d}{kT_K}\right) \cdot N \cdot \exp\left(-\frac{\Delta G_r^*}{kT_K}\right) \quad (4.8)$$

For nucleation of pure metal, the first three terms in the right side of Eq. (4.8) are roughly constant, then:

$$I = I_o \cdot \exp\left(-\frac{\Delta G_r^*}{kT_K}\right) \quad (4.9)$$

Using data for pure metals,  $I_o$  takes a value of about  $10^{39} \text{ m}^{-3}\text{s}^{-1}$ . A consequence of the exponential term in Eq. (4.9) is that "I" increases suddenly when some temperature  $T_K$  or undercooling  $\Delta T$  is reached. Considering the above value of  $I_o$ , a nucleation rate of  $10^6 \text{ m}^{-3}\text{s}^{-1}$  (i.e., one nucleus per  $\text{cm}^3$  and second) is obtained when  $\Delta G^* \sim 76kT$  that corresponds to a reduced undercooling  $(T_m - T_K)/T_m$  of 0.18, see Fig. 4.4. Beyond this undercooling, the "I" value increases further and becomes virtually infinite within a small temperature interval.

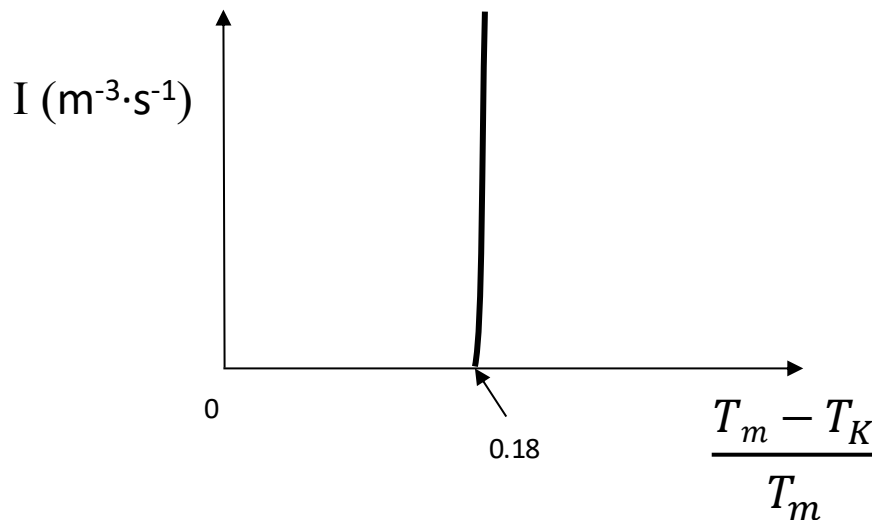


**Figure 4.4. Homogeneous nucleation rate as a function of the reduced undercooling, i.e. the undercooling normalized with the melting temperature.**

Homogeneous nucleation, as described above, could be observed provided the original melt is free from any exogenous-crystalline substrate. In such condition, high driving forces are needed for nucleation, and the highest solidification undercoolings are expected that have been looked for in some experimental works. For example, Turnbull and Cech [TUR50a] reported  $\Delta T/T_m = 0.18$  for the maximal solidification undercooling detected in different pure

metals. Perepezko [PER84] reported even higher  $\Delta T/T_m$  values with an improved experimental technique. Homogeneous nucleation on refractory metals has been studied by Vinet et al. [VIN02] who reported similar values of  $\Delta T/T_m$ .

This classical theory of homogeneous nucleation was developed for pure metals. In cast irons, austenite is certainly close to the behaviour of pure metal, but this is not necessarily the case for graphite. In future studies, it might be interesting to consider the following two aspects:

1. *The probability of graphite nuclei to be surrounded by carbon atoms.* According to Cini et al. [CIN00], both structural and concentration fluctuations are needed to nucleate solid embryos in liquid alloys. These authors propose a model for describing separately each of them while these two types of fluctuations have been previously considered as simultaneous events [CIN00]. This kind of theory is developing in other fields with the help of numerical simulation; see Chakraborty et al. [CHA13] and Wallace et al. [WAL13], for example. Within this framework, it is possible of having concentration fluctuations providing suitable conditions to get structural nucleation. That means that, in a solution, more carbon atoms are around the solid embryo by the effect of compositional fluctuations and then enhance the jump probability and thus the  $J_s$  value.

2. Considering graphite again, it should be reminded this is a faceted phase. Hence, it could be expected that only a small part of the nucleus surface provides sites for additional atoms to stick on. Such effect on graphite nucleation in cast iron has not yet been investigated.

### 4.3 Heterogeneous nucleation

Catalysis of nucleation by a substrate could significantly reduce the undercooling, or equivalently the driving force, required for nucleation; this is the so-called **heterogeneous nucleation**. From a theoretical point of view, this catalytic effect relates to  $\theta$ , the contact angle or wetting angle between the liquid and the substrate (Volmer cited by Turnbull [TUR50b]). The volume of the nucleus needed to overcome the energy barrier is a part  $f(\theta)$  of the sphere of critical radius represented with the hemispherical dark grey cap in Fig. 4.5, with:

$$f(\theta) = \frac{(2 + \cos\theta)(1 - \cos\theta)^2}{4} \quad (4.10)$$

The free energy value of the nucleus over the substrate is given as  $\Delta G_{het}^* = f(\theta) \cdot \Delta G^*$ . Hence, small values of  $\theta$  enhance nucleation kinetics which is now written:

$$I = I_o \exp\left(-\frac{\Delta G^*}{kT} \cdot \frac{(2 + \cos\theta)(1 - \cos\theta)^2}{4}\right) \quad (4.11)$$

With the help of proper substrates, the nucleation undercooling for important industrial metals as iron and aluminium alloys could be reduced to values of a few degrees. A structural fluctuation with a size smaller than  $r^*$  according to Eq. (4.4) could however reach this critical size by the wetting effect if the contact angle  $\theta$  is small enough as illustrated on Fig. 4.5.

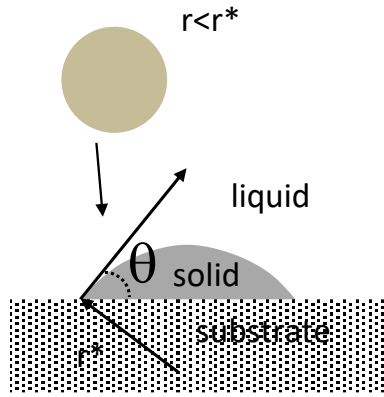


**Figure 4.5. Heterogeneous nucleation over a substrate for a given  $\theta$  value.**

To understand the cooling rate effect in refining grain, first, let us assume that a single wetting angle value characterizes all heterogeneous substrates present in a particular melt. When heterogeneous nucleation occurs during cooling this melt, all the substrates are activated within a limited undercooling range. Accordingly, the nucleation rate increases sharply and decreases rapidly within this range by consumption of the substrates, as illustrated in Fig. 4.6-a. This rapid and complete consumption of substrates has been pointed out by Turnbull on a time basis [TUR50b]. Within these lines, Hunt modelled the nucleation process over a given type of substrates by simplifying Eq. (4.11) to:

$$I = (N_o - N_a) \cdot 10^{20} \cdot \exp\left(-\frac{u}{\Delta T^2}\right) \quad (4.12)$$

where  $N_o$  is the initial number of substrates on a volume basis,  $N_a$  is the number of activated substrates,  $u$  is a constant depending on the substrates, and  $\Delta T$  is the undercooling.

However, it can be expected that substrates of different types, i.e. characterised by different values of the wetting angle, are present in the melt and can be activated as nuclei at different undercoolings as shown in Fig. 4.6-b. When the cooling rate increases, more substrates of different wetting angles are activated, providing grain refinement.

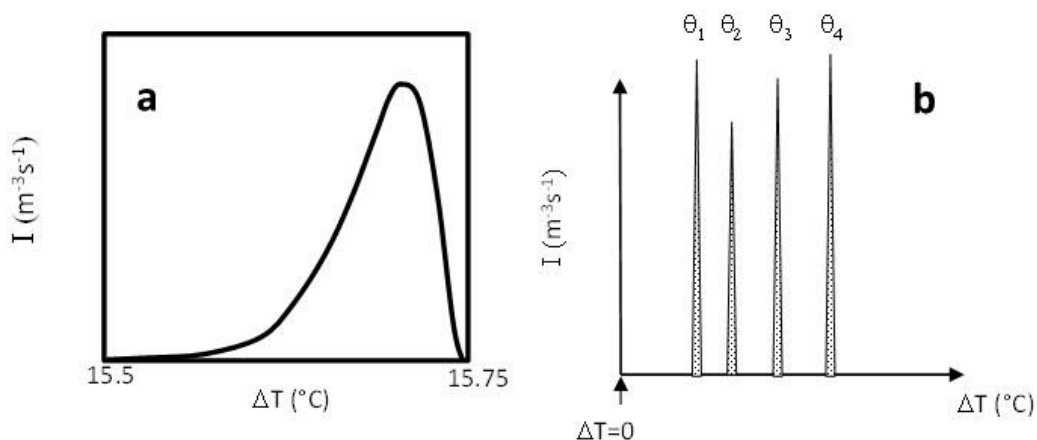


**Figure 4.6. Heterogeneous nucleation on substrates. Over a substrate with a given  $\theta$  value (a), and over substrates with different  $\theta$  values:  $\theta_1 < \theta_2 < \theta_3 < \theta_4$  (b).**

There may be several reasons why different types of substrates may be present in an industrial melt. In the case of cast irons, substrates are generated or activated by inoculation of the melt which involves dissolution of the inoculant and precipitation of the substrates. It is therefore a highly transient process in which the liquid-substrate equilibrium can change from place to place on a small scale.

Another way of having an extended range of activation undercooling of heterogeneous nucleation events is when the substrates show a size distribution. Eq. (4.10) was obtained considering an “infinite” substrate size while substrates found in graphite nodules [IGA98] or graphite lamellas [RIP03] are sometimes a couple of microns in size but typically smaller than a micron. Such small sizes are expected to affect nucleation kinetics.

The effect of substrate size on nucleation has been analysed in ice formation in a classical work by Vonnegut, who mentioned that the effectiveness of silver iodide particles as ice nuclei depends to a certain extent on the size of the particles [VON47]. This effect was later quantified by Fletcher, considering spherical substrates [FLE58] whose approach has been applied to graphite nucleation [CAS91] as illustrated with Fig. 4.7. At a given  $\theta$  value, the undercooling to activate nucleation increases as the size of the substrate decreases. This effect becomes significant at values of the radius smaller than 0.2 microns, while the assumption of “infinite” size applies for radius values higher than 1 micron.

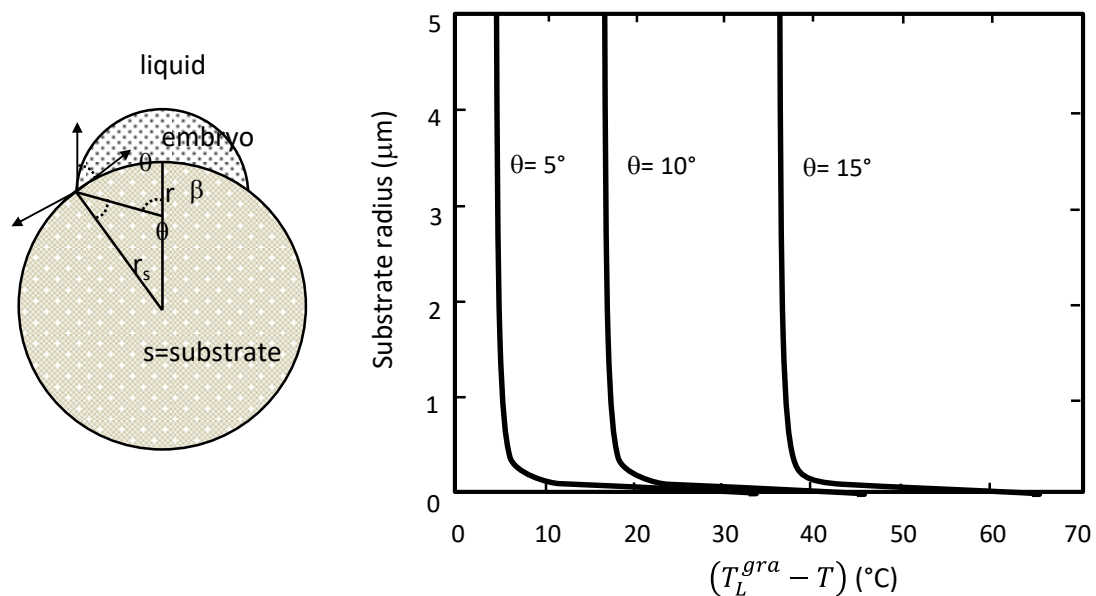


**Figure 4.7. Effect of substrate size on the nucleation undercooling related to the graphite liquidus. Results are shown for three different wetting angles [CAS91].**

The substrate size effect on heterogeneous nucleation has also been analysed considering flat discs and conical cavities [LAC90]; see Fig. 4.8. Flat surfaces (Fig. 4.8-a) allow nucleation if their equivalent radius  $r_s$  is equal to or higher than the product  $r^* \cdot \sin(\theta)$ . Thus, for a given undercooling, too small substrates could not become active and the necessary undercooling for such circular substrates will be higher than that required to activate substrates of “infinite” size. This approach gives a first estimate of the effect of substrate’s size on heterogeneous nucleation and has been used in the modelling of chilling tendency [FRA93].

In contrast to the case of the discs, Lacaze et al. [Lac90] then considered conical cavities as illustrated on Fig. 4.8-b. As long as  $\theta + \alpha < \pi/2$ , all conical cavities are expected to have graphite embryos shortly after the temperature of the melt falls below the graphite liquidus temperature. This is because the change in free energy associated with such process is always negative. Further growth of the embryos out of the cavities will occur with a positive radius of curvature of the melt/graphite interface in relation with the size distribution of the cavities. This approach reproduces also an extended distribution of activation undercoolings. Note that it has been recently (as for 2022) evidenced that effective growth of graphite precipitates beyond the nucleation stage needs high undercoolings [LAC17a] as mentioned at the end of Chapter 3 and further detailed in Chapter 10.

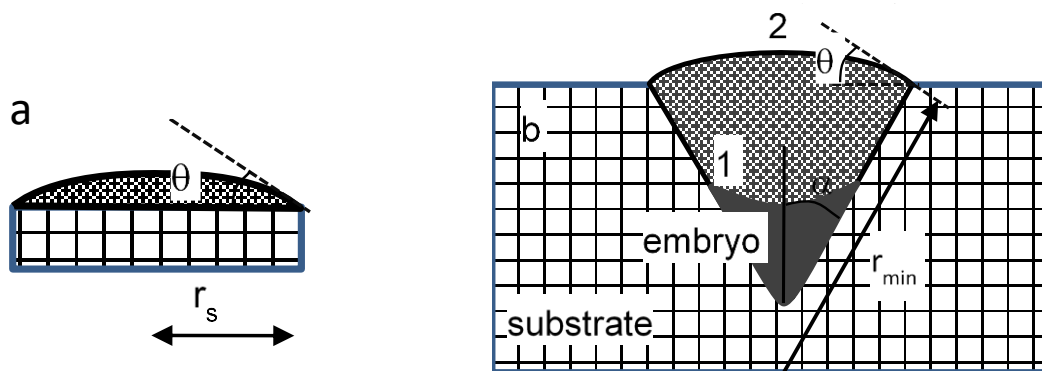


**Figure 4.8. Model of nucleation sites for a flat circular surface (a) and a conical cavity (b) [LAC90].**

#### 4.4 Crystallographic similitude concept

The concept of crystalline similarity between the solid to be precipitated and the substrate guides the search for substrates that allow low undercooling values. According to this concept, the more similar a crystallographic plane of the substrate is to a dense plane of the solid to be nucleated, the more efficient the substrate is for nucleation catalysis. The similitude between two crystal structures could be quantified by the linear mismatch,  $\delta$ , between two lattices as illustrated in Fig. 4.9 [TUR52], or by planar disregistry according to Bramfitt [BRA70].

This concept has been applied by Cibula [CIB49] to analyse grain refinement of aluminium alloys and should be suitable as well for graphite nucleation. The crystallographic similitude between substrate particles and graphite is thus often given as evidence of their nucleation catalysis performance. However, in most studies, the crystallography of substrates has not been assessed but inferred from their chemical analysis. Using this kind of approach, and based on experimental evidence, Gad and Bennett concluded that the addition of Ca in an inoculant allows the formation of Ca silicates that are suitable substrates for graphite nucleation [GAD85] and this has been refined by Skaland et al. [SKA93].

Skaland et al. [SKA93] evidenced that the population of inclusions formed by the Mg treatment in ductile iron could be composed of sulphides and magnesium silicates. They showed that this kind of inclusions has a higher planar lattice disregistry with graphite than the CaO, SrO, BaO, Al<sub>2</sub>O<sub>3</sub> silicates or even  $\alpha$ -Al<sub>2</sub>O<sub>3</sub> generated by the inoculant addition. The latter kind of silicates has thus higher graphite nucleation capabilities than Mg silicates, see Fig. 4.10.

These authors also proposed successive steps for the formation of inclusions that catalyse graphite nucleation with the most suitable inclusions consisting of a sulphide core with an outer shell made of the silicates mentioned above. This means that the primary inclusions play an essential role in the inoculation process. Therefore, altering the composition of Mg silicates or changing only their surface composition could help to promote the nucleation of silicates that will provide good substrates for graphite nucleation.

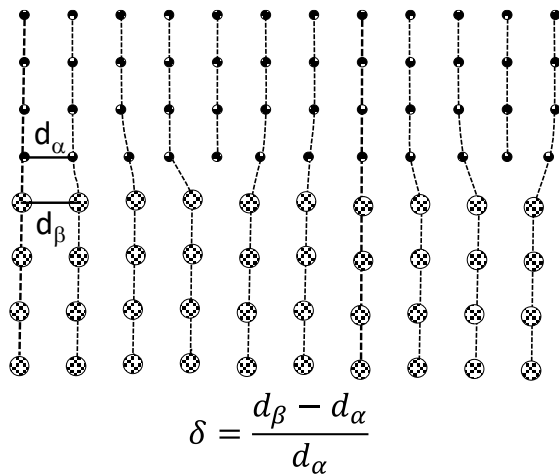


**Figure 4.9. Schematic of misfitting,  $\delta$ , between two simple cubic lattices (adapted from Turnbull and Vonnegut [TUR52]).**

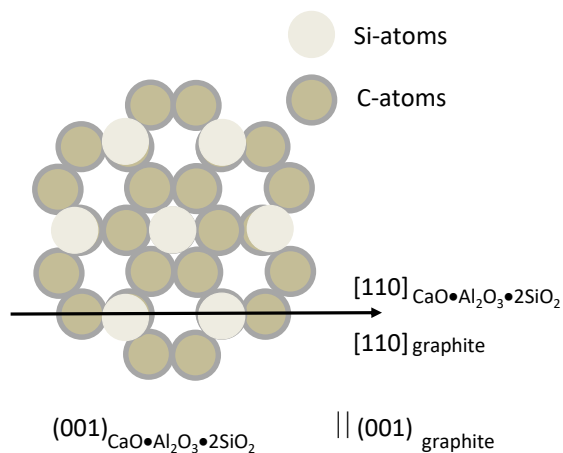


**Figure 4.10. Planar crystallography coherency between  $\text{CaO}\cdot\text{Al}_2\text{O}_3\cdot 2\text{SiO}_2$  and graphite (adapted from Skaland et al. [SKA93]).**

Other compounds than the sulphides and oxides mentioned above have been considered for graphite nucleation: graphite, silicon carbide,  $\text{CaC}_2$ -like carbides and nitrides. Details of these works were summarised in several reviews [ALO17, LOP98, SKA93, ZHO10]. Graphite powder would appear as perfect substrate and Loper et al. [LOP85] explored its use as an inoculant. It showed good potential for inoculation of LGI but not for SGI, but the authors also mentioned several inconveniences that may hinder the application of such kinds of particles in an industrial process.

Though more difficult to characterize, the presence of nitrides in graphite nuclei has been reported for a long time as reviewed by Zkou Jiyang [ZHO10], e.g. by Igarashi et al. [IGA98] and Solber et al. [SOL01]. Furthermore, according to Eustathopoulos et al. [EUS88], nitrides are more suitable for inoculation of metals than oxides are. However, their importance in graphite nucleation was not considered until recently. The presence of nitrides as graphite nuclei and their composition depend on the chemistry of alloys. Nakae and Igarashi [NAK02] found faceted nitride in Mg-treated cast iron with a very low sulfur content (0.0022wt.%S), while no nitrides were present at higher sulphur levels (0.0052 to 0.083wt.%S). Studying the effect of Ti content, from 0.007 wt.% to 0.036 wt.%, on nodule count, Alonso et al. [ALO18] reported the presence of (Mg,Si,Al) nitrides and Ti(C,N) when  $\text{Ti} > 0.01\text{wt.}\%$ . They found that nodule count increased in the range of 0.02-0.03% Ti, where Zr was also observed in Ti(C,N) carbonitride inclusions. Detailed crystallographic and chemical characterization of a complex graphite nucleus has been reported by Laffont et al. [LAF20]. They found that the outer part of

the nucleus that acted as substrate for graphite was a (Al,Mg,Si) nitride. The same kind of nitrides has also been reported by Qing et al. [QIN21] in the outer shell of inclusions that promoted graphite nucleation.

Fig. 4.11 illustrates the capabilities of modern analytical means by transmission electron microscopy to evidence the complexity of the precipitation steps leading to a graphite nucleus [PUG19]. Fig. 4.11-a shows a diametrical section of a graphite spheroid with its nucleus that is better seen in the close-up in Fig. 4.11-b. The upper part of this nucleus shows contrast indicating it is multi-phase and this was investigated using diffraction and **energy dispersive spectrometry (EDS)** with a nanometre-size probe. The Fe, S and Ti EDS maps have been superimposed in Fig. 4.11-c. The Fe-rich centre could be indexed as bcc-ferrite, and is surrounded by a Mg-S halo that could not be indexed because being too thin. The fan-like Ti-rich precipitate was indexed as a Ti(C,N) carbo-nitride, while the small Fe-rich spots on the outer part could not be indexed either. The remaining of this rounded part and the tail appeared to be a (Al,Mg,Si) nitride on which graphite nucleated. It can be postulated that the bcc centre was a remain of the Fe-Si inoculant and that up to three phases precipitated onto it before graphite.

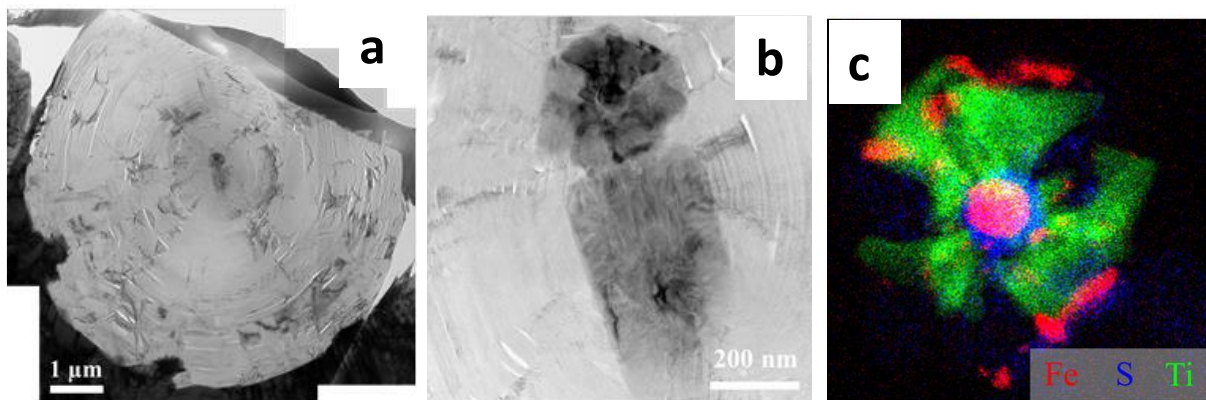


**Figure 4.11. a: Mosaic image made of TEM bright field micrographs; b: BF image of the nucleus; c: superimposition of EDS mapping of Fe (red), S (blue) and Ti (green) of the upper part of the nucleus [PUG19].**

In principle, a term describing the elastic energy associated with the disregistry between the substrate and the phase to precipitate should appear in the expression of the surface energy [EUS88]. However, this term is negligible if the elastic modulus of one or both of the solid phases is low, which can occur during solidification, whereas it is usually significant for solid state precipitation. In this line, it is worth reminding that amorphous sulphides may also act as substrates for graphite nucleation [IGA98], in which case very little elastic energy accumulates between the liquid substrate and the solid nucleus. It can therefore be expected that the energy barrier for graphite nucleation is lower on an amorphous substrate than on its crystalline equivalent.

#### 4.5 Development of inoculants

Inoculation for enhancing graphite precipitation has been developed using FeSi alloys containing minor quantities of other elements that are avid of oxygen and sulphur, like Al, Ba, Ca, Sr, Zr, etc. Some of the oxy-sulphides of these elements could allow the nucleation of graphite if their crystallographic structure has planes of low  $\delta$  value with the planes of graphite.

Typically, the information given by Ellingham's or similar diagrams is used to qualitatively understand the composition of commercial inoculants. Ellingham's diagrams rank the elements regarding their affinity with oxygen, sulphur or nitrogen, given that the elements and compounds are pure, see Fig 4.12-a. This figure shows that Ca is the most oxygen avid element among the other elements considered in that figure. Note that their ranking by oxygen affinity could change with temperature.

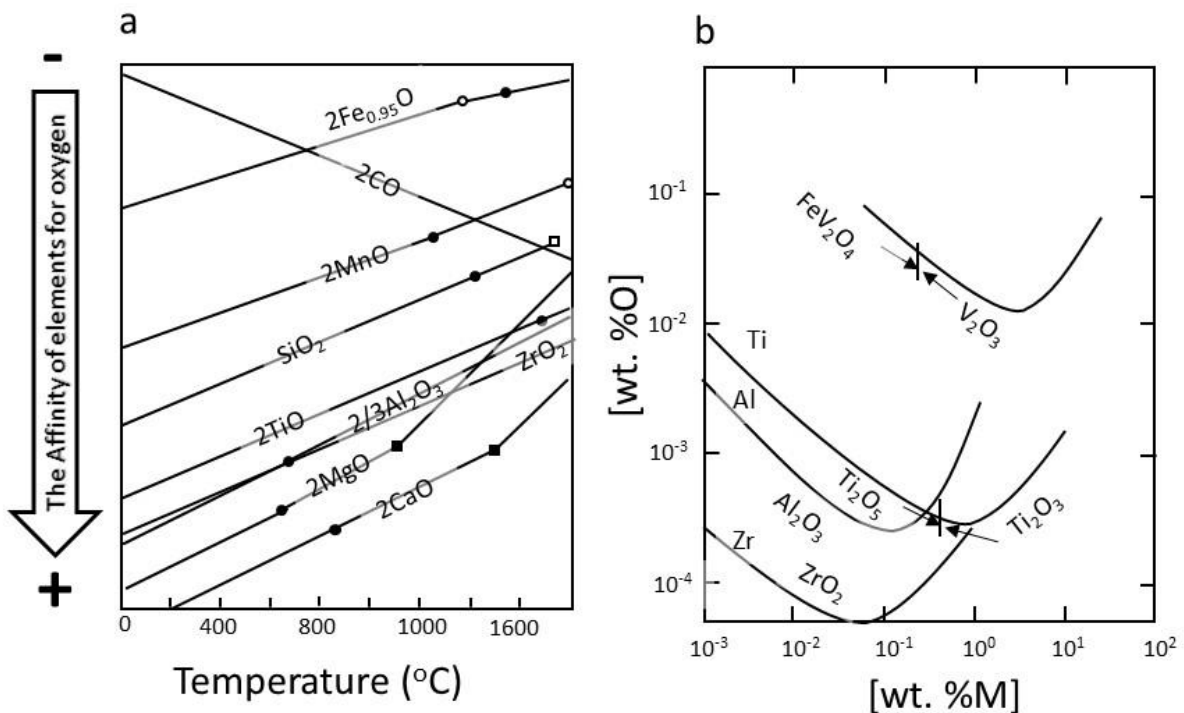


**Figure 4.12. a) Oxides Ellingham's diagram, adapted from C.H.P. Lupis [LUP83]. Dots and black squares identify melting and boiling temperatures of the metals, respectively; circles and open squares identify melting and boiling temperatures of the oxides, respectively. b) Deoxidation equilibrium in liquid iron at 1600 °C, adapted from Gosh and Murthy [GOS86]. M stands for Al, Fe, Ti, V or Zr.**

Although the information in Ellingham's diagrams corresponds to an ideal case, namely thermodynamic equilibrium of pure elements and simple (binary, at most ternary) compounds, these diagrams have proved to be very relevant for steelmakers to understand the limits of processes designed to eliminate inclusions or modify their composition. Conversely, the same type of information could be used to determine suitable substrates for graphite nucleation in cast iron, namely oxides, sulphides and nitrides.

Ellingham diagrams do not provide information on the effect of the concentration of elements in a melt on their oxygen affinity ranking. At a given temperature, this ranking can vary according to the concentrations of the elements concerned. This is illustrated for the case



of Al and Ti in Figure 4.12b where it can be seen that Al determines the oxygen concentration at low Ti levels, whereas Ti does at higher concentration levels, given that both elements have the same concentration in the melt. Figure 4.12b also shows that the deoxidation products could change with the concentration of the deoxidising elements; Then, it is possible to form other oxides in the high concentration areas related to the dissolution of the inoculant than those indicated by the Ellingham diagram. This could explain the formation of Al<sub>2</sub>O<sub>3</sub> in the presence of Mg in spheroidal graphite cast irons.

A more precise analysis of inclusion formation in relation to inoculation requires considering time-dependent dissolution and precipitation effects of elements in iron melts and modelling of the inclusion constituent. Most of the available data for such calculations have been obtained at temperatures relevant to the steelmaking process, i.e. at 1500-1600°C, though a few studies have been carried out in the same line on cast irons. Harding and Saunders did thermodynamical simulations to study the formation of nitrides in cast irons containing various amounts of Ti, Nb, V and N [HAR98]. Lekakh et al. have studied the thermo-chemistry of non-metallic inclusions in ductile iron during the transitory step of inoculation [LEK09] with particular focus on the effect of pre-treatment with Ca-La mischmetal before spheroidising and of ladle inoculation. They did both chemical characterisation of the inclusions and thermodynamic calculation using thermodynamic databanks and software packages. The results show a wide range of composition of inclusions at every step of melt treatment. More recently, Lekakh applied thermodynamic calculations for predicting the most suitable inclusions for graphite nucleation [LEK18].

#### 4.6 Nucleation laws as a function of temperature

As a consequence of section 4.3 it should be possible to set up nucleation laws that would be useful to simulate grain refinement in castings. In a pioneering work based on experimental data, Oldfield established the following law for nucleation of lamellar eutectic cells in cast iron [OLD66]:

$$N_V = A_n \cdot (\Delta T_{EUT})^n \quad (4.13)$$

where  $N_V$  is the volume number of cells,  $A_n$  and  $n$  are constants that depend on the process and  $\Delta T_{EUT}$  is the undercooling with respect to the stable eutectic temperature.

This kind of nucleation law agrees with calculations based on the classical nucleation theory in that heterogeneous nucleation over a given type of substrate proceeds in a minimal range of temperature. It can be assumed that all existing substrates of a given type get exhausted as soon as their activation undercooling is reached. By virtue of Eq. (4.13), Oldfield [OLD66] and later Hunt [HUN84] therefore assumed that a population of substrates exists in the melt, with each type of substrates being activated at different undercooling.

Several other forms of nucleation laws have been proposed since Oldfield's work, either as a function of temperature or including time dependence. The former kind of laws is firstly considered because they account for the essentials of the nucleation phenomena, while time effects are discussed in section 4.8.

Based on the work by Oldfield, Lacaze et al. [LAC89, LAC90] proposed a nucleation law where graphite nucleation is related to the graphite liquidus undercooling,  $\Delta T_L^{gra}$ , as it should be:

$$N_V = A_n \cdot (\Delta T_L^{gra})^n \quad (4.14)$$

This law was then used in its differential form expressed as:

$$dN_V = n \cdot A_n \cdot (\Delta T_L^{gra})^{n-1} \cdot g^{liq} \cdot d(\Delta T_L^{gra}) \quad (4.14')$$

where the liquid volume fraction,  $g^{liq}$ , has been included as an attenuation factor, i.e., assuming that nucleation sites disappear with liquid consumption.

For aluminium alloys, Rappaz et al. suggested a nucleation law in which the number of sites that can be activated follows a Gaussian law of the liquidus undercooling  $\Delta T_L$  [RAP86]:

$$N_V = \frac{N_{max}}{\sqrt{2\pi}\Delta T_\sigma} \int_0^{\Delta T_L} \exp\left(-\frac{(\Delta T_L - \Delta T_0)^2}{2(\Delta T_\sigma)^2}\right) \cdot d(\Delta T_L) \quad (4.15)$$

in which  $\Delta T_\sigma$  and  $\Delta T_0$  are the standard deviation and the mean of the undercooling distribution, respectively, and  $N_{max}$  the maximum number of substrates.

Eq. (4.14') and (4.15) both give a similar bell shape to the distributions of activated sites as a function of undercooling, Eq. (4.14) because of the attenuation factor and Eq. (4.15) due to the use of a Gaussian-type law.

The parameters of the laws depend on each particular melt preparation process, but are not directly related to the characteristics of the substrates from the nucleation catalysis itself. Clearly, the inoculation process of cast irons is quite complex, involving both transitory and various chemical phenomena which are not described by the laws just seen.

#### 4.7 Experimental determination of graphite nucleation laws

In all practicality, inoculation of cast irons is frequently related to the observed number of eutectic cells in LGI or spheroids in SGI, which is then set equal to the number of activated graphite nuclei. Because of that, the nucleation of graphite is most generally associated with the undercooling with respect to the stable eutectic temperature. Unfortunately, using this reference could lead to confusion when experimental data of cast iron solidification is analysed. As the driving force for graphite nucleation is related to the graphite liquidus,  $T_L^{gra}$ , it is the undercooling relative to this temperature that must be considered.

It might be useful to look at the evolution of this driving force by following the solidification path in relation with the description made in Chapter 3. The change of carbon content of the liquid during solidification of a hypoeutectic alloy is schematized in a Fe-C isopleth section on Fig. 4.13. Upon cooling from the liquid state,  $N_\gamma$  austenite grains nucleate when an undercooling  $\Delta T_L^\gamma$  is reached, though generally not giving rise to recalescence on TA records. After its nucleation, austenite dendrites keep some undercooling to grow during further cooling. When the temperature of the metal has decreased below the eutectic temperature, graphite nucleation becomes theoretically possible because the liquid composition is now below the

graphite liquidus. However, experimental observations consistently show that graphite precipitation needs some significant undercooling to proceed, meaning that the metal has to cool further. During this additional cooling below  $T_{EUT}$ , austenite continues growing until sufficient graphite nuclei have formed for bulk eutectic to start at  $T_{e,min}$  in Fig. 4.13. In practice, the number  $N_{g,1}$  of spheroids that have appeared at that temperature is related to  $T_{e,min}$  and not to the maximum undercooling for graphite nucleation  $\Delta T_L^{gra}$  as it should be (note that the undercooling  $\Delta T_L^{gra}$  is about 4 times the undercooling  $\Delta T_{EUT}$  for temperatures below  $T_{EUT}$ ). However, in agreement with the above description of the activation process, nucleation stops with recalescence because  $\Delta T_L^{gra}$  diminishes. At later time, the metal temperature can decrease below  $T_{e,min}$  before solidification completion, in which case a second nucleation “wave” occurs with the formation of  $N_{g,2}$  additional nuclei.

The above description calls for two remarks. First, graphite does not nucleate over the austenite but on substrates within the liquid. As a matter of fact, austenite growth leads to a continuous increase of the carbon content in the liquid, and hence to a constant rise in the undercooling with respect to graphite liquidus which finally favours graphite nucleation. Unfortunately, only indirect experimental evidence supports this solidification path as there is no practical means to follow the carbon content of the remaining liquid during eutectic solidification. The second remark is that the observed undercooling before bulk eutectic solidification of a hypoeutectic cast iron has been attributed to the nucleation stage. It has been mentioned in Chapter 3 that graphite growth also needs that a large enough  $\Delta T_L^{gra}$  value has been reached [CAS20] and this can certainly interfere with the early growth of eutectic entities.

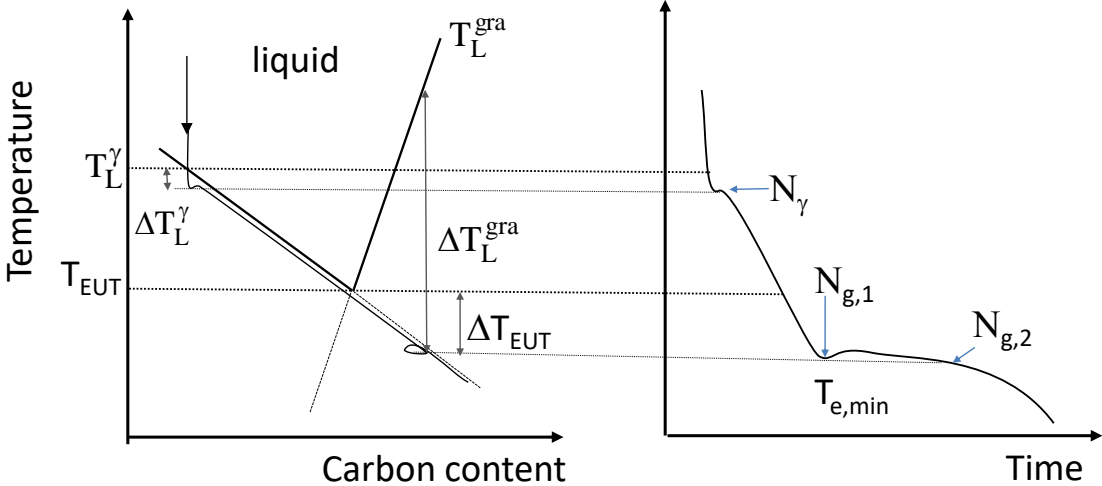


**Figure 4.13. Evolution of the carbon concentration in the liquid during solidification of a hypoeutectic cast iron, and its relationship with undercooling associated to graphite liquidus,  $\Delta T_L^{gra}$ , or to eutectic temperature,  $\Delta T_{EUT}$ . Note that at temperature lower than  $T_{EUT}$ ,  $\Delta T_{EUT}$  is about  $\frac{1}{4}$  of the corresponding  $\Delta T_L^{gra}$  value [LAC98a].**

Figure 4.14 is a graphical representation of an experimental procedure that would allow determining the parameters of any nucleation law, e.g. Eq. (4.13) or better Eq; (4.14). For this, castings solidified at different cooling rates are equipped with properly located thermocouples. After solidification, the number of eutectic cells or nodules is obtained from microstructure

analysis and the data are transformed from 2D to 3D values using the Saltykov procedure or any other, and the microstructure results are then correlated to the corresponding undercooling values estimated on the cooling curves. In doing so, every attempt to keep the nucleation law as simple as possible is made, meaning that the use of only one or two parameters must be preferred, like  $A_n$  and  $n$  in the nucleation law of Fig. 4.14.

Figure 4.14 shows cooling curves similar to those obtained by thermal analysis, which is used to monitor the quality of the liquid metal but is limited to a cooling rate. In contrast, knowing of how undercooling of the eutectic plateau changes with varying cooling rates is essential to detect which metal could lead to carbide formation in critical areas. This prediction could be more straightforward when the nucleation law is known. Further, the parameters of a nucleation law depend on the particular process of each foundry because of the rather complex nucleation phenomena. A good practice could thus be to calibrate a nucleation model with parameters corresponding to the worse conditions, i.e. to the results of the most deficient inoculated metal obtained in regular melt processing. Then thinnest casting sections could be checked against the predictions made for this worse case. This information would be useful when fine-tuning the production of castings.

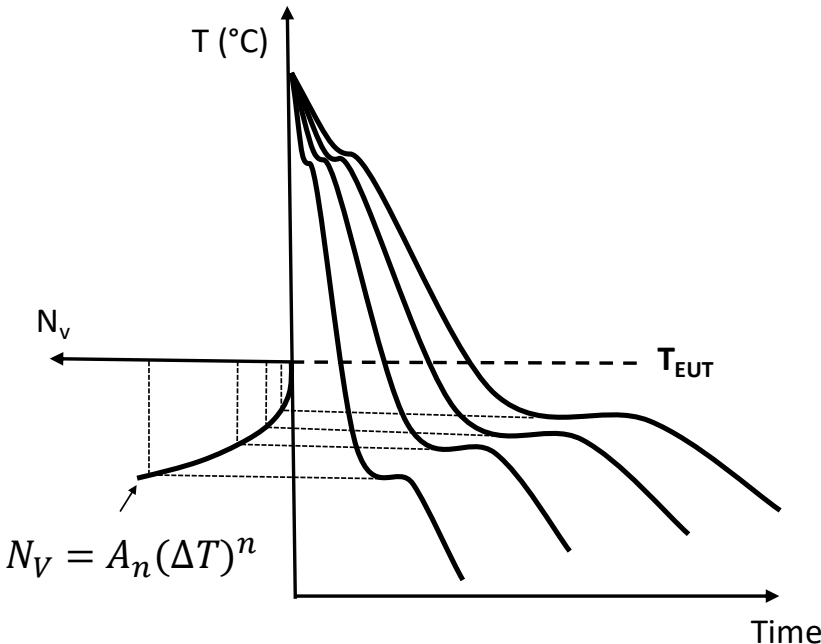


**Fig 4.14. Graphical representation of the procedure for obtaining the graphite nucleation law from experimental data.  $\Delta T$  can be simply  $\Delta T_{EUT}$  as in Eq. (4.13) or better  $\Delta T_L^{gra}$  as in Eq. (4.14).**

**4.8 Inoculation as related to nucleation theory**

A way to enhance nucleation of solid particles in a melt is to generate or activate substrates under a local undercooling that can be of thermal or chemical nature. Inoculation can support the process but could present different difficulties depending on the phase to precipitate, namely austenite and graphite for what concerns cast irons.

Materials with rapid growth kinetics could hardly be grain refined because the high heat release rate during early solidification of such materials quickly leads to recalescence that hinders activation of new nucleation sites. Pure metals with non-faceted growth, such as fcc and bcc metals, are examples of such materials. Alloying these pure metals, such as austenite in cast irons, reduces the growth kinetics of the primary phase, but this kinetics generally remains so high that grain refining keeps limited. However, the cooling of the metal by contact with the mould wall provides a local thermal undercooling that induces profuse nucleation and explains the so-called chill zone observed at the skin of castings for many alloys including iron alloys. This gives some hope of finding appropriate substrates for nucleating austenite in cast iron as done successfully for the fcc phase of aluminium alloys and claimed for austenitic steels [LEK17]. Interestingly for cast irons, Lekakh et al. observed that the precipitation of MnS on TiN poisons the potential of these nitrides as a substrate for austenite.

Accordingly, some research has been done to characterize austenite nucleation in cast irons where austenite grains size is about a few mm [DIO07, ELM10, MIY98]. The maximum undercooling for austenite nucleation on samples melted and cooled in the same crucible was observed to be about 14°C [MIY98]. Such an undercooling value is well within the observed range for the  $T_{LA}$  arrest discussed in relation with TA in Chapter 3. In the usual case where austenite nucleates at and grows from the surface of the TA cup, it is quite possible that change in the nucleation undercooling affects the TA records. In practice, the use of the characteristic temperature of austenite solidification to control the carbon equivalent austenite liquidus, CEL, in cast iron assumes that austenite solidification, i.e., nucleation and growth of austenite, in the thermal cup is relatively unchanged by variations in the melt processing other than the variations of carbon equivalent.

On the contrary to the case of austenite, inoculation of cast irons has proved to be effective for graphite nucleation. Inoculation is defined as the late addition of Fe-Si alloys to molten iron to produce changes in graphite distribution without any significant change in the overall chemistry of the iron. Inoculation could be realised in the furnace or during transfert of the melt to the mould. This latter is known as post-inoculation, which could be made in the ladle, in-stream or else in the mould, the two latter being known as late inoculation techniques [BIE98]. In ductile irons, the so-called preconditioning inoculation is also used that consists in adding inoculant together with the nodulizing agent [FOU05].

The choice of the inoculation treatment depends on casting thickness and foundry setup. Thin walls castings need improved inoculation using in-stream inoculation to avoid mottled structure in spheroidal graphite iron or type D graphite in grey cast iron, though in-mould inoculation could also be applied. In-stream inoculation requires special equipment to spray inoculant particles into the liquid metal in a controlled way and also an automatic pouring system. Thick wall castings poured with the traditional pouring ladle process are generally primary inoculated, i.e. when the melt is transferred to the pouring ladle.

Commercial inoculants are tailored depending on when they are used during the process. Typically, fast dissolution of inoculants is suitable in the late inoculation processes though some compromise must be achieved between dissolution and fading kinetics. According to Fuller [FUL79], the inoculant effect could be lost in some tens of seconds after its addition. This suggests that the maximum effect of inoculation is got immediately after adding the

inoculant, while it has not been fully dissolved. The addition of FeSi bearing inoculants produces **local chemical undercooling** in the high Si regions around the dissolving FeSi particles. In these regions, the liquidus temperature is increased and the carbon solubility in the melt is decreased, thus increasing the driving force for graphite precipitation [HAR98]. In-stream and in mould inoculation do certainly take advantage of this latter mechanism, which is also complemented with the formation of new substrates and the chemical modification of the primary inclusions (see below) because of the elements added to the Fe-Si alloys.

The importance of FeSi dissolution effect in graphite nucleation has been pointed out in several studies, e.g. those by Fredriksson [FRE84], by Loper [LOP99] and by Lekakh and Loper [LEK03]. On the contrary, Feest et al. [FEE83] argued that the dissolution time of FeSi is of a few seconds and concluded that it is not possible to keep Si-rich zones for any enough time of practical interest. However, the outstanding performance of the late inoculation techniques confirms that chemical undercooling is essential for the casting process, but this may be less important for the casting of large sections where the inclusions will be closer to equilibrium.

In practice, foundrymen face unexpected variations in inoculation performance, even if the inoculation process is controlled in a “known” allowed range. The nature and number of primary inclusions could be one of the reasons of such variations. Primary inclusions are defined here as those present in molten metal before any late inoculation treatment. In this regard, the effect of primary inclusions on graphite nucleation has been studied only in **preconditioning inoculation treatment**. This initial inoculation can be performed with barium-bearing ferrosilicon as an alternative to 75% Ferrosilicon or SiC products. If preconditioning is well done, a better control of the post-inoculation is expected [FOU05]. Furthermore, primary inclusions must be present in the molten metal even without preconditioning treatment. Their nature could depend on several factors, for example, the chemical composition of the melt or the thermal cycle of metal into the furnace.

Regarding the inclusion composition, it could be mentioned that it takes several minutes for the inclusions in steel to diminish their chemical composition differences due to contact of liquid metal with deoxidisers or alloying elements [HER98]. Similarly, it may be considered that the modification of inclusion composition initiated by FeSi dissolution takes longer time than the time for pouring and solidification of typical medium-size castings. It is thus not surprising that, in post-inoculation studies, inclusions that work as a catalyser for graphite nucleation show wide composition ranges [ALO17, LEK09, RIP03, SKA93]. Unfortunately, the time between inoculation and solidification of the cast is rarely reported in such studies. This complicates the evaluation of these data if a better picture of the evolution of inoculation is sought.

Finally, inoculation fading is another essential aspect that has been mostly associated with coalescence, Ostwald ripening and floatation of the inclusions, although chemical undercooling by FeSi could also play a vital role. Skaland et al. [SKA93] proposed a nucleation model accounting for the time elapsed between stream inoculation and casting solidification, considering that inoculation fading is due to Ostwald ripening:

$$N_V = c[\ln(1.33 + 0.64t_e) - \ln(1.33 + 0.64t_s)] \quad (4.16)$$

where  $c$  is a kinetic constant and  $t_s$  and  $t_e$  are the time intervals between inoculation and start and end of solidification, respectively. Stream inoculation was performed immediately before pouring the melt in the mould.

Svensson and Diòszegi [SVE03] studied the inoculation of grey iron by ladle inoculation. The estimated time between inoculant addition and melt pouring was 40-60 seconds. They proposed the following nucleation law that gives an idea of the time evolution of inoculation performance:

$$N_V = \frac{K}{t} \quad (4.17)$$

In summary, several phenomena occur during the late inoculation of cast iron melts, as schematised in Fig. 4.15, leaving some questions still open that would also be of interest for medium and large castings. One of them is the usefulness of modifying the Mg silicates provided by the spheroidising treatment with further additions, Ca for example. Also, another unknown is the time such modified inclusions could survive in the melt. Further, it should be clarified if, in the presence of Ca, Sr, Ba and Al silicates, the local chemical undercooling is needed or not. Moreover, more fundamental details concerning inclusion evolution during preconditioning and primary inoculation are required. Finally, the importance of better understanding the nature of primary inclusions may become essential with changes in the composition of steel scraps used in foundry plants. These informations could allow separating the effect of different aspects of inoculation to improve the cast iron process, but their understanding requires both thermodynamics tools and experimental setups other than foundry shop.

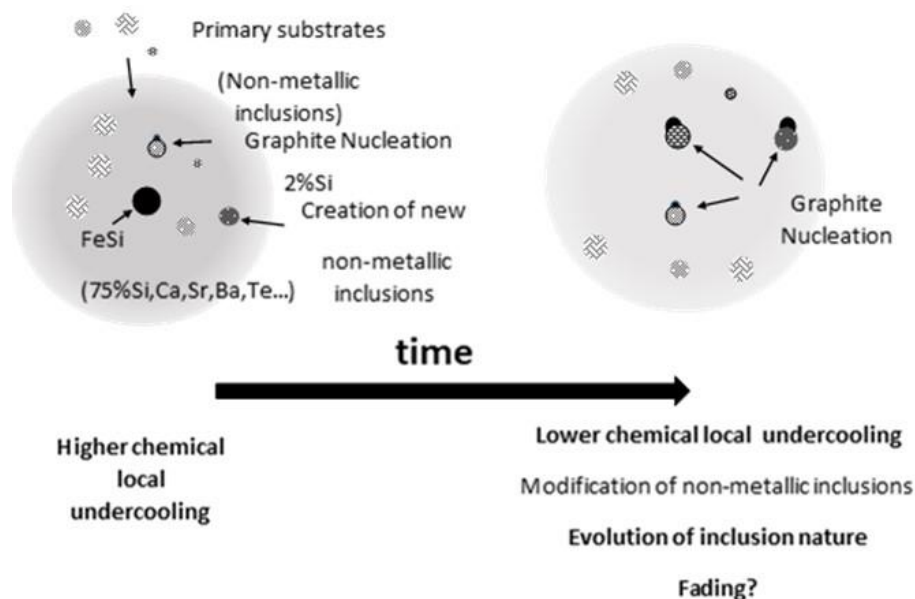


**Figure 4.15. Evolution of inclusion nature from the beginning of inoculation to the time at which the FeSi based inoculant is entirely dissolved.**

#### **4.9 Summary**

Microstructure refinement and graphite inoculation in cast iron castings is a prerequisite for casting soundness and high service properties. Contrary to austenite that is hardly refined, inoculation by late addition of specific Fe-Si alloys to molten iron produces the expected changes in graphite distribution. The general context in cast iron shows that nucleation and growth of graphite, which is a faceted phase, are somewhat complex and need particular focus.

The classical theory of nucleation provides the framework needed for understanding the effect of cooling rate on microstructure refinement. According to this framework, substrates can activate the nucleation of crystalline solids at characteristic undercooling, and are entirely consumed when they catalyse nucleation. Furthermore, a population of substrates with various sizes and chemical compositions certainly exist in the molten liquid. It is believed that the differences in their characteristics gives rise to a nucleation law that is a continuous function of undercooling. Moreover, the parameters of this law can be experimentally fitted to any particular casting process.

The crystallographic similitude concept complements the general picture of inoculation. Experimental work according to this approach shows that some oxysulphides are suitable to promote graphite nucleation. Consequently, industrial inoculants contain elements avid of sulphur and oxygen, such as Ca, Sr, Ba, etc., (Mg,Al,Si) nitrides are also found as suitable substrate for graphite nucleation and might be favoured when Al is added to the inoculant. Surprisingly, the substrates associated to graphite nodules show a huge range of chemical compositions whose description is a real challenge. On the other hand, the nucleation of austenite has been less studied and it is not certain that it can be controlled.

It is believed that the use of modern thermodynamic and thermokinetic tools will help to describe and control inoculation performance and fading, taking into account in particular thermal and chemical undercooling. This will certainly support future efforts to manage the evolution of steel scrap used for the preparation of cast iron melts.





# Chapter 5 – Primary graphite, crystallography and morphology

In describing the growth of graphite during the solidification of cast irons, it is important to consider first primary growth, i.e. the direct precipitation of graphite from the liquid. Indeed, the simultaneous growth of austenite and graphite during eutectic solidification imposes additional constraints to which the graphite shape may be sensitive, even if the internal structure of the graphite remains the same. Hypereutectic alloys should be used to study the primary growth of graphite, and the more hypereutectic the alloy is, the larger the graphite crystals are. However, there is a risk of rapid floating at low cooling rates, so a compromise must be found for such experiments.

Fig. 5.1 presents the various shapes of primary graphite crystals in cast irons that are discussed in this chapter. In this figure, the horizontal axis represents the change of growth conditions, i.e., either the undercooling  $\Delta T$  or cooling rate. Note that: 1) The cooling rate is the one imposed under constrained growth (directional solidification and cooling) or the one measured before solidification starts in the case of thermal analysis and casting; 2)  $\Delta T = \Delta T_L^{gra}$  is here related to graphite liquidus as we deal with primary graphite. The double vertical axis in Fig. 5.1 shows upwards the effect of spheroidizers and downwards that of oxygen and sulphur, while "pure" alloys are located on the horizontal axis.

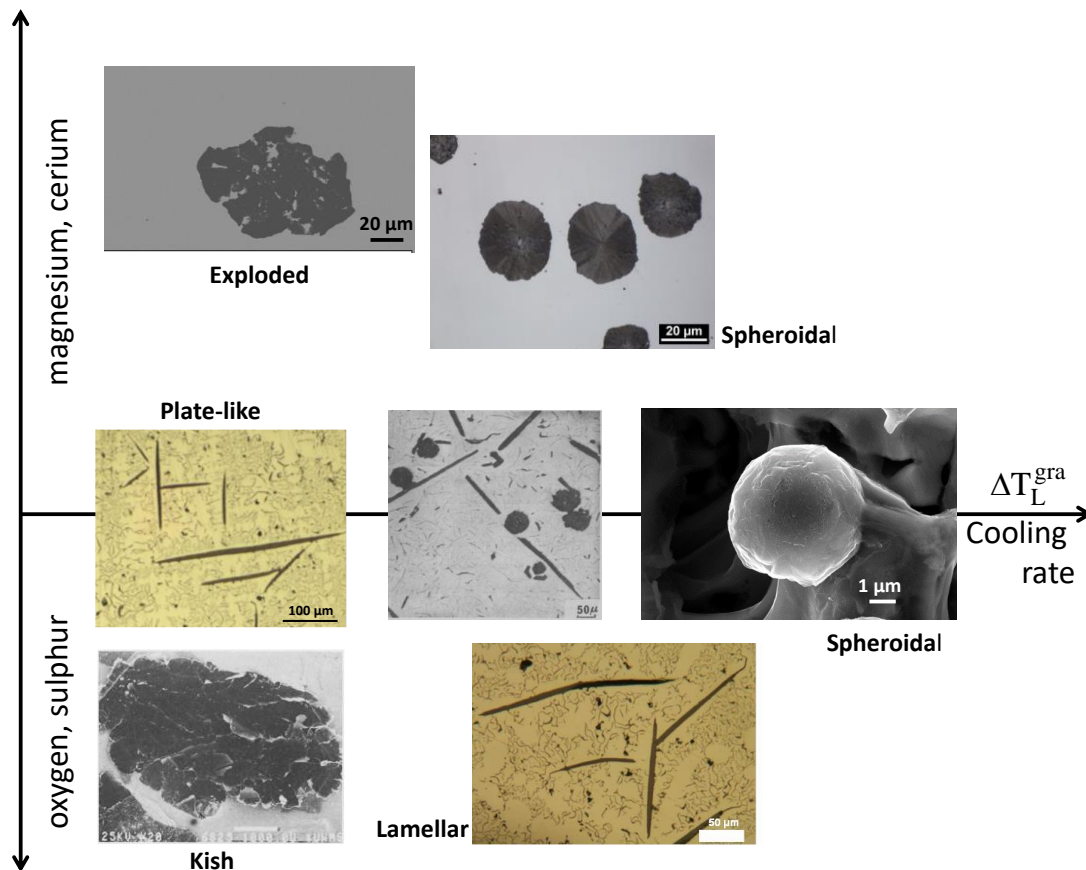


Figure 5.1. Various shapes of primary graphite in cast irons

Even at a very low growth rate or cooling rate, plate-like graphite is observed in "pure" melts, which however is not the equilibrium form, see section 5.1. With increase in  $\Delta T$ , both lamellae and spheroids are observed and at very high undercooling only graphite spheroids precipitate that get embedded in a matrix of metastable eutectic. Cast iron melts that have not been spheroidized do contain oxygen and sulphur, and show lamellar graphite as well as kish graphite in the case of floatation in highly hypereutectic alloys, see section 5.2. Unusual and other characteristic features of lamellar graphite are described in section 5.3. Melt that have been spheroidized lead to spheroidal graphite that is described in sections 5.4 and 5.5. As the solidification time increases, spheroidal graphite tends to degenerate and so-called exploded graphite precipitates are often observed in large castings of hypereutectic composition. Finally, the transition from lamellar to spheroidal graphite along the  $\Delta T$  axis in Fig. 5.1 is shortly discussed in section 5.6 for its theoretical interest.

### 5.1 Crystal structure and equilibrium shape of graphite

The stable crystallographic shape of graphite is hexagonal compact with a ABAB stacking, Fig. 5.2. The cell thus consists of an hexagonal base with the distance between carbon atoms in the basal planes being much shorter than that between these planes, in direct relation with the strength of the corresponding electronic bonds. A rhombohedral structure is sometimes reported which may be obtained from the most stable one by inserting point defects as described in detail by Qing et al. [QIN17] in their analysis of the structure of graphite spheroids.

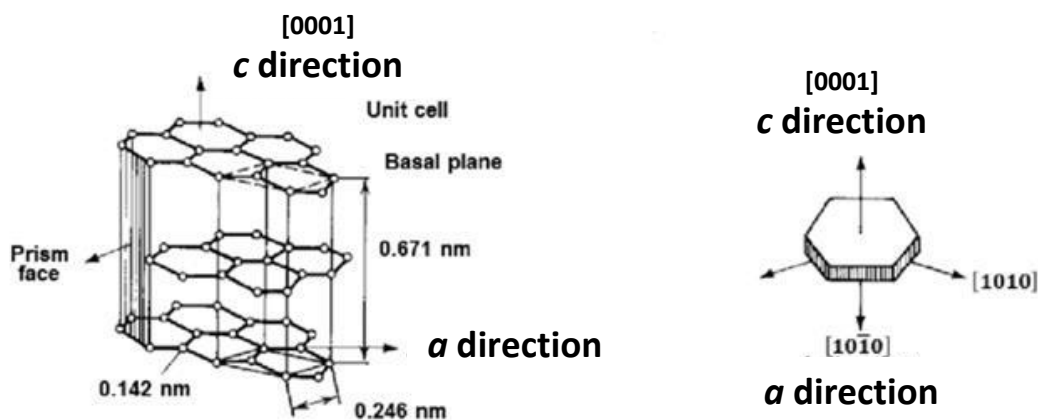


Figure 5.2. Crystallographic structure of the stable hexagonal shape of graphite.

The very weak bonds between basal planes account for the great capability of graphite to present defects at the scale of atomic stacking, but also to show an impressive variety of shapes at the scale of precipitates. A catalogue of these shapes has been made [STE18] which are not all relevant for cast irons. The present monograph is limited to those of these shapes that are observed in cast irons, and this chapter puts emphasis on the relation with the background crystallography, on the one hand, and the presence of impurities or added elements, on the other hand. A more complete view of the effect of low level elements on graphite shape and so-called degeneracy is presented in Chapter 8.

The equilibrium shape of a crystal is the one that minimizes the **interface energy** between the crystal and its environment. Attempts have been made to measure the interface energy

between carbon saturated melts and graphite,  $\sigma^{\text{Gra/L}}$ , by using the sessile drop method with a graphite substrate, see Fig. 5.3-a. If care is taken to ensure that there is no dissolution of the substrate, the following Young's equation establishes the mechanical equilibrium at the triple line:

$$\sigma^{\text{L/V}} \cdot \cos\theta = \sigma^{\text{Gra/V}} - \sigma^{\text{Gra/L}} \quad (5.1)$$

where  $\theta$  is the contact angle,  $\sigma^{\text{L/V}}$  is the surface energy of the melt and  $\sigma^{\text{Gra/V}}$  that of graphite.

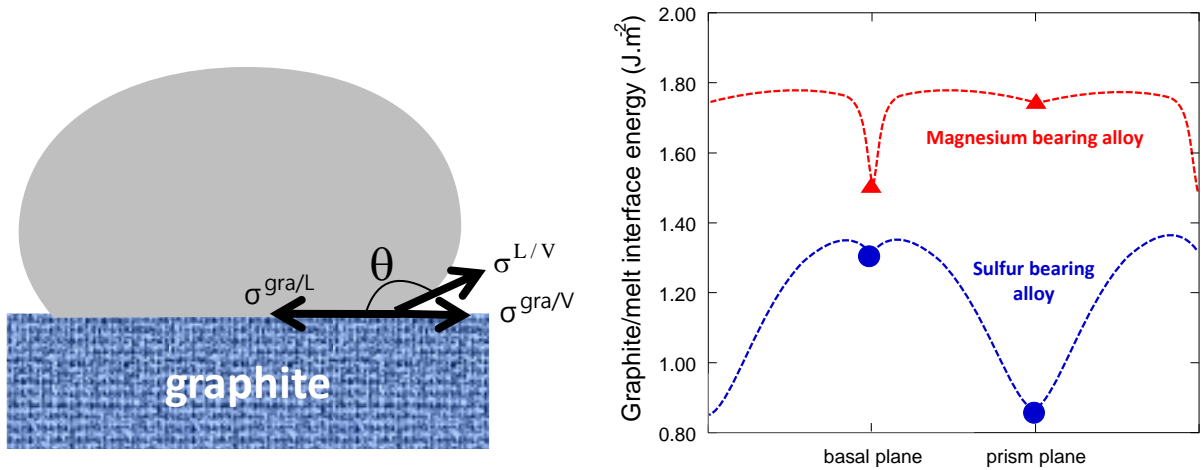


**Figure 5.3. a: Equilibrium shape of a melt drop on a graphite substrate. b: Graphite/melt interfacial energy. Symbols are experimental values [MCS74], lines are tentative evolution in the  $(\bar{1}\bar{1}20)$  plane (after [TOR16]).**

What is best established is the **surface energy** of the melt,  $\sigma^{\text{L/V}}$ , and sulphur and oxygen are amongst the most **surface active** elements in iron melts, together with As, N and Te. By removing oxygen and sulphur from the melt, the spheroidizing treatment does lead to an increase of its surface energy at the temperature at which this treatment is carried out. Other surface active elements are Sb and Sn, while C, Si and P have very little effect. A review of literature data suggested the following expression for the surface tension of cast iron melts [LAC22a]:

$$\begin{aligned} \sigma^{\text{L/V}} = & 1880 - 0.41 \cdot (T_K - 1811) - 0.153 \cdot T_K \cdot \ln \left( 1 + 4 \cdot 10^{-5} \cdot \exp \left( \frac{355000}{R \cdot T_K} \right) \cdot a_O \right) \\ & - 0.107 \cdot T_K \cdot \ln \left( 1 + 0.03 \cdot \exp \left( \frac{232000}{R \cdot T_K} \right) \cdot a_S \right) \\ & - 46.1 \cdot w_{Si} - 30 \cdot w_P - 1690 \cdot w_{Sb} - 560 \cdot w_{Sn} \end{aligned} \quad (5.2)$$

where  $w_i$  is the wt.% content in element  $i$  and  $T_K$  the temperature in Kelvin.  $a_O$  and  $a_S$  are oxygen and sulphur activities, respectively, calculated with pure gas as reference.

Thanks to Young's equation and with the knowledge of  $\sigma^{\text{L/V}}$ , the evaluation of the contact angle  $\theta$  gives  $\sigma^{\text{Gra/L}}$  provided  $\sigma^{\text{Gra/V}}$  is known. Unfortunately, this straightforward evaluation is impaired by the poor knowledge of the surface tension of graphite [LAC22a]. Nevertheless, Fig. 5.3-b shows the four data points from McSwain et al. [MCS74] which were selected as

being self-consistent and in the range of reported values for this graphite/liquid interface. The dashed lines are tentative and do not account for probable local minima corresponding to intermediate or vicinal facets. It is seen that with addition of magnesium, and thus with removal of sulphur and oxygen from the melt, the interface energies of prismatic and basal planes both increase. Furthermore, the latter increases more than the former, leading to invert their sorting: prism planes have higher interface energy than basal planes in spheroidized melts while the reverse is true in untreated melts. This has often been considered to explain the change in shape from flake to spheroidal graphite, whereas this is not the case as shown in Chapter 8 in relation to the study of trace element effects.

Owing to the data in Fig. 5.3-b, the expected shape of graphite crystals grown at infinitely small velocity from an **impure melt** should be a double pyramid with the faces consisting of prismatic planes. Such natural crystals have in fact been observed, see Fig. 5.4, though the pyramids are truncated in this particular case.

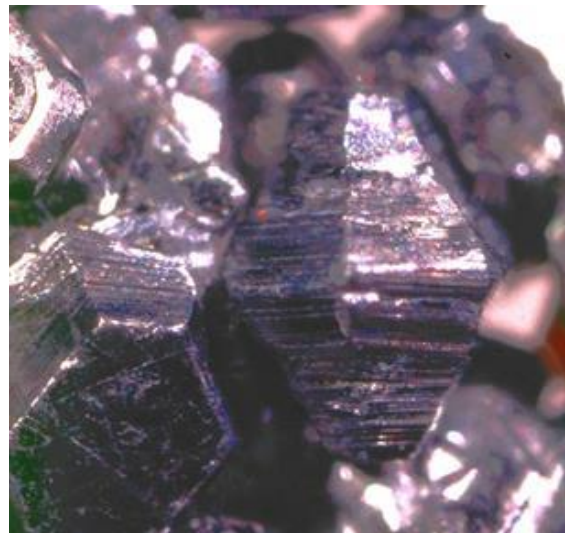


**Figure 5.4. Graphite crystal pyramids from Sterling Hill [JAS94].**

In contradistinction, the plate-like or lamellar shape of graphite is related to growth kinetics with carbon atoms attaching preferentially to the prismatic faces where the **energy gain** per atom is much higher than for basal faces. In crystal growth theory, it is expected that the densest crystallographic planes of a phase -as are the basal planes of graphite- may facet provided that the faceting factor  $F$  is larger than 2:

$$F = \frac{\Delta E^{\text{Int}}}{R \cdot T_m} > 2 \quad (5.3)$$

where  $\Delta E^{\text{Int}}$  is the molar energy of interfacial exchange,  $R$  the gas constant and  $T_m$  the melting temperature of the crystal. For metals, and we will accept it here for graphite as well,  $\Delta E^{\text{Int}}$  may be expressed as function of the interfacial tension between the crystal and the melt, i.e. here  $\sigma^{\text{Gra/L}}$ , giving:

$$F \approx 2 \cdot \frac{N_A \cdot A_a \cdot \sigma^{\text{Gra/L}}}{R \cdot T_m} \quad (5.4)$$

where  $N_A$  is the Avogadro number and  $A_a$  the area occupied by one carbon atom in the basal plane.

Setting  $\sigma_{\text{gra}/L}$  to  $1 \text{ J}\cdot\text{m}^{-2}$  and  $T_m$  to the eutectic temperature (1450 K), and using the data in Fig. 5.2 to calculate  $A_a$  leads to  $F$  of the order of 5. This value is well above the critical faceting value of 2, so that graphite precipitates are expected to develop as plates extended in directions containing the prismatic crystallographic directions and having large side faces consisting of basal planes.

Between the two opposite basal faces of a graphite plate, "prismatic" facets develop which could be true prismatic crystallographic faces, with an armchair or zigzag configuration. However, the development of vicinal faces such as those shown in Fig. 5.5 is quite easy and leads to the presence of jogs and kinks which are locations where new carbon atoms can be easily added.

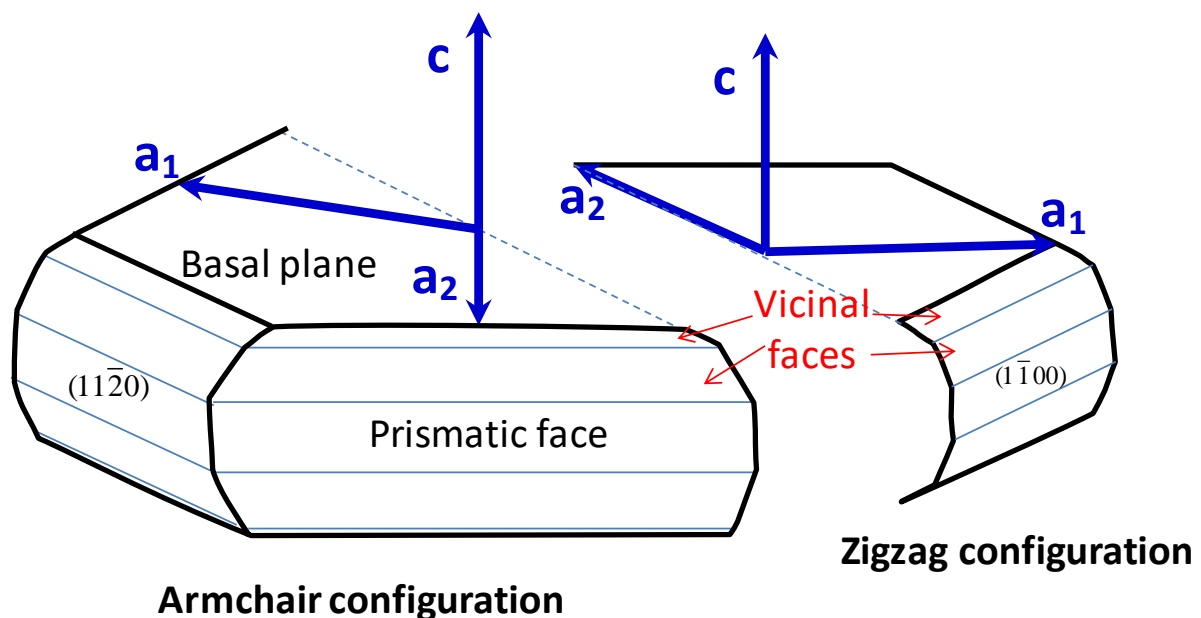


Figure 5.5. The two possible lateral faces of graphite plates (after [AMI13]).

The preferential attachment of carbon atoms on the prismatic faces and the faceting of graphite precipitates applies to any forms of graphite as further detailed below. In fact, a clear schematic for the growth of graphite precipitates in cast irons emerges regardless their overall outer shape: graphite grows as **blocks elongated in the prismatic  $a$  directions**, i.e. with carbon atoms attaching at the prismatic faces. This will be seen along this chapter and it will be stressed that the overall shape of the graphite particles is in close relation with the length of these blocks.

## 5.2 Primary growth of graphite lamellae

For low and intermediate cooling rates or undercoolings, graphite crystals grown from a Fe-C-Si melt (or Ni-C melt) that has not been treated for spheroidization consist of long plates with even thickness or lamellae as in Fig. 5.6-a. Such straight precipitates may be of millimetre size in length while their internal structure consists of a stack of graphite layers as illustrated

with the fracture surface in Fig. 5.6-b [LIU90a] obtained with a **scanning electron microscope (SEM)**. The typical thickness of these individual layers is 10-500 nm but there is no information in the open literature on the parameters that do control it.

The sample in Fig. 5.6-a was obtained by carbon saturating a piece of iron held in a pure graphite crucible at 1300°C, then cooling to 1180°C (i.e., above the eutectic temperature) and holding it for 30 minutes before being rapidly cooled to room temperature. The experiment was made in a closed furnace which was initially under laboratory air. The large lamellae developed during the first cooling and holding at 1180°C while the background matrix consisting of a few small, rounded graphite precipitates and ex-austenite dendrites bounded by fine graphite flakes resulted from rapid solidification during the final cooling. The micrograph in Fig. 5.6-b relates to a sheet of graphite grown at the surface of a hypereutectic cast iron melt [LIU90a].

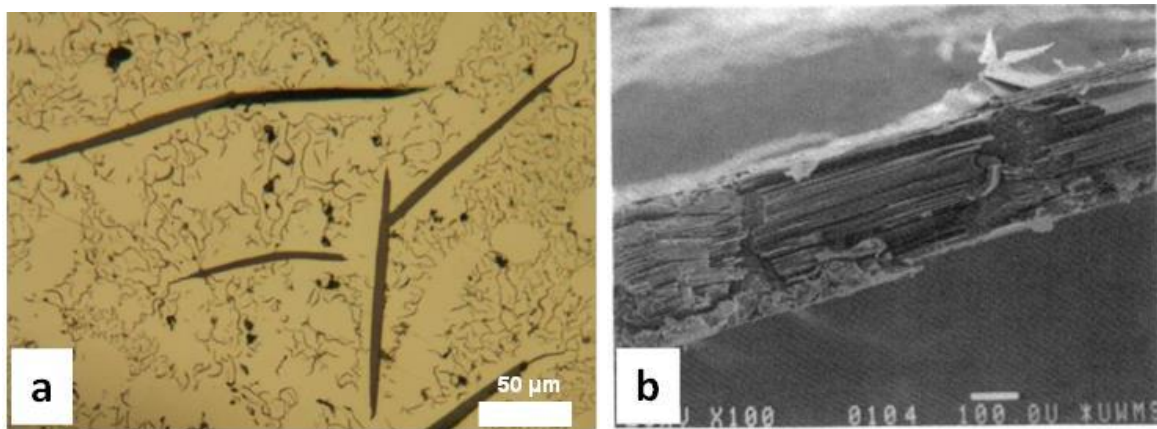


**Figure 5.6. Optical micrograph of primary graphite crystals [THE13] (a) and SEM micrograph of a fractured sheet of graphite [LIU90a] (b).**

**Transmission electron microscopy (TEM)** is the appropriate tool to get relevant information at the scale of graphite stacking. TEM study of crystals such as those in Fig. 5.6-a has shown that the layers may be twisted<sup>3</sup> between each other around their common **c** axis by an angle ensuring quasi-epitaxy [DOU71, BOL75]. This suggests that the thickening of the graphite plates/lamellas occurs by **nucleation of new layers onto the basal face** of the plate, which then extend parallel to this face thus generating the stacking.

This schematic has been considered and made quantitative by Amini and Abbaschian for explaining their experiments on hypereutectic Ni-C alloys [AMI13]. These authors studied the growth of graphite precipitates in an alloy that has been saturated in carbon at 1800°C and then cooled to room temperature at various rates. They measured the length and thickness of the lamellar precipitates and then compared these results to predictions obtained with a model illustrated in Fig. 5.7. In this approach, the lengthening of the graphite precipitates in the direction parallel to the basal plane is controlled by diffusion of carbon atoms in the liquid and their attachment on the prism faces. By contrast, the thickening of the precipitates proceeds

---

<sup>3</sup> The classification proposed by Austerman et al. [AUS67] will be used, according to which twisting refers to cases where the basal planes are rotated while remaining parallel to each other, and tilting refers to cases where the basal planes do not remain parallel to each other.

by epitaxial nucleation of new layers whose height is  $h$ , which then extend laterally along the basal surfaces of the precipitate.

At equilibrium or very low cooling rate, the lateral faces of the graphite plate should also be faceted and correspond to prismatic planes. Growth of such faces could proceed only by nucleation of new layers which needs that a minimum undercooling  $\Delta T_L^{\text{Gra,p}}$  has been reached, where p in the superscript stands for prismatic. On the contrary, at increased undercooling, the driving force for crystallization is higher and carbon atoms can attach in any location on the prismatic faces. The surface is then said rough at the atom scale, in contrast with a smooth faceted surface. When the surface is rough, what limits further growth of the graphite precipitate is the diffusion of carbon atoms in the liquid as was assumed by Amini and Abbaschian. Accordingly, there should be a transition from faceted growth controlled by nucleation of new layers to non-faceted growth controlled by diffusion when the undercooling increases. This change is schematically shown in Fig. 5.8-a. One can imagine that the formation of vicinal facets on the side faces of graphite plates is quite easy, which means that  $\Delta T_L^{\text{Gra,p}}$  is certainly quite small.

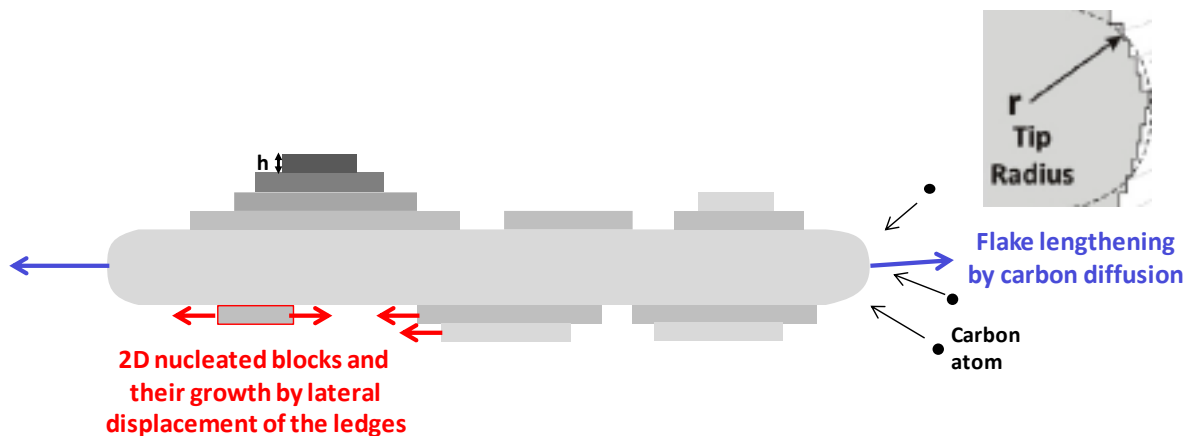


**Fig. 5.7. Schematic of the growth and thickening processes of a graphite flake (adapted from [AMI13]). Lengthening of the plate is controlled by carbon diffusion to the tips. Thickening proceeds by 2D nucleation of new growth blocks onto the basal faces of the plate and their lateral growth parallel to the basal faces. The insert at the top right illustrates the kinks at the graphite surface where the carbon atoms can easily attach.**

It is often suggested that growth along the c-axis, for radial growth of spheroidal graphite as well as for thickening of plate graphite, should involve spiral growth around a defect such as an emerging screw dislocation. Another mechanism has been considered by Amini and Abbaschian for thickening of the graphite plates, namely 2D nucleation and lateral spreading of new layers. In both cases, a minimum undercooling  $\Delta T_L^{\text{Gra,b}}$  should be reached for growth in the basal direction to proceed, where the superscript b stands for basal. However, this undercooling would be negligible for activating spiral growth while it should have a finite value for 2D nucleation. The observation of finite undercooling for primary growth of lamellar graphite in hypereutectic alloys (Chapter 3, Fig. 3.15) and the twisting of stacked layers mentioned above are considered as proofs that the main mechanism for thickening of graphite plates and lamellae is by 2D nucleation.



Cahn et al. [CAH64] predicted that the transition between lateral spreading of layers and diffusion-control proceeds when undercooling changes from  $\Delta T^*$  and  $\pi \cdot \Delta T^*$ , where  $\Delta T^*$  is given as:

$$\Delta T^* = \frac{\sigma^{\text{Gra/L}} \cdot \zeta \cdot V_m^{\text{gra}} \cdot T_m}{a \cdot \Delta H^{\text{gra}}} \quad (5.5)$$

with  $V_m^{\text{gra}}$  the molar volume of graphite ( $5.31 \cdot 10^{-6} \text{ m}^3 \cdot \text{mol}^{-1}$ ),  $a$  the distance between two successive basal planes ( $3.51 \cdot 10^{-10} \text{ m}$ ),  $\Delta H^{\text{gra}}$  the dissolution enthalpy of graphite ( $1.62 \cdot 10^6 \text{ J} \cdot \text{kg}^{-1}$ ) and  $\zeta$  a parameter called interface diffuseness. One gets  $\Delta T^* = 1130 \cdot \zeta$  and a value of  $\zeta$  of 0.1 was found convenient for describing spheroidal growth [LAC17a], see Chapter 9. Using this value, the transition should occur at an undercooling  $\Delta T_L^{\text{Gra}}$  of the order of  $100^\circ\text{C}$ .

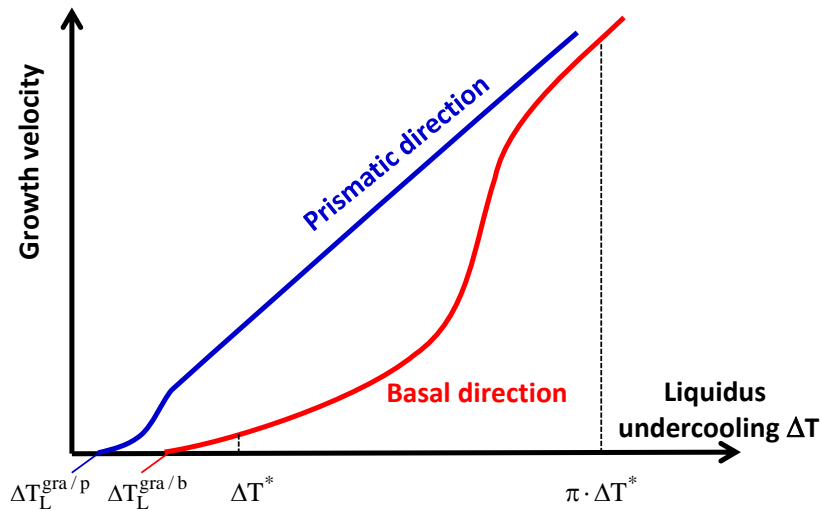


**Figure 5.8. Evolution with undercooling  $\Delta T_L^{\text{Gra}}$  of the growth rate along the prismatic and basal directions of graphite.**

### 5.3 Some unusual features of primary graphite

The best known is kish graphite which consists of large graphite precipitates observed on the surface of hypereutectic melts. Loper and Zakharchenko [LOP84] differentiated kish graphite from primary graphite because they found no evidence of agglomeration resulting from floatation. Primary graphite precipitates in the bulk of a highly hypereutectic LGI are expected to consist of straight plates with few branches, as described above, and Loper and Zakharchenko [LOP84] stated that they could only observe a few in samples sucked from the melt. This is in contrast to previous reports of graphite floatation in LGIs, and also to the results of Sun and Loper [SUN83a] who observed spheroid floatation in hypereutectic spheroidal and compact graphite irons. For SG and CG irons, the primary spheroids accumulated on a thick zone below the melt surface and it is quite interesting to note that their spherical shape was apparently preserved. It is not clear how this observation on SGI and CGI can be reconciled with the results of the studies on kish graphite by Loper and Zakharchenko mentioned above.

The above observations by Loper and Zakharchenko have been confirmed by Liu and Loper who compared industrial and laboratory kish graphite [LIU90a, LIU91]. In this study, the growth characteristics of the kish graphite were observed to differ at the upper surface in

contact with the atmosphere and at the lower surface in contact with the melt. Under oxygen, Liu and Loper observed the development of foliated dendrites quite similar to those reported by Saratovkin when studying the crystallization of cadmium iodide crystals out from water solution [SAR59]. Under argon, pyramidal growth was noticed on the melt side of kish graphite, see Fig. 5.9-a. This microstructure appears very much alike to that obtained by Munitz and Nativ investigating a Ni-C-3Pb (wt.%) alloy, Fig. 5.9-b [MUN82]. This latter micrograph may be seen as an illustration of the 2D nucleation process with lateral extension of the new growth blocks limited by accumulation of Pb atoms. Such a process could be consistent with the concept of interface instability used by Munitz and Minkoff [MUN78] and by Liu and Loper [LIU91] to describe their observations.

As discussed in relation to Fig. 5.8, spiral growth around a screw dislocation, if it exists, is favoured by low undercooling (or cooling rate) and therefore should be observed preferably in large crystals. Roscoe et al [ROS71] examined the characteristics of graphite single crystals grown from iron-carbon solutions and concluded that the spiral growth mechanism plays only a MINOR role in the graphite growth process as spiral growth was only occasionally observed. Austerman et al. [AUS67] conducted similar experiments with graphite precipitates from slowly cooled Fe-C and Ni-C solutions and arrived at the same conclusion. These authors further noticed that cleavage and shear of the graphite precipitates was so easy that this attested “to a low or nil concentration of defects that would provide cross-linking between adjacent basal planes”. Thus, while Liu and Loper [LIU90a, LIU91] could see spiral growth in features such as the one to the left in Fig. 5.9-a, the above mentioned works lead to rather suggest the overlapping of the lobes of a graphite flake as in Fig. 5.9-c.

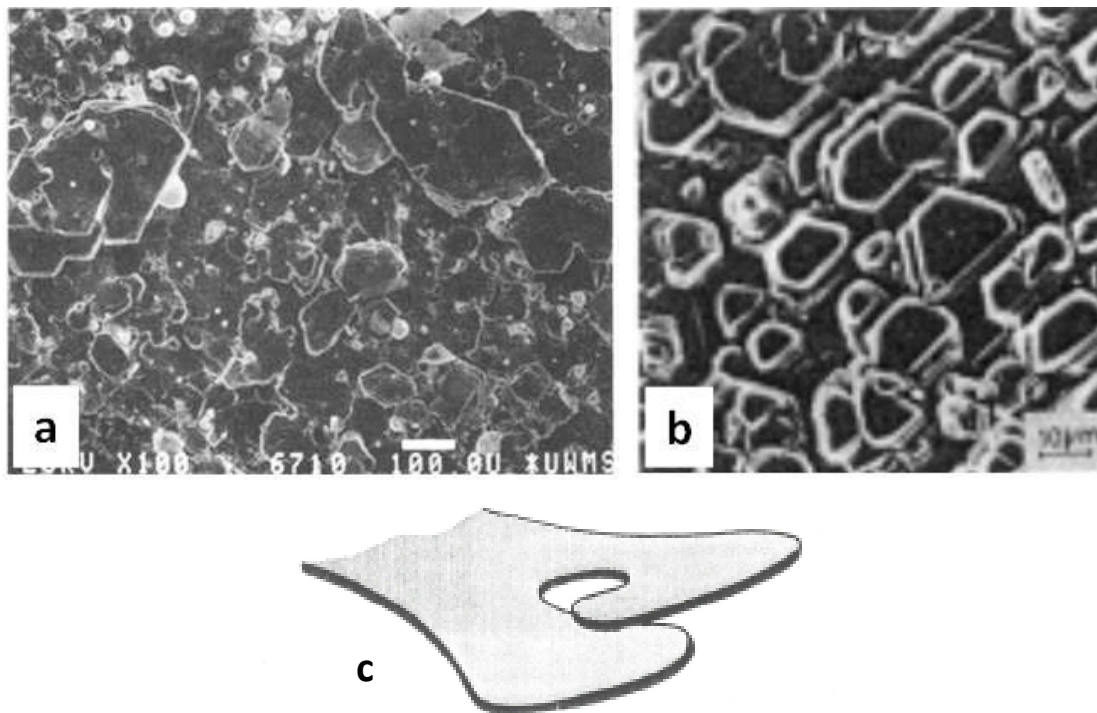


**Figure 5.9. SEM micrographs of the basal plane of a graphite crystal.**  
**a: melt side of kish graphite grown under argon in a synthetic cast iron [LIU90a].**  
**b: Ni-C-3Pb alloy [MUN82]. c: Diagram showing the division and overlapping of the lobes of a graphite flake.**

Minkoff and his collaborators investigated the effect of several elements when added at quite high level for triggering morphological changes [MIN83]. Studies with additions at level closer to that used industrially are however quite rare. Investigating the effect of antimony added to Fe-C melts solidified under air, Theuwissen [THE16] evidenced that the primary graphite precipitates appeared slightly branched and wavy when viewed under optical microscope; see Fig. 5.10-a (upper right) and compare with Fig. 5.6-a. Closer examination shows, however, that this wavy appearance is only apparent because the precipitates are made up of straight segments between the bends. This was confirmed with TEM which showed that successive straight growth blocks were tilted between each other by a rotation around an axis located in the basal plane (Fig. 5.10-a, left). Because growth of the graphite plates proceeds in the prismatic directions, this observation suggested that antimony atoms accumulated on these planes of the graphite/liquid interface and eventually hindered further straight growth and forced the crystal to tilt. In the same type of experiments conducted under air with cerium added instead of antimony, the primary graphite precipitates appeared straight though much shorter and thicker, see Fig. 5.10-b. Cerium certainly adsorbs onto the prismatic planes leading to the shortening of the lamellae, but it is not clear why it forces the lamellae to thicken whereas antimony leads to tilting without impeding growth in the prismatic directions. This may have to do with interface segregation of antimony that is further discussed in Chapter 8 [LAC22a].

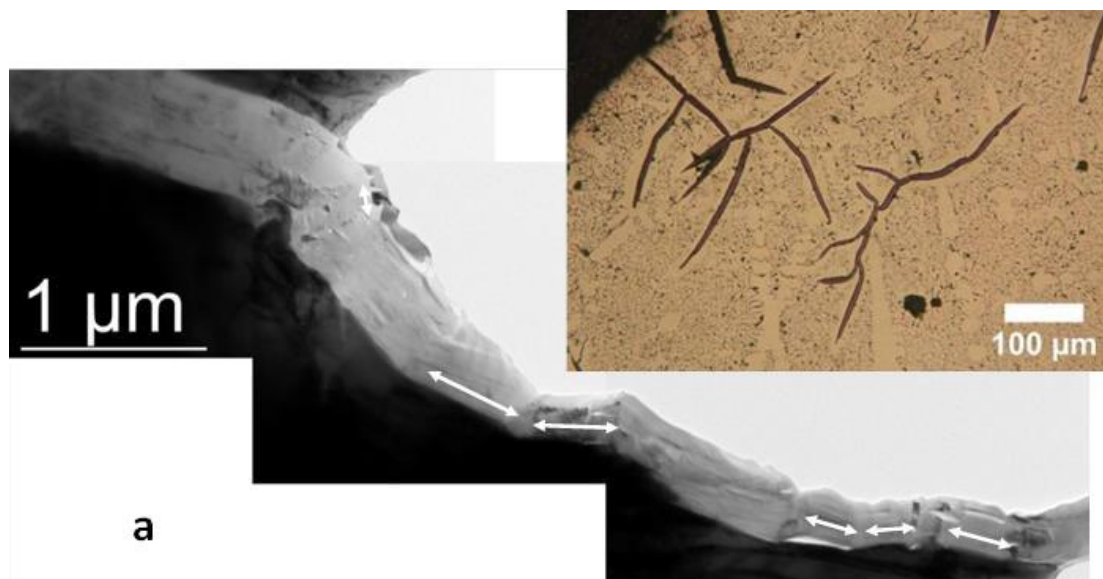


**Figure 5.10.**

**a:** Optical micrograph (upper right) of a Fe-C-Sb sample processed under air as the Fe-C alloy in Fig. 5.6-a was, and mosaic of TEM micrographs of one of the primary graphite precipitates (left) [THE16].

**b:** Optical micrograph of a Fe-C-Ce sample similarly processed (under air) [THE16].

In relation with the observation of growth features of graphite, it is worth noting the possible use of polarized light in optical microscopy that gives indication of the change in orientation of the stacking in graphite precipitates as illustrated in Fig. 5.11. Fig. 5.11-a shows two lamellae at 90° each other and appearing with opposite contrast. Within each of the lamellae, the graphite layers are therefore similarly oriented along their length, except for some limited areas which are growth defects appearing with a different contrast. TEM showed that these limited areas can be highly misoriented with respect to the direction of the lamella, and also that the interface between growth blocks of differing orientations show bent and rippled graphite layers on a thickness of about 10 nm [THE16].

More widespread use of polarised light in optical microscopy could be useful for rapidly detecting the structure and orientation of graphite in a sample, though it needs a really good surface preparation and is limited by optical resolution at 0.5-1  $\mu\text{m}^4$ . As an example, the spheroid to the left in Fig. 5.11-b illustrates the well-known fact that the graphite in spheroids has everywhere its *c* basal axis orientated parallel to the spheroid's radius as described in the next section. Further, the large graphite precipitate to the right in Fig. 5.11-b is a so-called exploded spheroid in which the continuity of the graphite orientation from the centre to the outer surface of the precipitate is noticeable.

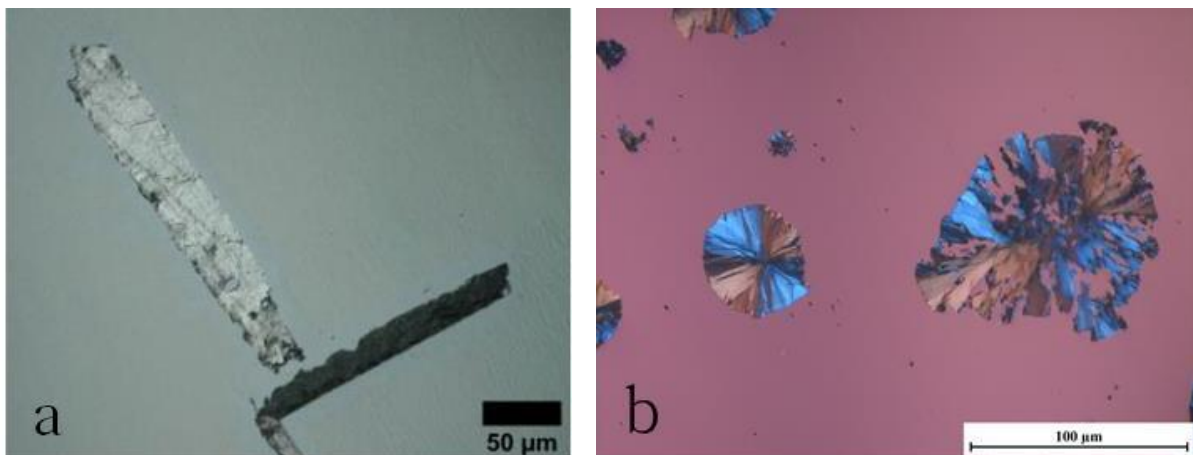


**Figure 5.11. Polarized light optical micrographs illustrating the local changes in orientation of graphite stacking. (a) Lamellar graphite [THE16]; (b) Spheroidal graphite and an “exploded” spheroidal graphite (Courtesy B. Tonn).**

#### 5.4 Spheroidal graphite

Early growth of graphite in melts that have been spheroidized has been studied since a long time by quenching samples at an appropriate temperature during cooling from the liquid state. Even when all efforts have been made to increase the quenching rate, it may be expected that freezing of the remaining liquid asks for a couple of seconds. This is exactly this time, 2-3 seconds, which is estimated for the whole solidification of thin-wall tubes centrifugally cast in a water-cooled die. The microstructures of quenched laboratory samples or centrifugally cast tubes present similar features, a more or less developed network of dendrites, graphite spheroids and cementite or ledeburite (see Fig. 2.8). When a metallographic section is

<sup>4</sup> The short note by Ahmed and Gawlick [AHM83] can be mentioned as one of the very few detailed descriptions of the preparation of cast iron for metallographic observation.

observed after polishing, these primary nodules appear to have a maximum diameter of 5-10  $\mu\text{m}$  for centrifugal casting, see Fig. 5.12-a. The same spheroidized and inoculated alloy shows spheroids up to 30  $\mu\text{m}$  in diameter when cast in a Y2 **keel-block**, see Fig. 5.12-b. Thus, even if spheroids nucleated and grew for at most 2-3 seconds (Fig. 5.12-a), they show the same internal structure as spheroids having grown for much longer time (Fig. 5.12-b).

Growth of the spheroids from the liquid was interrupted by metastable solidification in the case of the sample in Fig. 5.12-a. On the contrary, solidification went to its end in the stable system for the sample in Fig. 5.12-b, which means that at some time in the process the spheroid got encapsulated in an austenite shell. Its further growth proceeded by diffusion of carbon from the remaining liquid through the austenite shell, see chapter 7. There is no visible boundary in the spheroid to indicate where this change has occurred, and it is noticeable that the spheroids are very compact.

Use of polarized light for capturing the micrographs in Fig. 5.12 evidences the change in the graphite orientation with the **c** axis of graphite stacks roughly parallel to the radius of the spheroid in any location. However, the rotation of the c-axis is not continuous, resulting in so-called sectors in which the changes in orientation of the c-axis are limited. By rotating the sample under polarised light, neighbouring but differently oriented sectors appear with different contrast, allowing the boundaries between sectors to be delineated, as illustrated by the dashed lines in Fig. 5.12.

The internal radial features within each of the sectors are continuous, clearly indicating that the graphite has grown by the same mechanism in the first stage (directly from the liquid) and the second stage (by carbon diffusion through austenite). This applies as well to the limited growth in solid-state, namely during continuous cooling in the austenite field (third stage) and possibly also during the ferritic transformation (fourth stage). It will be seen in Chapter 7 that spheroids can sometimes be less regular than those in Fig. 5.12 and this may explain why several authors have suggested a change in the growth mechanism associated with the transition from free growth from liquid to growth in an austenite shell [STE17b]. The above observations suggest this is by far not the general case.

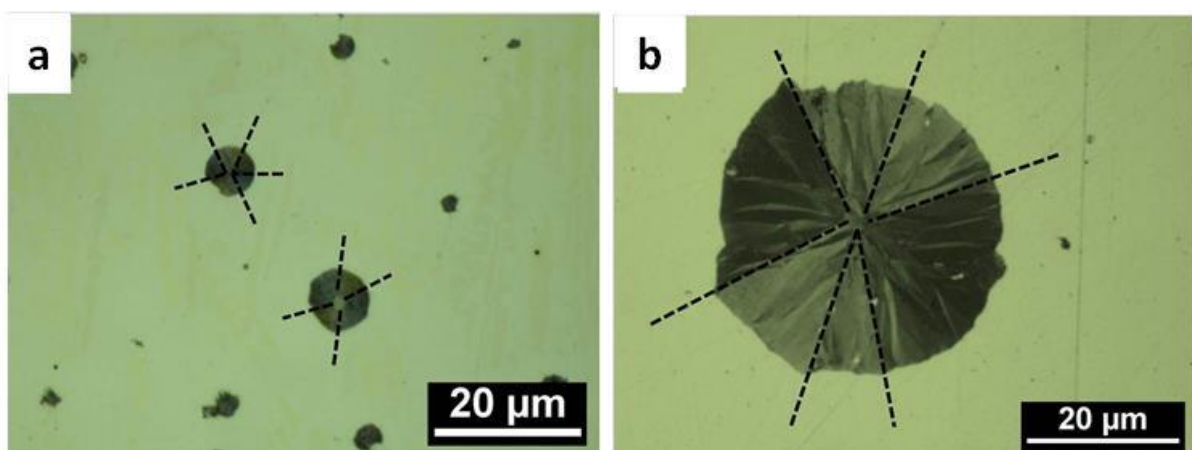


**Figure 5.12.** Optical micrographs of an alloy that has been centrifugally cast (a) and cast in a Y2 keel-block (b). Use of polarized light allowed evidencing the internal structure which consists of sectors [BOU18].

More detailed characterization of the graphite stacking in spheroids could be achieved by use of TEM. Fig. 5.13-a shows the diametrical section of a spheroid similar to the one in Fig. 5.12-b that was obtained by field ion beam (**FIB**) milling to be electron transparent, and was submitted to local diffraction patterning (**ACOM**) in a TEM [THE14]. Graphite orientation was determined in points located along a grid with a 17 nm step size. Fig. 5.13-b shows the projection parallel to the Z direction of the graphite orientations and Fig. 5.13-c gives the colour code for the orientations. Fig. 5.13-b shows first that all (0002) planes of the studied spheroid section are effectively contained in the section plane as only blue and green show up and no red (the small red and pink areas in the upper right of the image are matrix inclusions). It further demonstrates that graphite is organized in large sectors which appear to be strongly disoriented between each other as the transition between blue and green areas is quite sharp.

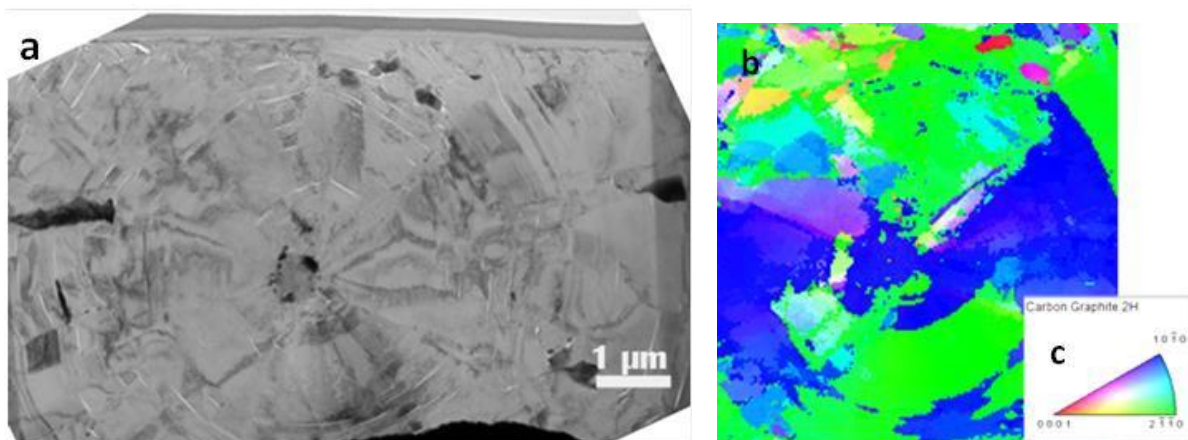


**Figure 5.13. Mosaic of TEM micrographs showing the central part of a spheroid (a) and projection along the Z axis (out of plane) of the ACOM mapping performed with a 17 nm step spacing (b and c).**

TEM was also used to study the interface between sectors [THE16]. In Fig. 5.14, the contrast changes in the bright-field TEM image (top left) evidences boundaries between neighbouring sectors. A **selected area electron diffraction (SAED)** pattern was recorded over two adjacent sectors in the area defined by the white circle. The pattern (lower left of Fig. 5.14) shows two distinct **c** axis orientations rotated by  $31^\circ$  with respect to each other. A **high-resolution TEM (HR-TEM)** lattice fringe image taken at the interface between the sectors shows straight fringes on left and right hand sides which are characteristic of a highly graphitic material. Nevertheless, **c** axes from both parts of the image do not have the same orientation and they are separated by an interface within which the graphite layers are rippled in a transition zone with a width from 4 to 12 nm. An attempt was made to obtain the distribution of angles which showed that the twist between neighbouring sectors does not generally correspond to the known twin boundaries [THE13].

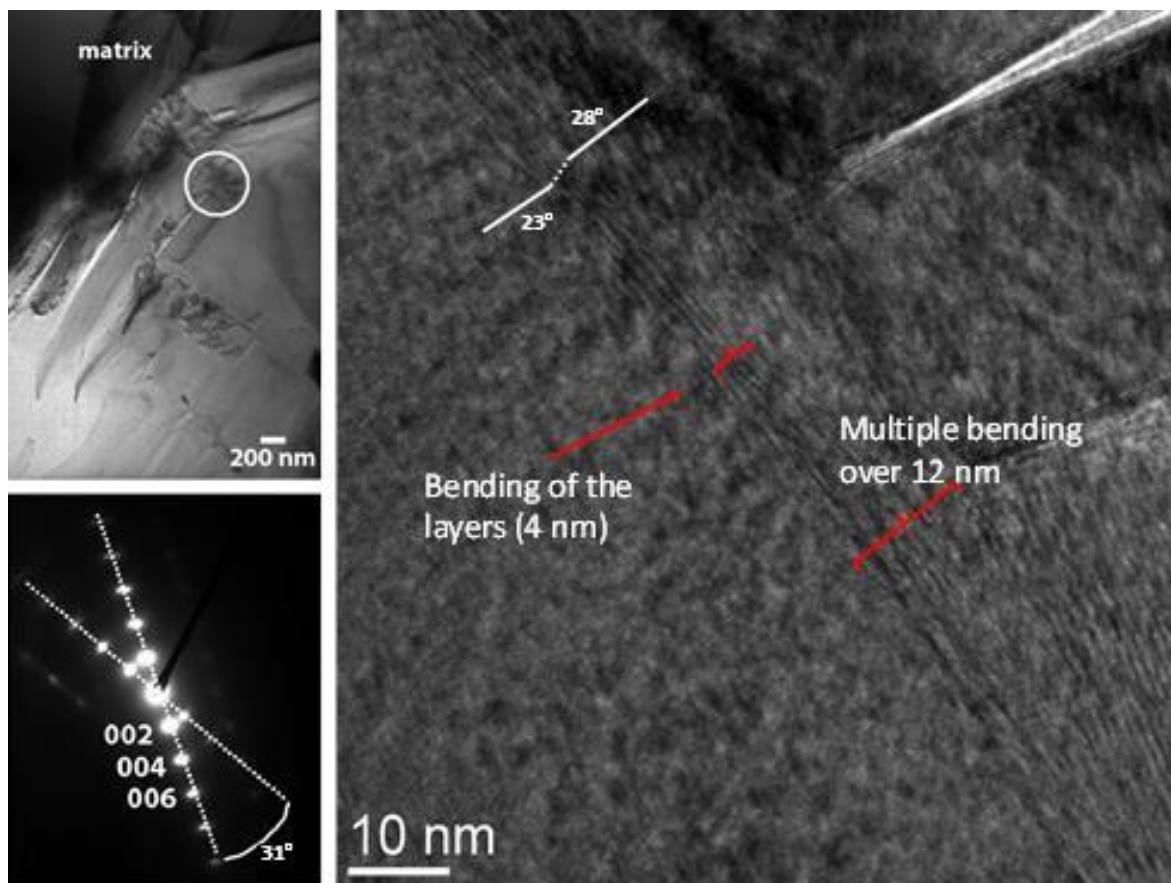


**Figure 5.14. Bright-field TEM image (top left) with the white circle showing the location of the SAED pattern (lower left) and HR-TEM lattice fringe image of the boundary between the two sectors (to the right) [THE16].**

TEM has also been used to evidence that the sectors in spheroids consist of growth blocks stack on each other [MIA94, MON01, QIN17]. These blocks are slightly elongated in the prismatic directions, i.e., parallel to the outer spheroid's surface, with a length that is micrometric and a thickness that is in the range 10-100 nm. Characterizing individually these blocks needs resorting to dark-field imaging in the TEM which is very tedious but has been proved possible by Qing et al. [QIN17]. These authors put emphasis on the graphite structure in the blocks, showing they have a high crystallinity though with point defects.

There are only two schematics in the literature that describe usual graphite spheroids, i.e. spheroids that are compact and consisting of sectors: i) A beam of screw dislocations around which graphite grows by an helical or spiral mechanism [HIL54, DOU74, MIA94], Fig. 5.15-a; ii) A beam of adjacent sectors on top of which graphite grows by continuous nucleation of new layers at the interface between sectors, Fig. 5.15-b [DOU75], or anywhere at the outer surface of the sectors, Fig. 5.15-c [LAC17a]. Note that, in all cases, carbon atoms attach on the prismatic faces as in lamellar growth. As no evidence of screw dislocations could be found [THE12, QIN17], or either of any helical axis of growth, we are left with the second mechanism.

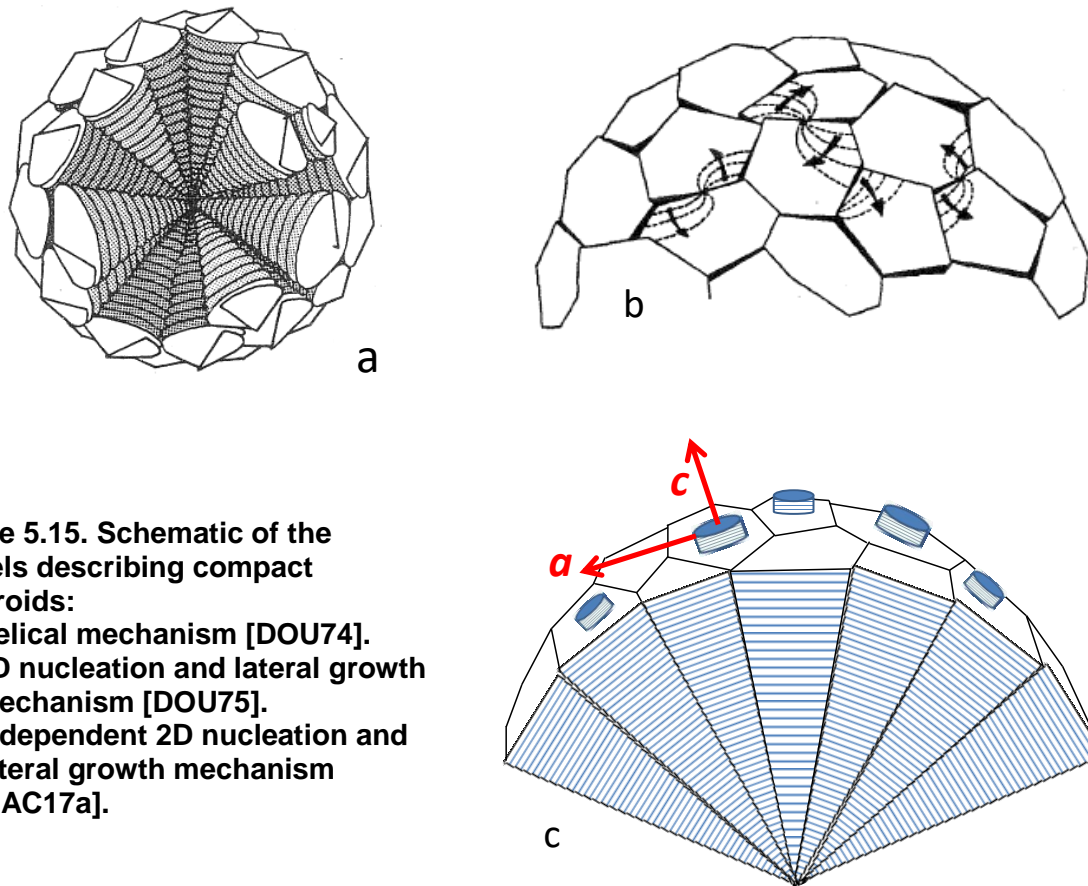


**Figure 5.15. Schematic of the models describing compact spheroids:**  
**(a) Helical mechanism [DOU74].**  
**(b) 2D nucleation and lateral growth mechanism [DOU75].**  
**(c) Independent 2D nucleation and lateral growth mechanism [LAC17a].**

Moreover, the observation of exploded graphite spheroids (see Fig. 5.11-b) suggested that the nucleation of new growth layers is not necessarily related to the boundary between adjacent sectors or sub-sectors. In other words, the new nuclei may be anywhere on the outer surface of each sector or sub-sector as depicted with Fig. 5.15-c. Quantitative aspects using this latter model [LAC17a] will be considered in Chapter 10. It is worth noting that such a 2D nucleation/growth mechanism was proposed by Herfurth [HER64] a long time ago, while many other suggested mechanisms have been reviewed in the literature [LUX70b, STE17b]. Among these suggestions, the circumferential growth model put forward by Sadocha and Gruzleski [SAD75] would give compact precipitates but without sectors [GRU75]. Some features of early spheroid growth could be associated with this model - see next section - while the external overgrowth described as 'cabbage leaves' are artefacts that are not representative of the internal structure of graphite spheroids [BOU20].

### 5.5 Initial growth of graphite spheroids

It is easier to find nuclei in SGI by searching for them in samples with small spheroids such as those obtained by quenching during solidification. In one such study, Stefanescu et al. [STE19] quenched thermal cup samples at an early stage of solidification and reported micrographs such as the one in Fig. 5.16-a that shows a graphite precipitate around a multi-phase nucleus. It can be seen that this graphite precipitate shows facets that demonstrate early formation of well-defined sectors. Similar features can be seen in other works, e.g. that of Ng et al. [NG21]. It is noteworthy that the thickness of the graphite is not even around the



nucleus, which may be indicative of either that several successive nucleation events occurred or that there were preferential directions for graphite growth. In any case, these observations invalidate the possibility of growth by wrapping of graphite sheets around the nucleus, as well as by uniform agglomeration of carbon atoms.

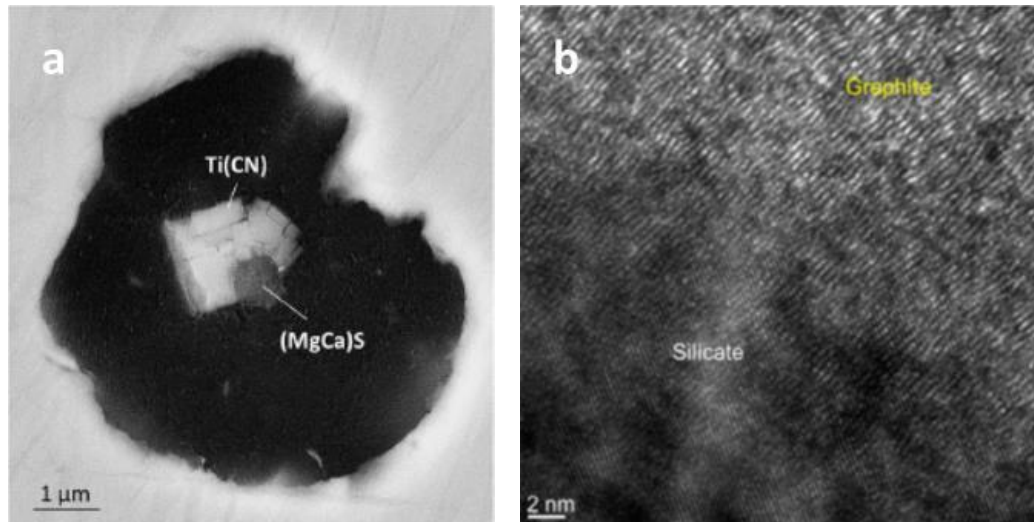


**Figure 5.16. SEM micrograph [STE19] (a) and HR-TEM image [QIN20] (b) showing both the nucleus and adjacent graphite in laboratory samples quenched during solidification.**

Studying similarly early growth stage of spheroidal graphite on quenched samples, Qing et al. [QIN20] provided a HR-TEM image of the interface between the nucleus and graphite, Fig. 5.16-b. The spheroid that was selected was 5 μm in diameter, i.e., may have been very similar to the ones shown in Fig. 5.12-a. A stack of graphite layers can be seen which are slightly irregular and present point defects that Qing et al. associated to the presence within graphite of many foreign elements, especially elements associated with the inoculation step. The authors concluded that these point defects could contribute to the curvature of the graphite layers to envelop the core and generate the spheroidal morphology, thus implicitly suggesting that the early spheroidal growth proceeds by the circumferential mechanism. This conclusion seems to contradict what has been deduced above from Fig. 5.16-a, and it would be very interesting to make HR-TEM images of graphite all around the nucleus of a small spheroid to settle this question.

In a few studies [HAR14, BRO18, LAF18], bright field TEM images of small spheroids showed nuclei surrounded by a featureless  $\approx 0.5$  μm thick zone as illustrated with Fig. 5.17. At larger distances from the spheroid's centre, the graphite shows the usual contrasts indicating of its high crystallinity and delineating small sectors developing outwards that have been characterized by **transmission Kikuchi diffraction (TKD)** [BRO18]. Selected area electron diffraction patterns recorded in the inner featureless zone showed oblong shape [HAR14, LAF18] that was suggested to be related to a deformation of the graphite stacking generated by compressive stresses applied to the spheroid [LAF18]. In the studies by Laffont et al. [LAF18] and Brodu et al. [BRO18], these stresses might have been generated because solidification ended in the metastable system with shrinkage of about 4%. These stresses are maximum at

the graphite nucleus interface and decrease sharply away of it [LAF18]. Therefore, the presence of this featureless zone is not relevant to the growth process as it is generated after the graphite has actually precipitated.

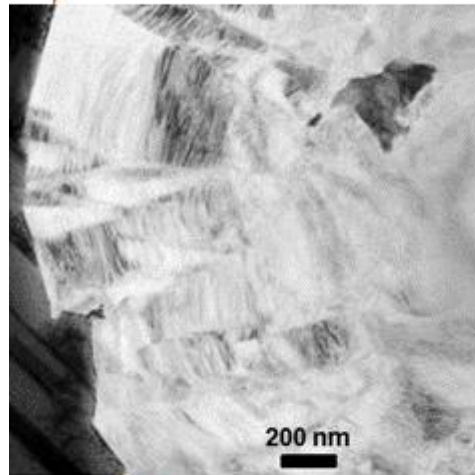


**Figure 5.17. Bright field image of the periphery of a graphite nodule from as-cast centrifuged SGI (Courtesy E. Bouzy et al., LEM3, Metz, France). The orange disc locates the centre of the circle defined by the contour of the spheroid.**

### **5.6 Transition from lamellar to spheroidal graphite**

Amongst those studies resorting to quenching during solidification, a few were performed with pure Fe-C-Si alloys, i.e. alloys in which no spheroidizer had been added. This led to the observation that both plate-like and spheroidal graphite may precipitate from the melt, see Fig. 5.18, and some authors suggested that the natural growth shape of graphite should be spheroidal. It is worth noting that, because of the high cooling rate, the undercooling achieved with respect to the graphite liquidus is extremely high –presumably above  $\pi \cdot \Delta T^*$  in Fig. 5.8- and growth of graphite may well be controlled by diffusion of carbon atoms in the melt. In such conditions, Tiller showed that spheroidal growth is favoured in comparison to lamellar growth [TIL68]. A further interesting result was reported by Dhindaw and Verhoeven [DIN80] who noticed that if a "pure" melt was maintained under vacuum for a long period of time before cooling - so as any exogenous particles in the melt have disappeared - then spheroidal growth was replaced by a coupled eutectic with coral graphite (see Chapter 6). Finally, using **Quenching during Directional Solidification (QDS)** experiments, Riding and Gruzleski observed a critical freezing rate below which spheroidal graphite would not form even in the presence of adequate quantities of spheroidizer [RID71]. Thus, there is no single shape resulting from graphite growth that could be described as 'natural'.

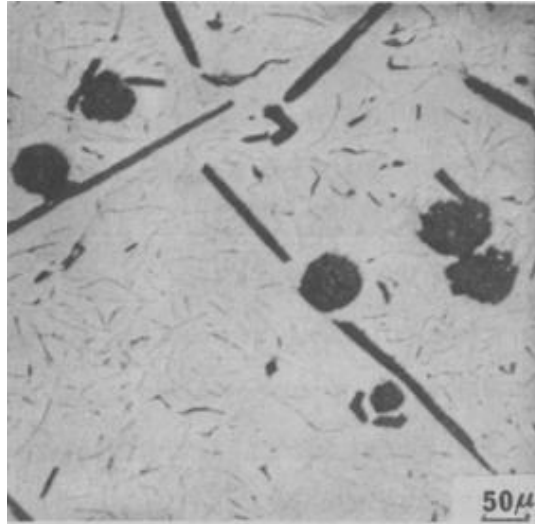


**Figure 5.18. Observation of plate-like and spheroidal primary graphite in a pure Fe-C-Si alloy [VIG73].**

### **5.7 Summary**

Whatever the overall external shape of the primary graphite crystals, growth occurs by the addition of carbon atoms at prismatic sites. Highly crystalline growth blocks develop, the length of which is related to the type of graphite, i.e. up to hundreds of microns in the case of flake graphite and only a few microns in the case of spheroidal graphite.

In agreement with the known growth behaviour of faceted phases, graphite precipitates in pure Fe-C-Si alloys are plates at low growth rate or undercooling and spheroids at high cooling rate or undercooling. However, it has been reported that spheroidal growth is replaced by coupled growth with coral graphite in highly pure Fe-C-Si melts, suggesting that spheroidal graphite growth occurs only from exogenous nuclei.

In cast iron melts that always contain some sulphur (and oxygen), primary graphite is commonly lamellar and is changed to spheroidal graphite after addition of magnesium and/or cerium. The primary role of this addition is to decrease the amount of sulphur (and oxygen) remaining dissolved in the melt but a wealth of experimental observations show that some free magnesium must be present in the melt for graphite to grow as spheroids (see Chapter 8). Because sulphur (and oxygen) are strongly surface active in iron melts, it is often considered that the graphite shape relates to the graphite/liquid interface and thus, by virtue of Young's relation, to the surface tension of the melt. It will be seen in Chapter 8 that there is no unique relation between the surface tension and graphite shape, and also that interface segregation at the graphite/melt interface is of importance.

Present knowledge suggests that thickening of plate-like or lamellar graphite and growth of spheroidal graphite proceed similarly by 2D nucleation of new growth blocks on the basal planes facing the liquid, and that they then extend laterally. The mechanism explaining the shape transition certainly involves adsorption of spheroidizing elements at the graphite melt interface, and consideration should be given to the presence of surface active trace elements that can segregate at this interface.

# Chapter 6 – Two-phase growth in non-spheroidized melts. Austenite-graphite and austenite-cementite coupled eutectics.

In Fig. 6.1 are presented the various shapes of graphite that has grown together with austenite, i.e., during eutectic solidification. Most of these shapes result from so-called coupled growth when both phases grow side by side -in contact with the liquid- and benefit of each other for minimizing the undercooling. The only exception is spheroidal graphite that grows encapsulated by an austenite shell so that it has become usual to dub it as uncoupled growth. As in Fig. 5.1, the horizontal axis represents the change of growth conditions, i.e., either the undercooling  $\Delta T$  or the cooling rate, and the double vertical axis shows upwards the effect of spheroidizers and downwards that of oxygen and sulphur, while "pure" alloys are located along the horizontal axis. The undercooling to be considered in this chapter refers to the eutectic temperature, namely the stable eutectic as in Fig. 6.1 and in most of the chapter, except in section 6.7 where the metastable eutectic is treated. Spheroidal graphite as obtained by the spheroidizing treatment as well as chunky graphite will be dealt with in chapter 7 where compacted graphite will also be described.

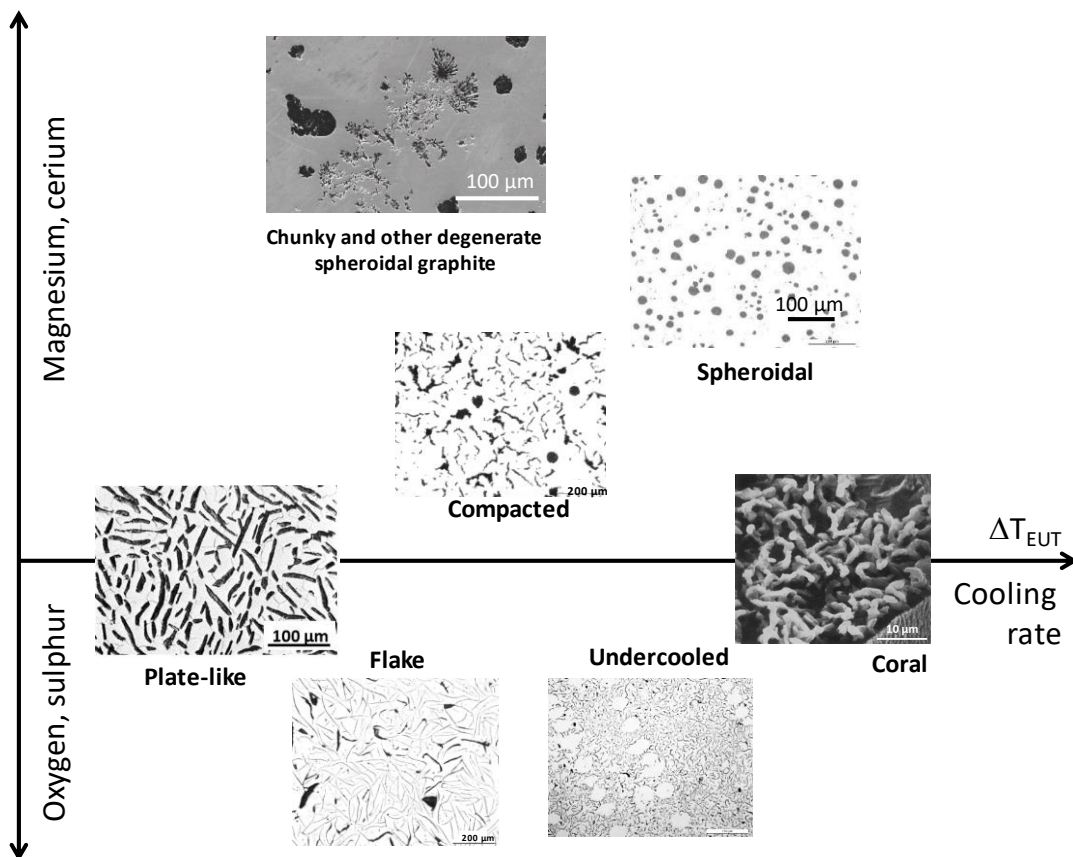


Figure 6.1. Various forms of eutectic graphite

The principle of coupled growth is presented in section 6.1, while sections 6.2 and 6.3 detail the specificity of the eutectics with lamellar and undercooled graphite and their growth laws, respectively. It will be seen in section 6.4 that the coupled growth of austenite and graphite can be affected by the presence of low level elements, and section 6.5 will illustrate that the graphite shape can even be modified. In section 6.6, a short introduction of the coupled zone concept applied to cast irons will end this presentation of the austenite-graphite coupled eutectic. Before leaving this chapter, the metastable eutectic, also called white eutectic, will be considered in section 6.7.

### 6.1 The Jackson-Hunt model of two-phase growth and its extension to irregular eutectics

The schematic in Fig. 6.2 shows a two-phase solidification front for the **coupled** growth of a **regular** eutectic corresponding to the reaction  $\text{liquid} \rightarrow \gamma + \beta$ , being  $\gamma$  and  $\beta$  the two solid phases formed. In this figure,  $V_{\text{growth}}$  represents the growth rate of the eutectic front which is assumed to move in the direction of the upwards arrow. For the solidification to proceed, **redistribution** of elements must occur in the liquid ahead of the front; this is illustrated with the two green curved arrows. Eutectic growth may be characterized by the inter-lamellar **spacing**,  $\lambda$ , and the average front **undercooling**,  $\Delta T$ , expressed with respect to the related eutectic temperature. In the case of cast iron,  $\Delta T$  refers to  $\Delta T_{\text{EUT}}$  for the stable eutectic and  $\Delta T_{\text{EW}}$  for the metastable one. If the fractions of the phases are very different, rod-like morphology may be preferred to plate-like one [HOG71]. For regular eutectics, isotropy of the three interfacial surface tensions is assumed so that the **mechanical equilibrium** at the triple junction follows Young's law as exemplified by the set of three black arrows in the figure. If this were not the case, the Young-Herring condition that accounts for anisotropy of interfacial tensions should be used [HOF72].

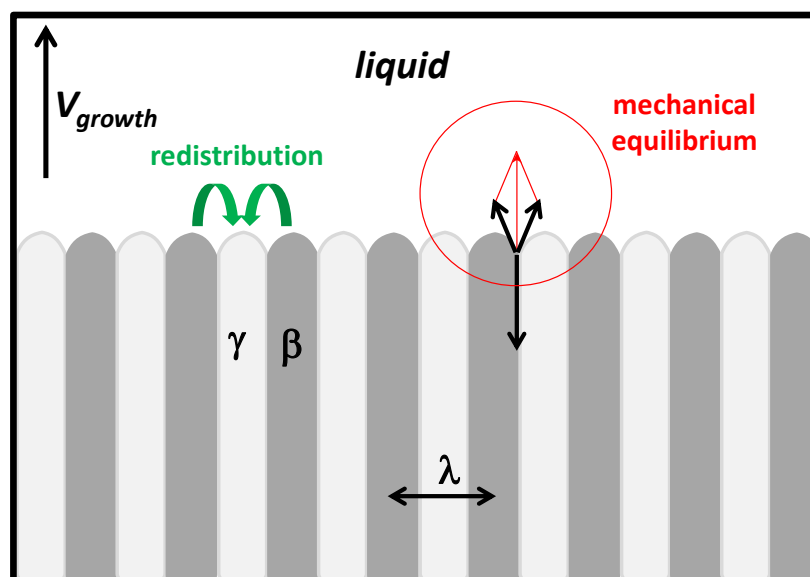


Figure 6.2. Schematic of the solidification front of a perfectly regular two-phase eutectic (longitudinal section of a directionally solidified sample). The green arrows show the path for elements entering preferentially in  $\gamma$ , opposite arrows would show the path for elements concentrating in  $\beta$ .

Analytical models of such regular eutectics have been developed since long, with the work by Jackson and Hunt [JAC66] being the reference one that will be used in this chapter. For a comprehensive description of eutectic growth see the corresponding chapter in Dantzig and Rappaz [DAN09] that also presents recent experimental and simulation advances. It will be seen in the following that both the stable and metastable eutectics in Fe-C alloys can hardly be considered as regular. This is due to the fact that the interfacial tension between the liquid and graphite (resp. cementite) is anisotropic leading to the well-known **faceted** lamellar (resp. plate-like) morphology. Growth of faceted phases proceeds along specific crystallographic directions with branching according to particular angles. This gives rise to so-called **irregular** structures in contrast to non-faceted eutectics which often show highly **regular** patterns. Nonetheless, the majority of the works devoted to eutectic growth of austenite and graphite or austenite and cementite refer to the growth laws developed for regular eutectics.

Redistribution of the elements ahead of the solidification front leads to an average chemical undercooling  $\Delta T_C$  which scales as  $\lambda \cdot V$  while the average curvature undercooling  $\Delta T_K$  is proportional to  $1/\lambda$ . Assuming no other source of undercooling - such as interfacial reaction - the total average undercooling  $\Delta T = \Delta T_K + \Delta T_C$  of the eutectic front is written:

$$\Delta T = \frac{a}{\lambda} + b \cdot V_{\text{growth}} \cdot \lambda \quad (6.1)$$

The evolution of  $\Delta T$  as function of  $\lambda$  at given growth velocity  $V_{\text{growth}}$  is illustrated in Fig. 6.3 which shows that it exists an **extremum** inter-lamellar spacing ( $\lambda_0$ ) at which  $\Delta T$  is **minimum**. According to the so-called Zener's postulate, this defines the condition at which the eutectic front grows. Writing that  $\partial(\Delta T)/\partial\lambda = 0$  at this extremum, one gets the following relationships from Eq. (6.1):

$$\lambda_0 = \sqrt{\frac{a}{b \cdot V_{\text{growth}}}} \quad (6.2)$$

$$\Delta T_0 = 2 \cdot \sqrt{a \cdot b \cdot V_{\text{growth}}} \quad (6.3)$$

$$\Delta T_0 = 2 \cdot \frac{a}{\lambda_0} \quad (6.4)$$

where the subscript 0 refers to the extremum condition for a given velocity  $V_{\text{growth}}$ , and a and b are material dependent constants.

These relations have been quite successful in the case of non-faceted/non-faceted (regular) binary eutectics [KUR79], but much less in the case of faceted/non-faceted (irregular) eutectics such as Al-Si and Fe-graphite ones. Moreover, experimental investigations on both regular and irregular eutectics in directional solidification experiments have shown that the actual inter-lamellar spacing distributes between  $\lambda_{\text{min}}$  and  $\lambda_{\text{br}}$  that can differ significantly.  $\lambda_{\text{min}}$  has for long been considered as being equal to  $\lambda_0$  but may in fact be smaller than this value [AKA04].  $\lambda_{\text{br}}$  is the maximum inter-lamellar spacing at which branching must occur for the coupled growth to be maintained.

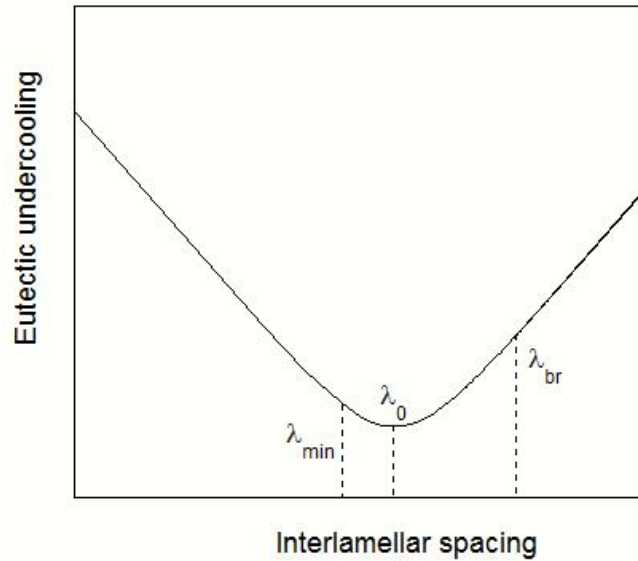


**Figure 6.3. Evolution at given  $V_{\text{growth}}$  of the average eutectic undercooling as function of inter-lamellar spacing  $\lambda$ .  $\lambda_0$ ,  $\lambda_{\text{min}}$  and  $\lambda_{\text{br}}$  are the extremum, minimum and maximum values of  $\lambda$ .**

For accounting of this range of inter-lamellar spacings just mentioned, Jones and Kurz [JON81] suggested that eutectic growth could be represented by an **optimum** average inter-lamellar spacing  $\lambda_{\text{opt}} = \varphi \cdot \lambda_0$  which should lie in between the two extrema,  $\lambda_{\text{min}}$  and  $\lambda_{\text{br}}$ . They further suggested that the previous theoretical approach could be used, leading to the following equations:

$$\lambda_{\text{opt}} = \varphi \cdot \lambda_0 = \varphi \cdot \sqrt{\frac{a}{b \cdot V_{\text{growth}}}} \quad (6.5)$$

$$\Delta T_{\text{opt}} = \frac{1}{\varphi} \cdot (1 + \varphi^2) \cdot \sqrt{a \cdot b \cdot V_{\text{growth}}} \quad (6.6)$$

$$\Delta T_{\text{opt}} = (1 + \varphi^2) \cdot \frac{a}{\lambda_{\text{opt}}} \quad (6.7)$$

where the subscript "opt" refers to the optimum.

## 6.2 Eutectic with lamellar and undercooled graphite

When studied by directional solidification, the inter-lamellar spacing of the austenite-graphite eutectic was observed to decrease with an increase in growth rate as expected from Eq. (6.5). This decrease is obtained by the so-called branching mechanism of graphite flakes that is necessary for the two-phase growth interface to adapt to the local growth conditions. Fig. 6.4-A shows the two types of branching mechanisms identified by Nieswaag and Zhuitoff [NIE75] on directionally solidified samples and Fig. 6.4-B shows how Sun and Loper [SUN83a] saw them in small castings. Both figures illustrate the same two branching types, in-plane splitting and out-of-plane branching. Using the classification proposed by Austerman et al. [AUS67], the out-of-plane branching is thus tilting, while splitting may or not be assisted by in-plane twisting. According to Sun and Loper, the twisting and curving of graphite occur when branches come close to each other.

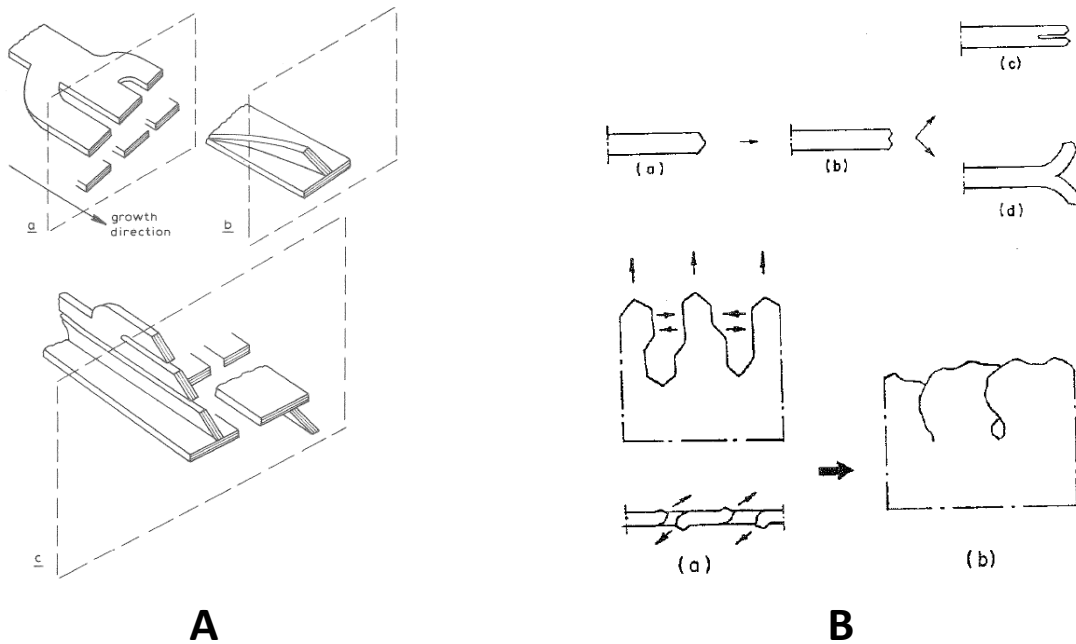


**Figure 6.4. Branching mechanisms of graphite from observation of directional solidification experiments [NIE75] (A) and of small castings [SUN83a] (B). In both cases, in plane splitting and out-of-plane tilting were identified.**

The faceting of graphite flakes leads to the dispersion of interlamellar spacing values as mentioned above. Moreover, Fig. 6.5 shows that there is a twofold distribution that corresponds to the change from lamellar to undercooled graphite. In the graph, the upper line relates to lamellar graphite while the lower line corresponds to undercooled graphite [HIL68], and it is seen that the data by Jones and Kurz [JON80, JON81] spans the interval between these two lines. The transition between these two graphite shapes can be either smooth [HIL68] or quite sharp [NIE75] but this difference appears to be a matter of wording. A smooth transition means that there is a range of growth rates in which both structures coexist, but the undercooled graphite develops in the grooves between the cells with flake graphite with a sharp transition between either areas, see the micrograph in Fig. 6.5. By quenching during directional solidification, Park and Verhoeven [PAR96] could evaluate at about 10°C the temperature difference between the fronts of these two eutectics growing side by side.

In castings, the eutectic cells consist most generally of one given type of flake graphite, lamellar or undercooled. However, change in graphite shape can occur both ways; Fig. 6.6 shows a case where solidification started at high undercooling with undercooled graphite which switched to lamellar graphite upon further growth and recalescence. It is noteworthy that the transition from lamellar to undercooled graphite and the reverse transition evidenced in Fig. 6.6 are abrupt. This is thought to be due to the fact that off-plane branching becomes active only when some undercooling has been reached, and disappears when the undercooling becomes lower than this critical value.



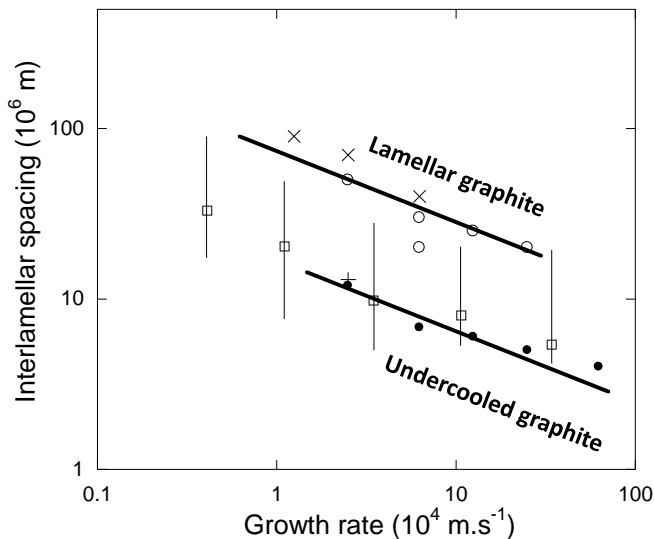


**Figure 6.5.** Change of the inter-lamellar spacing of the austenite/graphite eutectic. Dots and crosses are from Hillert and Rao [HIL68] and squares from Jones and Kurz [JON80, JON81]. The micrograph illustrates lamellar and undercooled graphite forms growing side by side in a directionally solidified sample (the growth direction is upwards) [HIL68].

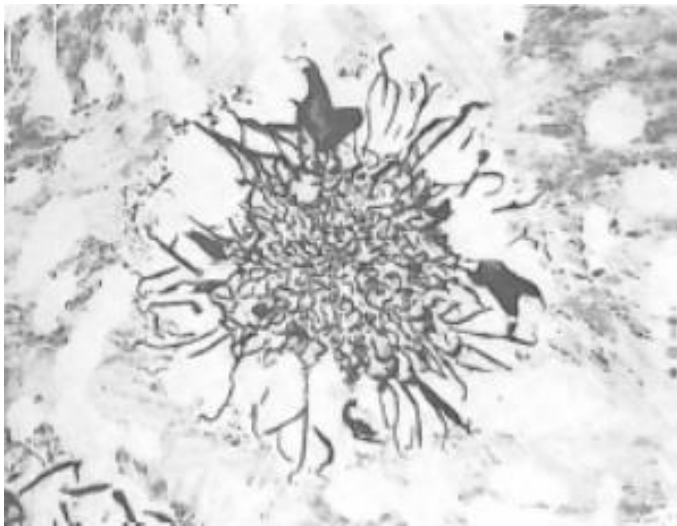


**Figure 6.6.** Eutectic cell showing undercooled graphite in the centre and much coarser lamellar graphite at the periphery [FRE75a]. Fredriksson and Wetterfall emphasized the sharpness of the microstructure change.

### 6.3 Growth laws of austenite-graphite coupled eutectic

Hillert and Rao considered that the eutectic with lamellar graphite is loosely coupled, with graphite protruding in front of austenite, when the eutectic with undercooled graphite is strongly coupled and presents a nearly planar – and thus isothermal - front. The difference between these two growth fronts is illustrated with the micrograph in Fig. 6.7 that was obtained on a sample quenched during directional solidification. Hillert and Rao conducted a theoretical analysis for coupled growth that gave  $V_{\text{growth}} = 5 \cdot (\Delta T_{\text{EUT}})^2 \mu\text{m}\cdot\text{s}^{-1}$  and the inter-lamellar spacing was predicted at half of the observed values [HIL68]. The authors concluded that growth of lamellar graphite is not entirely controlled by diffusion. Using Eqs. 6.5 to 6.7 with appropriate material's parameters, Jones and Kurz [JON81] obtained  $a = 2.3 \mu\text{m}\cdot\text{K}$  and  $b = 0.080 \text{K}\cdot\text{s}\cdot\mu\text{m}^{-2}$  and selected  $\varphi = 3.9$  to fit their data on interlamellar spacing, though it gave too low undercoolings. Analysing literature data, these authors noticed that  $\varphi$  would vary in between 2

and 10. With the above material's parameters, this range of  $\varphi$  values gives a change from  $V_{\text{growth}}=0.9 \cdot (\Delta T_{\text{EUT}})^2 \mu\text{m} \cdot \text{s}^{-1}$  to  $V_{\text{growth}}=0.05 \cdot (\Delta T_{\text{EUT}})^2 \mu\text{m} \cdot \text{s}^{-1}$ , i.e., up to 10 times lower than Hillert's estimate. Magnin and Kurz [MAG87] corrected the material's constants previously evaluated by Jones and Kurz to  $a=4.93 \mu\text{m} \cdot \text{K}$  and  $b=0.146 \text{K} \cdot \text{s} \cdot \mu\text{m}^{-2}$  while keeping  $\varphi$  nearly unchanged. With these new values, the predicted undercooling agreed with experimental values.

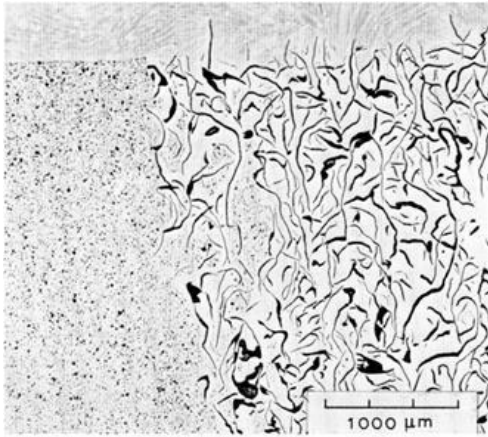


**Figure 6.7. Longitudinal section of a quenched directionally solidified sample showing a composite solidification front with the quenched liquid at the upper part of the image (growth direction was upwards). There is a sharp transition of the structure, with fine graphite on the left and coarse lamellar graphite on the right. On the left, the eutectic is strongly coupled while on the right this is not the case with graphite flakes protruding ahead of the two-phase front. [NIE75].**

Precise measurement of eutectic undercooling in directional solidification experiments is quite difficult and shows large scattering [LUX68]. Jones and Kurz [JON80] challenged this and designed a special experimental procedure to decrease the uncertainty on the eutectic undercooling to a few tenths of degree. This was done on binary Fe-C alloys and we are still in need of such precise experiments to validate the relationships used when analysing solidification of cast irons.

A somehow simpler method than directional solidification to estimate the relation between growth undercooling and growth rate consists to record the temperature-time evolution in a small casting that shows a clear eutectic plateau at nearly constant temperature. From the measured eutectic undercooling and the number of eutectic colonies evaluated on a metallographic section, an average growth rate may be estimated and related to the undercooling. In such experiments, the eutectic cells grow in a equiaxed mode that is in contrast to directional solidification experiments. During such equiaxed solidification, the interlamellar spacing might change as a result of geometrical constraints [ZOU89] or change in growth rate [CAT96]. However, experimental data shows that the eutectic growth undercooling of flake graphite eutectic is very similar in directional solidification and casting experiments [LUX68]. For equiaxed solidification of a Fe-C-Si eutectic alloy with 2.5 wt.% Si, Zou Jie found  $\varphi$  should be set to 6.5 [ZOU89].

Fig. 6.8 shows with dotted lines the evolution of the growth undercooling as function of the growth rate calculated with the corrected values of  $a$  and  $b$  and  $\varphi$  set to 3.9 [JON80] and 6.5 [ZOU89]. Solid lines are fits to experimental results by Lux and Kurz [LUX68] for alloys with S content lower than 0.001 wt.% and by Throgimsson [THO86] for cast iron with either lamellar or undercooled graphite. All curves show a similar behaviour except the experimental one for lamellar graphite. Because Thorgrimsson reported that the transition from lamellar to undercooled graphite occurs at an undercooling of 10 K, the curve for lamellar growth has not been drawn to high undercooling. From this figure, it is concluded that most of the experimental

results reported in the literature does in fact relate to undercooled graphite. This conclusion is sustained by the fact that Jones and Kurz [JON81] noticed the presence of “degenerate” flakes in their directional experiments for undercooling higher than 10°C, i.e., in the range where undercooled graphite is expected.

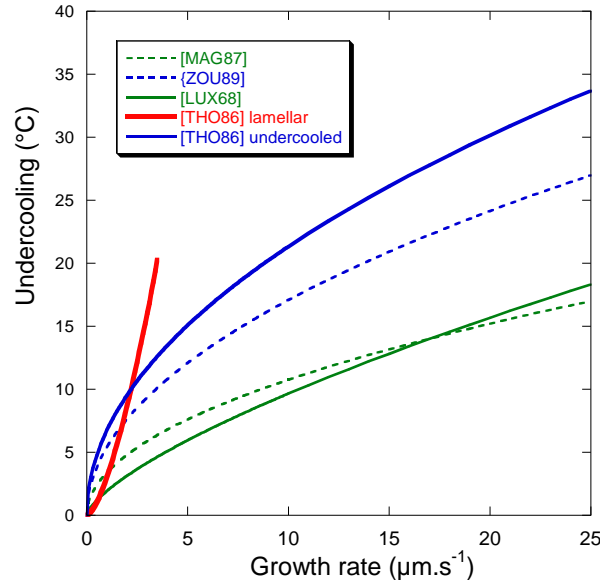


**Figure 6.8. Change in undercooling (°C) with growth rate (µm·s<sup>-1</sup>).**  
**The following equations were used:**

$$\Delta T = 3.4 \cdot (V_{\text{growth}})^{0.5} \text{ [MAG87]}$$

$$\Delta T = 5.4 \cdot (V_{\text{growth}})^{0.5} \text{ [ZOU89]}$$

$$V_{\text{growth}} = 0.37 \cdot \Delta T^{1.43} \text{ [LUX68]}$$

$$V = 0.48 \cdot (\Delta T)^{0.66} \text{ } \mu\text{m} \cdot \text{s}^{-1} \text{ for lamellar graphite [THO86]}$$

$$V = 0.022 \cdot (\Delta T)^2 \text{ } \mu\text{m} \cdot \text{s}^{-1} \text{ for undercooled graphite [THO86].}$$

#### 6.4 Effect of additional elements

The effect of alloying, e.g. with silicon, on the inter-lamellar spacing of graphite appears to be very limited. This can be rationalised by recognising that: i) graphite growth is related to the diffusion of carbon towards the graphite tips that may not be greatly affected by the alloying elements at the level where they are present; ii) the solubility of most alloying elements in austenite is sufficiently high that they only slightly affect its growth. However, these elements can change slightly interfacial energies and thus alter the growth characteristics to some extent. Also, the reference eutectic temperature might change with alloying.

More importantly, elements such as sulphur have very low solubility in both austenite and graphite, and their redistribution in the liquid can significantly alter the growth temperature. In their early work, Lux and Kurz [LUX68] reported a large number of data on Fe-C-Si alloys with about 2 wt.% Si. The whole set of data seemed at first highly scattered, but the authors found a clear effect of the sulphur content which explained much of the scatter. They summarized their results with the help of a  $(T, V_{\text{growth}})$  graph schematically reproduced in Fig. 6.9 and showing the evolution of the temperature of the solidification front with the growth rate (note the reverse axis).

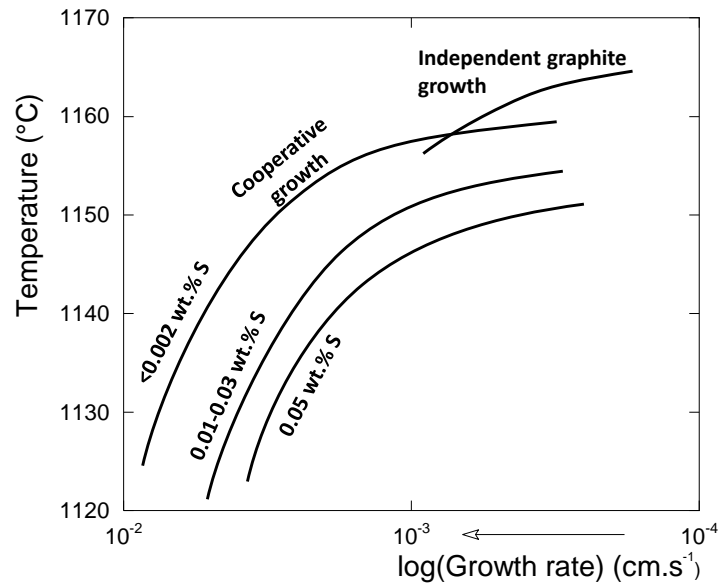


**Figure 6.9. Growth temperature versus growth rate as function of the sulphur level (adapted from Lux and Kurz [LUX68]).**

Fig. 6.9 shows in particular that S decreases the temperature of the growth front. This could be an effect of S on the growth kinetics of graphite, but is most probably also related to the rejection of sulphur in front of the eutectic front that leads to a decrease of the local equilibrium eutectic temperature. At imposed growth rate as in the directional experiments, this temperature decrease thus does not necessarily mean that the eutectic undercooling has changed, i.e., it does not mean that the relationship between growth rate and eutectic undercooling has been affected by sulphur.

Over the years, there have been a few attempts to extend the analytical two-phase eutectic growth model of Jackson and Hunt [JAC66] to ternary alloys [DON68, HIL71, MAC80, WIL05] or multi-component alloys [CAT15]. This latter work was applied specifically to cast iron and more particularly to the effect of silicon. As expected, the effect on the lamellar spacing was small and the agreement for the growth undercooling was observed to be satisfactory only for growth rates below  $10 \mu\text{m}\cdot\text{s}^{-1}$ . It should be emphasized that the model was closed up assuming an isothermal eutectic front which cannot represent growth of lamellar graphite eutectic. In summary, the analytical models for eutectic growth developed so far are unable to give answer to the question of the transition between lamellar and undercooled graphite and to give proper and accurate estimates of the effect of growth rate on both lamellar spacing and growth undercooling. Phase field modelling has been used successfully to describe the morphological transitions associated to modification of eutectic in Al-Si alloys [EIK15] but this has not yet been extended to the description of graphite/austenite eutectic in cast irons.

Solute redistribution can definitely affect growth conditions when microsegregation develops and leads to a change in the mean composition of the remaining liquid. This changes the reference eutectic temperature and thus the driving force for growth, and has been considered in modelling solidification of casting [FRE86, FRA95]. In the case of directional solidification, a steady-state composition field is rapidly established ahead of the eutectic front that does not evolve if the growth conditions are constant.

To conclude on these theoretical approaches, it is worth mentioning two other effects known to affect eutectic growth, namely the presence of a temperature gradient and the possibility of interfacial reaction between the melt and the faceted phase. It was pointed above that experimental data shows that the eutectic growth undercooling of flake graphite eutectic is very similar in directional solidification and casting experiments [LUX68]. This certainly means that the expected effect of the temperature gradient in directional solidification [PER13] could not be detected because of the experimental scattering. Finally, Hillert and Rao [HIL68] showed that theoretical predictions are away from experimental data, with separate growth of graphite (leading phase) giving by far too high undercoolings while cooperative growth predicted too low undercoolings. Part of the answer may be that growth is not only controlled by diffusion and capillarity, but also by interfacial kinetics. Accounting for this was worked out independently a long time ago by Fredriksson [FRE75b] and Lesoult and Turpin [LES75]. Fredriksson considered that the change of the interfacial kinetics constant needed to reproduce experimental information was related to change in the sulphur content of the alloys. This remains an open area in the case of cast irons while some progress has been made by means of phase field simulations in the case of Al-Si alloys.

### **6.5 Graphite-austenite coupled growth with other graphite shapes**

In addition to undercooled and lamellar graphite, there are other forms of graphite growing coupled with austenite which are derived from flake graphite. In pure alloys, i.e. with low levels of oxygen and sulphur, there are plate-like and coral graphite which are mostly of theoretical interest. Chunky graphite and compacted graphite that are also growing in a coupled eutectic with austenite will be dealt with in chapter 7.

It has been seen that there is a transition between lamellar and undercooled graphite as the growth rate is increased in directional solidification experiments (Fig. 6.5). Note that the same transition occurs when the undercooling for eutectic growth is increased by increasing the cooling rate as can occur in casting. The very detailed directional solidification experiments performed by Nieswaag and Zuithoff [NIE75] allow showing that decreasing the sulphur content of synthetic Fe-C-(Si) alloys increases the growth rate at which this transition occurs. This is illustrated with the two lower curves in Fig. 6.10 where it is assumed that the structure growing is the one presenting the lowest undercooling.

This effect of sulphur has been confirmed by Fujikawa et al. [FUJ99] who however noticed an inversion at high sulphur content, at about 0.06 wt.%. At such high values, the transition occurs at higher growth rate, and this was in fact observed also by Nieswaag and Zuithoff.

In synthetic Fe-C-(Si)-O alloys, there is similarly a transition from plate-like to coral graphite when the growth rate is increased [PAR96], see the two upper curves in Fig. 6.10. And again, it is noteworthy that decreasing the amount of oxygen does increase the critical growth rate for the transition.

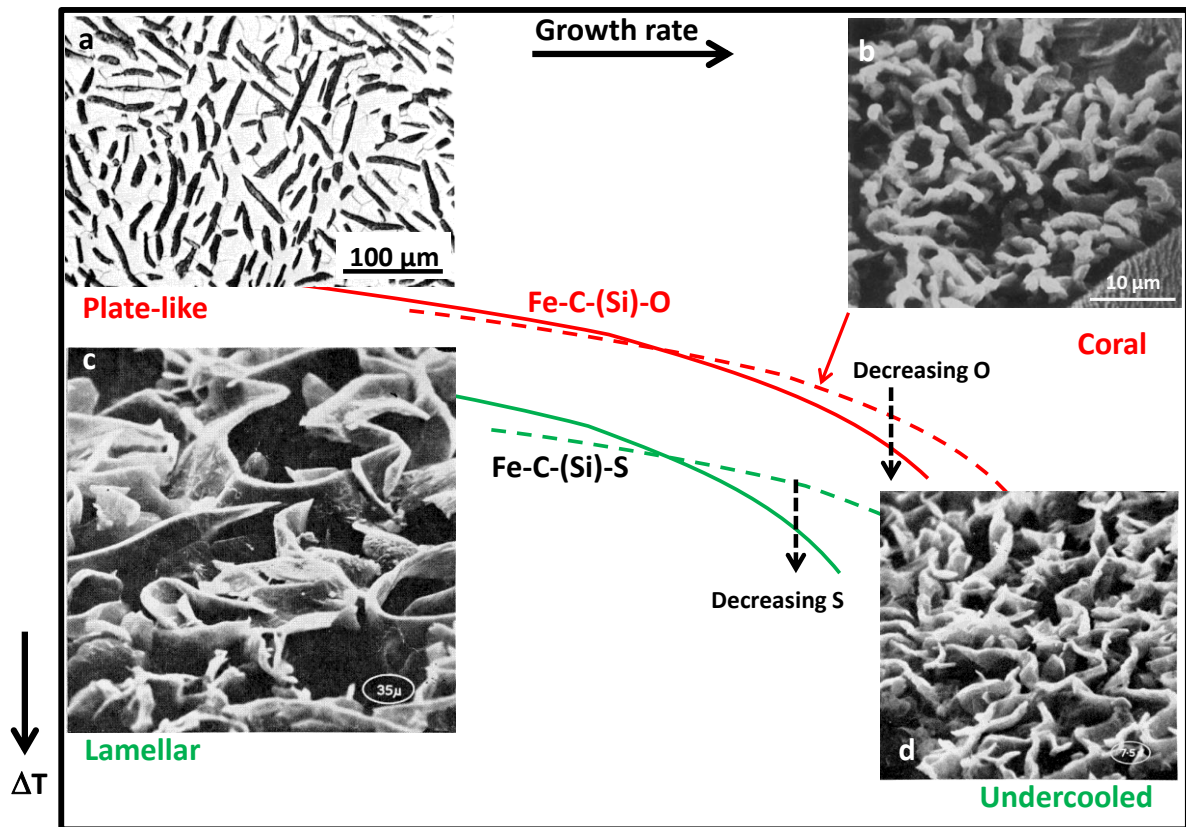


**Figure 6.10. Schematic showing the change of eutectic undercooling  $\Delta T$  versus growth rate for the four types of flake graphite coupled eutectics [LAC19].  
a: plate-like, b: coral, c: lamellar and d: undercooled graphite.**

All kinds of flake graphite, namely plate-like, lamellar, undercooled and coral graphite, have in common that the growth direction of graphite is parallel to the prismatic direction, with the prismatic faces in direct contact with the liquid thus easing attachment of carbon atoms. This has been illustrated several times in the literature with SEM images that show these graphite forms consisting of piling up of growth blocks elongated in the prismatic directions, but very few precise characterizations are available. **Electron back-scattered diffraction (EBSD)** would be the most suitable means to determine local crystallographic orientations but requires a perfect surface preparation that is highly difficult with graphite embedded in a metallic matrix. Accordingly, very few attempts have been reported such as the few spot orientations of lamellar graphite shown in Fig. 6.11-a [HOL07]. Hence, one has to resort to TEM and very few studies have been carried out for shapes others than lamellar or plate-like. However, it is worth mentioning the early work by Lux et al. [LUX69] on coral graphite which is illustrated in Fig. 6.11-b, which shows that growth occurs along the prismatic direction, albeit with many crystal defects reported again by Park and Verhoeven [PAR96].

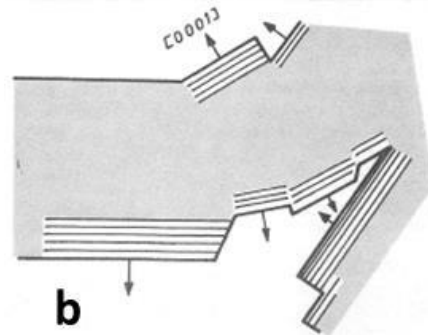
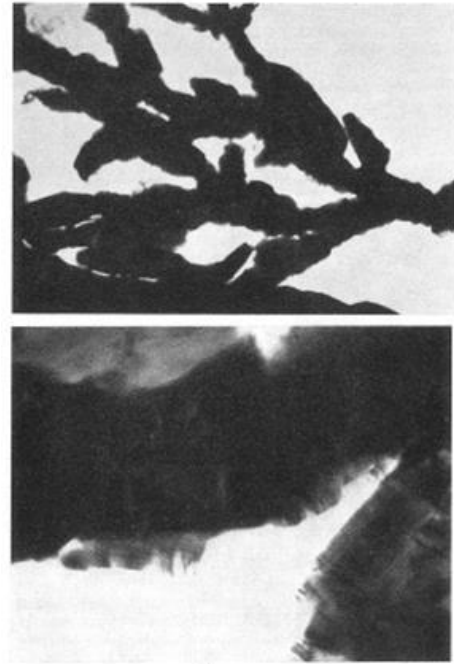
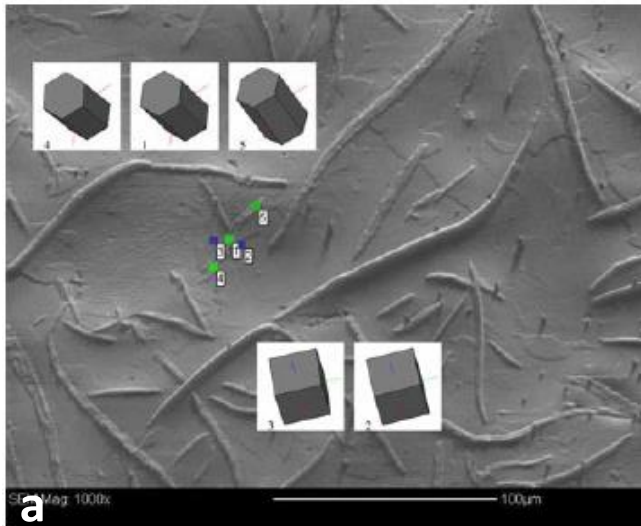


**Figure 6.11.**

- a. Crystallographic orientation of lamellar graphite and ferrite matrix as detected by EBSD in spot mode [HOL07].
- b. TEM micrographs and schematic of graphite stacking in coral graphite [LUX69].

### 6.6 The coupled zone

In a binary system with a eutectic point, the **coupled zone** is defined as the domain in the temperature-composition diagram in which the two phases of the eutectic can grow side by side at the same rate. This coupled zone is represented with the hatched domain for the stable Fe-C phase diagram in Fig. 6.12 according to Lakeland and Hogan [LAK68]. This domain is necessarily located in between the extrapolation of the two liquidus lines below  $T_{EUT}$ , and it is skewed towards the graphite side. Under a temperature gradient, the eutectic can also be stabilized against dendrites or primary precipitates [HIL78, KUR79, DAN09]. This is represented with the greyed area in Fig.6.12. This possibility is limited to very low growth rate and to high temperature gradient and will not be further considered here.

Lakeland and Hogan drew the coupled zone in the Fe-C system based on experimental observations. A few authors later attempted to calculate it, and it is noteworthy that the coupled zone according to Kurz and Fisher [KUR79] differs significantly from the one by Fredriksson [FRE75b]. The interest of the latter work is that it was also an attempt to introduce interfacial kinetics into graphite growth, which is eluded in all other approaches, although it certainly has an impact for faceted phases [LES75].

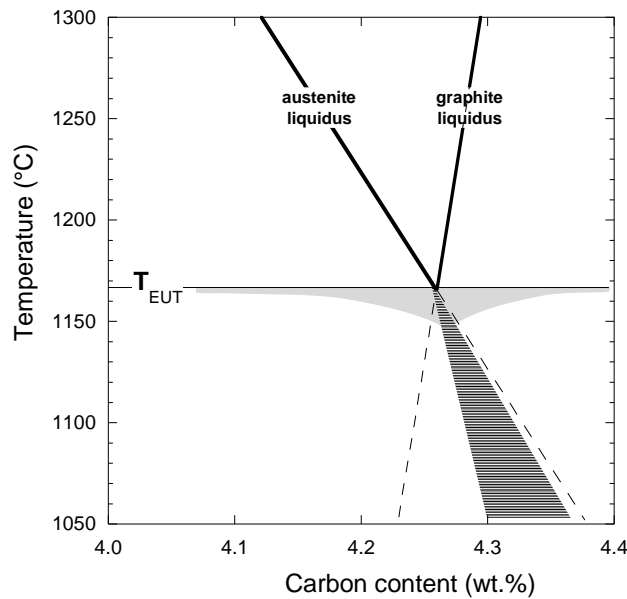


**Figure 6.12 Schematic of the coupled zone in the Fe-C phase diagram for equiaxed growth (hatched area) and its extension for growth in a temperature gradient (light grey area).**

With this coupled zone concept, Lakeland and Hogan described the solidification path of synthetic and industrial cast irons, focusing mainly on explaining how austenite dendrites may appear in hyper-eutectic alloys as in hypo-eutectic ones. The solidification path, i.e., the evolution of the composition of the remaining liquid, during solidification of such a hypereutectic iron is illustrated in Fig. 6.13. Fig. 6.13-a is according to Lakeland and Hogan and evidences two solidification stages: A) primary precipitation of graphite needs some undercooling followed by a limited recalescence and a growth stage slightly below the graphite liquidus; B) Austenite appears with a significant undercooling and a small recalescence and, while growing, rejects carbon that drives the remaining liquid within the coupled zone. Unless as in Fig. 6.12, the upper apex of the coupled zone in Fig. 6.13-a is below the eutectic temperature for emphasizing the need of a minimum undercooling for eutectic growth.

If now account is made of the thermal analysis results described at the end of chapter 3, the solidification path is according to Fig. 6.13-b: A) primary precipitation and growth of graphite both need a significant undercooling so that the solidification path is nearly parallel to but well below the graphite liquidus; B) Austenite appears with some undercooling that is certainly smaller than the undercooling for graphite precipitation and growth, leading to a point B that may be inside the coupled zone or slightly below it. Once austenite has appeared, both off-eutectic austenite dendrites and eutectic entities could start growing. The microstructure that will be obtained depends on the number of eutectic entities (see Chapter 3):

1) if they are numerous enough, bulk eutectic starts as soon as austenite has appeared and there will be little off-eutectic austenite dendrites. The thermal record could show a first arrest associated to primary graphite and a second arrest that will be the eutectic plateau.

2) if there are little graphite precipitates when austenite can appear, off-eutectic austenite dendrites grow and enrich the liquid in carbon, thus increasing the number of graphite nuclei until bulk eutectic can take place at a lower temperature. The thermal record shows again two



arrests, the first one corresponding to austenite formation and similar to the one recorded on hypoeutectic alloys, followed by the eutectic plateau at a lower temperature.

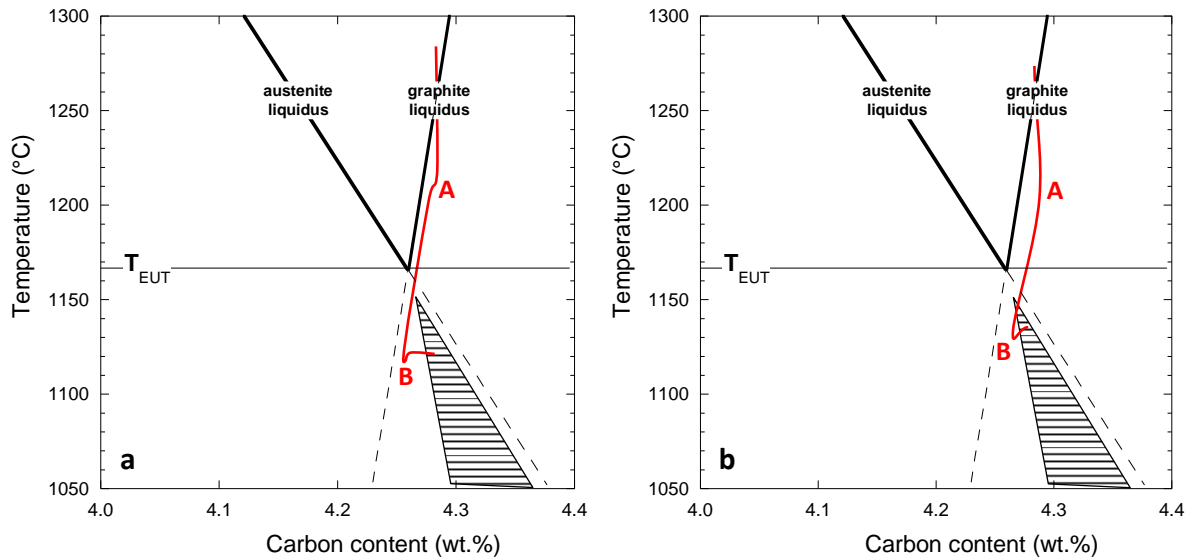


**Figure 6.13. Solidification path of a hyper-eutectic cast iron plotted onto the related Fe-C isopleth section. a: according to Lakeland and Hogan [LAK68]; b: accounting for large undercooling for graphite growth and smaller for austenite growth.**

### 6.7 The metastable austenite-cementite eutectic and the competition of stable (grey) and metastable (white) solidification

Fig. 6.14 shows a schematic of a  $\gamma$ -Fe<sub>3</sub>C eutectic cell which grows both with a **plate-like** type with cementite plates and a **rod-like** type called ledeburite. Fig. 6.15 illustrates how such a two-fold microstructure may appear on a metallographic section of a **mottled** cast iron having solidified partly in the stable system and partly in the metastable one. Based on metallographic observations, it was considered by Hillert and Rao [HIL68] that the so-called edge-wise growth could be described using a model for separate plate-like growth ahead of the eutectic, and the side-wise growth by a eutectic model for coupled growth. These authors however noticed that coupled growth gave a better agreement for the inter-plate spacing than their estimate for growth controlled by cementite plates leading the eutectic.

Considering a plate-like coupled-growth, Jones and Kurz evaluated the parameters a and b in Eqs. 6.5 to 6.7 to  $a=0.74 \mu\text{m}\cdot\text{K}$  and  $b=0.012 \text{K}\cdot\text{s}\cdot\mu\text{m}^{-2}$ , and their experimental information could be satisfactorily reproduced with  $\phi=2$ . With  $\Delta T$  being now the undercooling expressed with respect to the metastable eutectic, this gives:

$$V=18\cdot\Delta T^2 \mu\text{m}\cdot\text{s}^{-1} \quad (6.8)$$

which is not so far from the value of  $30\cdot\Delta T^2 \mu\text{m}\cdot\text{s}^{-1}$  obtained by Hillert and Rao for cooperative growth of austenite and cementite with a rod-like geometry.

The relation between growth rate and inter-lamellar spacing is illustrated in Fig. 6.16 [HIL68]. Both Hillert and Rao [HIL68] and Jones and Kurz [JON81] considered that the austenite-cementite eutectic behaves much as a regular eutectic based on the observation that the inter-lamellar spacing does nearly follow equation 6.5. It is however seen in Fig. 6.16 that the agreement is not that perfect, with the experimental slope lower than the theoretical

one. Indeed, Tiller has shown that this divergence may be a sign that interfacial kinetics enter into play [TIL68] while this has been attributed by Catalina et al. [CAT03] to a change in the growth mode with growth rate.

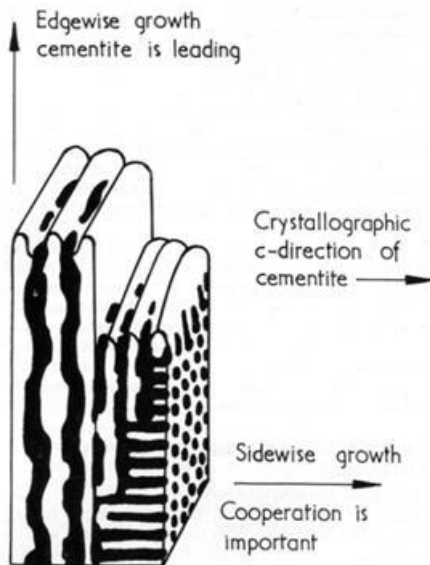


**Figure 6.14. Development of the white  $\gamma$ -Fe<sub>3</sub>C eutectic showing a plate-like structure led by cementite and a rod-like coupled growth growing sidewise [HIL68].**

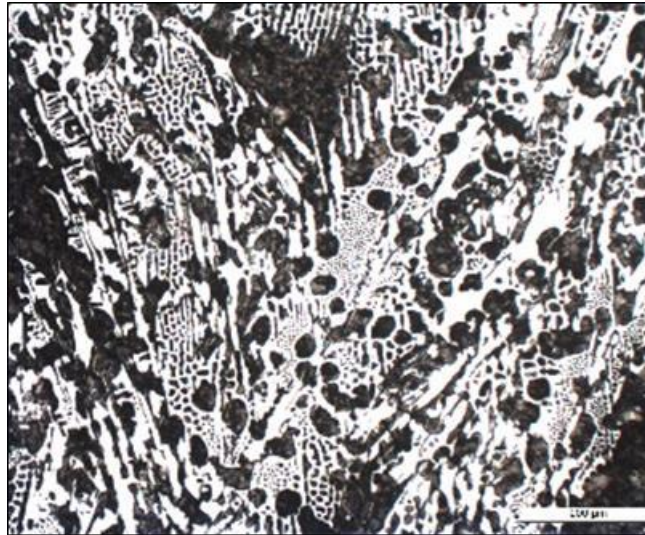


**Figure 6.15. Optical micrograph: appearance of cementite (white) on the metallographic etched section of a mottled CGI.**

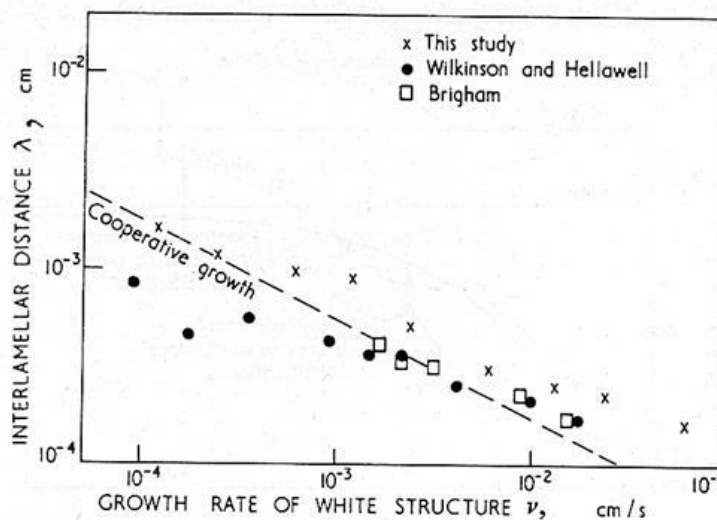


**Figure 6.16. Evolution of the inter-lamellar spacing of the white eutectic with growth rate as measured on directionally solidified samples [HIL68].**

In a literature review performed in the early 1990s, Selig could not find information that would define which of the two structures of the white eutectic would be preferred in relation to growth conditions [SEL94]. Analysing directional solidification results, Catalina et al. [CAT03] noticed that the experimental information seems showing that the two structures grow at the

same undercooling at high growth rates ( $>100 \mu\text{m/s}$ ). This is in contradiction with the information reported by Kante and Leineweber [KAN18] who showed the white eutectic consisting mainly of cementite plates at large growth rates. This thus seems to be an open subject with some possible importance for surface hardening of cast irons.

It has been noticed previously that nucleation of graphite is easier than that of cementite, while growth of ledeburite is faster than that of lamellar graphite eutectic (see [Appendix B](#)). This has important consequence on the formation of the stable and metastable microstructures in a casting as described by Hillert and Rao [HIL68]. If solidification started grey, it will proceed upon cooling in this way until a cementite nucleus is formed; when this happens, white solidification then proceeds very rapidly and overtakes stable solidification. Conversely, if the eutectic solidification has started in the metastable system, it will change to stable eutectic when the cooling rate is decreased enough provided a graphite nucleus has appeared. These transitions are schematized in Fig. 6.17 where is plotted the growth temperature versus growth rate for stable (blue curve) and metastable (red curve) eutectics. The gap in growth rate between these two transitions defines a hysteresis and a range of cooling rates where both structures could coexist. This is important for understanding the microstructure seen in the wedge castings dedicated to investigate the chill tendency of cast irons. This also explains the so-called inverse greyness when a casting that is expected to solidify fully white presents a grey case and a white core [HIL68].

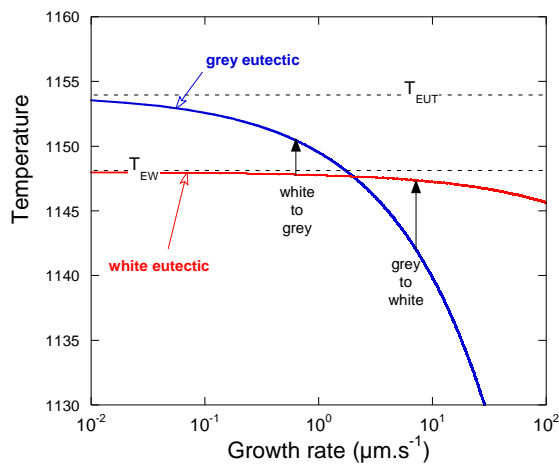


**Figure 6.17. Temperature at the solidification front as function of the growth rate (adapted from [HIL68]).**

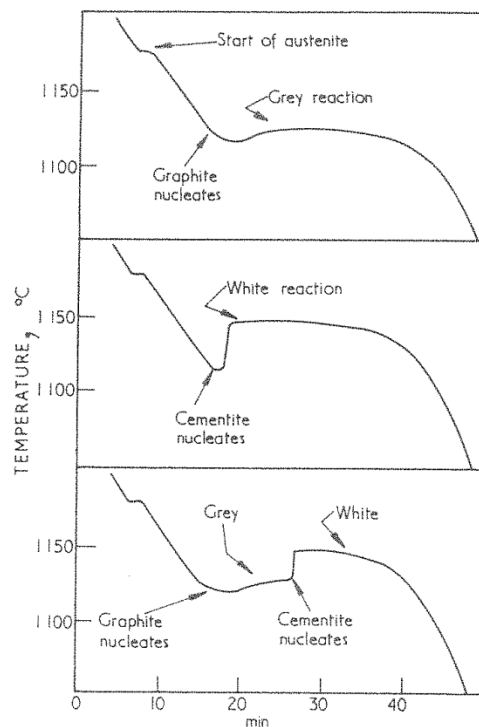


**Figure 6.18. Typical cooling curves for iron solidifying grey (top), white (middle) or mottled (bottom) [HIL68].  $T_{EW}=1148^{\circ}\text{C}$ .**

Fig. 6.18 shows the various temperature records obtained from a eutectic cast iron with a fully grey structure (top), a fully white structure (middle) and a mottled structure (bottom). An example of this latter case has also been published by Heine [HEI77]. The recalescence associated to the formation of white eutectic may be much less pronounced than shown in these schematics. In particular, growth of white eutectic in thermal cups most often shows little recalescence if any as was pointed out in Chapter 3. Finally, it should be emphasized that **microsegregation** can play a significant role on the grey to white transition: negative segregation of silicon during stable solidification decreases the stable temperature and increases the metastable temperature corresponding to the remaining liquid.

### 6.8 Summary

Experimental characterizations of graphite-austenite and cementite-austenite coupled eutectics have been achieved in the 1960s and 1970s, both by directional solidification –under controlled thermal gradient and growth velocity- and by small castings such as TA cups. They provided quantitative information on the relation between growth conditions and lamellar spacing (eutectic with graphite), or plate or rod spacing (eutectic with cementite), but very few precise data is available on the growth undercooling. It is worth mentioning that experimental studies on faceted/non-faceted eutectics remains an attractive research area for its intrinsic non-steady behaviour [SHA16] and the frequent non-crystallographic branching of the faceted phase [MOH20].

The modelling of these irregular eutectics along the lines developed for regular structures by Jackson and Hunt is "updated" from time to time [GUZ06]. This approach has given some rough estimates of their growth law but ends up with limited success when compared to details of experimental data. However, it is a useful tool for a semi-quantitative understanding of important phenomena such as inverse greyness and inverse chill. It should be noted that the transition from flake graphite to undercooled graphite remains a challenge that could potentially be addressed by phase field modelling or other approaches.



# Chapter 7 - Spheroidal graphite-austenite eutectic

Quenching during directional solidification (QDS) is a laboratory method of visualising the entire solidification sequence in a single sample, as shown in Fig. 7.1 for a hypo-eutectic SGI. After thermal equilibration at a temperature at which the alloy is liquid in the upper part of the furnace, the sample is withdrawn downwards through the fixed temperature field so that solidification proceeds upwards. The evolution of the graphite spheroids is seen on the longitudinal section that has not been etched while the evolution of the solidification structure is evidenced on the etched longitudinal section and on the etched transverse sections A, B and C. As the temperature decreases, solidification starts with dendritic austenite until a temperature at which the eutectic reaction sets up that is associated with profuse graphite precipitation. The progress of the eutectic reaction with further cooling is clearly evidenced by comparing the transverse sections B and C.

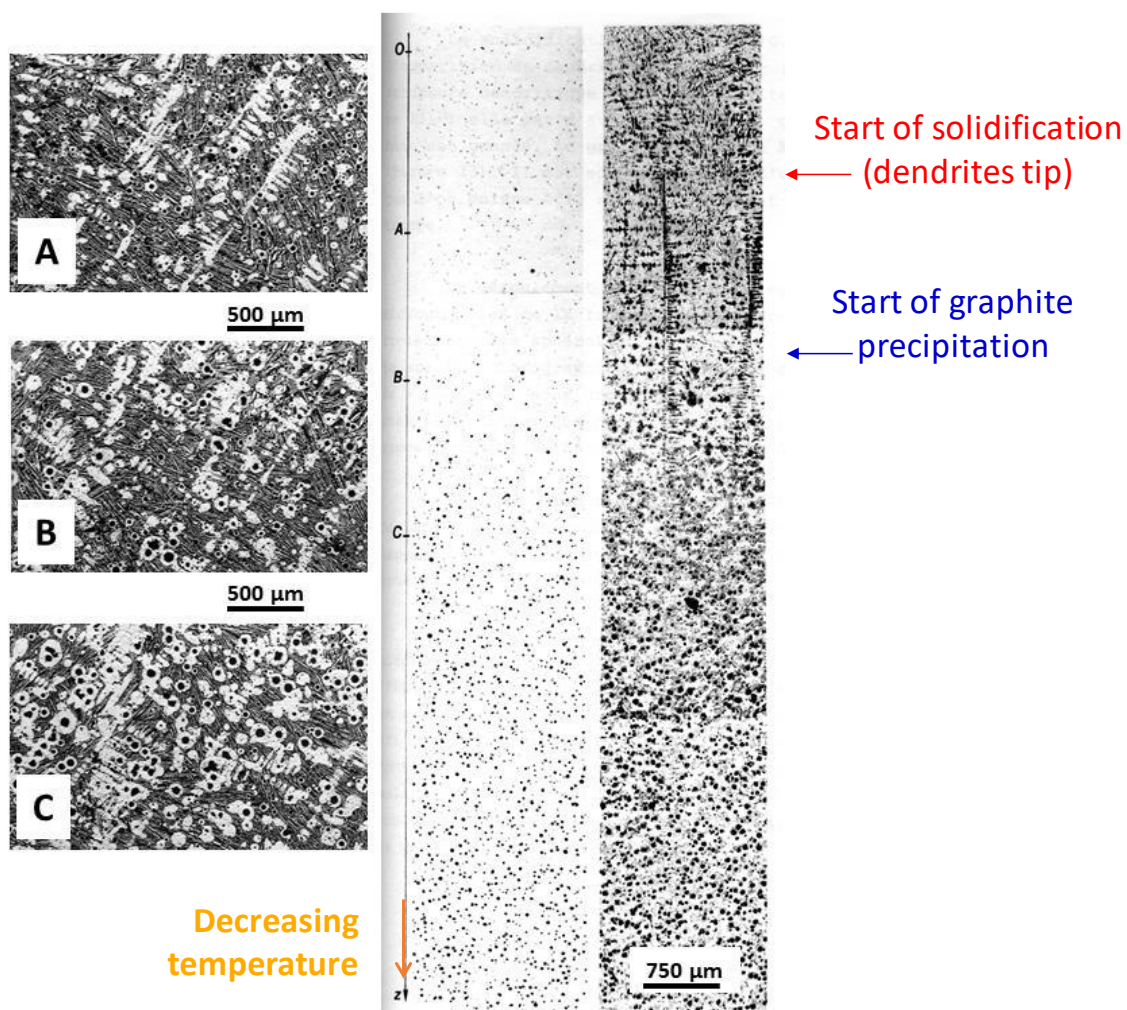
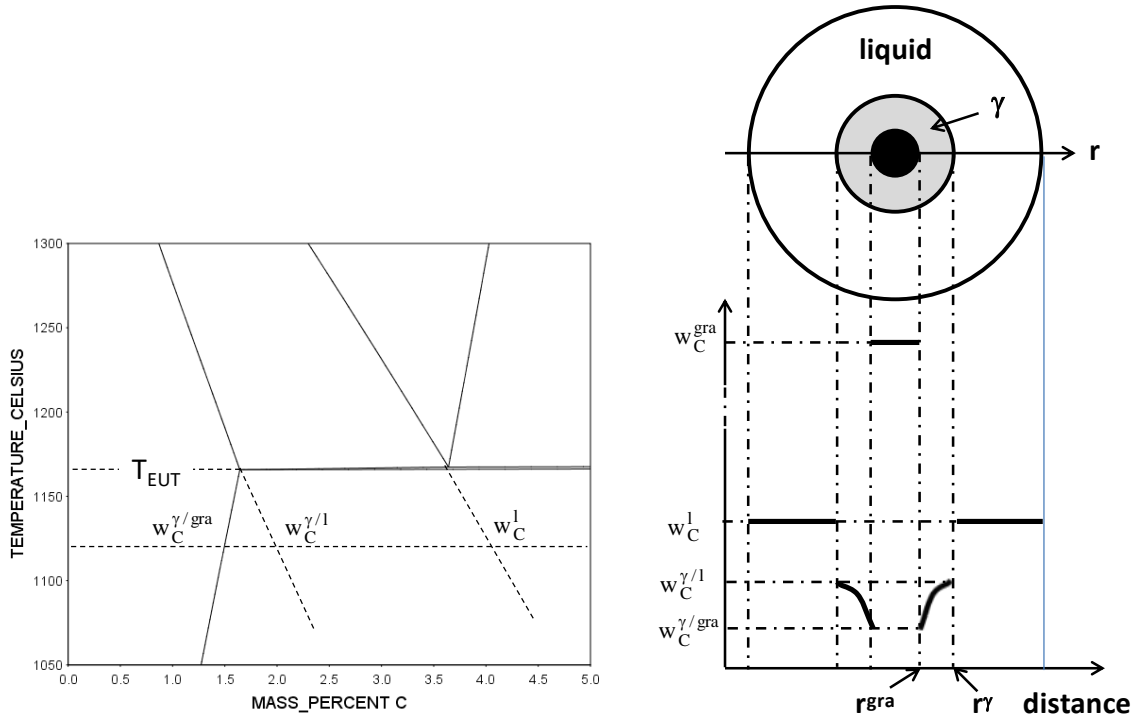


Figure 7.1. Longitudinal section of a QDS sample before and after Nital etching. Micrographs A, B and C were taken on transverse sections at the indicated locations [THE79].

In this chapter, we will first consider an idealized eutectic transformation with spheroidal graphite (section 7.1) and then particular characteristics of this eutectic will be detailed (sections 7.2 and 7.3). The second part of the chapter will be devoted to various undesirable growth characteristics of graphite in spheroidal alloys, limiting itself to cases where the overall growth direction of graphite remains the basal c-direction, i.e. irregular and exploded spheroids (section 7.4) and chunky graphite (section 7.5). Next, compacted graphite whose growth begins with the precipitation of spheroids will be discussed in Section 7.6 and some further information on spheroidization will be mentioned in Section 7.7.

### 7.1 Idealized eutectic solidification with spheroidal graphite

Consider an alloy with eutectic composition that is initially liquid. When the temperature of the material falls below  $T_{EUT}$ , both austenite and graphite may precipitate and do so with each graphite nucleus being instantly encapsulated by an austenite shell. Further growth of the graphite nuclei as spheroids proceeds by transfer of carbon atoms from the liquid to graphite, through this austenite envelop. This mechanism has been first quantified by Wetterfal et al. [WET72] who noticed the similarity with solid-state graphitisation of white or mottled cast iron. Their approach considered isothermal conditions and assumed that growth of graphite is controlled by carbon diffusion through the austenite shell with composition at the interfaces given by equilibrium extrapolated below the eutectic temperature in the appropriate Fe-C isopleth section (Fig. 7.2, to the left). The carbon profile is represented in Fig. 7.2 (to the right) with the compositions also indicated on the Fe-C isopleth section.



**Figure 7.2. Schematic of carbon distribution around a graphite spheroid (black circle), within the austenite shell and in the liquid. Equilibrium is assumed at the interfaces so that the compositions are read on the appropriate Fe-C isopleth section.**

The above assumptions have been kept in all the models developed since then. As a matter of fact, diffusion control appears quite satisfactory, which means that the actual mechanism of carbon attachment onto the graphite spheroids does not affect the kinetics of the eutectic reaction. As the austenite envelops thicken, the growth rate of the individual eutectic entities decreases and so does the overall transformation kinetics. In casting such as in TA cups, the eutectic transformation of SGI thus proceeds at higher undercooling and over a larger temperature interval than LGI. This suggested that the shape of the eutectic plateau may be correlated with graphite shape [CHA74].

The density of graphite is much lower than that of liquid or of austenite, which may be similarly stated by noticing that the molar volume of carbon atoms increases dramatically when precipitating on graphite [EIK20a]. Once graphite precipitates are encapsulated by austenite, this latter is pushed away which leads to the well-known expansion of SGI that occurs during solidification as well as during final cooling after casting; see section 10.10 for a comparison with LGI. In this process, the crystallographic structure of the fcc matrix - i.e. the network of substitutional atoms (Fe, Si, Cu, Mn, etc.) - is preserved. Hillert rationalized this by stating that the substitutional site fraction is preserved, whatever the contents in interstitial atoms (C, N, O) in austenite. This is illustrated in Fig. 7.3 [EIK20a] where interstitial atoms are seen to move in between rows of substitutional atoms.

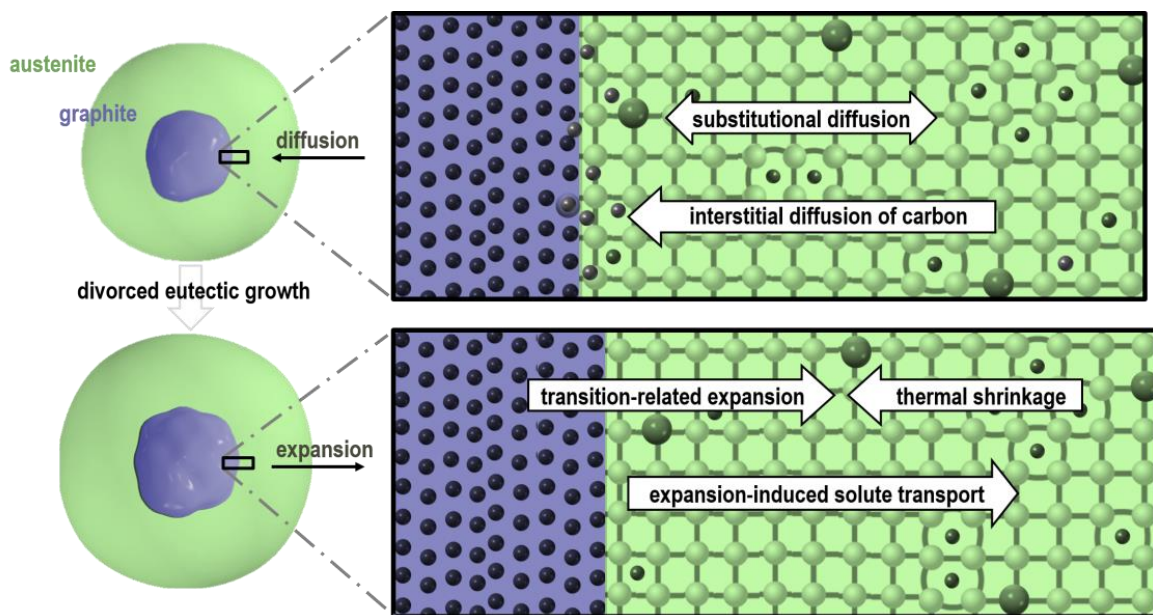


**Figure 7.3. Schematic of graphite precipitation by carbon diffusion through the substitutional fcc lattice and expansion of the austenite envelop (Courtesy J. Eiken).**

This ideal schematic can be easily extended to hypoeutectic and hypereutectic alloys if it is considered that the composition of the remaining liquid follows the austenite/liquid equilibrium line of the appropriate Fe-C isopleth section. In the case of hypoeutectic compositions, austenite first forms and, when the eutectic temperature is reached, graphite nuclei appear that are immediately encapsulated by austenite. In the case of hypereutectic compositions, graphite spheroids first precipitate that get encapsulated in austenite as soon as the eutectic temperature has been reached.



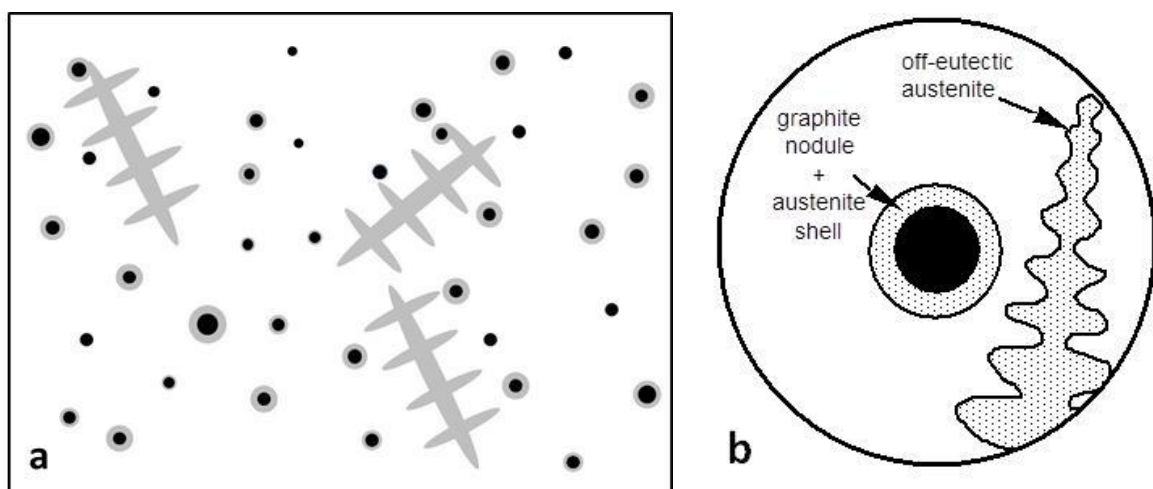
This ideal behaviour is not followed for various reasons, amongst which:

- Austenite growth might proceed with some undercooling as already mentioned in Chapter 3 and further discussed in Chapter 10.
- Nucleation of graphite spheroids is not instantaneous but increases with undercooling as detailed in chapter 4. This has the important consequence of leading to the formation of off-eutectic austenite dendrites in eutectic and hypereutectic cast irons; see next section.
- Growth of primary graphite in hypereutectic alloys is time-dependent, meaning that the solidification path during primary graphite precipitation is located below the graphite liquidus.

## 7.2 Further features of the eutectic reaction in SGI

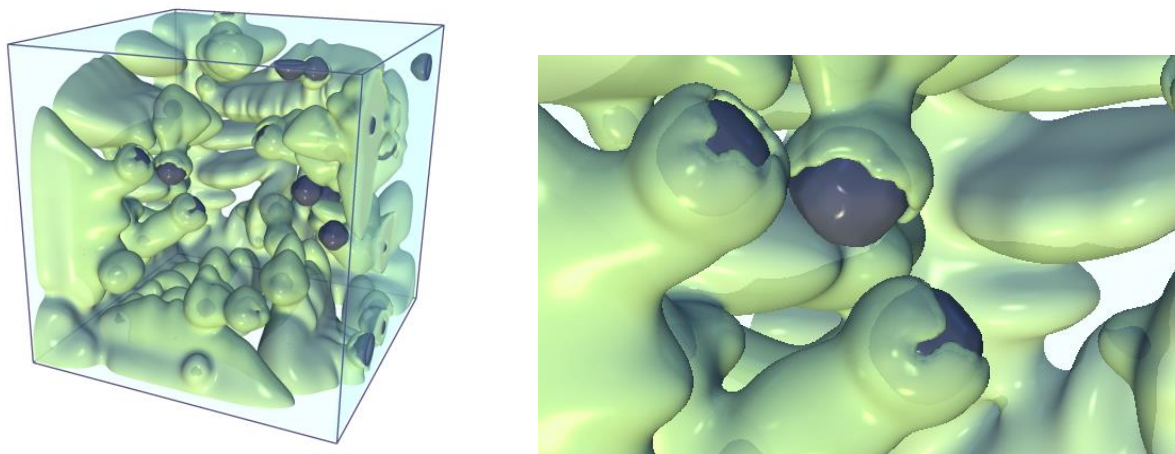
Considering again an alloy of eutectic composition, let us assume that graphite nucleation is low which means that very few spheroidal graphite eutectic entities develop. In order for the liquid composition to remain on the austenite liquidus extrapolation, **off-eutectic austenite** must develop, which is assumed to occur without undercooling. This is a well-known feature that austenite dendrites are observed or readily revealed in eutectic and hyper-eutectic cast irons, and not only in hypo-eutectic cast irons.

Fig. 7.4-a shows accordingly the various solid entities that are present at a millimetre scale at some early stage during solidification of a SGI. These are isolated graphite spheroids, spheroidal graphite eutectic cells and austenite dendrites, and this schematic applies to hypo- as well as hyper-eutectic alloys. A comprehensive model taking into account off-eutectic austenite has been developed [LES98a] which uses appropriate mass balances written first for a volume as in Fig. 7.4-b, and then extended to distributions as in Fig. 7.4-a. In its early version, this model used the assumptions described above, that graphite spheroids get encapsulated by austenite as soon as they form, that austenite grows with no undercooling and also that the composition of the remaining liquid is along the austenite liquidus; see Chapter 10 for further details.



**Figure 7.4. Schematic of the representative volume for describing solidification of SGI (a) and close-up on the constituents and interfaces that are accounted for in the mass balances and kinetics equations (b).**

Although the formation of the austenite shell is most often perceived as being so rapid that it can be considered instantaneous, Figure 7.4-a suggests that graphite spheroids can grow freely in the liquid before being encapsulated in agreement with several observations. Indeed, it has been reported that the spheroids are not encapsulated until they reach a critical diameter, the value of which ranges from 7 to 17 microns depending on the authors. Wetterfal et al. [WET72] claimed that this was related to the time required for the spheroids to make contact with the nearest austenite dendrite by floatation, but there may be other fundamental reasons that have not yet been investigated. A second feature is the observation of several ex-austenite precipitates around some graphite spheroids in a quenched sample, suggesting that the austenite shells can consist of several grains. However, a phase field calculation showed that austenite can adopt a kind of dendritic shape when encapsulating a spheroid as illustrated with Fig. 7.5, suggesting that the dendrite arms could be these pieces observed in cross-section.



**Figure 7.5. Phase field modelling of the dendritic development of the austenite envelope around a graphite spheroid (courtesy J. Eiken).**

Fig. 7.5 illustrates also that several spheroids can be attached to a given austenite grain, and this has been discussed at length as the so-called “multi-nodular” model [RIV02]. In the same vein, Boeri et al. [BOE18] considered that the notion of coupled zone (see section 6.6) does not apply to SGI because individual eutectic entities cannot be defined. However, another view consists to consider the final microstructure instead of the details of the solidification process. Using the previously mentioned model, this has been done assuming that a SGI could be qualified as eutectic if the amount of off-eutectic austenite is less than some small limit [LES98b]. By setting this limit to 5% of the volume, the pseudo-coupled zone could be predicted as done in Fig. 7.6. For this, a law was set for nucleation of graphite and calculations were performed for varying casting modulus (10 to 20 mm in Fig. 7.6). For each modulus, the carbon content of the alloy was incremented until the off-eutectic austenite fraction equalled 5%. A composition could effectively be found for a modulus of 20 and 15 mm and it was reported with a circle on the figure at the temperature of the eutectic arrest. On the contrary, for the 10 mm modulus, the amount of off-eutectic austenite was always larger than 5% for the selected nucleation law. With these results, the left and lower boundaries of the pseudo-coupled zone could thus be drawn as seen in the figure with the dot-dashed line. The question

of setting the boundary to the right of this coupled zone in the case of SGI may be of practical interest.

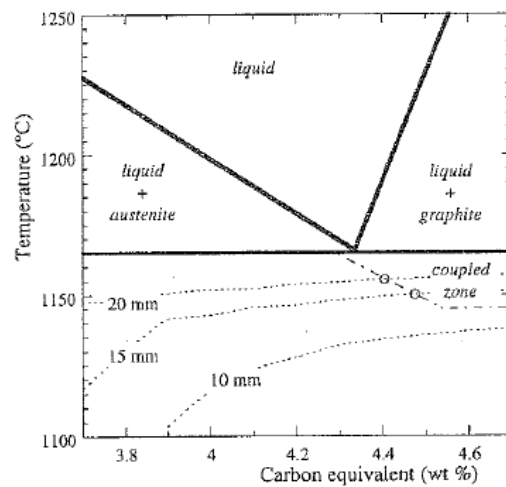


**Figure 7.6. Location of the pseudo-coupled zone of SGI [LES98b].**

### 7.3 Irregular spheroids

There are two types of degenerate graphite that bear the same growth characteristic as spheroidal graphite, i.e., having an overall growth direction along the *c* crystallographic direction of graphite. These are exploded graphite, which is described later in this section, and chunky graphite, which is described in the following section. Liu et al. [LIU83] suggested continuity between these various shapes as illustrated with Fig. 7.7.

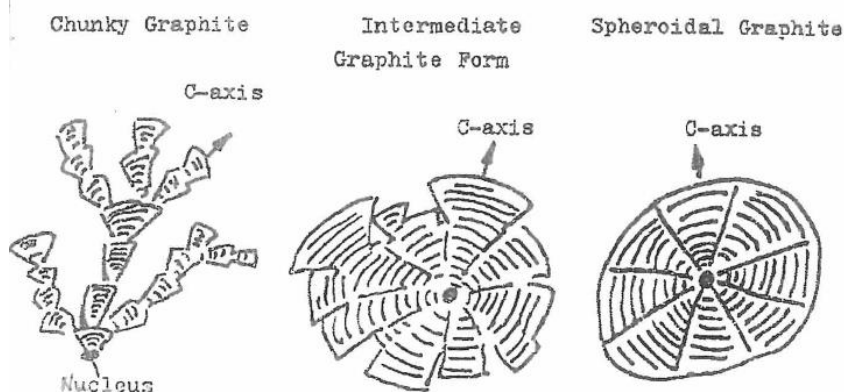


**Figure 7.7. Schematic of the transition between spheroidal, exploded and chunky graphite [LIU83].**

Phase field simulation such as in Fig. 7.3 or Fig. 7.5 showed that irregularities can appear at the surface of the spheroids during encapsulation by austenite [EIK20a]. These morphological instabilities can thus form at early stage during the eutectic reaction and seem to develop further as the transformation proceeds. By X-ray synchrotron tomography, it has been shown that this is a rule: graphite spheroids are less and less regular as they grow larger [AZE18]. At a certain stage of solidification, austenite forms large grains which contain several spheroids [RIV02] as a result of both growth of austenite dendrites and impingement of SG eutectic cells. The eutectic entities are therefore less well defined and the distance the carbon

has to diffuse from the remaining liquid to the spheroids may have a wide distribution. It is thought that this leads to irregular spheroids [AZE18] and a modification of the model shown in Fig. 7.4 has been developed to account for this distribution [BJE18].

It is clear that inhomogeneous distribution of graphite within the austenite grains will lead to uneven growth of the spheroids and will favour such irregularities. This leads to the practical statement of increasing inoculation or cooling rate to getting higher spheroid count and thus better nodularity. It is however unclear if these irregularities grow only by solid-state diffusion of carbon through the austenite shells or if they can also form a kind of decoupled eutectic with both austenite and graphite in contact with the liquid and growing away from the original spheroids [WIG21].

Irregular spheroids as described above are however much more compact than exploded graphite spheroids. The latter are most often associated with primary graphite growth and possible flotation. Fig. 7.8-a shows a small spheroid evolving as an exploded spheroid in Fig. 7.8-b during further growth. The transition could at first be understood on the basis of the carbon available in the liquid for graphite growth, i.e. the carbon supersaturation of the liquid [SUN83b]. Following nucleation of the spheroids, one expects an initial period of rapid growth during which most of the carbon supersaturation is consumed. A steady state flux of carbon then establishes which may be insufficient for the spheroids to keep compact, this is when irregular and then exploded graphite starts showing up. However, laboratory experiments illustrated in Fig. 7.8-c showed that separate sectors are readily seen when Ce is added to Fe-C melt and processed under vacuum. This strongly suggested that the lateral growth of the sectors was inhibited leaving space between the sectors since the very early growth stages of the spheroid. It means that the rate of lateral extension of the new growth blocks nucleated at the top of the sectors, see Chapter 5, is sensitive to the amount of spheroidizers, Mg or Ce. The fact that both Mg and Ce are known to increase solidification undercooling may be seen as an indirect confirmation of this latter conclusion.

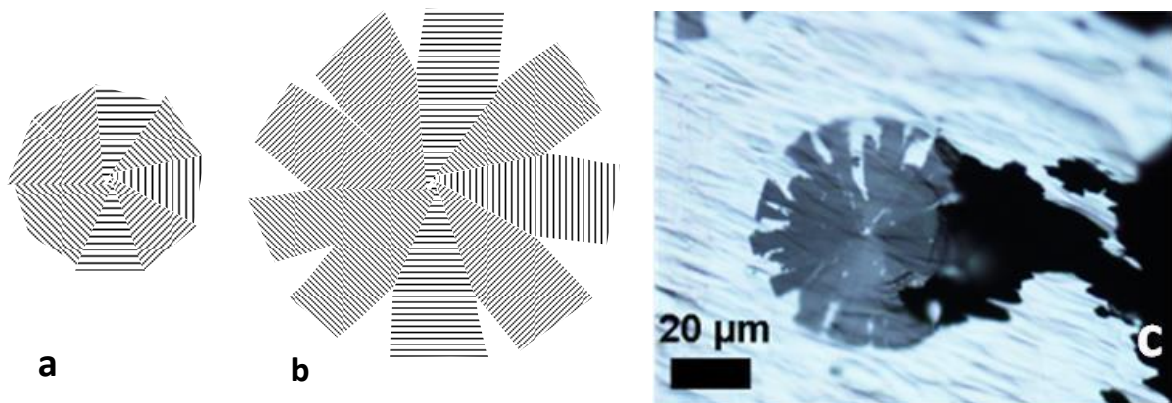


**Figure 7.8. Schematic of the growth of a spheroid with sectors becoming separated when a large enough size has been attained (a, b) and thin foil of a spheroid in a Fe-C-Ce alloy [THE13] (c).**

It may be worth mentioning that various forms of exploded graphite have been described which do not all seem to relate to overall growth along the *c* direction such as so-called star-like graphite with faceted graphite precipitates radiating from a single centre [SUN83b]. It is

noticeable as well that the effect of Mg over-treatment mentioned in Chapter 8 leads to protuberances that are certainly not growing along the *c* direction. Unfortunately, it does not seem that any attempt has been made to clarify the reasons for these changes.

A feature which seems closely related to the formation of exploded graphite is the observation of large spheroids or irregular spheroids with iron-rich precipitates encapsulated by graphite. It has been known since long that spheroidal graphite presents a magnetic signature because of iron-rich particles embedded in it. These particles are typically of a few  $\mu\text{m}$  in size and are thus easily noticed on metallographic sections as white spots inside the graphite particles, see Fig. 7.9. The schematic at the right in Fig. 7.9 suggests that these iron-rich particles get engulfed in the spheroid when lateral extension of the sectors is not too much inhibited. This closing could possibly relate to a change in growth rate of graphite, e.g. when getting encapsulated in austenite as has been suggested [GHA19], and this does not need any change in the growth mechanism at the graphite scale.

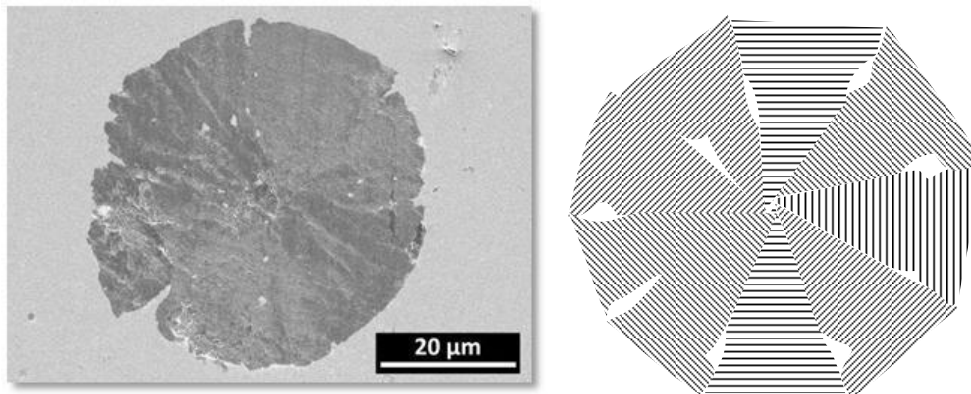


**Figure 7.9. Micrograph of a spheroid showing iron-rich particles in white contrast that got embedded within graphite [BOU17] and schematic of the process.**

Another usual feature of spheroids is the radial “line” structure which is clearly evidenced under polarized light optical microscopy, see Fig.7.10-a. These lines are due to a relief on the surface of the polished spheroid section. In Fig. 7.10-b are drawn the lines seen in Fig. 7.10-a, with the apparent boundaries between sectors in red and other lines in black. It appears that the sectors get more and more sub-divided by these black lines as graphite growth proceeds from the centre to the periphery of the spheroid.

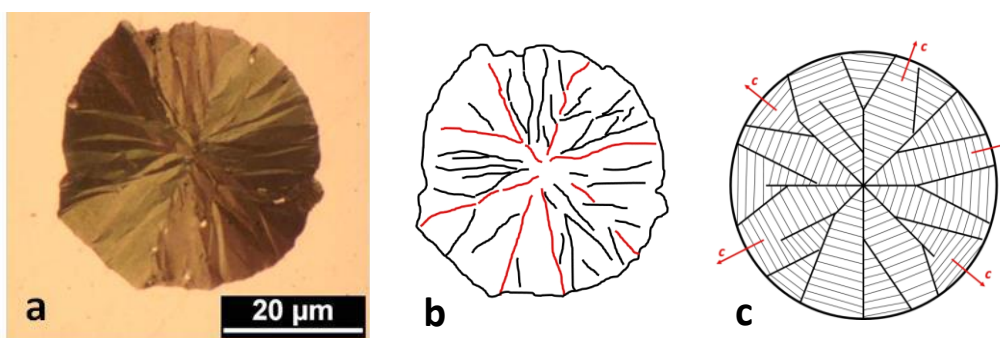


**Figure 7.10. Optical micrograph under polarized light (a) and schematic of the radial line structure, without differentiating sectors (b) and after drawing their boundaries (c) [BOU20].**

The above schematic is akin to a process where new sub-sectors are generated and then compete with previous sectors to fill the space, in agreement with the divergent nature of spheroidal growth, see Fig. 7.10-c [BOU20].

#### 7.4 Chunky graphite

Chunky graphite in spheroidal graphite cast irons has been described several times in the literature and the interested reader is directed to the reviews by Lacaze et al. [LAC13b] and Baer [BAE20]. It is sufficient here to remind that it appears most often as large cells of tiny graphite precipitates when seen on 2D sections, e.g. on Fig. 7.11-a, while being a network of interconnected strings [LAC13b]. When formed in the last to solidify areas, chunky graphite may show isolated strings which explain it has been confused with vermicular graphite during years. Chunky graphite is favoured by silicon, cerium and long solidification time, which makes it frequent in high silicon cast irons developed nowadays and in large castings. In practice, it has been found that adding antimony decreases significantly the amount of chunky graphite and this has been related to RE-Sb interactions cancelling each other deleterious effect by precipitation of compounds. However, it is known that tiny additions of As, Pb and Sb do improve nodularity in low silicon cast irons and this gave the idea of adding 40 ppm antimony to a high silicon cast iron spheroidized and inoculated without RE addition. While the reference high silicon alloy with very low RE content and without Sb addition showed chunky graphite, it was found that chunky graphite was replaced by some spiky graphite, i.e. the most usual degenerate graphite (see next chapter), when adding Sb. In the same line, attempts were carried out with tin addition which has also been reported to decrease chunky graphite occurrence in low silicon cast irons. Trials on high silicon cast iron with addition of 250, 500 and 1000 ppm of Sn showed chunky graphite disappeared at 500 and 1000 ppm, being replaced by some spiky graphite, but that both spiky and chunky graphite could be observed at 250 ppm, see Fig. 7.11-b [SER21].

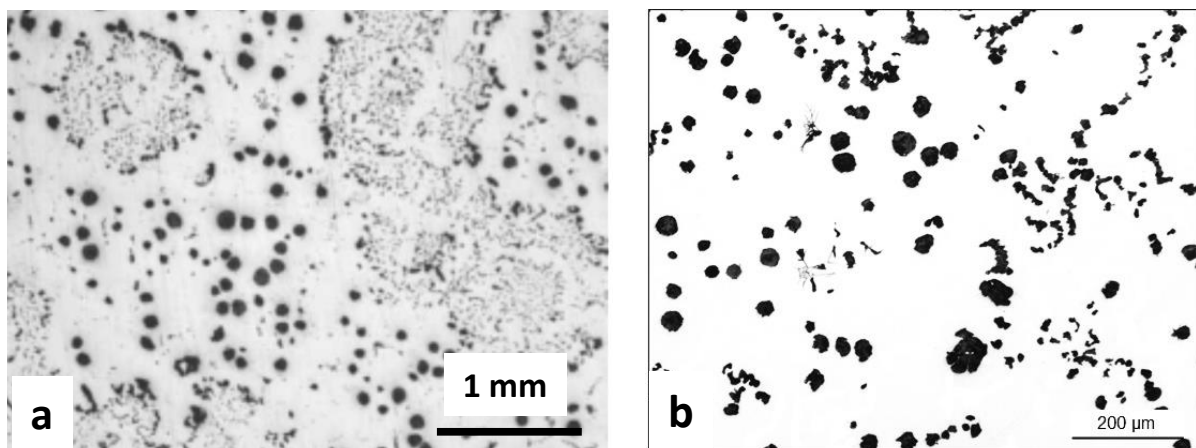


**Figure 7.11. Microstructure of: (a) a low-Si SGI cast in a Y4 keel-block [TOR16]; (b) a high-Si SGI with 250 ppm Sn and no RE cast in an isolating mould. Chunky cells in (a), spiky and chunky graphite in (b).**

A mechanistic model to describe the growth of chunky graphite has been proposed which would benefit from further development. Let us consider a melt that has been modified so that

the overall (or apparent) growth direction of graphite is the  $c$  direction. Though it is accepted that cells of chunky graphite do grow in some coupled way, details of the liquid/eutectic interface and growth mechanism are unknown. A simplified schematic of the interface is anyway proposed in Fig. 7.12 where basal planes of graphite are now in contact with the liquid but where steps and intermediate facets develop on the edges of graphite. According to the orientation change in  $\gamma^{L/gra}$  proposed in Fig. 5.3-b for spheroidized alloys, the anisotropy effect at the triple junction may be very low and could be neglected (see [TOR16] for more details). With the value of  $\gamma^{gra/L}$  at 1.5–1.7 J·m<sup>-2</sup>,  $\gamma^{L/gra}$  of the order of 0.9–1 J·m<sup>-2</sup> and  $\gamma^{L/\gamma}$  much lower at about 0.2–0.3 J·m<sup>-2</sup>, it is seen in Fig. 7.12 that the balance of forces is not satisfied, with  $|S| < |\gamma^{L/gra}|$ . In such conditions, chunky graphite would not be expected to grow. However, a slight over treatment of the melt with Mg and/or Ce, or the accumulation at the graphite–liquid interface of other "active" elements, may easily decrease  $\gamma^{L/G}$  below a critical value of about 1.3 J·m<sup>-2</sup> where the balance of forces could be achieved and chunky graphite could grow.

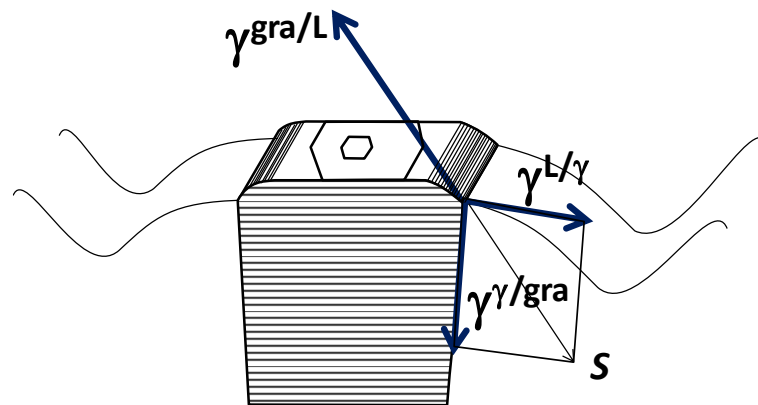


**Figure 7.12. Schematic of coupled growth of graphite when graphite grows along the basal direction with positive curvature of austenite at the triple junction. The forces acting at the triple junction are shown in bold lines.  $S$  is the resultant of the forces involving austenite and opposes the liquid/graphite interface tension.**

It has been suggested that spheroidal growth may well result from the fact that the above equilibrium is not satisfied [TOR16]. Then the delicate question of the conditions leading to the formation of austenite shells reappears.

### 7.5 Compacted graphite

CGI have better mechanical properties than LGI and are cast as slightly hypereutectic alloys so as to minimize solidification shrinkage. Compacted graphite (CG) may be obtained by various processes [NEC82] amongst which a partial spheroidizing treatment that is most often carried out with magnesium. It has been reported that graphite starts growing as spheroids that evolve in compacted shape during the eutectic reaction. As mentioned in Chapter 5, this primary step has been demonstrated by Sun and Loper [SUN83a] who observed floatation of only spheroids when casting highly hypereutectic CGI.

Fig. 7.13 shows a photograph of a 3D reconstruction of the graphite of a compacted graphite cell. At first sight, it appears much as a cell of interconnected graphite flakes. However, it is seen that there are round or hemispherical bumps both on the lateral surfaces of the flakes and at the extremities, which show that some free magnesium was still present in the melt after

the compaction treatment. As suggested by Stefanescu et al. [STE16], it is quite possible that the bumps at the outer cell boundaries grow by diffusion of carbon through austenite after graphite tips lost contact with the liquid. Similarly, growth of the bumps seen on the lateral faces of the flakes could possibly proceed by solid-state diffusion of carbon behind the solidification front of the CG cells. Based on X-ray tomography observations of samples quenched at different stages of solidification, Shi et al. [SHI20] concluded that neighbouring CG cells could merge to eventually appear as millimetre size cells. Such a merging had been reported by Pan et al. [PAN82] a long time ago but was overtaken for quite a while.



**Figure 7.13. Photograph of a 3D printing of graphite in a compacted graphite eutectic cell. The model was built from a tomographic study [CHU15].**

Fig. 7.14 compares the microstructure of lamellar and compacted graphite alloys which have been solidified in the same conditions, namely a standard thermal cup. It is seen that compacted graphite is much coarser than lamellar graphite while having the same kind of 3D structure, i.e. cells with interconnected flakes of graphite having grown in the prismatic directions. This suggests that the difference in coarseness stems in the capability of branching of graphite which appears to be very much limited in the case of compacted graphite [LAC18, LAC19]. As a matter of fact, addition of low amounts of magnesium to the melts first decreases the activity of oxygen and sulphur, and can thus lead to coarser flakes according to Fig. 6.10.

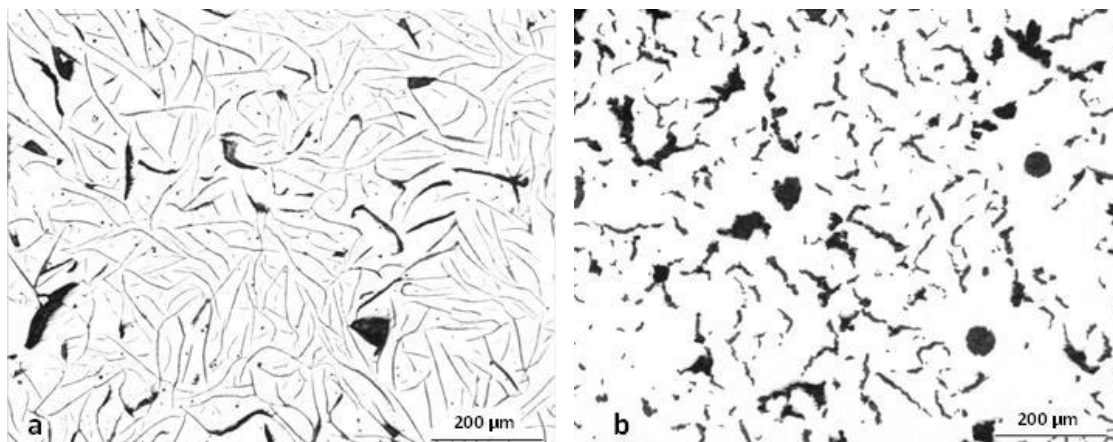


**Figure 7.14. Comparison of lamellar (a) and compacted (b) graphite in alloys solidified in a TA cup.**



Considering the similarity in the topology of CG and LG cells, the decrease in the branching capability of compacted graphite may be expressed by setting  $\varphi$  in the growth law, Eq. (6.5), at a much higher value than that for lamellar graphite eutectic. Fig. 7.15 shows that this corresponds to much higher undercooling, at given growth rate, than for lamellar graphite. Indeed, modelling of solidification of CGI in TA cups setting  $\varphi$  at the maximum possible value of 10 allowed recovering the values of the maximum undercooling and of the recalescence [LAC21b].

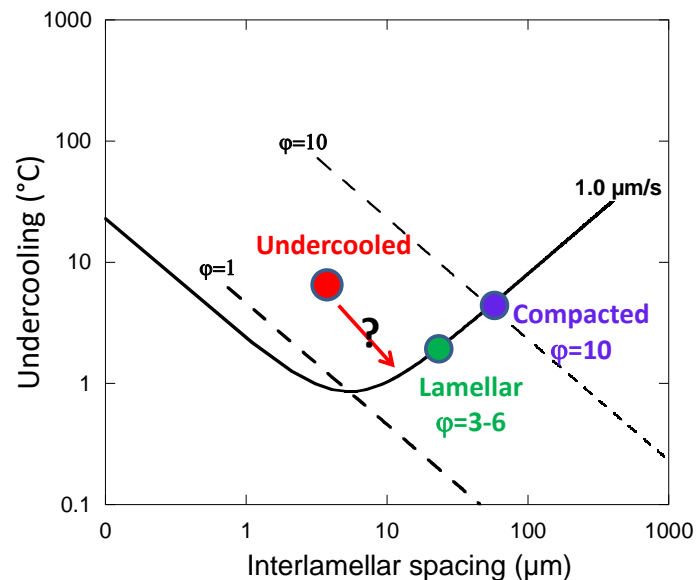


**Figure 7.15. Positioning of lamellar and compacted graphite in the  $\Delta T(\lambda)$  graph. The possible location of undercooled graphite on the basis of branching is indicated. The theoretical relation has been drawn based on Eq. (6.7) with  $a=2.3 \mu\text{m}\cdot\text{K}$  and  $b=0.080 \text{K}\cdot\text{s}\cdot\mu\text{m}^{-2}$ .**

This relation between branching capability and undercooling illustrated for LG and CG in Fig. 7.15 suggests to consider again undercooled graphite. It has been stated above that the change between flake and undercooled graphite consists in increased branching of the latter with respect to the former. However, it is also admitted that the coupling of graphite and austenite is much tighter in undercooled graphite, meaning that it should be better described with a  $\varphi$  parameter lower than that used for flake graphite. If this were so, Fig. 7.15 shows that the undercooling of the eutectic with undercooled graphite should then be lower than that of flake graphite eutectic when this is the opposite that is experimentally reported. One possible explanation is that the temperature of the growth front is decreased by rejection of S and O ahead of the eutectic growth front. In this case and at given sample temperature, the reference eutectic temperature and undercooling are expected to both decrease. The positioning of undercooled graphite in Fig. 7.15 would then be the correct one.

Finally, there is a further feature to stress about CGI which is that inoculation changes compacted graphite to spheroidal graphite. A similar transition is obtained by increasing cooling rate and this is certainly related to the fact that this increases the number of graphite precipitates. If this shape change could be seen as a transition related to the size, then it could be considered as similar to the transition from spheroidal to exploded graphite. The difference

is that protuberances grow along the **a** direction in CGI due to the low Mg content while they grow along the **c** direction in exploded graphite.

### 7.6 More about spheroidization

Even though it is agreed that Mg and other spheroidizers tight oxygen and sulphur, they should also adsorb at the surface of graphite. However, their actual role to trigger the formation of spheroids has not yet been explicitly revealed. This section presents images of degenerate forms of spheroidal graphite that may give some hints for future research. The primary graphite precipitates illustrated in Fig. 7.16 were observed in the floatation zone of small samples of an industrial cast iron contained in a pure carbon crucible, which were remelted and then cooled at 20°C/min from 1350°C. It is seen in Fig. 7.16-a that most of the graphite precipitates are spheroidal while part of them appear as the "doughnut" (or "croissant") precipitates reported by Sadocha and Gruzleski [SAD75, GRU75]. In the work of Sadocha and Gruzleski, the use of polarized light evidenced that the precipitates consisted of successive blocks with the stacking of the graphite in each block as perfect as in spheroids. Accordingly, well-defined boundaries were evidenced between two successive blocks that have been smoothed by etching in the enlargement in Fig. 7.16-b. The overall curving of these precipitates is due to tilting between successive growth blocks, and it is noteworthy that tilting is always in the same direction for a given precipitate, clockwise or counter clockwise. This is in contrast with the turnings of primary graphite lamellae exemplified in Fig. 5.10-a that were observed in both directions. This observation has certainly to do with the spheroidization mechanism.

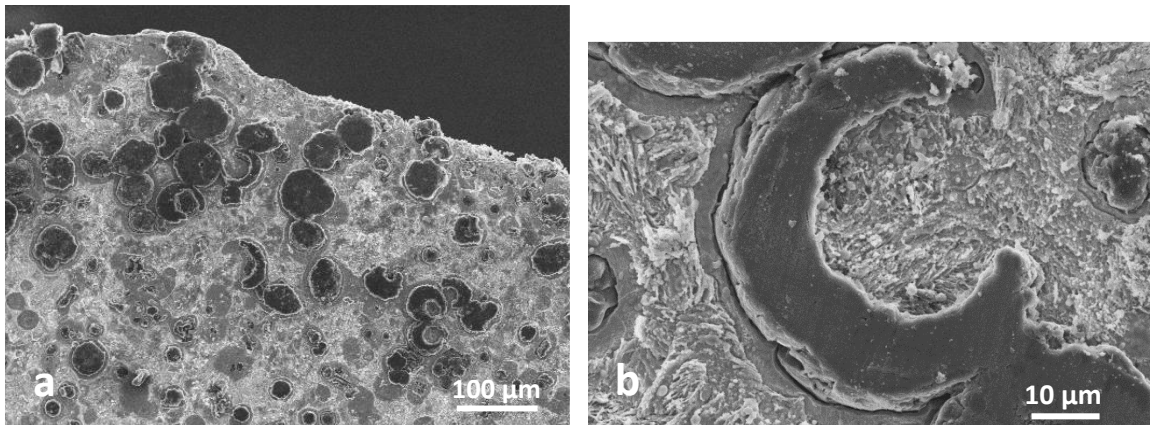


**Figure 7.16. SEM micrographs of primary graphite precipitates in the floatation zone of a sample cooled from 1350°C at 20°C/min (R. Ghergu, unpublished).**

Amongst the many attempts to use Auger analysis for studying distribution of elements in cast irons, the most deceptive results are certainly that magnesium could not be detected either within graphite or at the surface of graphite spheroids [JOH74], leading Johnson et al. [JOH75] to conclude that adsorption of spheroidizer is not necessary for modifying graphite shape. However, this could mean as well that the spatial distribution of Mg was such that it could not be detected with Auger. As a matter of fact, the detection limit of Auger is of the order of a couple of percent while much lower values may be reached with electron microprobe. With appropriate analysis conditions for microprobe analysis, Bourdie et al. [BOU18] could effectively detect Mg within graphite and at the graphite-matrix interface of some spheroids

and discuss other similar results. In fact, low level of Mg at the interface was detected after heat-treatment of the casting [DIE96, BOU18] while it was not in the as-cast state, suggesting absorption of Mg during growth and later expulsion as graphite crystallinity increases. In the case of slowly cooled casting, Mg could be detected within graphite and sometimes accumulated at the graphite/matrix interface using EDS in a SEM on FIB thinned lamellae [DOM21]. Using both atom probe and EDS in a TEM, Qing et al. showed the presence of many foreign elements in graphite amongst which Mg and Ce [QIN20]. These results are in line with earlier works by Franklin [FRA79] and Fidos [FID82] who demonstrated that graphite in cast irons does contain foreign elements in amounts that are much larger for spheroidal graphite than for lamellar graphite. This shows that elements which are not surface active can anyway be absorbed in graphite after having been adsorbed at its surface.

### **7.7 Summary**

It appears to be accepted that spheroidal graphite begins to grow directly from the liquid before being encapsulated by the austenite, although no theoretical approach has yet attempted to quantify the critical diameter that spheroids can reach by free growth. Once the spheroids are encapsulated, it has been shown that the kinetics of the eutectic reaction is controlled by the diffusion of carbon through the austenite shell. However, the spheroidal shape can degenerate due to the inhomogeneous distribution of diffusion distances, particularly in the case of slowly cooled castings which result in large spheroids. In contrast, more pronounced shape irregularities, such as exploded graphite, are associated with primary precipitation and are not attenuated during the eutectic transformation. Other degenerate forms of spheroidal graphite have been described, namely exploded graphite and chunky graphite that are associated with over spheroidizing treatment and compacted graphite that is intentionally obtained with under spheroidizing treatment.

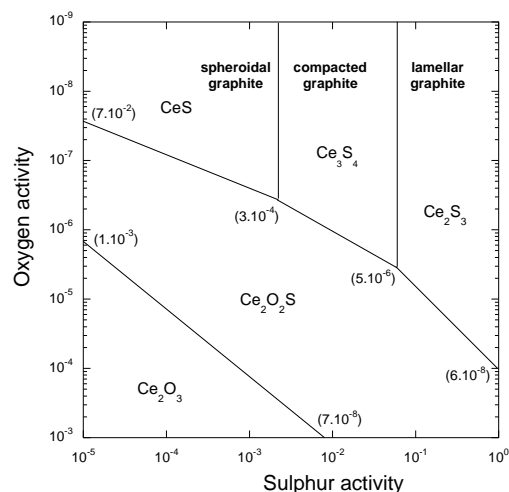
# Chapter 8 – Trace elements: graphite growth and degeneracy

This chapter is devoted to the effect of low-level and trace elements on the transition from lamellar to spheroidal growth of graphite, and vice versa. For this, the relation between oxygen, sulphur and spheroidizers is outlined in section 8.1. Section 8.2 deals quickly with the spheroidizing treatment and emphasizes that over-treatment leads to spheroidal graphite degeneracy. A more general view of graphite degeneracy associated with the presence of trace elements is presented in section 8.3. Efforts for understanding growth and shape change of graphite are presented in section 8.4 that includes both atomistic calculations and analysis of sessile drop experiments. Finally, section 8.5 attempts to rationalise the information obtained on the surface energy, the work of adhesion between graphite and liquid melt, and the interfacial segregation of specific elements, in order to establish a possible mechanism for spheroidal growth.

## 8.1 Oxygen, sulphur and spheroidization

Spheroidizing of graphite is achieved by adding elements to the left of the periodic table such as Ca, Ce and Mg. Systematic studies have been carried out to find other spheroidizers [LYU63] but it is accepted that Mg is more efficient than Ce, which is itself far better than any other elements. It is sometimes stated that the only role of the spheroidizers is to decrease the content in oxygen and sulphur of the melt, and Fig. 8.1 shows that there is a well-established relation between the thermodynamic activity of these elements and the shape of graphite [SUB82]. Note that the calculations were performed with data for 1500°C – i.e. the temperature for melt treatment - and that the activity scale of oxygen is reversed. The graph was drawn considering cerium and the authors patented a method for obtaining compacted graphite using this element. A similar graph could have been devised for magnesium and for calcium. Furthermore, the use of modern thermodynamic software packages allows making more complete predictions, and in particular looking at the simultaneous effect of various additives, e.g. Ca, Ce and Mg [LEK06].

**Figure 8.1. Graphite morphology control diagram established at 1500°C (adapted from [SUB82]). The axes give the activity of S and O that together control graphite shape. Note that the activity of oxygen along the Y axis increases downward. The numbers between brackets give the residual Ce activity. The stable compounds of Ce, O and S are indicated.**



Attempts have been made to relate knowledge about crystal growth and observations of graphite shape in cast irons [MIN83]. It has thus been stated [SUB80] and often accepted that: "...the role of spheroidizing elements is to control the residual concentration of surface active elements in the melt. These elements, such as sulphur and oxygen, are adsorbed on the graphite prism face, promoting a transition from an atomically smooth (faceted) interface of low mobility, to an atomically rough interface of high mobility. The growth of the rough prism face can then compete favourably with that of austenite." These statements call for the following remarks:

- It is certain that adding elements such as Ca, Ce and Mg to an iron melt does decrease the free content of oxygen and sulphur in the melt, see Fig. 8.1.
- However, most of foreign elements are surface active on a pure melt as shown in Fig. 8.2 for iron. Moreover, the relation which is often implicitly assumed between the liquid-vapour surface tension of a melt and the liquid-solid interface energy between this melt and a crystalline phase (here graphite) is not straightforward, see later in this chapter.

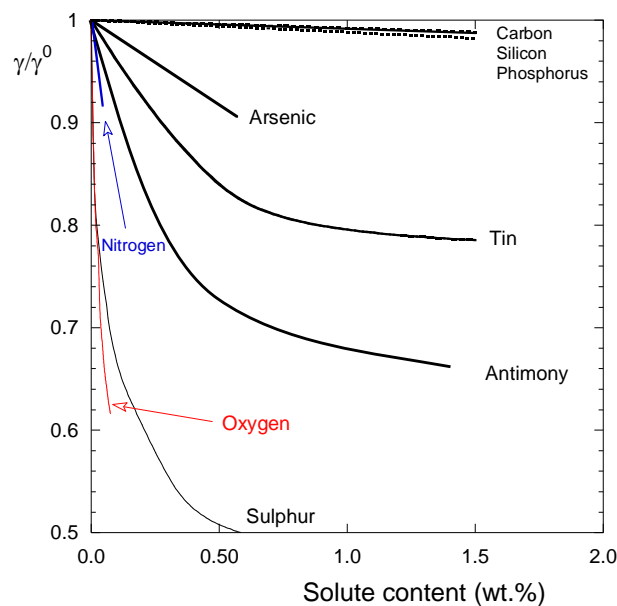


**Figure 8.2. Effect of various dissolved elements on the liquid-vapour surface tension of iron melt,  $\sigma$ , referred to its value  $\sigma^0$  for pure iron. Data from Kozakevitch and Urbain [KOZ61] at 1550°C.**

- If it may be safely stated that some oxygen and sulphur atoms do adsorb onto graphite, it does not seem straightforward to conclude that O and S both adsorb on the prismatic planes. Auger maps of fractured sample with lamellar graphite clearly showed sulphur covering the matrix facing the large faces of graphite with channels of oxygen crisscrossing the surface [PAR96]. It was easy to associate sulphur to the basal planes and oxygen to growth steps, i.e. prism planes, of the graphite lamellae. On the other hand, SIMS measurements along a transverse section of graphite lamellae evidenced regular maxima in sulphur, see Fig. 8.3 [FRA85a]. The authors related the location of

these maxima to the interface between growth blocks of the graphite lamellae, and could thus associate sulphur to the basal planes.

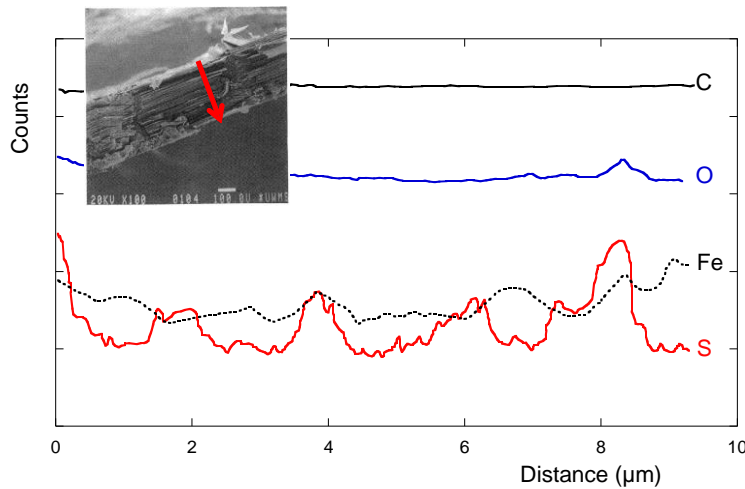


**Figure 8.3. SIMS distribution of C, O, Fe and S through the thickness of a graphite lamella. O is evenly distributed while S shows maxima that are regularly spaced. These distributions suggest that O adsorbed on the prismatic planes while S did on the basal planes. Adapted from Franklin and Stark [FRA84, FRA85a]**

The above statement by Subramanian et al. finally makes the link with crystal growth knowledge which considers that growth of rough interfaces is much more rapid than growth of faceted interfaces. Following these authors, adsorption of sulphur and oxygen is expected to roughen the graphite prismatic faces. Conversely, removing S and O with spheroidizers would hinder growth along the prismatic faces leaving the possibility for growth along the basal direction. This calls again for the following remarks:

- If such a roughening transition would exist, this should be easily seen when comparing the growth rate of primary graphite plates in melts with various S and O contents, but such experimental values do not seem to exist.
- Following the most accepted model at the time they published, Subramanian et al. considered that growth in the basal direction is defect controlled, i.e. by spiral growth around dislocations, and they explicitly excluded growth by a 2D nucleation mechanism that has been considered in Chapter 5. It is quite surprising that no attempt to put numbers on spiral growth of graphite in cast irons can be found in the literature.

This section recalled the role of the spheroidizing treatment in reducing the oxygen and sulphur contents of the melts, but also highlighted the few experimental evidences available on the spatial distribution of oxygen and sulphur which contradict the often accepted view of lamellar growth and the transition to spheroidal growth. The remainder of this chapter analyses this transition by following the opposite path, i.e. by focusing on the degeneration of spheroidal graphite.

## 8.2 Magnesium treatment

Trojan and Flinn [TRO64] sought to determine the solubility of Mg in cast iron as a function of pressure, composition and temperature. They worked with an open crucible placed in an overpressure vessel, and observed a negligible effect of pressure at 1232°C (2250°F). On the other hand, an addition of 1% carbon increases the solubility of magnesium by 0.5%, whereas it takes 3% silicon to have the same effect; see Fig. 8.4. Note that due to the decrease in the solubility of carbon in the liquid with addition of silicon, the solubility of magnesium is actually

decreased in cast irons, though remaining at levels far above the amount needed to spheroidize graphite.

This work was completed a few years later by characterising the effect of silicon on the miscibility gap in the Fe-Mg system and the variation in Mg saturation pressure along this gap [GUI71]. It was found that the vapour pressure of magnesium decreases sharply with the silicon content on the iron-rich side. In this work, the saturation vapour pressure of pure magnesium was given by:

$$\log P_{\text{Mg}}(\text{atm})=4.928-6778/T_K \quad (8.1)$$

where  $T_K$  is the temperature in Kelvin.

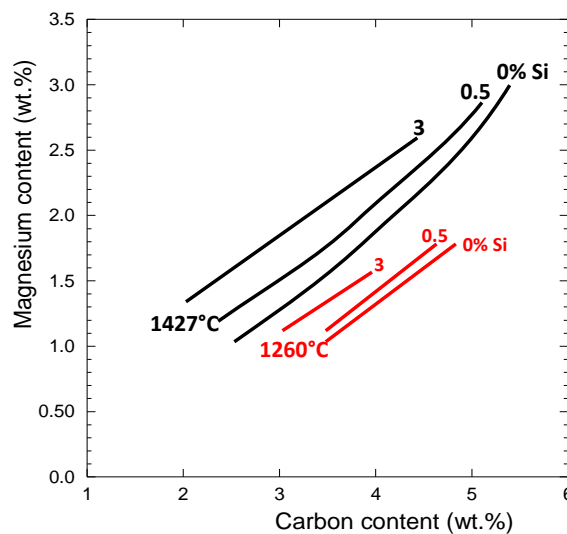


**Figure 8.4. Solubility of magnesium as a function of carbon content in a liquid Fe-C-Si alloy at 0, 0.5 and 3 wt.% Si, for two temperatures: 1260°C and 1427°C. Data from [TRO64].**

It may be worth mentioning also the work of Speer and Parlee [SPE72] who studied the dissolution of Mg and the desulphurisation of the melt at sub-atmospheric partial pressures. At 1260°C (2300°F), they showed a minimum of 5 ppm dissolved S at a Mg content of 0.23% in a carbon-saturated Fe-C liquid.

In Fig. 8.5 is shown the evolution of nodularity with addition of either Mg or Ce to Fe-C-Si melt cast in bars with various sizes [BAS73]. Cerium is seen not to be a perfect spheroidizer and shows a limited optimum range around 0.06 wt.% at which the maximum nodularity is at most 80%. Magnesium appears to give much higher nodularity and is efficient on a larger domain, 0.04-0.08 wt.%.

Beyond this limit of 0.08 wt.%, magnesium has been reported to lead to degeneracy as illustrated with the micrograph in Fig. 8.5. It is noticeable that graphite degenerates with the formation of spiky and crab-like graphite further detailed in a later section of this chapter. Such protuberances grow along the prismatic direction as lamellar graphite does, and not along the basal direction as chunky graphite. However, Lux [LUX70a] has reported that exploded graphite (see Chapter 7) can appear because of magnesium or cerium over-treatment. This could be an indication that spheroidal graphite degeneracy associated with over-treatment differs depending on the solidification stage, with primary graphite precipitation leading to

exploded spheroids while spiky graphite and other overgrowths are associated with the eutectic reaction. Further study in this area would be greatly helpful for a better understanding of the spheroidization mechanism.

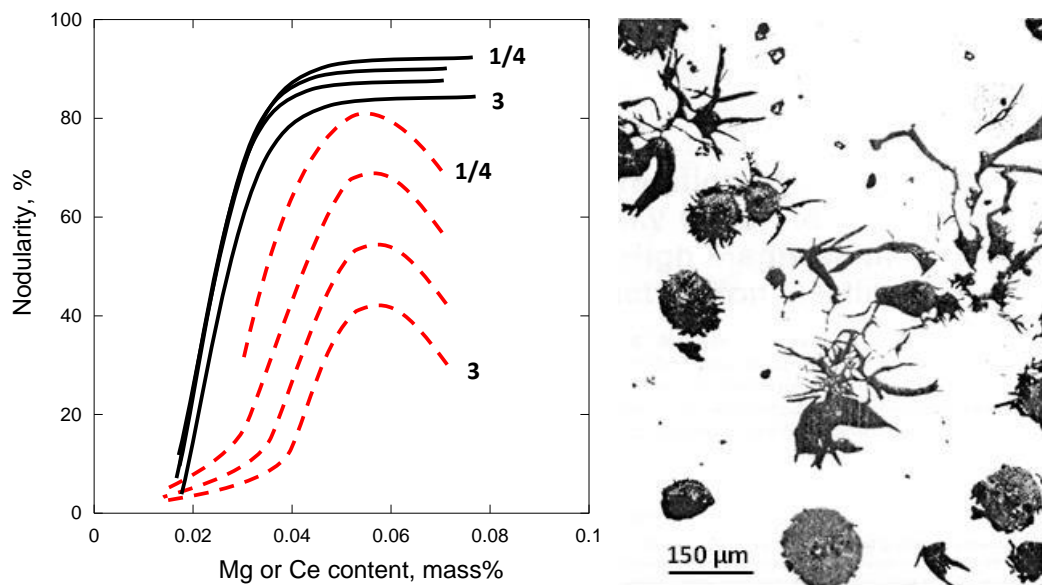


**Figure 8.5. Effect of addition of either Mg (solid lines) or Ce (dashed lines) on the graphite nodularity in a Fe-C-Si alloy cast in bars of different diameters (0.25, 0.5, 1 and 3 inches), adapted from White et al. [WHI83]. Micrograph illustrating graphite degeneracy due to Mg over-treatment [BAS73].**

### 8.3 Spheroidal graphite degeneracies with change in graphite growth direction

Since the Millis et al. patent [MIL49], RE are known to counteract the deleterious effect of low-level elements on spheroidizing with magnesium. These so-called impurities or trace elements may be everything else than Fe, C and Si and spheroidizers, they can be impurities from the minerals used for pig iron manufacturing or trace elements coming from steel or cast iron returns. A long time ago, Thielemann [THI70] proposed an index  $S_b$  quantifying the appropriateness of a charge to give spheroidal graphite according to the deleterious elements considered at that time:

$$S_b = 1.6 \cdot w_{Al} + 2.0 \cdot w_{As} + 370 \cdot w_{Bi} + 290 \cdot w_{Pb} + 5.0 \cdot w_{Sb} + 2.3 \cdot w_{Sn} + 4.4 \cdot w_{Ti} \quad (8.2)$$

where  $w_i$  is the content in element  $i$  (wt.%).

If  $S_b$  is lower than 1 no action is required while RE should be added if it is higher than 1. What is interesting in this index is that it shows that heavy elements such as Bi and Pb are far more deleterious than others. Plotting the critical level of various elements for graphite degeneracy in nodular irons [LAC17b] versus the corresponding atomic mass shows a clear correlation that confirms this trend: the heavier are the atoms the lower is their critical level, see Fig. 8.6. As the atomic weight relates to the size of the atoms and to the number of their outer electrons, such a relationship - which has been suggested long ago as mentioned by Lux [LUX70a] - can be easily associated with an increased possibility for these elements to adsorb at the graphite surface.



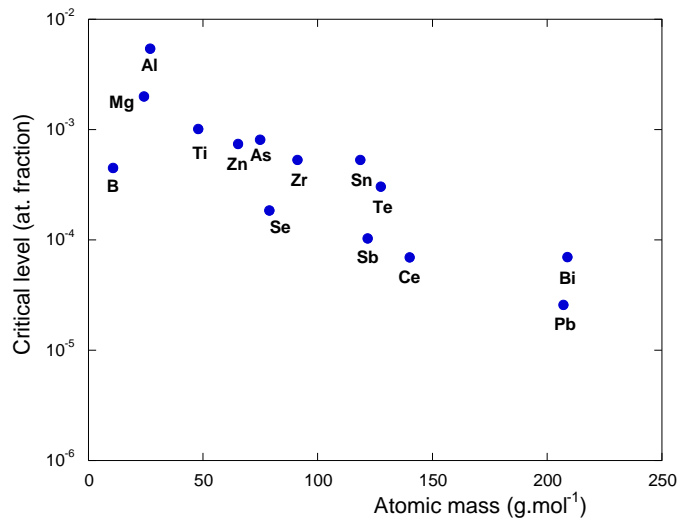


**Figure 8.6. Relation between atomic mass of elements poisoning nodular irons and their reported maximal acceptable levels. Adapted from [LAC17b].**

To get further insight in the effect of these trace elements, studies where no RE was used were selected [LAC19]. It was found that all of the deleterious elements for which information was available lead to graphite degenerating in the same way, namely first giving protuberances named spiky graphite, that may or not develop in crab-like and eventually in mesh graphite, see Fig. 8.7. It has been confirmed by ACOM that these protuberances do develop along the prismatic *a* crystallographic direction of graphite [DOM21]. An important peculiarity of these protuberances is that they start from the spheroids and eventually extend to the last to solidify zones where they sometimes falsely appear disconnected from the first graphite precipitates [TON18].

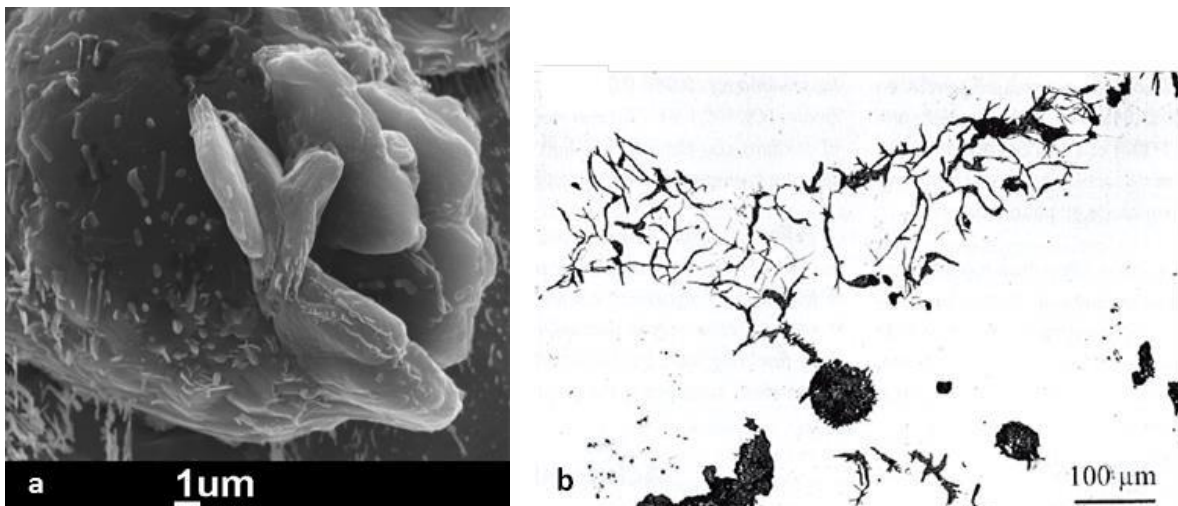


**Figure 8.7. a: Spiky graphite due to Pb (courtesy of B. Tonn). b: mesh graphite due to Ti [HEC00]. Crab-like graphite is illustrated with the micrograph in Fig. 8.5.**

At about the same time as Thielemann designed his  $S_b$  index, Herfurth found that adding together impurities with Ti showed a more pronounced effect than being simply additive

[HER66], see Fig. 8.8. The more recent review by Javid and Loper [JAV95] shows that we lack enough quantitative data to really characterize these interactions. However, we do have a semi-quantitative way for understanding these effects by considering the schematic proposed in the preceding chapter for growth of spheroidal graphite, namely that spheroidizing is achieved by Mg atoms adsorbing on the prismatic faces. This attempt is related to atomistic calculations that are presented in the next section.

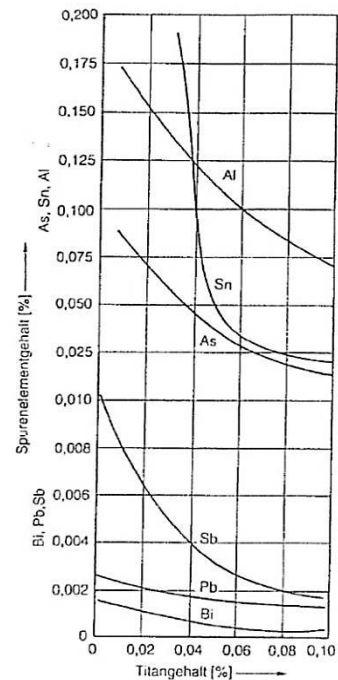


**Figure 8.8. Effect of Ti content on the critical level of Bi, Pb and Sb (lower scale) and Al, Sn and As (upper scale) [HER66].**

#### 8.4 Adsorption energy as calculated by density-functional theory (DFT)

Calculations allowed comparing the adsorption energy of various elements (Al, C, Ca, Fe, Mg, O, S, Sb, Sn, Te, Ti) on the basal and prismatic planes of graphite. Both arm-chair and zig-zag configurations (see Fig. 5.5) were considered for the prismatic planes [LAC19]. Table 8.1 shows that: 1) all elements can adsorb on the basal planes except Sb; 2) that the energy of adsorption is larger on the arm-chair sites than on the basal planes, and even higher on the zig-zag sites. Focusing on the most favoured zig-zag sites and excluding the main elements C and Fe (that are the main constituent of graphite and of the liquid, respectively) the data for the zig-zag sites gives the following sorting for adsorption energy:

$$O > Ti > S > Sn > Al > Te > Ca > Sb > Mg$$

Thus, magnesium has the lowest adsorption energy which means that any of these foreign elements could easily replace magnesium on the prismatic planes, or at least compete successively with it for adsorption. The spheroidizing effect of Mg would thus be strongly altered. Note that Ti has the highest adsorption energy after oxygen, with a value which is much higher than that for the other deleterious elements. This may well explain that the curves in Fig. 8.8 are not linear, i.e. not reflecting a simple additive rule. It would be of interest to investigate at which level of adsorption a type of sites gets saturated and to analyse interactions between adsorbed elements.

element	basal	Arm-chair	Zig-zag
C	-1.46	-6.30	-10.86
Al	-1.26	-3.64	-9.58
Ca	-1.11	-3.27	-9.20
O	-2.07	-5.37	-11.48
Fe	-1.25	-3.54	-8.74
Mg	-0.29	-2.05	-7.96
S	-0.77	-5.22	-10.06
Sb	0.46	-3.69	-9.10
Sn	-0.64	-3.96	-9.64
Te	-0.29	-3.97	-9.28
Ti	-2.11	-4.82	-11.17

**Table 8.1. Results of DFT calculations of adsorption energy  $E_{ad}$  (eV) for basal and prismatic (arm-chair and zig-zag positions) sites [LAC19].**

It should be noted, however, that the environment for DFT calculations is vacuum, which corresponds to a graphite-vapour surface that may not correctly represent the interface between graphite and iron melt. As an example, S and Te are located in the middle of the above sorting but are found preferentially associated with basal planes and not prismatic ones [PAR96, VER89]. An interesting feature was observed when plotting the difference in electronegativity,  $\Delta E_N$ , between carbon and the elements listed in Table 8.1, see Fig. 8.9. The three elements that have the lowest  $|\Delta E_N|$  value are S, Sb and Te. The fact that they do not form polar bonds with carbon could possibly mean that their preferential adsorption is associated with the liquid phase or the iron-rich matrix. In that respect, dynamic molecular calculations would be of great interest but considering interfacial segregation as in the next section may also provide some hints.

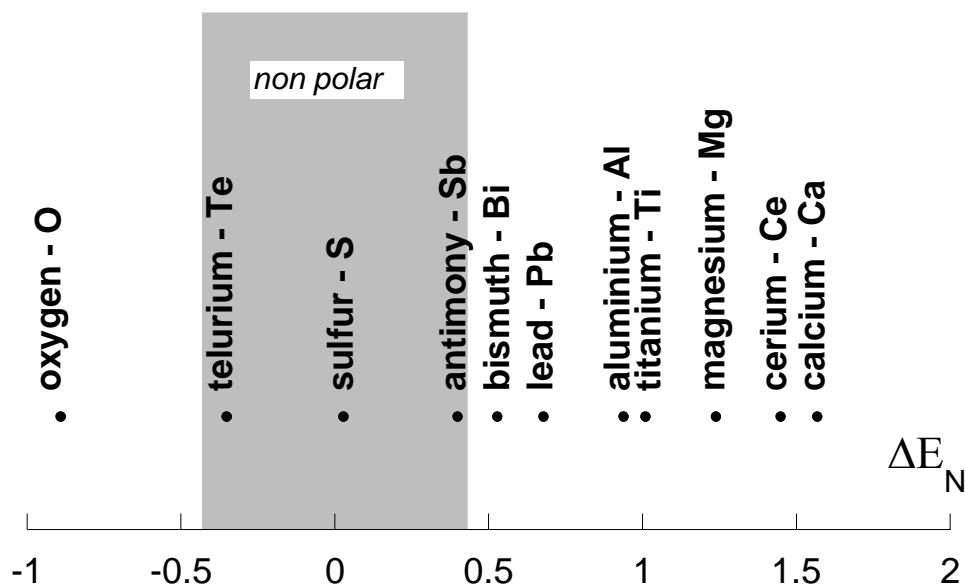


**Figure 8.9. Difference in electronegativity between carbon and elements having an effect on graphite growth in cast irons. Adapted from [LAC19].**

### 8.5 Adhesion work at the graphite/melt interface [LAC22a]

In many of the liquid-vapour surface energy measurements (called surface tension in the following) using the sessile drop technique with cast iron melts, the substrate was graphite for evaluating at the same time the properties of the graphite/liquid interface. It is known that carbon-saturated iron melts do not wet graphite, i.e., the contact angle  $\theta$  (see Fig. 5.3-a) is higher than  $90^\circ$ . In that case, Young's equation applies at the triple junction:

$$\sigma^{L/V} \cdot \cos \theta = \sigma^{Gra/V} - \sigma^{Gra/L} \quad (8.3)$$

where  $\sigma^{Gra/L}$  and  $\sigma^{Gra/V}$  are the interface energy between graphite and liquid and the surface energy of graphite, respectively.

$\sigma^{L/V}$  can be evaluated from the shape of the upper part of a drop deformed by its own mass along Laplace's equation, while  $\theta$  is measured on appropriately projected images. Thus, if  $\sigma^{Gra/V}$  is known,  $\sigma^{Gra/L}$  could be calculated using Eq. (8.3) and the effect of elements added to the melt evaluated. However,  $\sigma^{Gra/V}$  is badly known and can be affected by the elements added to the melt as already indicated long ago by Kevejian and Taylor [KEV57] in a study dedicated to cast iron. As a matter of fact, Jung et al. [JUN08] carried out experiments with partial dissolution of the graphite substrate which allowed determining the three interfacial energies. They could evidence that sulphur added to the cast iron melt certainly adsorbs at the free graphite surface and therefore affects its surface energy. To investigate the graphite/melt interface, it was thus considered more appropriate to study the adhesion work defined as:

$$W_a = \sigma^{L/V} \cdot (1 + \cos \theta) \quad (8.4)$$

The work of adhesion is directly proportional to the strength of bonds established at the graphite/liquid interface and it could therefore also be used in order to investigate interfacial phenomena such as the influence of additives on graphite/melt interfacial segregation.

Mil'man et al. [MIL76] made an extensive work using the sessile drop technique on graphite substrate to measure the surface tension and the contact angle. The experiments were carried out at  $1300^\circ\text{C}$  with either prismatic or basal planes facing the melt. A large number of alloys were investigated, amongst which two untreated melts with very different S content (0.004 and 0.019 wt.%) as well as one Mg- and one Ce-bearing alloy. The authors observed either flake graphite or spheroidal graphite in the solidified drops and reported surface tension that was higher in the case of spheroidal graphite than for lamellar graphite in agreement with other reports. As a few other authors, Mil'man et al. made also addition of "anti-spheroidizing" elements such as Bi, Sb or Sn together or not with Ce to Mg-treated melts. Aluminum was also added to an un-treated melt and gave a higher surface tension while graphite remained lamellar.

The results of Mil'man et al. are shown in Fig. 8.10 where the values of  $W_a$  have been plotted versus the corresponding surface tension values of the liquid. In this graph, samples with lamellar graphite are represented with solid symbols and those with spheroidal graphite with open symbols. It is seen that un-treated melts show high  $W_a$  value while melts containing Mg all show a low  $W_a$  value, whatever is the graphite shape. Amongst these latter, those presenting lamellar graphite (within the ellipse) relate to relatively low surface tension while those with nodular graphite (open symbols) show high surface tension. In the figure is also

illustrated the effect of adding aluminum which increases the surface tension without changing the lamellar graphite shape. This figure clearly illustrates that the surface tension alone does not determine graphite shape, while the simultaneous knowledge of two interfacial parameters such as surface tension and work of adhesion allows predicting the graphite shape.

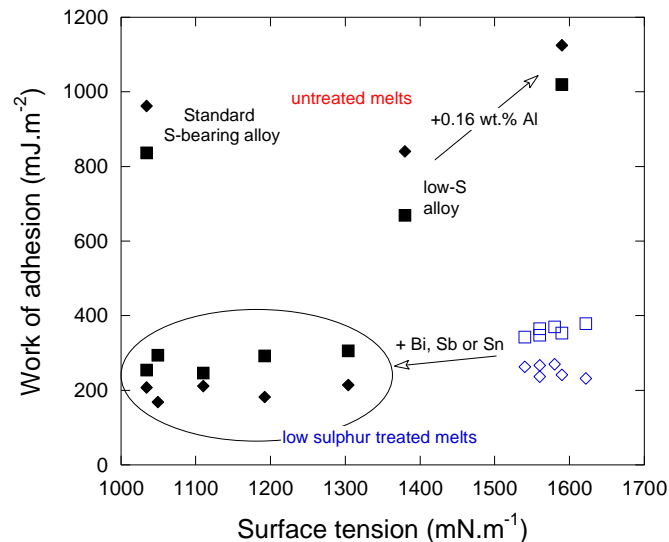


**Figure 8.10. Work of adhesion as function of surface tension. Results picked up from the table 2 in Mil'man et al. [MIL76]. Open symbols are for spheroidal graphite and solid symbols for lamellar graphite; squares are results on basal planes and diamonds on prism planes.**

The work of adhesion can also interestingly be compared with the cohesion of the iron melt that is equal to twice the  $\sigma_{LV}$  value. The work of adhesion thus represents about 10% of the cohesion of the melt for low sulfur activity spheroidized alloys but the ratio dramatically increases up to about 40% with sulfur activity giving a clear evidence of the increase of bond strength established between graphite and the melt. In summary, removing sulphur from the melt by adding Mg or Ce increases the surface tension but also decreases  $W_a$ , suggesting that the bonds between liquid and graphite are significantly weakened.

Adding surface-active elements such as Bi, Sb and Sn, after the spheroidizing treatment leads to a decrease by a factor of about 1.4 of the surface tension. If there were no effect on the other interfacial energies, one should expect a sharp increase of the contact angle in this case of non-wetting conditions. Such an increase has not been reported, which means that the decrease of the liquid-vapour surface tension is counter-balanced by a concomitant effect on the graphite/liquid interfacial energy,  $\sigma^{Gra/L}$ , and/or the surface energy of graphite,  $\sigma^{Gra/V}$ . At the time of Mil'man et al.'s work, segregation of Sb (or other metallic elements) at the graphite/matrix interface was ruled out, which may have distorted their conclusions. Interfacial segregation and its consequences on graphite shape are detailed in the following sections.

## 8.6 Interfacial segregation

One of the appropriate means to study interfacial segregation is certainly Auger analysis that is used in spot and mapping modes. Johnson and Smartt [JOH75] evidenced the presence of both oxygen and sulphur at the surface of a graphite flake in a cast iron containing 0.04 wt.%

S. From their Auger spectrum which shows also intense Fe peaks and little carbon, this segregation should have been on the matrix side. An important insight was gained by Franklin and Stark [FRA84, FRA85a] as described in section 8.1 (see Fig. 8.3). These findings have been confirmed by Park and Verhoeven [PAR96] who investigated the distribution of oxygen and sulphur in flake and undercooled graphite of high purity and sulphur doped (0.02 wt.% S added) Fe-3.4C-2Si alloy (wt.%). When the sulphur content of the iron was high enough for the sulphur to saturate the graphite matrix interface, oxygen segregation was limited to the prism planes of graphite at the growth ledges. If the sulphur content was decreased as in their high purity alloy, S and O were found lying in large adjacent patches along the graphite flakes, again on the matrix side.

For melt control before casting, thermal analysis with Te-bearing cups are often used which lead to solidification in the metastable system. For investigating the action of Te, Verhoeven et al. [VER89] carried out directional solidification experiments with quenching, changing the growth rate so as to shift from the stable to the metastable solidification. Auger analysis of samples with undercooled graphite, i.e., solidified at a growth rate just below the transition, showed the presence of a one atom layer of Te at the graphite-matrix interface, on the matrix side. This demonstrates that the effect of Te on impeding graphite growth is through segregation at the graphite-liquid interface.

In spheroidal graphite cast irons, Sb enrichment has been observed with Auger analysis by several authors, see [LAC22a] for a review. Dekker et al. [DEK20] clearly showed that Sb is on the matrix side and not the graphite side of the interface, and that a small amount of sulphur was also seen in agreement with other reports. The total thickness of the surface layer was estimated to be of the order of 1 nm, though in some locations the Sb signal was weaker indicating the coverage may not have been homogeneous. This layer appeared anyway enough to limit spheroidal graphite growth during solidification [DEK20] and to promote metastable eutectoid transformation of the matrix to pearlite [LIU90b], that is to say it hinders the transfer of carbon to graphite precipitates which would be necessary for the stable eutectoid transformation. Further study using atom probe resolution TEM showed that Sb segregates along both graphite protuberances and spheroids [LAC22b].

In summary, all four elements O, S, Sb and Te that are known to be strongly surface active in cast irons have been effectively found to also segregate on the matrix side of the graphite/matrix interface. However, oxygen is found facing prismatic sites of graphite while the other three are rather associated with basal sites. It is quite possible that this difference has to do with the capability of oxygen to form polar bonds with carbon while the other elements cannot, as shown by Fig. 8.9. Similar information on Bi and Sn is still missing.

### **8.7 Shape of primary graphite**

It has been seen that the spheroidizing treatment of cast iron melts increases their surface tension, and this is due to the decrease of free sulphur and oxygen in the melt. This leads to the often used statement that spheroidal graphite will be obtained provided the melt has a high surface tension, compacted graphite when the surface tension is intermediate and lamellar graphite at low surface tension. However, it was concluded from Fig. 8.10 that surface tension alone does not control graphite shape and that two interfacial parameters are required. The

above statement has sometimes been extended in the literature to the graphite/liquid interface energy considering it scales with  $\sigma^{L/V}$  if the surface energy of graphite  $\sigma^{Gra/V}$  is constant, which we have seen is not ascertained. Moreover, interface energy dictates equilibrium shape of crystals, not the habit planes during their growth. In other words, one should not try to consider the change in the relative value of the interface energy between basal and prism planes to predict graphite shape.

The other school of thoughts to explain graphite shape considers the adsorption of elements at the graphite melt interface [JOH74]. Elements that are surface active are expected to segregate to the graphite/matrix interface, being the matrix either liquid or austenite. This parallel between surface and interface segregation stands on the relation established between surface tension and grain boundary segregation in steels and other alloys [SEA75] which has been theorized [GUT77, WYN06]. However, the graphite spheroidizers, Mg and Ce, are not active at the liquid-vapour surface and it has been seen that they do not show up as a film at the graphite/matrix interface. Together with the micro-analysis results mentioned in section 7.6, these latter observations sustain the hypothesis that Mg and Ce act as a spheroidizer by adsorption at discrete places at the surface of graphite and not accumulated as a film. Further, it has been seen that Mg behaves in fact as a few other elements, spheroidizer up to a certain level and leading to spheroidal graphite degeneracy beyond that level.

The present review on the segregation of surface active elements suggests a schematic for the control of graphite shape that is more subtle than the previous approach limited to DFT calculations (section 8.4). It has been seen that S segregates at the graphite/matrix interface and triggers a strong bonding between these phases. This leads to growth along the prismatic planes being strongly favored, giving lamellar graphite. If the free-S content, and thus its activity, in the melt is strongly decreased by adding spheroidizers, Mg and/or Ce, the bonds between graphite and matrix weakens. In that case, growth along the prismatic direction would be still favoured except if the spheroidizers adsorb on the prism planes and decrease their extension kinetics. In that case, growth along the basal direction can be preferred leading to spheroidal growth. However, "anti-spheroidizing" elements such as Sb annihilates the spheroidizing treatment and leads to degeneracy when added above a critical level. This suggests that above this critical level, Sb also segregates in locations facing the prismatic planes of graphite and repels the spheroidizing elements in the bulk of the melt.

## 8.8 Summary

Graphite shape in cast irons is determined by two interfacial parameters, e.g. the surface tension of the melt and the work of adhesion between graphite and melt, and not only one. Analysis of literature information shows also that surface active elements are prone to segregate at the graphite/melt and graphite/austenite interfaces. Amongst these elements, S, Sb and Te that are known to limit carbon transfer to graphite segregate in relation with the basal planes of graphite. In contrast, spheroidizing elements are not surface active and do not show any segregation or accumulation. Yet, accepting their spheroidizing effect is due to adsorption on prismatic planes of graphite allows rationalizing graphite spheroidization and spheroidal graphite degeneracy.

## Chapter 9 – Eutectoid transformations

Once solidification is completed, the as-cast matrix of silicon cast irons depends on the cooling schedule to room temperature, RT. For use in the as-cast state, the intended matrix should be either fully ferritic or fully pearlitic. This relates to the eutectoid transformation of the high-temperature austenite processing in the stable or metastable system, respectively. Mixed matrices are sometimes looked for, which are characterized by the so-called bull-eye microstructure in the case of SGI which is illustrated in Fig. 9.1. Such a microstructure has the great interest of showing the main principle of the eutectoid transformation, namely that, upon continuous cooling, ferrite nucleates at the graphite/austenite interface, encapsulates the graphite spheroids and then grows by diffusion of carbon from austenite to graphite through the ferrite halo. The transformation rate is thus expected to decrease as the transformation proceeds, leading eventually to nucleation and growth of pearlite in the metastable system. This latter constituent having a much higher growth rate than ferrite, it rapidly fills the untransformed matrix volume. This schematic has much in common with the competitive solidification in the stable and metastable systems.

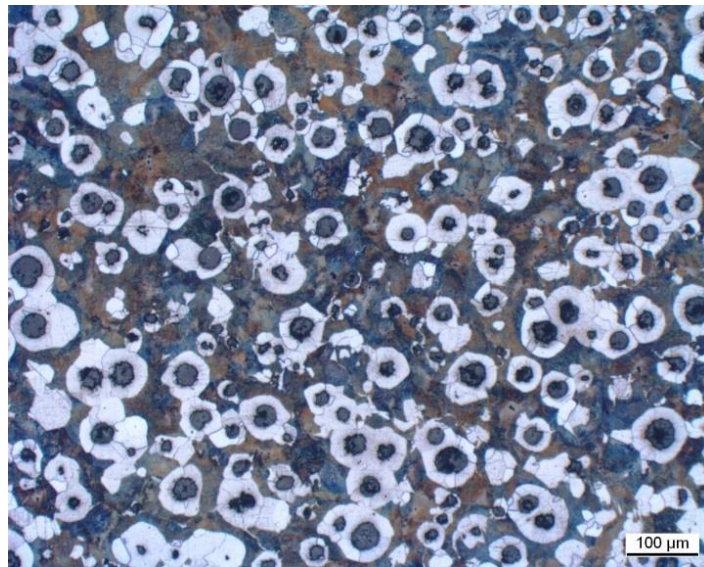


**Figure 9.1. Bull-eye microstructure in a SGI, optical micrograph after Nital etching.**

The first part of this chapter deals with the growth conditions at the interface between austenite and ferrite or pearlite as they explain the so-called hysteresis of the eutectoid transformation, namely the fact that it proceeds at much lower temperature upon cooling than the reverse transformation upon heating. Then, it is emphasized that these growth conditions do not depend on graphite shape and distribution while the overall transformation kinetics does. Solid-state growth of graphite is also shortly considered.

In all the following, the “cooling rate” stands for an imposed cooling rate or for the cooling rate measured just above the eutectoid temperature range in case of casting and thermal analysis.



### 9.1 The transformation hysteresis

Owing to the fact that silicon cast irons are multicomponent alloys based on Fe-C-Si compositions, it exists an equilibrium three-phase field that involves austenite, ferrite and graphite. This field defines the well-named **critical temperature range**. The most accurate methods for studying solid-state transformations are dilatometry and differential thermal analysis (DTA). Standard DTA is well suited to investigate the effect of scanning rate from a few tenths to a few tens of °C/min. At lower scanning rate, the signal becomes too weak while higher scanning rates are not achievable. This range of scanning rates is however compatible with those encountered in castings and thermal analysis, so that study of the scanning rate effect with DTA is of practical interest.

The use of DTA is illustrated in Fig. 9.2 in the case of a SGI with 2.08 wt.% Si and 0.13 wt.% Mn that was ferritic-pearlitic in the as-cast state. The figure shows the case of heating the as-cast alloy to 950°C, holding it for 5 minutes and then cooling it to RT. Both heating and cooling were carried out at 5°C/min. Data records consist of time, temperature and differential signal (corresponding to the temperature difference between the sample and an inert reference), and it is usual to plot the DTA signal versus temperature.

In Fig. 9.2, the record upon heating shows three peaks: the Curie transformation of ferrite and then two peaks associated to pearlite and ferrite decomposition at increasing temperature. Upon cooling, ferrite precipitates first, followed by pearlite whose kinetics is seen to be much more rapid. It is noted that the start of the transformation upon heating occurs at a temperature significantly higher than the start of its decomposition upon cooling, this is the so-called **hysteresis**. Note that the Curie peak does not appear upon cooling as there is no ferrite already formed when the Curie temperature is reached.

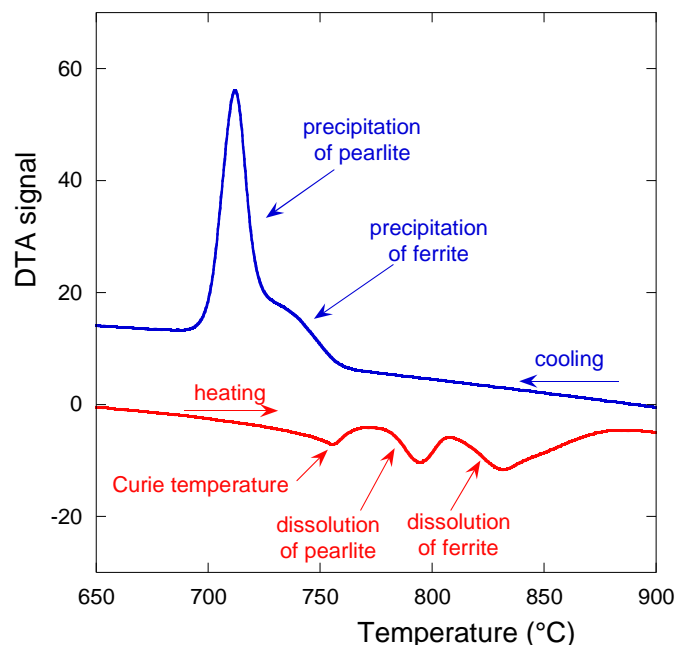


**Figure 9.2. Differential thermal analysis record upon heating and cooling at 5 °C/min of a SGI.**

Thus, attempts to characterize the upper and lower temperatures of the **equilibrium** domain with dilatometry and differential thermal analysis will fail because of this hysteresis.

## 9.2 The three-phase field

This situation led a few authors, a long time ago, to determine the location of the equilibrium three-phase field by very slow rates of transformation or by quenching samples from various temperatures after isothermal holding. These results have been discussed previously [GER00] and are represented in Fig. 9.3. In this figure, open symbols show the upper temperature at which ferrite could be observed under near-equilibrium conditions. Most importantly, it was observed that ferrite was not necessarily associated to graphite nodules and precipitated everywhere in the metallic matrix. This observation may be understood by considering that achieving equilibrium in the three-phase field needs redistribution of **substitutional solutes** between ferrite and austenite. This involves **long range diffusion** of these solutes which is very slow, so that full equilibrium of carbon may be assumed at any time during isothermal holding or very slow cooling rate. In such a case, ferrite may have better nucleating at austenite grain boundaries rather than at the graphite/austenite interface, and its growth is then controlled by redistribution of substitutional solutes and not by carbon diffusion. In Fig. 9.3, the solid line was calculated using the equation for the upper limit of the stable three phase field,  $T_{\alpha}^0$ , given below and a good agreement is observed for most of the data.

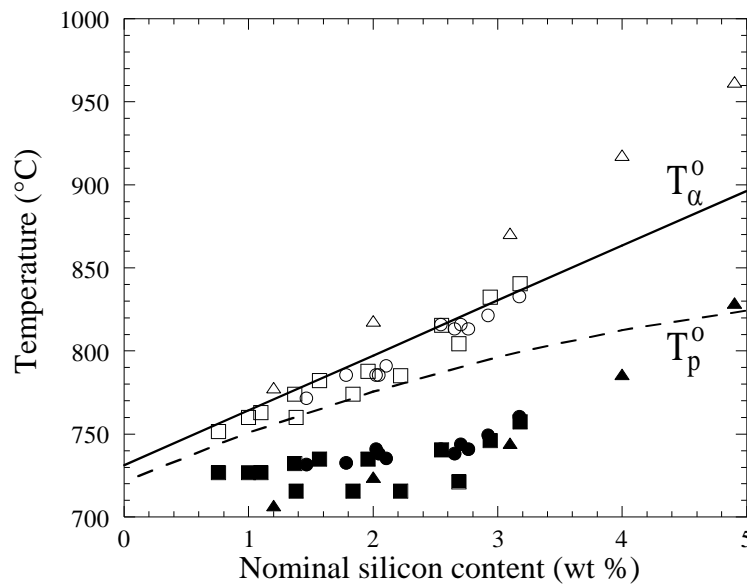


**Figure 9.3. Effect of the silicon content on the upper (empty symbols) and lower (solid symbols) temperatures of the "stable" three phase field determined experimentally.**

**Solid and dotted lines are the predicted  $T_{\alpha}^0$  and  $T_p^0$  temperatures for Fe-C-Si alloys with 0.4 wt.% Mn [GER00].**

It appeared even more difficult to determine experimentally the lower limit of the three-phase field in the stable system. In fact, the authors of the experiments represented by solid symbols in Fig. 9.3 realised that pearlite systematically formed which then partially or totally decomposed into ferrite and graphite. To demonstrate the possibility of pearlite precipitation at

these temperatures under isothermal or low cooling conditions, the upper boundary of the metastable three-phase field,  $T_p^0$ , has been drawn with a dashed line that is indeed well above the experimental points. Figure 9.3 also shows that the experimental points for a Si content of less than 3.0 wt.% all lie at almost the same temperature, which may be related to the fact that pearlite forms first in the low silicon areas of the last to solidify zones. These difficulties are apparent in many of the available TTT and CCT diagrams, see next section.

In Fig. 9.4 are superimposed the isopleth Fe-C sections of the stable and metastable phase diagrams at 2.5 wt.% Si. It is seen that they are very close to each other and, in fact, overlap in the low-temperature range thus explaining the above difficulties. In the figure, four temperatures are defined along the extrapolation of the austenite/ferrite equilibrium, two in the stable system,  $T_\alpha^0$  and  $T_\alpha$ , and two in the metastable one,  $T_p^0$  and  $T_p$ , that are the upper and lower temperatures of the three phase fields, respectively. Expressions of these temperatures as function of alloying content have been calculated using first the work by Uhrenius [UHR77] and then complemented with TCFE8. These are:

$$T_\alpha^0 = 739 + 31.5w_{Si} - 7.7w_{Cu} - 18.7w_{Mn} + 3.3w_{Mo} - 10.7w_{Cr} - 26.0w_{Ni} \quad (9.1)$$

$$T_\alpha = 739 + 18.4w_{Si} + 2.0(w_{Si})^2 - 14.0w_{Cu} - 45.0w_{Mn} + 2.0w_{Mo} - 24.0w_{Cr} - 27.5w_{Ni} + 5.1w_{Sn} \quad (9.2)$$

$$T_p^0 = 727 + 30.07w_{Si} - 1.98(w_{Si})^2 - 10.7w_{Cu} - 13.7w_{Mn} + 9.3w_{Mo} + 24.3w_{Cr} - 12.0w_{Ni} \quad (9.3)$$

$$T_p = 727 + 21.6w_{Si} + 0.023(w_{Si})^2 - 21.0w_{Cu} - 25.0w_{Mn} + 8.0w_{Mo} + 13.0w_{Cr} - 33.0w_{Ni} + 6.5w_{Sn} \quad (9.4)$$

These expressions were calculated with silicon content up to 3 wt.%, manganese, copper, chromium and nickel content up to 1 wt.%, and molybdenum content up to 0.5 wt.%, and should not be used out of this range.

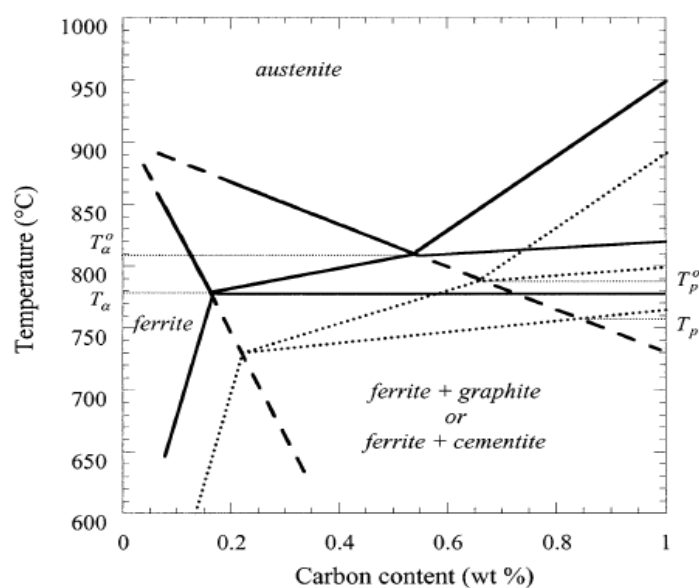


**Figure 9.4. Fe-C isopleth section of the stable (solid lines) and metastable (dotted lines) systems at 2.5 wt.% Si in the eutectoid range [TCFE8]. Note that the solubility of carbon in ferrite is not representative; it has been increased for ease of reading.**

### 9.3 TTT and CCT curves

Time-temperature-transformation (TTT) curves for cast irons are obtained by first austenitising and then quenching to a temperature at which the austenite transforms. Continuous-cooling-transformation (CCT) diagrams are obtained by again austenitising and then cooling at a given constant rate to RT. TTT and CCT diagrams were schematically presented in the ASM handbook of cast iron of 1995 as shown in Fig. 9.5. In both cases, the upper critical temperature (upper dotted horizontal line) that is shown certainly refers to the upper limit of the three-phase field, which implicitly shows that the authors considered that there should be a relationship between the equilibrium phase diagram and the transformation temperature. However, the lower horizontal dashed line was not named and seems to indicate the upper temperature at which pearlite appears.

In both diagrams, the most left curve indicates the beginning of the transformation while the one to the right locates the end of the transformation. As with many solid state transformations, the nose of the pearlitic transformation is a well known feature that results from a balance between increased nucleation and decreased diffusion processes as the transformation temperature is decreased. It can be seen that the same reasoning has been applied for the ferritic transformation but it is doubtful whether the proposed shape corresponds to any experimental information.

It will be seen in the following that all four characteristic temperatures,  $T_{\alpha}^0$  and  $T_{\alpha}$ ,  $T_p^0$  and  $T_p$ , should appear in complete TTT and CCT diagrams, though for usual cooling rates, only the lower limits are of interest for CCT diagrams as detailed in the sections to follow.

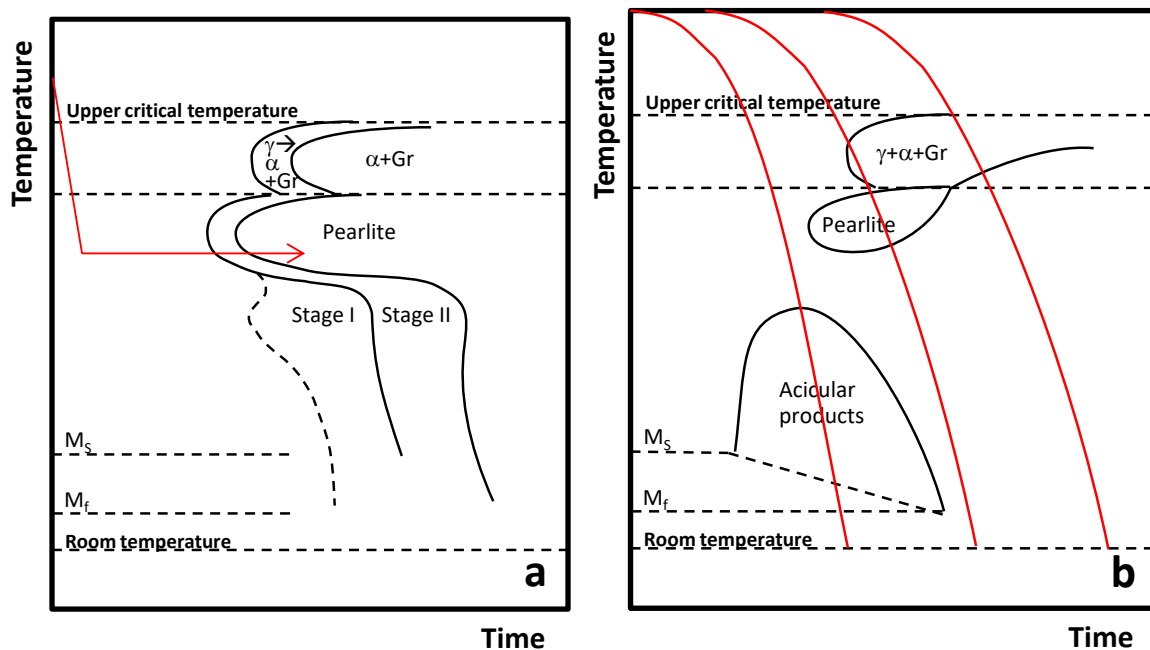


Figure 9.5. TTT (a) and CCT (b) diagram. Gr stands for graphite,  $M_s$  and  $M_f$  for martensite start and end, respectively, stages I and II are for ausferritisation. The red curves are cooling schedules.

#### 9.4 The ferritic transformation

In principle, the eutectoid transformation of silicon cast irons should bear many similarities with that of carbon steels. There is however an evident difference which is the presence of graphite particles which support the transformation in the stable system by acting as carbon sinks. Apart for this, the transformation of austenite to ferrite or to pearlite should obey the same rules as for steels, and could thus be understood following the approach by Hillert [HIL02, HIL04] or others, see [HIL04] for a short review. This has been stated by Venogopalan [VEN90] and later by Lacaze et al. [LAC94]. For basic studies, carbon steels have been replaced by Fe-C-X alloys, where X is a substitutional solute, i.e. substituting for Fe in the austenite or ferrite crystallographic structure, while C is an interstitial element as are also N and O. Interstitial elements do diffuse much more rapidly than substitutional elements in solid state, i.e. through the bcc and fcc matrices, while substitutional solutes are strongly tight in these matrices. To make it simple, one may consider that substitutional elements cannot move by diffusion within either ferrite or austenite, except at very low cooling rate or during extended isothermal holding. This implies that - **at usual cooling rates** - the product of austenite decomposition, i.e. ferrite for the transformation in the stable system and pearlite for the transformation in the metastable system, has the same composition in substitutional elements as the parent austenite. In turn, this inheritance implies that the eutectoid transformation can start upon continuous cooling only when the lower limit of the three phase field has been reached.<sup>5</sup>

This is described in Fig. 9.6 that shows two isothermal sections of the Fe-C-Si phase diagram. They correspond to the  $T_{\alpha}^0$  (a) and  $T_{\alpha}$  (b) temperatures of an alloy with a matrix at 2.5 wt.% Si. In these graphs, the red lines represent the tie-lines for equilibrium between ferrite, austenite and graphite (out of the figure). When the upper limit of the three phase field is reached, the ferrite to grow should have a significantly lower carbon content and higher silicon content than the parent austenite (Fig. 9.6-a). Because diffusion of substitutional solutes in austenite is very slow, growth of ferrite with “long range” redistribution of silicon or any other substitutional solutes is impossible. This is in line with the accepted view that growth of ferrite is controlled by carbon diffusion upon continuous cooling. The only possibility for the transformation of austenite to ferrite is that the system cools down further until ferrite with the same silicon content as the parent austenite becomes stable. It is seen with Fig. 9.6-b that this happens at the lower limit of the three-phase field. It is also shown in Fig. 9.9 that this is only at this temperature that the “driving force” for carbon diffusion becomes positive.

The above assertion that ferrite inherits the content in substitutional solutes of austenite during its growth can be rationalized by imagining that it does not. If this were the case, the

---

<sup>5</sup> In the case of ferrite growth, what is in fact conserved is the ratio of substitutional solutes in the bcc and fcc lattices, respectively. For expressing this, Hillert introduced the site fraction  $u_i = x_i / \sum x_i = x_i / (1 - x_C)$ , where  $x_i$  is the atom fraction of element  $i$  and the summation excludes

carbon and any other interstitial element. In the present chapter and in the cited references, this conservation has been approximated using the mass fraction of substitutional elements.

local equilibrium at the interface imposes a redistribution of these elements and thus their long-range diffusion. Ahead of the moving interface, a diffusion gradient builds up in austenite whose thickness  $\delta$  scales as  $D_i^{\gamma} / V_{\text{ferrite}}$ , where  $D_i^{\gamma}$  is the diffusion coefficient of element  $i$  in austenite and  $V_{\text{ferrite}}$  the growth rate of ferrite [WES96]. In the case of SGI,  $V_{\text{ferrite}}$  is easily estimated by dividing the average distance between spheroids by the total time for the eutectoid transformation, while  $D_i^{\gamma}$  is typically of the order of  $10^{-19}$ - $10^{-20}$   $\text{m}^2 \cdot \text{s}^{-1}$  at  $700^\circ\text{C}$ . For usual cooling rates,  $\delta$  thus takes values lower than the atomic distance in the fcc lattice, which is unphysical. The same reasoning applies to pearlite.

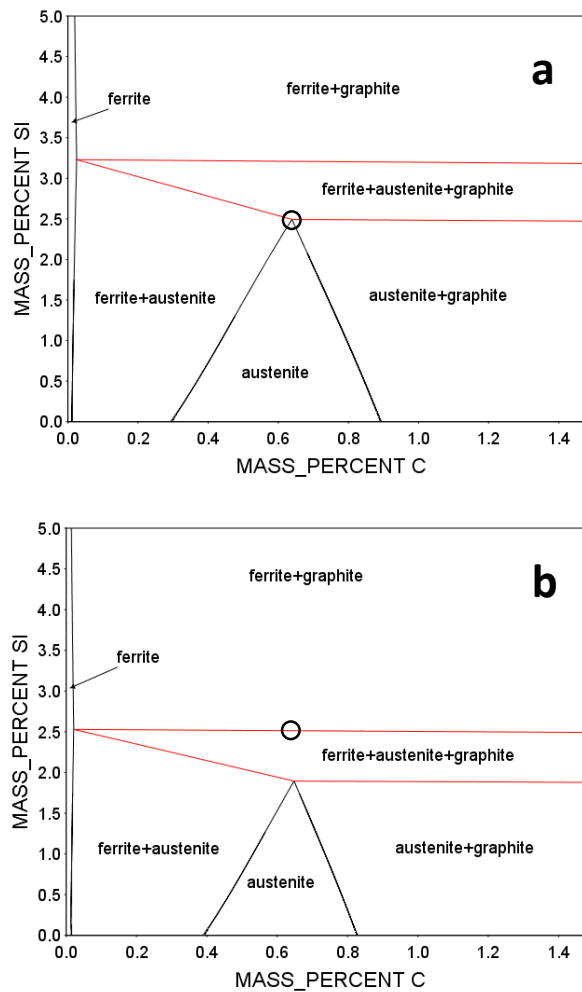


**Figure 9.6.** Isopleth sections of the Fe-C-Si phase diagram at the temperature  $T_{\alpha}^0$  (a) and  $T_{\alpha}$  (b) for a silicon content of 2.5 wt.%. The open circles indicate the location of the eutectoid alloy at 2.5 wt.% Si [TCFE8].

Experiments performed by Ekpoom and Heine [EKP78] showed this above condition for ferrite growth to be true whatever the graphite shape is. This is illustrated in Fig. 9.7 where all the data representing the onset of the eutectoid transformation during cooling are represented with blue solid symbols and lie on the  $T_{\alpha}$  curve.

An interesting feature that is shown on Fig. 9.7 is that the recorded starts of the reverse transformation, that is the formation of austenite upon heating from RT, are shown with red symbols and relate to  $T_{\alpha}^0$ . Open symbols correspond to the upper temperature of the three-phase domain as established by holding and quenching experiments.

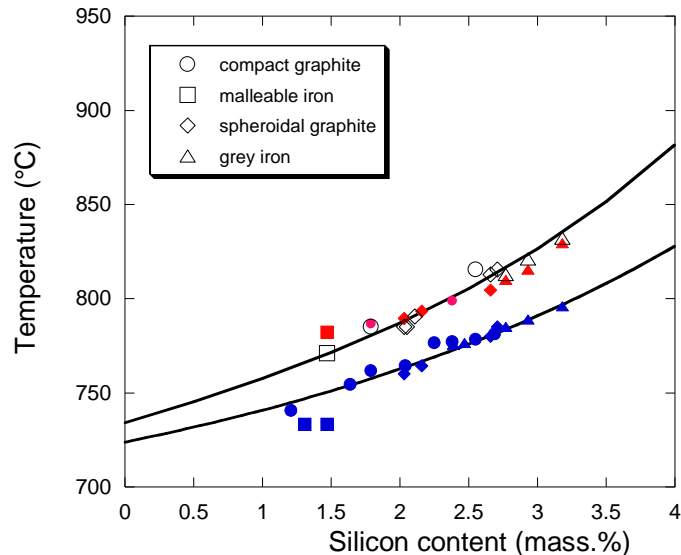


**Figure 9.7. Symbols represent experimental results from Ekpoom and Heine [EKP78] showing the start of the eutectoid transformation upon heating (red symbols) and upon cooling (blue symbols) and the upper limit of the equilibrium three-phase field (open symbols). The solid lines are the calculated upper,  $T_{\alpha}^0$ , and lower,  $T_{\alpha}$ , limits of the equilibrium three-phase field [TCFE8]. The various symbols enable to differentiate cast irons according to graphite shape, see insert. The opening of the three-phase field at 0 wt% Si is due to the fact that calculations were performed for alloys containing 0.3 wt.% Mn, i.e. the average Mn content of the experimental alloys [LAC17c].**

Finally, it should be mentioned that theoretically another possibility for ferrite to grow at the same composition as austenite is when their free energy is the same, which happens when the so-called  $T^0$  line is reached. For the eutectoid composition, this line is located far below the metastable three phase field which means that such a transformation is hardly possible in cast irons contrarily to steels.

### 9.5 Thermo-kinetics conditions for ferrite growth

If ferrite inherits the composition in substitutional solutes of austenite **upon continuous cooling**, then the stable eutectoid transformation is controlled by diffusion of carbon and may be described using the appropriate Fe-C isopleth section as the one illustrated in Fig. 9.8-a. Redistribution of carbon is described with the schematic in Fig. 9.8-b that is the basis for modelling ferrite growth in SGI and can be easily adapted for any other graphite shape. For ferrite to grow, carbon has to diffuse from the ferrite/austenite interface to graphite through the ferrite halo. This can proceed only if the quantity  $\Delta w_C = (w_C^{\alpha/\gamma} - w_C^{\alpha/\text{gra}})$  is positive, which happens only when the temperature is lower than  $T_{\alpha}$ . **Upon continuous**

**cooling – at a rate higher than  $\approx 1.2^\circ\text{C}/\text{min}$  [GER00] – ferrite cannot grow within the three-phase domain.** It may be worth stressing again that growth of ferrite proceeds at the expense of austenite, meaning that the ferrite/austenite interface has to move within parent austenite. At temperature above  $T_\alpha$ , this would require long-range redistribution of substitutional solutes which is impossible even if the carbon gradient in austenite was favourable. The transformation is thus characterized by the undercooling  $\Delta T_\alpha = T_\alpha - T$  that is positive. Note that this does not exclude redistribution and diffusion of carbon in austenite ahead of the ferrite/austenite interface, but this can happen only once ferrite has started to grow under a positive  $\Delta w_C$ .

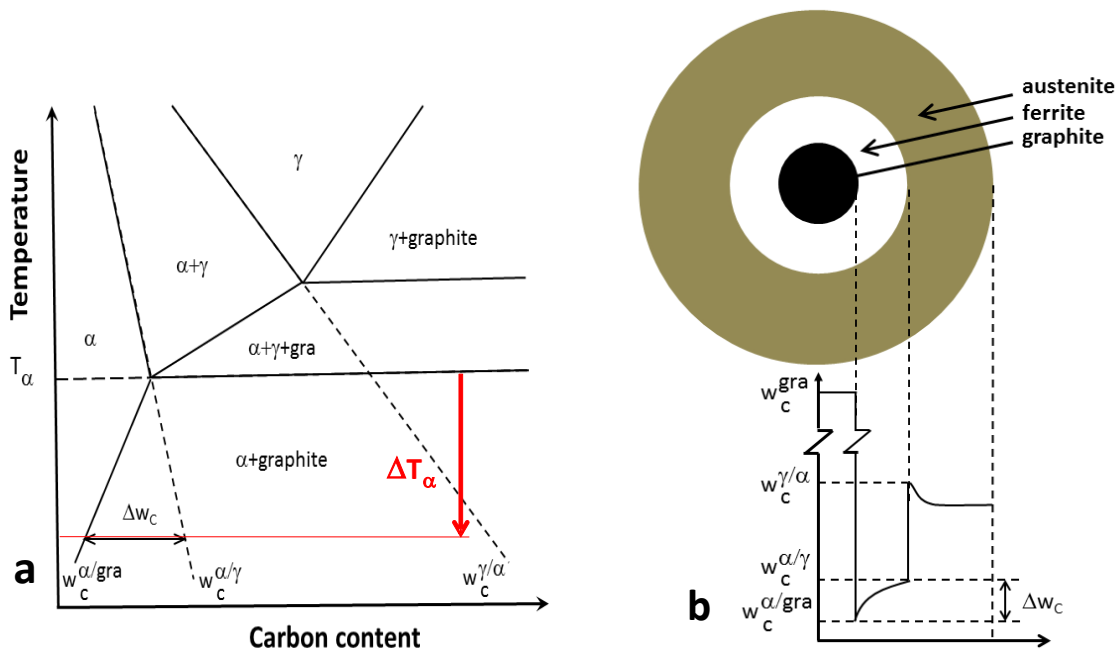


**Figure 9.8. Isopleth Fe-C section of the relevant stable phase diagram (a) and schematic of carbon redistribution during ferrite growth in SGI (b) (adapted from [LAC98b]). Note that the solubility of carbon in ferrite is not representative; it has been increased for ease of reading.**

In the description above, the matrix is assumed to be homogeneous in substitutional solutes. Owing to graphite precipitation, the content in substitutional solutes of this homogenous matrix should be corrected with respect to the nominal composition. This can be done using the mass balance of any substitutional  $i$  element considering graphite is pure carbon. The corrected composition is written:

$$\left(1 + (\rho^{\text{gra}} / \rho^\gamma) \cdot g^{\text{gra}} \cdot (1 - g^{\text{gra}})^{-1}\right) \cdot w_i^0 \quad (9.5)$$

where  $g^{\text{gra}}$  is the volume fraction of graphite and  $w_i^0$  is the nominal content of  $i$  element.

For  $g^{\text{gra}}=9\%$ , the corrected content in  $i$  element is 1.05 times the nominal content. Considering the main alloying element, namely silicon, it is totally fortuitous that this correction corresponds quite closely to the correction that should be applied to account for silicon microsegregation. Accordingly, there is no or little bias when using the corrected



composition for evaluating the temperature  $T_\alpha$  for the start of the ferritic transformation of a given cast iron.

Furthermore, the effect of microsegregation on the eutectoid transformation has been studied on samples processed by DTA at various cooling rates (1 to 10°C/min) [GER97], either as-cast or after an homogenization treatment of 1 hour at 1100°C. Microprobe measurements gave the distribution of substitutional solutes that were then converted to reference temperature  $T_\alpha$  for ferritic alloys and  $T_p$  for pearlitic alloys. It is seen in Fig. 9.9, for a ferritic alloy, that the  $T_\alpha$  temperature does not change much in 80% of the material (solid lines). This is only when the last 20% are to transform that microsegregation could possibly enter into play. The same was observed for pearlitic iron.

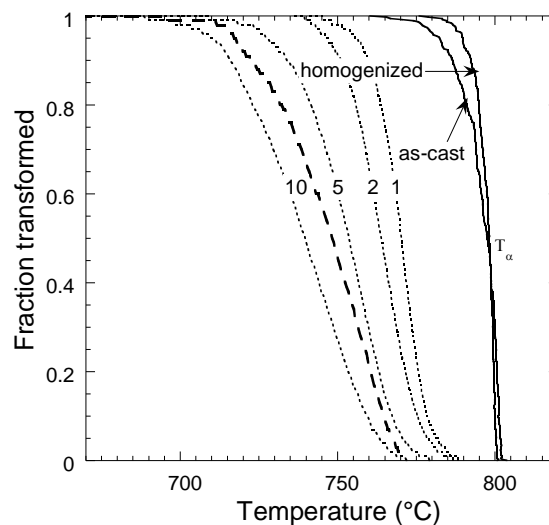


**Figure 9.9. Kinetics of austenite decomposition to ferrite at 1, 2, 5 and 10 °C/min as compared to the distribution of the  $T_\alpha$  temperature calculated based on microprobe measurements (solid lines) [GER97]. Dotted curves are for as-cast samples, the dashed curve for a homogenised sample.**

Under conditions where there is long range redistribution of substitutional solutes, i.e. at very low growth rates within the three-phase temperature range, a spike of substitutional solutes develops ahead of the moving ferrite/austenite interface. Hillert recalls that this may also lead to ferrite having the same composition as the parent austenite [HIL04] if a steady-state has time to settle. These conditions may be called false para-ferrite as there is in fact redistribution of substitutional solutes at the interface. As already mentioned, such a ferrite can grow anywhere in the cast iron microstructure because the carbon activity is the same throughout the material. Studying this thus needs quenching experiments to locating the transformation front and evaluating the composition on both sides of the interface.

### 9.6 The pearlitic transformation

The same condition holds for growth of pearlite: the mixture of ferrite and cementite must inherit the austenite content in substitutional elements. Accordingly, austenite can transform to pearlite only when the temperature has decreased below the lower limit of the three phase

field. This is illustrated with the two isothermal sections in Fig. 9.10. Fig. 9.10-a shows the isothermal section of the Fe-C-Si metastable phase diagram at the upper temperature,  $T_p^0$ , of the austenite/ferrite/cementite three-phase field for an alloy with 3.0 wt.% Si represented with the open circle. As the temperature decreases, the three-phase triangle moves to the left, see the yellow area in figure 9.10-b: the ferrite/cementite tie-line on the right side of the triangle eventually goes through the open circle when the temperature  $T_p$  is reached. When this latter condition is fulfilled, the parent austenite can readily decompose to ferrite and cementite without long range redistribution of substitutional alloying elements.

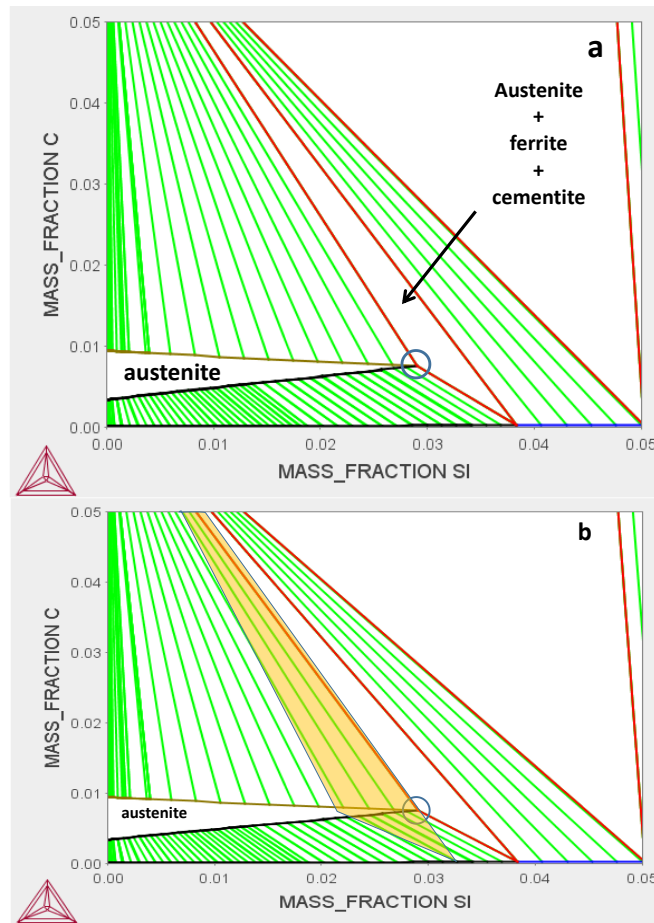


**Figure 9.10. Isothermal section of the Fe-C-Si system at the  $T_p^0$  temperature of an alloy with 3.0 wt.% Si (a) and illustration of the movement of the three-phase field (yellow triangle) when the temperature is decreased to  $T_p$  (b).**

Owing to the fact that nucleation of ferrite is easy, it is proposed to select as reference temperature the intersection of the austenite/ferrite equilibrium with the lower limit of the three phase field, denoted  $T_p$  in Fig. 9.11-a. The transformation is thus characterized by the undercooling  $\Delta T_p = T_p - T$ .

Numerous experimental values for the onset of eutectoid transformation, obtained either by thermal analysis or differential thermal analysis, are available. Though these results are scattered, analysis of such series of data showed an increase of  $\Delta T_\alpha$  and  $\Delta T_p$  with cooling

rate which is illustrated in Fig. 9.11-b [LAC94, SER10]. It is first seen that the undercooling for the start of ferrite growth may be extrapolated to zero at very low cooling rate (though remaining above the limit of 1.2°C/min mentioned above), which confirms that there is no nucleation barrier for this phase. On the contrary, the curve for pearlite extrapolates to an undercooling of about 40°C which can therefore be understood as corresponding to the driving force necessary for the nucleation of cementite.

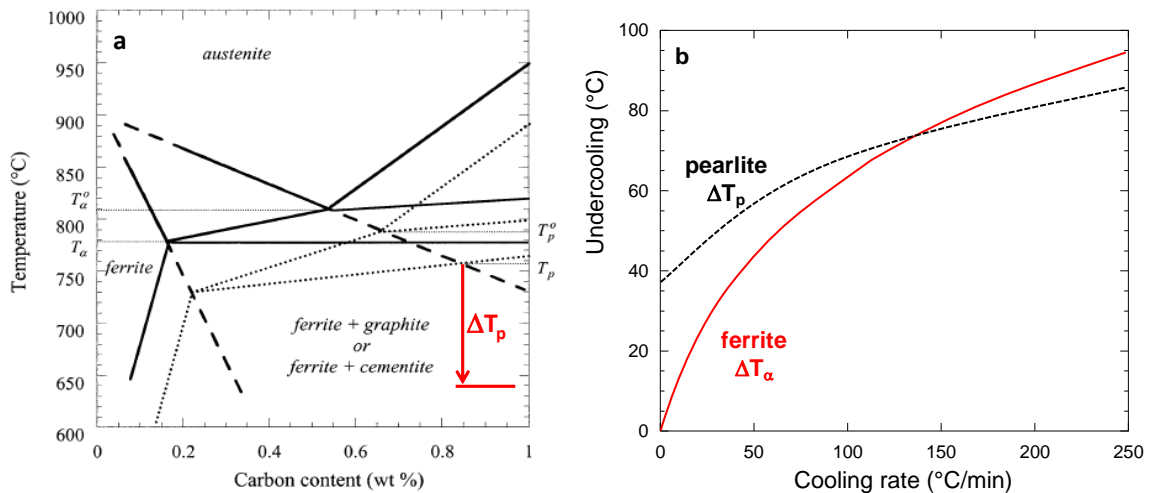


**Figure 9.11. a) Isoleth Fe-C section of the relevant stable (solid lines) and metastable (dotted lines) phase diagrams in the eutectoid temperature range. The undercooling  $\Delta T_p$  with respect to the selected  $T_p$  temperature is illustrated. b) Effect of the cooling rate on the undercooling for the start of the eutectoid transformation  $\Delta T_\alpha$  in the stable system and  $\Delta T_p$  in the metastable one.**

**Note that the solubility of carbon in ferrite in (a) is not representative; it has been increased for ease of reading.**

It has been observed that for SGI containing more than 0.05 wt.% Sn, the undercooling  $\Delta T_p$  is much lower and may well extrapolate to zero at a zero cooling rate. This has tentatively been understood as Sn cancelling the driving force for cementite nucleation and it has been proposed this is due to the transitory formation of a Kappa  $Fe_3SnC$  compound whose crystalline structure is close to that of austenite and shows epitaxy with cementite [LAC17d].

### 9.7 Construction of the CCT diagrams

The two curves in Fig. 9.11-b may be used to draw the envelop of the transformation domains in a CCT diagram and to illustrate how addition of Sn above 0.05 wt.% acts as a pearlite promoter. In Fig. 9.12 is shown the CCT diagram for the start of the ferrite and pearlite growth in a cast iron with 2.0 wt.% Si and 0.6 wt.% Mn that has been equilibrated at 950°C for carbon homogenisation. The curves labelled 2-200 are the cooling curves for cooling rates expressed in °C/min. The horizontal lines represent the  $T_\alpha$  and  $T_p$  temperatures, they are seen to be only a few degrees apart. When  $T_\alpha$  is reached, ferrite can

start growing at a temperature which decreases with the cooling rate as described with Fig. 9.11-b. This is represented with the blue dotted curve in Fig. 9.12. When  $T_p$  is reached, pearlite can start growing but some undercooling is needed for cementite nucleation if the alloy does not contain more than 0.05 wt.% Sn. Again, the actual temperature for the start of the pearlitic transformation decreases with cooling rate; this is represented with the black dashed curve. It is seen that a cooling rate higher than  $100^\circ\text{C}/\text{min}$  would be needed to reach the pearlitic domain without ferrite precipitation. In case of addition of tin, the pearlite start curve moves upwards (black solid curve) to such an extent that the window for ferrite formation is practically limited to the temperature difference ( $T_\alpha - T_p$ ). Traces of ferrite could thus be observed only at very low cooling rates, less than a few  $^\circ\text{C}/\text{min}$ .

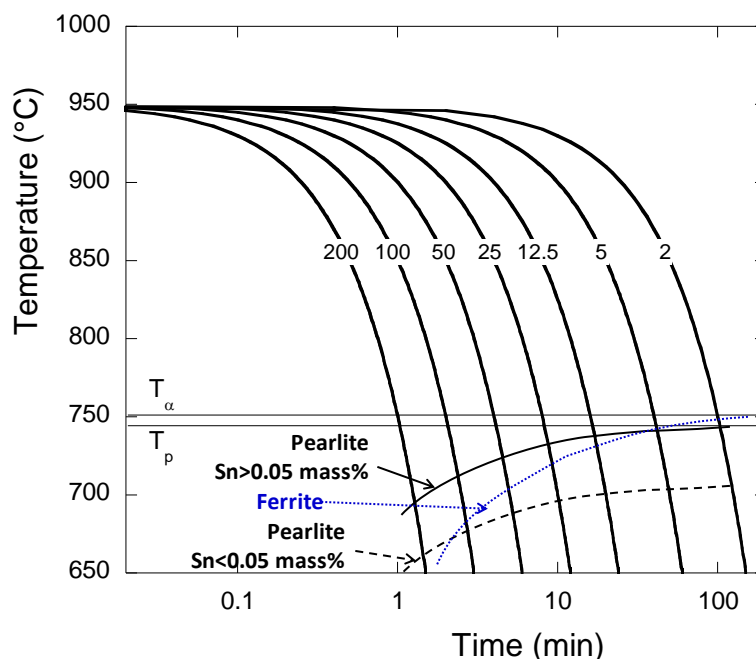


**Figure 9.12. CCT curve showing the start of austenite decomposition to ferrite and pearlite and illustrating the role of Sn. Cooling rates along the curves are in  $^\circ\text{C}/\text{min}$ .**

Once pearlite grains have nucleated, they grow with a more or less spherical front. Analysis of experimental data in the literature [LAL73, PAN87] has shown that their growth rate is not very sensitive to additions of As (up to 0.5), Cu (2.08), Mn (0.75) or Sn (0.15), where the values within the brackets give the maximum amount for each element (% by weight) that has been studied, see Fig. 9.13.

Fridberg and Hillert have studied growth of pearlite in Fe-C-Si alloys and could find up to four different types of transformation [FRI70]. The effect of silicon was compared latter to the effect of other elements [HIL81]. It seems that the only kind of pearlite that is relevant for cast irons is what was called "constant orthopearlite" whose growth is controlled by interfacial diffusion. The upper limit for this pearlite is the  $T_p$  temperature.

Further, calculations of the growth rate of pearlite in silicon steels [FRI70] showed that it is not much sensitive to silicon content. This suggests that carbon and silicon partitioning

between ferrite and cementite controls the growth rate of pearlite and that addition of other alloying elements at low level does not affect it as demonstrated with Fig. 9.13. Accordingly, and based on pearlite growth rate data in Fe-C-Si alloys, the following growth rate was proposed [LAC98b]:

$$1.63 \cdot 10^{-5} \cdot (\Delta T_p)^3 \text{ } \mu\text{m/s} \quad (9.6)$$

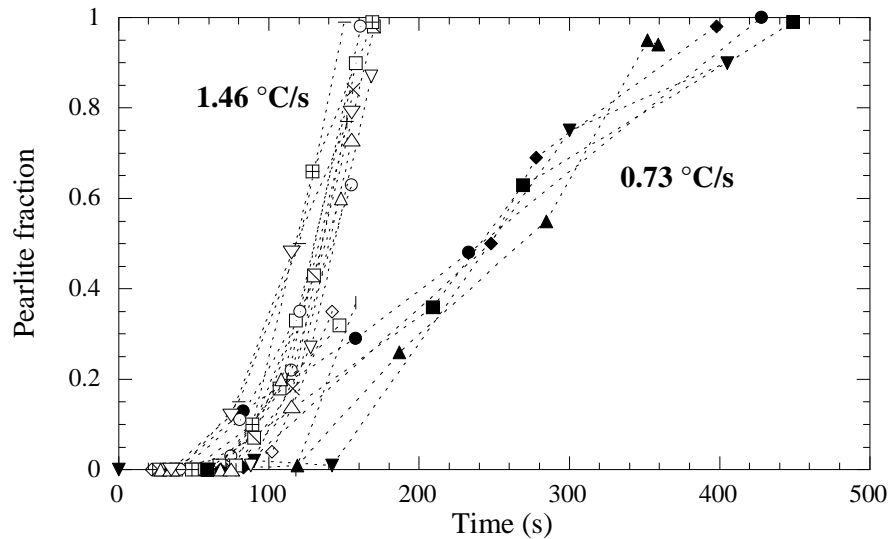


**Figure 9.13. Pearlite fraction versus time after the  $T_p$  temperature was reached for two cooling rates, 0.73 and 1.46 °C/s. Only fully pearlitic samples were selected. The various symbols represent alloys with different additions, As, Cu, Mn and Sn, see text. Adapted from [LAC99a].**

Combining this growth law and an appropriate nucleation law, it is possible to describe the so-called pearlite nose. This is illustrated in Fig. 9.14 [LAC99a].

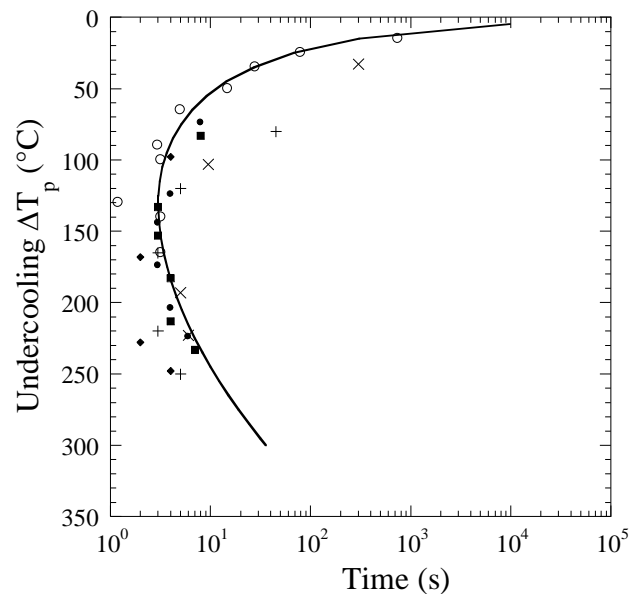


**Figure 9.14. Pearlite nose as function of  $\Delta T_p$ ; the symbols represent experimental data for Fe-C-Si steels (adapted from [LAC99a]).**

Molybdenum differs from the alloying elements mentioned above. It is known to strongly delay both the ferritic and pearlitic transformations, see the compilation of TTT and CCT curves by Röhrig and Fairhurst [ROH79], and this has been related to the associated significant decrease of carbon diffusion in both austenite and ferrite. A final note concerns the very low solubility of copper in ferrite and cementite which should lead to precipitation of free copper in pearlitic cast irons alloyed with this element. Such precipitation has been highlighted by TEM by Garcia et al. [GAR19] but does not appear to affect the growth kinetics of the pearlite.

### 9.8 Overall transformation

The above considerations apply to all silicon cast irons whatever the shape and distribution of graphite. However, the final amount of ferrite depends strongly on the growth kinetics of this phase. As a rule, the finer are graphite precipitates the higher is the amount of ferrite. For the same alloy composition, it has thus been shown that ferrite growth is much more rapid in CGI than in LGI, see Fig. 9.15. Similarly, undercooled graphite must be avoided in LGI castings which are intended to be fully pearlitic. In the case of SGI, it is known that the final amount of ferrite is very sensitive to nodule count at low nodule count, while formation of ferrite can hardly be avoided at high nodule count. Accordingly, for a given melt preparation solidifying within a large range of cooling rates, a minimum in ferrite content has sometimes been observed in SGI. As a matter of fact, increasing the cooling rate does increase the nodule count which would favour ferrite while at the same time this increases the undercooling for the eutectoid transformation that favours pearlite. Such a minimum has also been observed in CGI [GUE19].

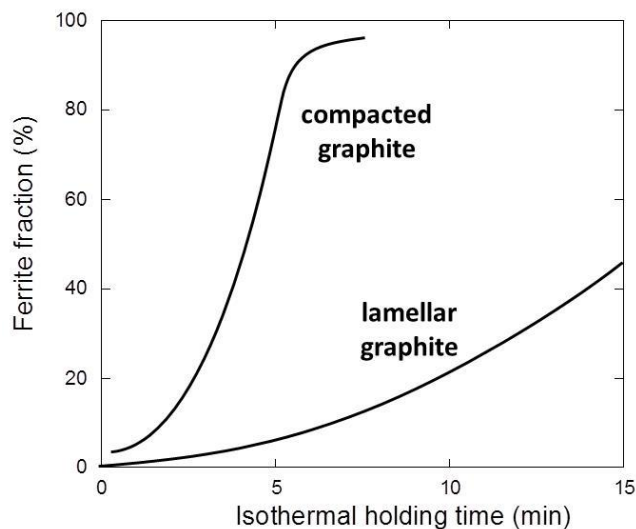


**Figure 9.15. Comparison of austenite decomposition kinetics of flake (LGI) and compacted (CGI) graphite irons isothermally held at 750°C (adapted from Pan et al. [PAN86]).**

To favour pearlite, appropriate combinations of Cu, Mn and Sn are industrially used. However, Cu and Mn are "soft" pearlite promoters, being about 10 times less effective than

Sn as suggested by the Sn equivalent,  $Sn_{eq}$ , proposed based on experimental information:  $Sn_{eq}=0.075 \cdot w_{Mn}+0.125 \cdot w_{Cu}+w_{Sn}$  [LAC16]. The fact that Cu and Mn do not affect pearlite growth kinetics (see Fig. 9.13) leads to the conclusion that their pearlite promoter effect is due to them affecting ferrite growth. Their "softness" further suggests a thermodynamic effect [LAC16]. Both of these elements decrease the  $T_{\alpha}$  temperature as expressed with Eq. (9.2), which then can become lower than the Curie temperature of ferrite. At this latter temperature, the diffusion coefficient of carbon gets divided by 3 [ÅGR86] and this certainly explains the role of copper. Further, Mn decreases also the driving force  $\Delta w_C$  for ferrite growth and this was proposed to explain its role. In this approach, the "barrier" effect sometimes proposed to explain the role of pearlite promoters is disregarded for Cu and Mn, whereas it can possibly apply to some specific elements, see next section.

### 9.9 The "barrier" effect

The effect of sulphur as pearlite promoter has been reported since a long time but is still of interest as it has never been fully clarified. Lietaert [LIE97] showed that oxygen and sulphur favour pearlite and this was again demonstrated for sulphur by Nakae et al. [NAK16] by means of an elegant experiment which consisted in casting a LGI with a very low sulphur content. While usual LGI are fully pearlitic, this special LGI was fully ferritic which suggests that, in usual LGI, S adsorbed at the surface of graphite hinders the transfer of carbon atoms from the matrix to the precipitates and thus blocks ferrite growth.

Antimony is known to have a strong pearlite promoter effect as well when present at level similar to that of sulphur. Auger spectroscopy evidenced the presence of 1-2 atom layers of Sb at the surface of spheroidal graphite [LIU90b, DEK20] which may account for this pearlite promoter effect. As for sulphur, this effect may be associated with a preferential segregation of antimony at the graphite/matrix interface and, in this way, could be called a barrier effect.

However, it seems totally excluded that micrometre size layers of one element could develop in between graphite and the matrix as proposed since a long time for copper. Indeed, such a thick layer would have been easily evidenced by micro-analysis techniques such as electron microprobe if it were to exist. The thick layer of copper shown by Zou et al. [ZOU12] seems to be an artefact because it was obtained after selective dissolution of the ferrite halo at an electrode potential removing iron but not copper which remained in place.

Hence, the interesting observation is that some of the elements which have been seen to strongly affect graphite shape during the solidification step - e.g. O, S and Sb - may as well determine the matrix structure resulting from the eutectoid transformation. Exactly as was the case for solidification, it may well be that this is not by preferential adsorption on prismatic or basal planes but rather by segregation on the matrix side of the graphite/matrix interface.

Despite what might be expected since it is also a surface-active element, no Sn-rich layer has been reported so far on as-cast cast irons, and its pearlite-promoting effect should rather be related to other reasons mentioned above. However, again using Auger

spectroscopy, Johnson and Kovacs [JOH78] observed an Sn-rich layer in a SGI doped with 0.11 wt.% Sn, but on a material that had been heat-treated for 150 hours at 1075°C after casting. The resulting layer was 40 Å thick, in sharp contrast to the values found for Sb in as-cast SGI. Although these results confirm the relationship between the effect of Sn on melt surface tension and interfacial segregation, it may be that the latter is too weak to induce the formation of an Sn-rich layer in as-cast irons.

### 9.10 Graphite growth during solid-state cooling and temperature cycling

During cooling after solidification has finished the solubility limit of carbon in austenite decreases and the cooling rate from the end of solidification to the eutectoid temperature range determines the carbon distribution in austenite. This has been modelled [LAC98b] and gave the features illustrated in Fig. 9.16-a for the change in the average carbon content of austenite. At low cooling rate, the carbon content in austenite gets nearly homogenized at any time and the average composition quite closely follows the graphite solvus. However, at high cooling rate, this average composition decreases little with respect to its value at solidification completion and thus is more and more away from the graphite solvus as the temperature decreases.

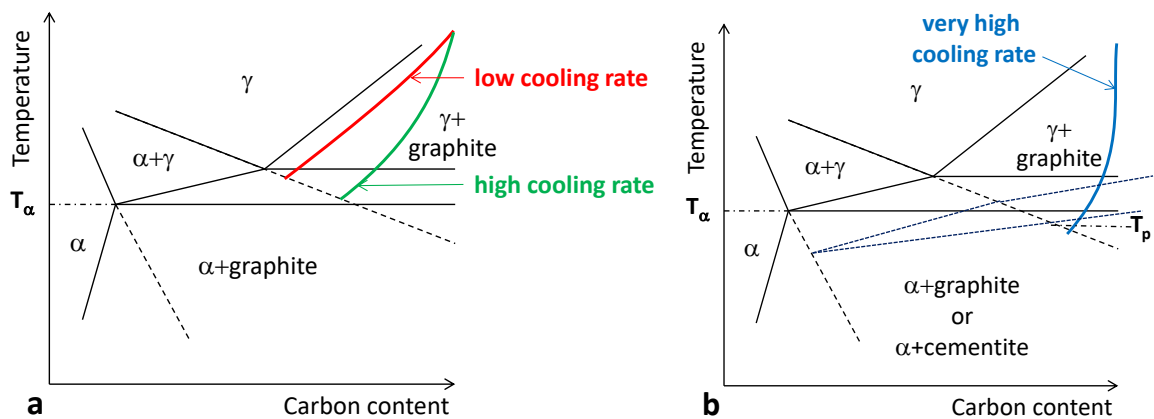


**Figure 9.16. a: coloured lines show the evolution of the average carbon content in austenite upon cooling at two different rates from high temperature. b: at much higher cooling rate, the average carbon content in austenite may change so little during cooling that the temperature at which the extrapolation of the austenite/ferrite boundary is reached is located below  $T_\alpha$  and  $T_p$ . The black solid lines show the relevant Fe-C isopleth section of the stable system. The dotted blue lines show the three phase domain of the metastable system. Note that the solubility of carbon in ferrite in (a) and (b) is not representative, it has been increased for ease of reading.**

At very high cooling rate, Fig. 9.16-b suggests that the path followed by the average austenite carbon content can reach the extrapolation of the  $\gamma/\alpha$  boundary at a temperature below  $T_\alpha$ . Reminding that  $T_p$  may be close to  $T_\alpha$ , see Fig. 9.11, the schematic in Fig. 9.16-b suggests that there can be conditions where ferrite may become stable at a temperature



lower than both  $T_\alpha$  and  $T_p$ . How this can affect our understanding of the eutectoid transformation in cast irons does not seem to have been studied so far.

Note that the barrier effect mentioned in the previous section is another means of keeping the austenite supersaturated with carbon, and thus following the path of Fig. 9.16-b at any cooling rate. The decrease of the carbon content in austenite during cooling after solidification leads to some graphite growth which is the so-called third stage while the fourth stage occurs when the eutectoid leads to a ferritic matrix. The maximum volume fraction of graphite at any temperature may be determined by means of the lever rule which gives:

$$g^{gra} = \frac{(w_C^0 - w_C^\varphi) \cdot \rho^\varphi}{(1 - w_C^0) \cdot \rho^{gra} + (w_C^0 - w_C^\varphi) \cdot \rho^\varphi} \quad (9.7)$$

where  $\varphi$  stands for either ferrite or austenite.

Based on the Fe-C phase diagram and considering an eutectic alloy (4.34 wt.% C), the amounts of graphite at the end of solidification, the end of austenite cooling and the upper limit of the ferritic field (738°C), as well as at RT were calculated and are listed in Table 9.1. Considering further a uniform distribution of nodules, these amounts may be converted to nodule radius,  $R=[g^{gra}/\pi N_A]^{0.5}$ . This has been done in table 9.1 for nodule counts  $N_A$  of 50 and 250 mm<sup>-2</sup>. It is seen that most of the solid state growth of the spheroids is predicted to occur during cooling in the austenite domain, with 26% of the final radius being due to growth during cooling from the end of solidification to RT.

Fig. 9.17 shows a near diametrical section of a SGI cast in a Y-block with the blue circle indicating the final outer radius. The red circle has a radius decreased by 26% and should thus more or less locate the transition between stages 2 and 3. It is seen that there is no evidence of this transition showing up. In contradistinction, specific cooling or heat treatments could explain why spheroids may show different growth stages as sometimes illustrated in the literature. Also, though not visible at the scale of optical microscopy, Monchoux et al. [MON01] have shown that the extreme surface of the spheroids consists of a superficial layer of polycrystalline graphite. The thickness of this layer, 1-2  $\mu\text{m}$ , suggests it corresponds to the fourth stage, i.e. growth during the ferritic reaction.

If the material is heated from RT through the eutectoid temperature range, then graphite dissolves due to the **higher carbon solubility in austenite** than in ferrite. In case of SGI, Monchoux et al. showed that this dissolution is not even along the spheroid outer surface [MON01]. For long holding time in the austenite field, so-called matrix penetrations develop within graphite, at a depth of the order of 1  $\mu\text{m}$  and parallel to the outer spheroid surface. After cooling again to RT, the periphery of the nodules is replaced by a crown made of a mixture of graphite and matrix arches [MON01].

An unexpected result was obtained by Bermont and Sikora [BER98] who cycled a pearlitic SGI in the **ferritic domain** to decompose pearlite. Growth of graphite - due to cementite dissolution - proceeded by the development of spikes as seen in Fig. 9.18-a. The work of Matsushita et al. [MAT15] suggests that this may be related to the distribution of cementite lamellae in the dissolved pearlite.

**Table 9.1. Fraction of graphite (given by the lever rule) and spheroid radius at different temperatures: eutectic, eutectoid (with either austenite or ferrite) and RT. See text for details.**

Temperature	Eutectic	Eutectoid, austenite	Eutectoid, ferrite	RT
$g^{gra}$ (%)	7.4	11.9	13.0	13.4
R ( $\mu\text{m}$ ) ( $N_A=50$ )	21.7	27.5	28.8	29.2
R ( $\mu\text{m}$ ) ( $N_A=250$ )	9.7	12.3	12.9	13.1

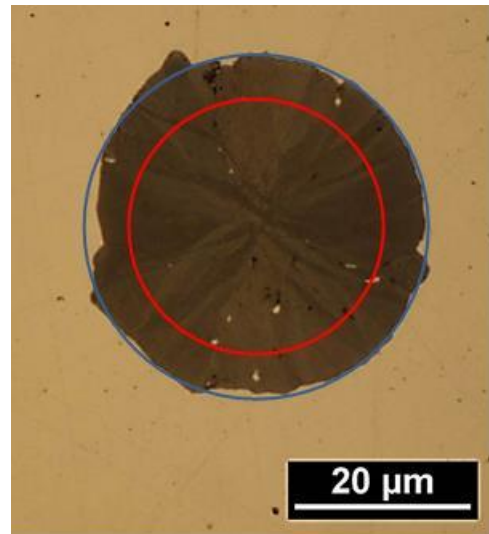


**Figure 9.17. Graphite nodule with the red circle indicating its approximate size at the end of solidification.**

Finally, after cycling 2000 times a fully ferritic high-silicon SGI from 100°C to 800°C, i.e. remaining **within the ferrite domain**, uneven dendritic precipitation of graphite could be observed on large spheroids, see fig. 9.18-b. This phenomenon has been associated with the growth of large spheroids at the expense of small ones that dissolve, and could be described quantitatively taking into account the increased solubility of carbon in high silicon ferrite at 800°C compared to temperatures below 700°C [EBE20].

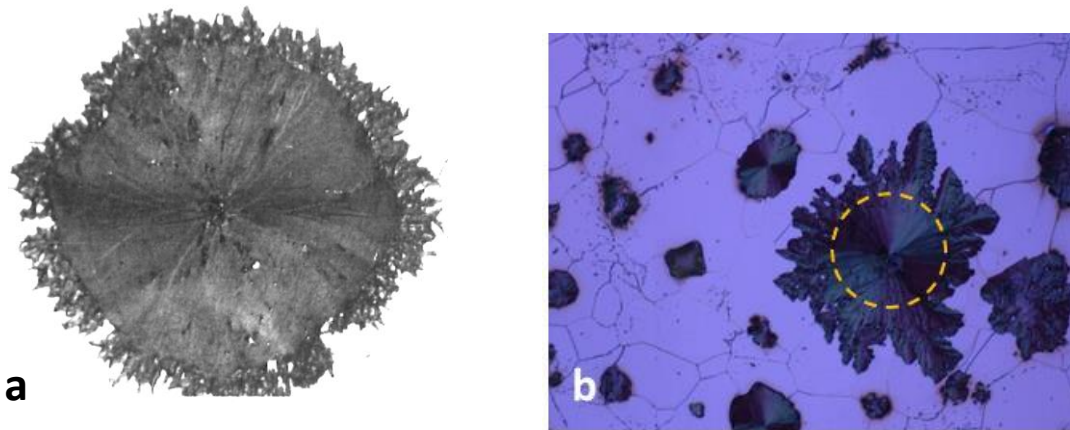


**Figure 9.18. a) Spiky graphite precipitated around a spheroid (25  $\mu\text{m}$  in radius) after 8 cycles from RT to 700°C for a total duration of 26 hours (adapted from [BER98]). The matrix was initially fully pearlitic and cementite decomposed during the process. b) Development of dendritic graphite protuberances onto the largest spheroids of a high-silicon SGI cycled 2000 times from 100°C to 800°C. The dashed circle –about 25  $\mu\text{m}$  in diameter- indicates the original size of the spheroid.**

### 9.11 Reverse eutectoid

Decomposition of the RT microstructure by reheating in the austenite field could be named reverse eutectoid. The transformation should be complete when dealing with heat-treating before ausferritising, while partial transformation will be considered for obtaining duplex matrix structure. The effect of heating rate and upper temperature on the formation of austenite has certainly been investigated many times in the past. The interest of the study by Wade and Ueda [WAD80] is that they compared materials with either ferritic or pearlitic initial microstructure. The former one decomposed more slowly than the latter one which may be due to the difference in the distance carbon has to diffuse for austenite formation. As a matter of fact, pearlite can change to austenite by carbon diffusion at the scale of the pearlite inter-lamellar spacing, while ferrite transforms by diffusion of carbon at the scale of the distance between graphite precipitates.

Wade and Ueda noticed that the transformation of ferrite to austenite starts mostly around the nodules at high heating rate, both around the nodules and at grain boundaries away from them at low heating rate. Their micrographs and the one shown in Fig. 9.19 suggest that microsegregation may also be of importance in determining the amount of ferrite transformed around the nodules and away from them. Thus, in contrast to the ferritic transformation during cooling, the modelling of austenite formation during heating apparently requires the consideration of microsegregations.

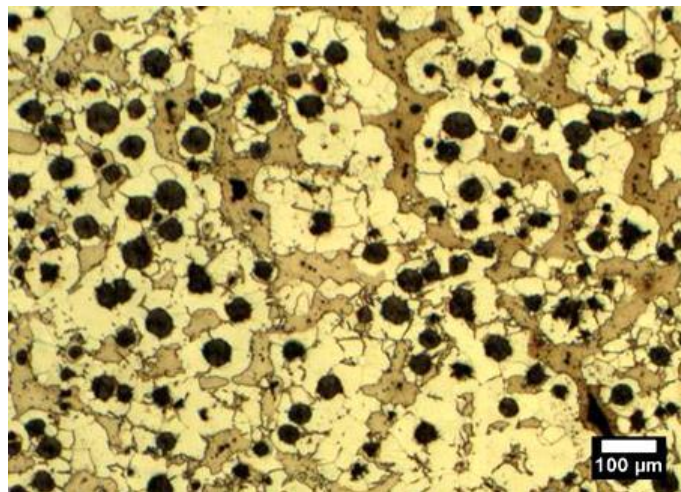


**Figure 9.19. Optical micrograph of a cast iron with 2.08 wt.% Si and 0.13 wt.% Mn. The sample was fully ferritised, then cooled to RT and finally introduced for 5 minutes in a furnace pre-heated at 800°C, and finally quenched to RT.**

### 9.12 A few words about fully pearlitic cast irons

The characteristics looked for pearlite are the same for all kinds of cast irons and were stated simply by Janowak and Gundlach [JAN82]: "fine pearlite with uniform strength and hardness". Such an aim calls for: 1) Increasing pearlite fineness, i.e. decreasing the interlamellar spacing, which increases hardness and improves strength, and: 2) Achieving a uniform interlamellar spacing of pearlite as it is thought to ensure uniform matrix hardness.

However, microsegregation develops in the last to solidify areas where it has been seen to decrease the reference eutectoid temperature of both the stable and metastable transformations, see Fig. 9.9. This can affect the formation of pearlite in fully pearlitic cast irons, leading eventually to heterogeneities in the interlamellar spacing of pearlite.

Rundman [RUN97] attempted to use alloying with elements segregating positively and negatively and selected so as to minimize the change in  $T_p$ . Several alloys were investigated around the following composition: 2.25% Si, 0.5% Mn, 0.5% Cu, 1% Ni and 0.1% Mo (in wt.%). As elaborated in chapter 10, a calculation based on Scheil's model for substitutional solutes but assuming rapid solid-state diffusion of carbon may conveniently represent the development of microsegregation during solidification of cast irons. Indeed, the temperature distribution  $T_p$  was found to be uniform for almost the entire matrix of the alloys selected by Rundman [LAC16] and this could be effective in uniforming the interlamellar spacing of the pearlite.

A very interesting result that could help for managing the development of microsegregation in silicon cast irons has been reported by Muhmond and Fredriksson [MUH15] and Franzen et al. [FRA19]. These authors observed that adding 1-3 wt.% Al to a high-Si cast iron reverses silicon segregation that becomes positive whilst that of Al remains negative.

Finally, the micrograph in Fig. 9.20 illustrates the large scattering of the size of the pearlite colonies in a CGI. It is quite possible that decreasing this size would improve the service properties.



**Figure 9.20. Polarized light micrograph of a pearlitic CGI.**

### 9.13 Summary

Stable and metastable eutectoid transformations compete so strongly during the cooling of silicon cast irons that up to 5% ferrite is often accepted in fully pearlitic grades, and similarly up to 5% pearlite in fully ferritic grades. The understanding of this competition is based on the description of carbon transfer from austenite to graphite as a controlling step

in the ferritic transformation. The most important feature remains that this process can only take place at a temperature below the critical three-phase domain and it has been detailed that a similar criterion applies to the pearlitic transformation. This condition is related to the fact that the ferrite or pearlite must inherit the content of substitutional solutes from the austenite.



# Chapter 10 – Microstructure modelling

Microstructure modelling consists in describing the formation or evolution of the phases during phase transformation. This is done in a so-called **representative volume element (RVE)** in which all quantities that characterize the microstructure are assumed to be homogeneous, i.e. constant at the scale of the RVE. Such a modelling is first developed through ad hoc schematics that represent the physical phenomena taking place, and may then be made quantitative if appropriate equations can be written.<sup>6</sup> The scale which is convenient for casting microstructure is typically the millimetre while the scale for heat transfer is instead the centimetre. Smaller scales could be necessary for the casting skin or for thin-wall castings solidifying rapidly, and larger scales are to be used for heavy-section castings.

Results obtained at a given scale may be used through averaging for dealing with phenomena taking place at higher scale. As an example, one can see the growth law of irregular eutectics described in Chapter 6 as resulting of an up scaling by averaging of branching phenomena occurring at lower-scale. In Fig. 10.1, the RVE for microstructure modelling is thus located between: 1) the nanometre scale which could be used to describe interface phenomena; and 2) the casting scale at which liquid pouring and mass movements are described. This chapter deals mostly with microstructure formation during solidification and shortly, at the very end, with solid-state transformation.

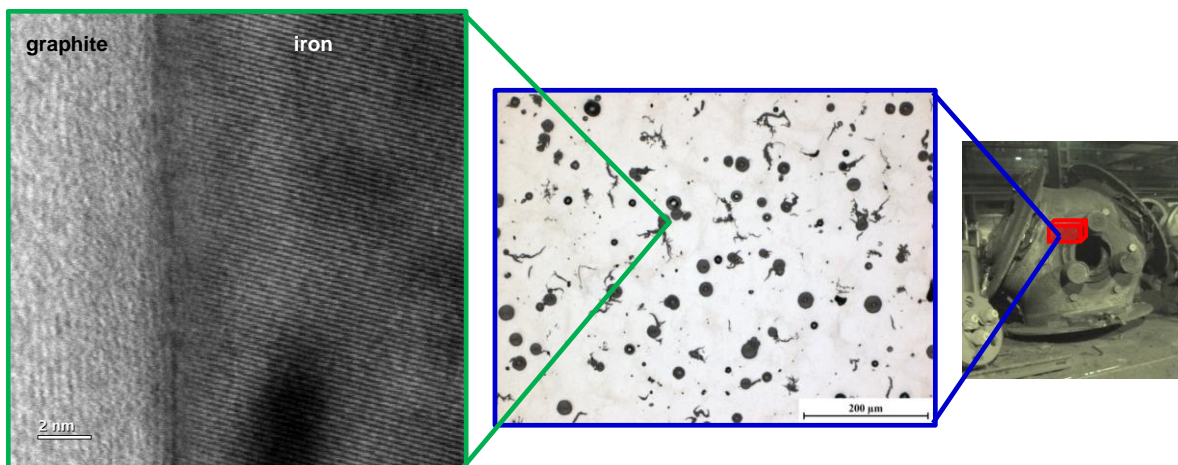


**Figure 10.1. Representative volume element at the scale of: a phase interface (left), microstructure (middle) and casting (red box in the image to the right). TEM micrograph by courtesy of Metallic Materials, FSU Jena.**

It has been emphasized in the preceding chapters that transformation kinetics in cast irons is mostly controlled by carbon redistribution. Accordingly, most of the approaches that

<sup>6</sup> In the whole of this chapter, compositions are given in mass fraction. As for example, the carbon content in graphite is  $w_C^{\text{gra}} = 1$ .

are presented below describe cast irons as pseudo-binary Fe-C alloys. However, it will be seen and illustrated that it is straightforward to account for redistribution of substitutional solutes by using Scheil's model to describe their microsegregation during solidification.

### 10.1 Historical steps: eutectic modelling

Oldfield [OLD66] pioneering work paved the way for micro-macro modelling of casting solidification and applied it to LGI. The evolving microstructure was assumed to be **fully eutectic**. Reviewing available data relating maximum eutectic undercooling and cell count, Oldfield proposed a nucleation law as  $N=A \cdot \Delta T^2$ , where  $\Delta T = \Delta T_{EUT}$ , i.e. stands for the undercooling with respect to the eutectic temperature. For step-by-step calculations, it was derived as  $dN=2 \cdot A \cdot \Delta T \cdot dT$ . With the background idea that nucleation sites are instantaneously activated when their characteristic undercooling is reached (see Chapter 4), this should have been written  $dN=2 \cdot A \cdot \Delta T \cdot d(\Delta T)$  as done by Su et al. [SU85]. We have also seen in Chapter 4 that it is more appropriate to use the undercooling with respect to the graphite liquidus rather than to the eutectic temperature when dealing with graphite nucleation. After nucleation, the eutectic cells grow and Oldfield ran preliminary calculations with a growth law for LG eutectic proportional to  $(\Delta T_{EUT})^2$  based on theoretical considerations (see Chapter 6). However, he found that minimum temperature and recalescence were better reproduced considering the growth rate being proportional to  $(\Delta T_{EUT})^{1.7}$ . Furthermore, the evident effect of **austenite dendrites** was mentioned but not included in the modelling approach.

A few years later Wetterfall et al. [WET72] performed a series of quenching experiments of SGI confirming that **spheroidal graphite** grows first directly from the liquid before getting encapsulated by austenite. For describing growth of a spheroid within an austenite shell, they considered the system represented in Fig. 10.2. These authors used mole fraction and molar volume when use will be made here of mass fraction and density. The size change of a spheroid of radius  $r^{gra}$  is such that the flux of carbon to the graphite/austenite interface equals the change of mass of the graphite spheroid. Equating these two quantities gives:

$$\pi \cdot (r^{gra})^2 \cdot D_C^\gamma \cdot \rho^\gamma \cdot \left. \frac{\partial w_C^\gamma}{\partial r} \right|_{r=r^{gra}} = \frac{dr^{gra}}{dt} \cdot \pi \cdot (r^{gra})^2 \cdot \rho^{gra} \cdot (w_C^{gra} - w_C^{\gamma/gra}) \quad (10.1)$$

where  $r$  is the radial position (for a frame attached to the spheroid centre) and  $\left. \frac{\partial w_C^\gamma}{\partial r} \right|_{r=r^{gra}}$  is the carbon gradient in austenite at the graphite/austenite interface. In the above equation and the following ones,  $w_C^{\phi/\varphi}$  is the carbon content of the phase  $\phi$  at the interface with the phase  $\varphi$ . Unless otherwise stated, local equilibrium is assumed at the interfaces, meaning  $w_C^{\phi/\varphi}$  values are given by the equilibrium phase diagram.

Considering a quasi-steady state diffusion process, the carbon content in austenite is expressed as  $w_C^\gamma = a/r + b$ . After identification of the constants  $a$  and  $b$ , one gets:

$$\left. \frac{\partial w_C^\gamma}{\partial r} \right|_{r=r^{gra}} = \frac{r^\gamma}{r^{gra}} \cdot \frac{w_C^{\gamma/1} - w_C^{\gamma/gra}}{r^\gamma - r^{gra}} \quad (10.2)$$



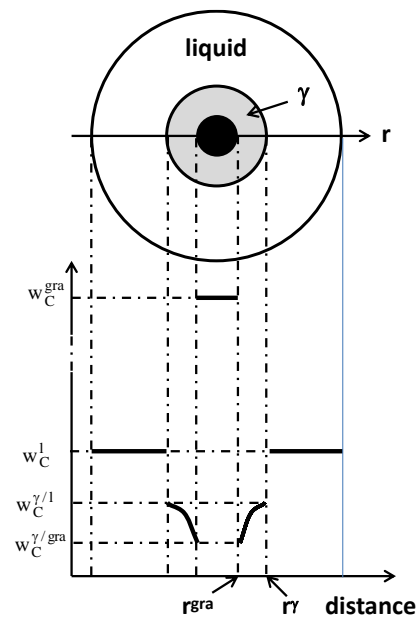
where  $r^\gamma$  is the outer radius of the austenite shell.

Introducing (10.2) in equation (10.1) gives the growth law for the graphite spheroid:

$$\frac{dr^{\text{gra}}}{dt} = D_C^\gamma \cdot \frac{\rho^\gamma}{\rho^{\text{gra}}} \cdot \frac{r^\gamma}{r^{\text{gra}} \cdot (r^\gamma - r^{\text{gra}})} \cdot \frac{w_C^{\gamma/1} - w_C^{\gamma/\text{gra}}}{w_C^{\text{gra}} - w_C^{\gamma/\text{gra}}} \quad (10.3)$$

Finally, Wetterfall et al. made a balance of carbon between austenite and graphite when all the liquid has transformed that was indeed the lever rule. Using it, they showed that the ratio  $r^\gamma/r^{\text{gra}}$  should be 2.4 during growth of the spheroidal eutectic entity. The authors verified this ratio by measurements on their samples, thus demonstrating that growth of graphite and austenite in SGI are related by a mass balance (see the discussion in section 7.2).

**Figure 10.2. Schematic of carbon distribution around a graphite spheroid (black circle), within the austenite shell and in the liquid. The origin of the distance is the spheroid's centre.**



A few years later, Owadano et al. [OWA77] used the above derivation to write a similar equation for describing the growth rate of the austenite shell. They considered that the liquid is homogeneous at a composition located along the metastable extrapolation of the austenite liquidus, though not accounting for possible change in temperature. They obtained the following growth law for the austenite shell:

$$\frac{dr^\gamma}{dt} = D_C^\gamma \cdot \frac{\rho^{\text{gra}}}{\rho^\gamma} \cdot \frac{r^{\text{gra}}}{r^\gamma \cdot (r^\gamma - r^{\text{gra}})} \cdot \frac{w_C^{\gamma/1} - w_C^{\gamma/\text{gra}}}{(w_C^{1/\gamma} - w_C^{\gamma/1})} \quad (10.4)$$

where  $w_C^{1/\gamma} = w_C^l$  as the liquid is assumed chemically homogeneous.

Later in this chapter, a more complete equation is given that accounts for the bulging effect of the graphite spheroid and for the effect of temperature change.

In the above approaches for LG and SG solidification, a **fully eutectic** microstructure was assumed as schematically represented in Fig. 10.3. Accordingly, the change of the

volume of solid during solidification,  $dV^s/dt$ , is given by summing up the volume change of all eutectic cells:

$$\frac{dV^s}{dt} = \sum_i n_i \cdot 4 \cdot \pi \cdot (r_i)^2 \cdot \frac{dr_i}{dt} \cdot \Psi \quad (10.5)$$

where  $n_i$  is the number of eutectic entities in class  $i$  (i.e. nucleated at the same instant) and  $r_i$  their radius at time  $t$ .  $\Psi$  is introduced to account for impingement between the growing eutectic entities, and is generally expressed as a power of the liquid volume fraction at time  $t$  (an exponent of 1 corresponds to the Johnson-Mehl-Avrami correction).

Following Oldfield's paper, the development of microstructure simulation started slowly as evidenced in the review by Su et al. [SU85] at the conference "The Physical Metallurgy of Cast Iron". During this conference, two other papers dealing with simulation of microstructure formation during solidification were presented [FRA85b, FRE85]. For SGI, eqs. (10.2) and (10.4) were used and gave cooling curves mimicking the experimental ones [SU85, FRA85b] with some discrepancies that were discussed in terms of nucleation kinetics of graphite. In the third work by Fredriksson and Svensson [FRE85], the modelling approach was extended by allowing for competition between stable and metastable eutectics in LGI and SGI.

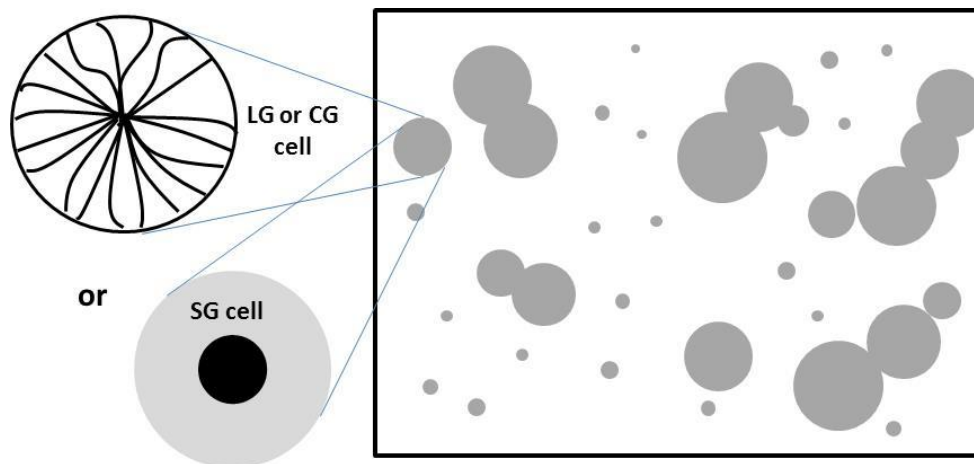


**Figure 10.3. The RVE is filled with liquid and either LG, CG or SG eutectic entities or cells.**

Two years later, many papers concerned with cast irons were presented at the conference "State of the art of computer simulation of casting and solidification processes". These included a few papers on microstructure formation but also simulations at the scale of the parts, i.e. putting emphasis on either or both filling stage and heat transfer. Some works considered the coupling between microstructure formation and heat transfer at the casting scale. Finally, at the next conference "Physical Metallurgy of Cast Iron" held in 1989, an entire session was devoted to solidification modelling, including a few papers on microstructure formation, although most of them dealt with simulation at the casting scale. At that time, no progress had been made in the equations describing eutectic solidification

of cast irons, but the role of **austenite dendrites** was again stressed [STE90] as they are observed in **both hypo- and hyper-eutectic alloys**. First modelling approaches of primary austenite growth were however proposed, see next section.

### 10.2 Nucleation and growth of primary austenite

Upon solidification of a hypoeutectic cast iron, it is expected that austenite grains form a chill zone at the surface of the mould that evolves in a columnar zone and possibly in a central equiaxed zone. While evidencing ex-austenite dendrites may be done by quenching or chemical etching, characterizing austenite grains in graphitic iron is performed by EBSD on quenched samples [HER19] or by **direct austempering after solidification** of the material (so-called **DAAS**, which requires nickel to be added to the alloy [RIV04]). The dendritic structure may be characterized by the primary and secondary arm spacings, and the grain structure by the size and density of the grains.

As a rule, the size of the austenite grains is much larger than eutectic cell size. In SGI, values of up to 2 mm in the columnar zone of a hypoeutectic alloy [GOR18] and 1 mm in the equiaxed zone of a hypereutectic alloy [RIV11] have been reported. They are even larger in LGI, being several millimetres in size in near eutectic [RIV11] and hypoeutectic [DIO07] alloys. Qualitatively, it seems established that austenite grain size increases when CE diminishes. Some works have also been done on inoculation of austenite grains which favours the columnar to equiaxed transition (CET) [DIO07, LOP20]. Finally, it is worth mentioning that, using the DAAS technique, Boeri et al. [BOE18] could demonstrate that microporosity is intragranular rather than intergranular in CGI.

Miyake and Okada [MIY98] studied the formation of austenite grains of hypoeutectic alloys which completed their solidification in the metastable system. In this case, the austenite grains could be easily identified by simple etching, see Fig. 10.4. The authors noticed that the macrostructure changes from equiaxed to columnar when either of the cooling rate, the superheating temperature and melt holding time were increased.

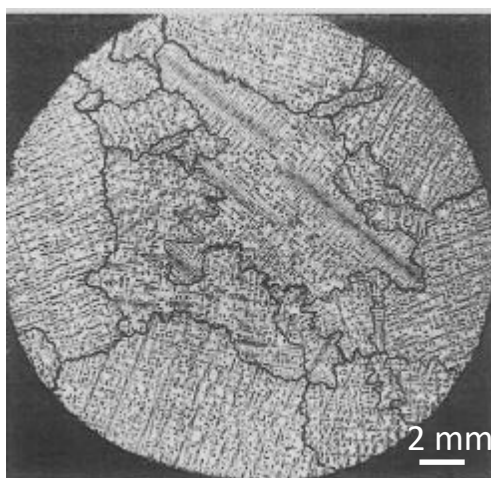


**Figure 10.4. Section of a hypoeutectic alloy having undergone white eutectic solidification [MIY98]. The various grains have been differentiated based on the orientation of their dendritic network.**

The simplest approach to describe austenite growth is to consider there is no barrier to its nucleation so that its growth starts as soon as the austenite liquidus of the alloy is reached. Moreover, upon further temperature change, the composition of the liquid at the austenite/liquid interface follows the austenite liquidus. With the further assumption that carbon diffuses infinitely rapidly in both austenite and liquid, the carbon mass balance obeys the **lever rule** that describes full equilibrium, which means that both solid and liquid are chemically homogeneous at any temperature within the solidification interval, and their respective composition given by the phase diagram. This corresponds to what was called ideal solidification in Chapter 3. Using compositions given per mass, the carbon balance is thus written:

$$w_C^\gamma \cdot f^\gamma + w_C^l \cdot f^l = w_C^0 \quad (10.6)$$

where the mass fractions of austenite,  $f^\gamma$ , and of liquid,  $f^l$ , are such that  $f^\gamma + f^l = 1$ , and  $w_C^0$  is the nominal carbon content of the alloy.

The austenite and liquid compositions are related by the equilibrium partition coefficient:

$$k_C^{\gamma/l} = w_C^\gamma / w_C^l \quad (10.7)$$

The liquid fraction and its derivative, when the partition coefficient is constant, are thus written:

$$f^l = \frac{w_C^0 - k_C^{\gamma/l} \cdot w_C^l}{w_C^l \cdot (1 - k_C^{\gamma/l})} \quad (10.8)$$

$$df^l = -df^\gamma = -\frac{w_C^0}{(1 - k_C^{\gamma/l}) \cdot (w_C^l)^2} \cdot dw_C^l \quad (10.8')$$

Such a simplified approach would not allow accounting for nucleation and growth undercooling of the austenite solidification front, and thus would preclude describing the **columnar to equiaxed transition (CET)** illustrated in Fig. 10.4. In fact, there is no report showing a relation between undercooling and number of austenite grains in cast irons so that any model for the CET could not be checked against experimental data. The few available models for primary austenite growth [CHA92, FRA97] only consider equiaxed grains and selected a nucleation law for austenite allowing fitting experimental thermal records.

Nevertheless, growth undercooling of dendrites can be predicted by considering that the dendrite tips at the front of both equiaxed and columnar grains are described with a parabolic shape obeying the following equation:

$$R_{\text{tip}} \cdot V_{\text{growth}}^\gamma / 2 \cdot D_i^l = (w_i^{l*} - w_i^l) / (1 - k_i^{\gamma/l}) \cdot w_i^{l*} \quad (10.9)$$

where  $R_{\text{tip}}$  is the tip radius,  $V_{\text{growth}}^\gamma$  the growth rate,  $D_i^l$  the diffusion coefficient of any solute  $i$  in the liquid,  $w_i^{l*}$  and  $w_i^l$  the  $i$  content in the liquid at the interface and far from it, respectively.

An additional relation is needed to get  $R_{\text{tip}}$  knowing  $V_{\text{growth}}^{\gamma}$  which is given by the so-called solvability criterion and well approximated by the marginal stability criterion. The extension to multicomponent alloys of the marginal stability criterion has been described [BOB88, RAP90] and applied to Fe-C-Si alloys [SIR93] and to cast irons by Mampaey [MAM98a, MAM98b]; see also Fig. 3.13-a in section 3.7. In the dendritic regime, this latter work gives the following relationship between the growth rate (in  $\mu\text{m/s}$ ) and the tip undercooling,  $\Delta T_{\text{tip}}$ , for a Fe-3.1C-2.0Si (wt.%) alloy:

$$V_{\text{growth}}^{\gamma} = 1.01 \cdot (\Delta T_{\text{tip}})^{2.60} \quad (10.10)$$

Because the partition coefficient of silicon is close to one, this relation is little sensitive to the silicon content.

In the case of equiaxed growth of austenite, solidification within the grains is then described following lines delineated in the review by Rappaz [RAP89]. Fig. 10.5 shows a comparison of calculated and experimental cooling curves [FRA97] of a cast iron solidified in a cylinder. Curves are for the centre ( $X=0$ ) and 1/3 of the radius away from the centre ( $X=0.3R$ ). It is seen that the temperatures of the thermal arrests are properly reproduced.

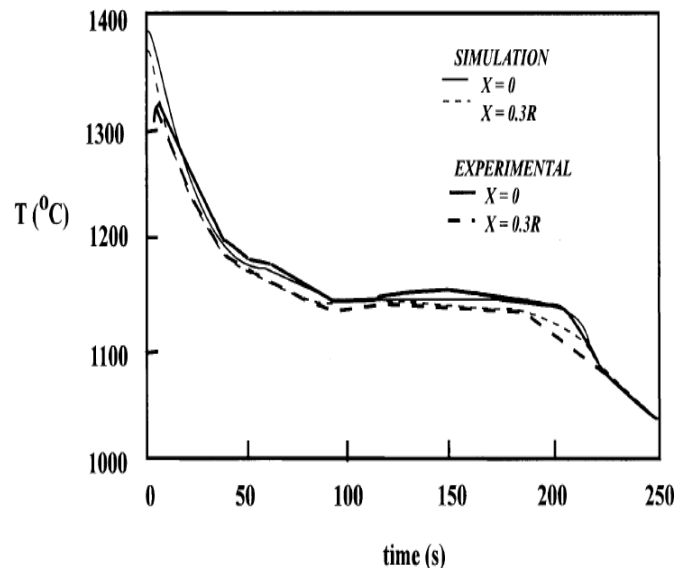


**Figure 10.5. Comparison of experimental and predicted cooling curves in a cylindrical casting of  $R=20$  mm in radius (adapted from [FRA97]).  $X=0$  and  $X=0.3R$  indicate the position with respect to the casting centre.**

In the works of Fras et al. [FRA97] and Chang et al. [CHA92], the calculated curves show eutectic solidification following primary precipitation of austenite. However, none of these works reported on the way the coupling between primary growth of austenite and eutectic solidification was carried out. This coupling was later achieved by using cellular automata [BUR12, ZHU15] but this technique is nowadays overtaken by phase field modelling. In the meantime, a physical approach that is described in section 10.5 was developed based on appropriate mass balances.

### 10.3 Microsegregation related to primary austenite

Other interstitial elements, such as O and N, are expected to follow the same behaviour as carbon. Accordingly, it may be considered that their solid-state diffusion rate is large enough so that their redistribution between liquid and austenite follows also the lever rule. On the contrary, solid-state diffusion of substitutional solutes (noted  $i$ , such as Cu, Mn, Si, etc.) is so slow that it can be neglected. Still maintaining the assumption of a homogeneous liquid composition leads to the so-called Scheil's model which states that the solute rejected by an increment of the austenite fraction (per weight),  $df^\gamma$ , equals the increase in solute in the liquid,  $dw_i^l$ , giving the following mass balance:

$$(w_i^l - w_i^{s*}) \cdot df^\gamma = (1 - f^\gamma) \cdot dw_i^l \quad (10.11)$$

where  $w_i^{s*}$  is the composition of the solid that deposits during the increment  $df^\gamma$ .

Except at very high solidification rates that are irrelevant for sand casting, and except for faceted phases such as graphite (see the following section), local equilibrium applies at the solid/liquid interface which means that  $w_i^{s*} / w_i^l = k_i^{\gamma/l}$  with  $k_i^{\gamma/l}$  the equilibrium partition coefficient of element  $i$ . The above Scheil's mass balance can be integrated by steps using  $df^\gamma$  as a variable if the partition coefficient changes during solidification. If the partition coefficient is constant, Eq. (10.11) can be integrated analytically, giving:

$$w_i^l = w_i^0 \cdot (1 - f^\gamma)^{1-k_i^{\gamma/l}} \quad (10.12)$$

or

$$f^1 = 1 - f^\gamma = \left( \frac{w_i^l}{w_i^0} \right)^{1/(1-k_i^{\gamma/l})} \quad (10.12')$$

where  $w_i^0$  is the nominal content of the alloy in  $i$  element.

In practice, the cooling rate in complex castings can vary in a large range so that, most generally, it might be considered that redistribution of solutes during solidification follows a path located between the predictions given by the lever rule and by Scheil's model. The lever rule will be approached in the heaviest sections while Scheil's model will apply at the casting surface. However, because the fraction of primary austenite is generally small, the build-up of microsegregation during this step is small and the difference between the lever rule and Scheil's predictions will anyway be limited. In other words, this is only during eutectic solidification that significant microsegregation can develop as described in a subsequent section.

### 10.4 Growth kinetics of primary graphite

Growth kinetics of primary graphite is to be studied on hypereutectic alloys with a CE value high enough for the size of the precipitates to become large enough before the eutectic reaction takes place. Very few quantitative results are available, in particular concerning LG. However, the classical studies by Chaudhari et al. [CHA74, CHA75] showed clear trends which have been reanalysed by accounting for the actual composition of the

alloys [CAS20]. The main output of this analysis is illustrated with the Fe-C isopleth section in Fig. 10.6 where the dashed lines indicate the temperature of the thermal arrest for primary precipitation of graphite that can be observed in LGI (LG) and SGI (SG). These lines are almost parallel to the graphite liquidus, indicating that thermal arrest occurs at about the same undercooling, independent of CE, but being about twice as large for SG as for LG. The experiments by Chaudhari et al. showed the results for SG not to be sensitive to inoculation, leading to conclude that the difference between LG and SG is to be found in the growth kinetics of primary graphite.

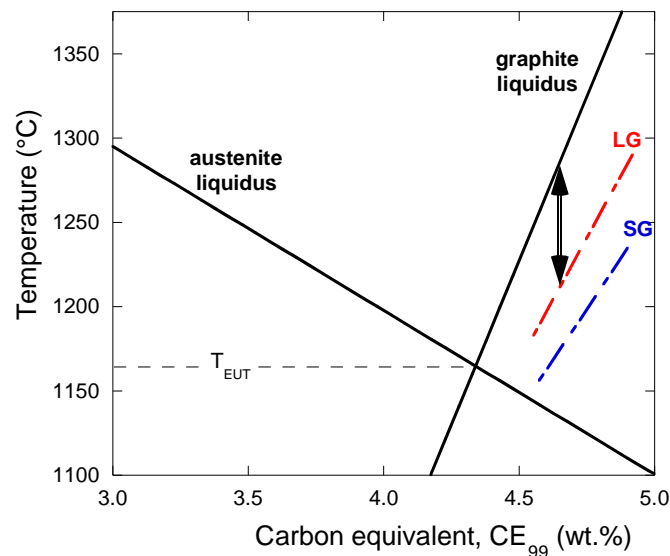


**Figure 10.6.** The solid lines represent the calculated liquidus (with their metastable extensions) for austenite and graphite for 2.6 wt.% Si (eqs. 2.2), while the dot-dashed lines represent the locus of the thermal arrest of primary graphite for LGI (LG) and SGI (SG) [CAS20]. The double arrow illustrates how is determined the undercooling with respect to the graphite liquidus for a particular  $CE_{99}$  value.

For modelling growth of primary lamellar graphite, Amini and Abbaschian [AMI13] assumed that the lengthening of the primary plates is controlled by carbon diffusion in the liquid while their thickening proceeds by means of **2D nucleation and lateral growth** of new blocks (see Chapter 5, Fig. 5.7). The authors compared their predictions to their own measurements which are the only ones available in the literature.

For spheroidal growth, two approaches have been considered, a diffusion based model [LES98a] and a modified form of the above 2D nucleation and lateral growth model illustrated with Fig. 5.15-c [LAC17a]. The diffusion based model considers that growth of spheroidal graphite from the liquid involves two mechanisms in series: 1. Diffusion of carbon from the liquid to the spheroids; and 2. Interfacial reaction of order 2 at the graphite/liquid interface characterized with a constant  $K$ . Assuming steady-state growth of the spheroids, the carbon flux must be the same for the two processes, leading to the following equalities for an isolated spheroid [ZHA97, LES98a]:

$$-\rho^{\text{gra}} \cdot (w_{\text{C}}^{\text{gra}} - w_{\text{C}}^{\text{i}}) \cdot \frac{dr^{\text{gra}}}{dt} = -D_{\text{C}}^{\text{l}} \cdot \rho^{\text{l}} \cdot \left. \frac{\partial w_{\text{C}}^{\text{l}}}{\partial r} \right|_{r^{\text{gra}}} = -K \cdot \rho^{\text{l}} \cdot (w_{\text{C}}^{\text{i}} - w_{\text{C}}^{\text{l/gra}})^2 \quad (10.13)$$

where  $w_{\text{C}}^{\text{i}}$  is the carbon content in the liquid at the graphite/liquid interface while all other terms have already been defined.

The assumption of steady state growth allows expressing the carbon gradient in the liquid, and from that solving the right part of Eq. (10.13) to express  $w_{\text{C}}^{\text{i}}$  and then calculate the growth rate of the spheroids using the left part of Eq. (10.13) [LES98a, CAS20].

The 2D nucleation lateral growth model of spheroids was derived more recently (see Chapter 5) and led to the following growth rate equation for a near-eutectic alloy [LAC17a]:

$$\frac{dr^{\text{gra}}}{dt} = 2.6 \cdot 10^{-11} \cdot (\Delta T_{\text{L}}^{\text{gra}})^{17/6} \cdot \exp\left(-\frac{720}{\Delta T_{\text{L}}^{\text{gra}}}\right) \text{ m.s}^{-1} \quad (10.14)$$

Equations (10.13) and (10.14) give the growth rate of individual spheroids. This must be coupled with a nucleation law to express the number of spheroids per unit volume and with a carbon mass balance to evaluate the change in carbon content of the liquid as graphite precipitates. Fig. 10.6 compares the output of these two models in the case of a highly hypereutectic SGI cooled at about 3°C/s [CAS20] when the nucleation constant is set to  $A_1=10 \text{ mm}^{-3} \cdot \text{K}^{-1}$  in the assumed nucleation law  $N_{\text{V}} = A_1 \cdot \Delta T_{\text{L}}^{\text{gra}}$ ; see Chapter 4, Eq. (4.14). While Eq. (10.13) predicts by far too large growth rates for  $K$  set to 0.5 m/s [GHE14], Eq. (10.14) allows reproducing the high undercooling needed before growth of SG becomes significant. This significant difference gives an indirect support to the latter model that considers spheroidal graphite grows by successive 2D nucleation of new growth blocks at their outer surface and the lateral growth of these blocks parallel to the surface.

What is also seen in Fig. 10.6 is that the solidification path of hypereutectic alloys hits the extrapolation of the austenite liquidus at a temperature that is significantly lower than  $T_{\text{EUT}}$ . Analysing the start of the eutectic reaction in near-eutectic and mildly hypereutectic alloys strongly suggested that the eutectic reaction in these alloys also needs that a high enough undercooling with respect to the graphite liquidus has been reached. In other words, this is **not only inoculation and graphite nucleation** that controls the eutectic reaction but also the need that the carbon content is high enough in the liquid to **ensure graphite growth** [CAS20]. For hypo-eutectic and mildly hyper-eutectic alloys, precipitation of austenite provides the necessary increase in carbon content in the liquid. For such alloys, one can imagine a strong interplay between austenite and graphite growth undercooling which may well explain that confusion arises when analysing the nature of near eutectic and mildly hypereutectic alloys on the basis of TA records [CHA74, CHA75].



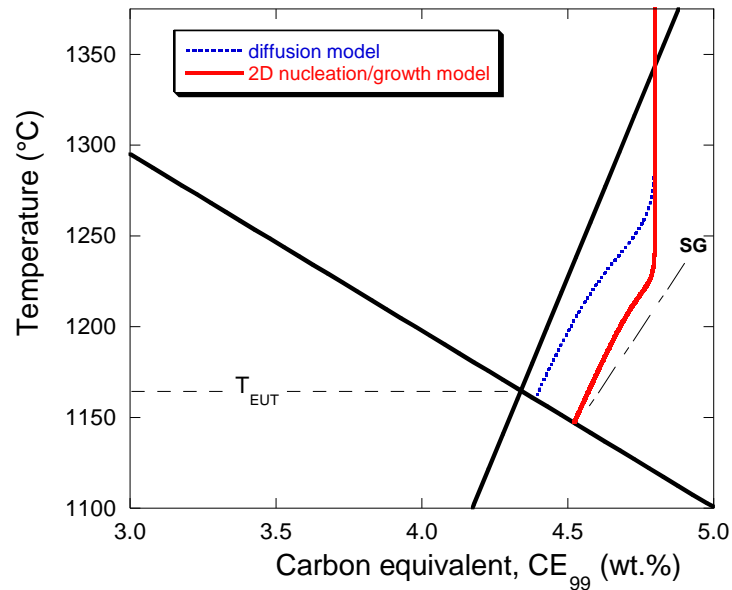


**Fig. 10.7. Solidification path during primary precipitation of spheroidal graphite according to the classical diffusion model (red curve) and to the 2D nucleation lateral growth model (blue curve). The black solid lines are the austenite and graphite liquidus calculated for 2.6 wt.% Si with Eqs. (2.2). The dashed line represents the arrest recorded during TA analysis of highly hyper-eutectic SGI, see Fig. 10.6. Calculations were performed with a nucleation constant  $A_1=10 \text{ mm}^{-3}\cdot\text{K}^{-1}$ .**

### 10.5 Eutectic solidification

After primary precipitation of austenite or graphite starts the main solidification stage, i.e. the eutectic reaction. The microstructure during eutectic solidification of any types of alloys is schematically illustrated with Fig. 10.8 that differs from Fig. 10.3 by the fact that off-eutectic austenite dendrites have been added.

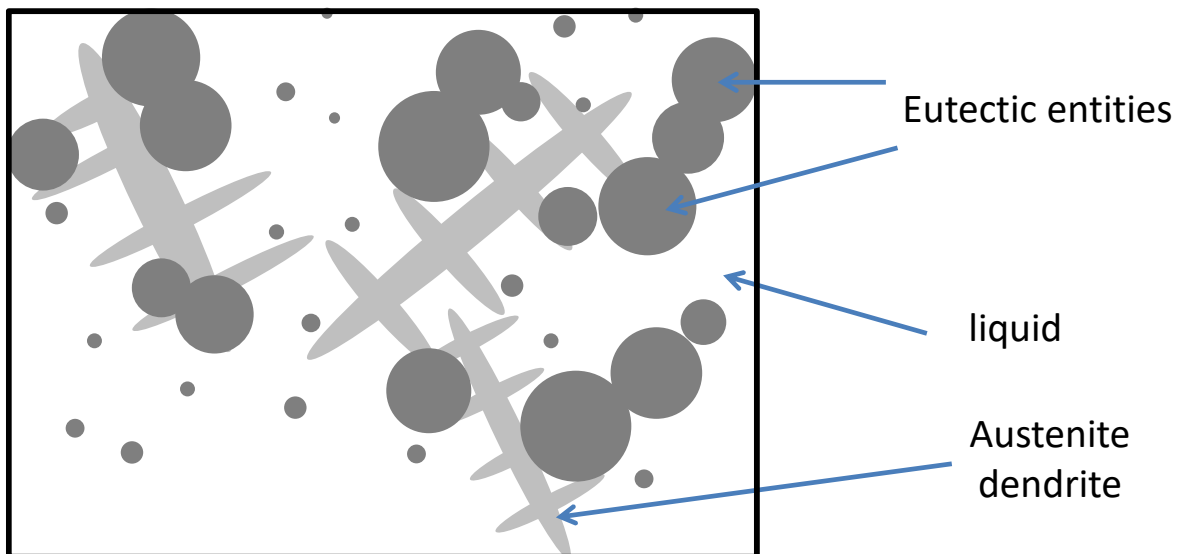


**Figure 10.8. The RVE is filled with liquid, austenite dendrites and either LG, SG or CG eutectic entities or cells. Same as in Fig. 10.3 with off-eutectic austenite added.**

The usual approach for solidification of hypoeutectic alloys considers that graphite can nucleate and grow as soon as  $T_{EUT}$  is reached, and thus that eutectic entities can form and start growing. The off-eutectic austenite dendrites are those formed during primary austenite precipitation that continue growing, or can partially remelt as suggested by Oldfield [OLD66] in case of recalescence, based on the idea that the liquid composition should follow the extrapolation of the austenite liquidus during the eutectic solidification. This view is one of the milestones on which experimental understanding of cast iron solidification has been based since the 1960s.

For hyper-eutectic alloys, austenite appears with some undercooling with respect to  $T_{EUT}$  as seen in the previous section, while nucleation and growth of primary precipitates of graphite might have already started. Experimental evidences show that there is a transient stage for the formation of eutectic entities during which off-eutectic austenite can develop. Once a high enough number of eutectic entities has been formed the bulk eutectic transformation takes place.

On a modelling point of view, this means that primary phase, either austenite or graphite, should be properly accounted for in the equations describing eutectic growth and such a description has been lacking until the mid of the 1990s. For this modelling, it may be safely assumed that local equilibrium is satisfied at the austenite/liquid interface even for thin-wall casting. If it is further considered that the composition of the liquid is homogeneous because of rapid diffusion of any solutes in the liquid, then the solidification path follows the metastable extrapolation of the austenite liquidus. These assumptions give the possibility of relating the temperature in the RVE to the composition of the remaining liquid. In turn, this allows to readily solving the growth equations which are based on the **overall mass balance** and the **carbon mass balance**. At any time during eutectic solidification, the RVE consists of a volume of primary phase P (either austenite or graphite depending on the nature of the cast iron),  $V^P$ , of off-eutectic austenite,  $V^{\gamma,off}$ , of eutectic,  $V^{eutectic}$ , and of remaining liquid,  $V^{liquid}$ :

$$V = V^P + V^{eutectic} + V^{\gamma,off} + V^{liquid} \quad (10.15)$$

The RVE is considered to be closed to exchange of matter, meaning that this is its mass which is conserved, while its volume  $V$  can differ from its initial value  $V^0$ . The total mass balance is expressed as:

$$\rho^{liquid} \cdot V^0 = \rho^P \cdot V^P + \rho^{eutectic} \cdot V^{eutectic} + \rho^{\gamma} \cdot V^{\gamma,off} + \rho^{liquid} \cdot V^{liquid} \quad (10.16)$$

where  $\rho^\varphi$  denotes the density of the constituent  $\varphi$ .

The carbon mass balance is then written:

$$w_C^0 \cdot \rho^{liquid} \cdot V^0 = \overline{w}_C^P \cdot \rho^P \cdot V^P + \overline{w}_C^{eutectic} \cdot \rho^{eutectic} \cdot V^{eutectic} + \overline{w}_C^{\gamma} \cdot \rho^{\gamma} \cdot V^{\gamma,off} + w_C^{liquid} \cdot \rho^{liquid} \cdot V^{liquid} \quad (10.17)$$

where  $w_C^0$  is the nominal carbon content of the alloy and  $\overline{w}_C^\varphi$  is the average carbon content in the constituent  $\varphi$  (P, eutectic and off-eutectic austenite). With the above

assumptions, the liquid composition is that of the austenite liquidus at the corresponding temperature:  $w_C^{\text{liquid}} = w_C^{1/\gamma}$ .

Austenite formed during the eutectic,  $V^{\gamma,\text{off}}$ , adds up to dendritic primary austenite in the case of hypoeutectic alloys while it is a new constituent in the case of hypereutectic alloys. For both cases, the austenite carbon content will be assumed homogeneous (as in the lever rule), i.e. such that:

$$\bar{w}_C^\gamma = w_C^\gamma = k_C^{\gamma/1} \cdot w_C^{1/\gamma} \quad (10.18)$$

For simulation using successive time increments, the above mass balances are differentiated with respect to time. Noting that primary deposition has stopped during the eutectic reaction, and assuming that the densities do not change with temperature and composition, the time derivative of the total mass balance Eq. (10.16) gives:

$$\rho^{\text{eutectic}} \cdot \frac{dV^{\text{eutectic}}}{dt} + \rho^\gamma \cdot \frac{dV^{\gamma,\text{off}}}{dt} + \rho^{\text{liquid}} \cdot \frac{dV^{\text{liquid}}}{dt} = 0 \quad (10.19)$$

Similarly, the time derivative of the carbon mass balance Eq. (10.17) is written:

$$\rho^{\text{eutectic}} \cdot \frac{d(\bar{w}_C^{\text{eutectic}} \cdot V^{\text{eutectic}})}{dt} + \rho^\gamma \cdot \frac{d(w_C^\gamma \cdot V^{\gamma,\text{off}})}{dt} + \rho^{\text{liquid}} \cdot \frac{d(w_C^{\text{liquid}} \cdot V^{\text{liquid}})}{dt} = 0 \quad (10.20)$$

where use has been made of Eq. (10.18).

The term for eutectic growth,  $dV^{\text{eutectic}}/dt$ , is expressed using the growth kinetics of individual eutectic entities. Accounting for size classes (index  $i$ ) issued from the nucleation step, this gives:

$$\frac{dV^{\text{eutectic}}}{dt} = \sum_i n_i \cdot 4 \cdot \pi \cdot (r_i)^2 \cdot \frac{dr_i}{dt} \cdot \Psi \quad (10.21)$$

where  $n_i$  is the number of eutectic entities in class  $i$  in the volume  $V$  and  $r_i$  their radius at time  $t$ .  $\Psi$  is the impingement factor as above.

The change of volume fraction of the solid for any time step during the eutectic transformation is thus given by the following sum:

$$dV^s = dV^{\text{eutectic}} + dV^{\gamma,\text{off}} \quad (10.22)$$

### 10.6 Step by step solidification modelling

For any time step, the change in solid fraction leads to latent heat release that should be coupled with an appropriate heat balance. For the case of a thermal analysis cup assumed having an homogeneous temperature at any time during cooling and solidification, the following heat balance has been found appropriate:

$$\rho \cdot V / A \cdot \left( C_p \cdot \frac{dT}{dt} - \Delta H \cdot \frac{dV^s}{dt} \right) = -\sqrt{\Delta} \cdot (T - T^0) \cdot t^{-0.5} \quad (10.23)$$

where  $\rho$  and  $C_p$  are, respectively, the density and the heat capacity of the metal at temperature  $T$ ,  $\Delta H$  is the latent heat of fusion of the metal,  $\Delta$  is a quantity characteristic of the mould and  $T^0$  is the ambient temperature.  $V$  is the volume of metal having an outer surface  $A$ , and  $V/A$  is the so-called casting modulus. During solidification, the specific heat  $C_p$  and the density  $\rho$  are calculated as a weighted average of the solid and liquid values.

The schematic diagram in Fig. 10.9 illustrates the calculations for microstructure prediction which have to be made between each heat balance calculation step. After liquid cooling down to the liquidus temperature,  $T_L$ , primary precipitation depends on the nature of the cast iron, either hypo- or hyper-eutectic. In most of the modelling approaches, the driving force for nucleation of austenite is neglected so that only its growth is described. Because solid-state carbon diffusion is rapid, the amount of austenite,  $V^\gamma = V^{\gamma,off}$ , is given by the lever rule applied to carbon. For hypereutectic alloys, nucleation of new graphite particles is subject to the condition that the maximum undercooling with respect to the graphite liquidus increases. The volume of precipitated graphite,  $V^{gra}$ , is then calculated using an appropriate growth law. This gives the carbon content in the remaining liquid with which the graphite liquidus of the remaining liquid and the undercooling are updated.

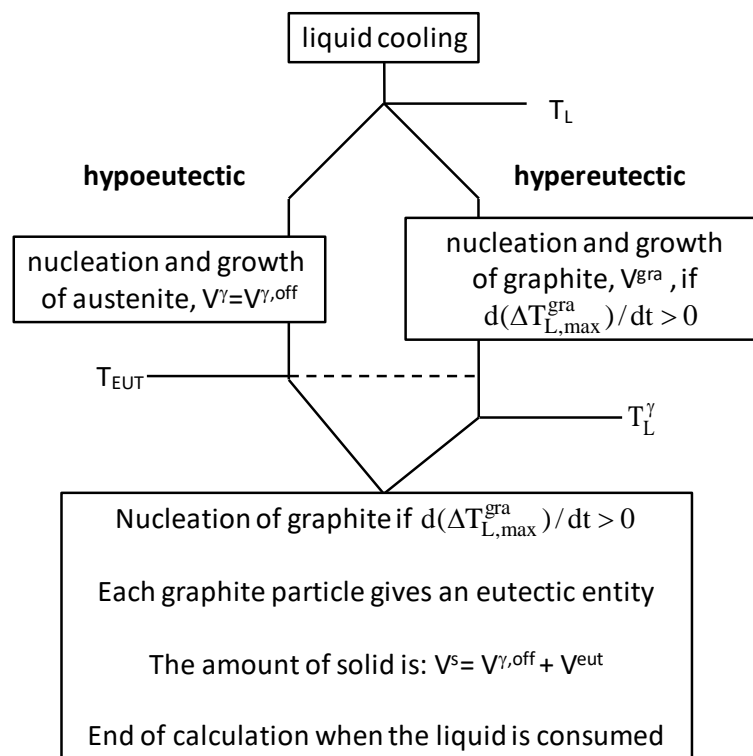


**Figure 10.9. Schematic of the successive steps for simulating microstructure formation during solidification of cast irons. For hypereutectic alloys, the temperature  $T_L^\gamma$  at which the austenite liquidus is reached depends on primary graphite precipitation and is in any case lower than  $T_{EUT}$ .**

In the classical approach, the eutectic stage of solidification of hypoeutectic alloys starts once  $T_{EUT}$  is reached, while this is when the metastable extrapolation of the austenite liquidus,  $T_L^\gamma$ , is reached for hypereutectic alloys. Eutectic solidification is then performed with the same routine for both types of alloys: every pre-existing graphite particle gives a eutectic entity. The possibility for nucleation of new graphite particles is checked as for primary graphite precipitation and, when this occurs, they are immediately changed to eutectic entities. The volume of solid is thus given by the sum of the eutectic entities,  $V^{eut}$ , and of the off-eutectic austenite, i.e. austenite dendrites,  $V^{\gamma,off}$ . The growth rate of the eutectic entities is calculated with the appropriate laws that depend on the kind of eutectic which is considered. After insertion in the derivative of the mass balances to get the change of the volume of solid,  $dV^S$ , this change is used to calculate the temperature evolution by means of Eq. (10.23).

A few possible improvements to the "classical" approach in Fig. 10.9 could be proposed that appear in red in Fig. 10.10. These are:

- Primary austenite in hypo-eutectic alloys grows with a tip undercooling  $\Delta T_{tip}$ . Accordingly, primary deposition ends when the solidification path encounters the extrapolation of the graphite liquidus, which happens at a temperature  $T_L^{G*}$  which is such that  $T_L^{G*} = T_L^\gamma - \Delta T_{tip}$ .

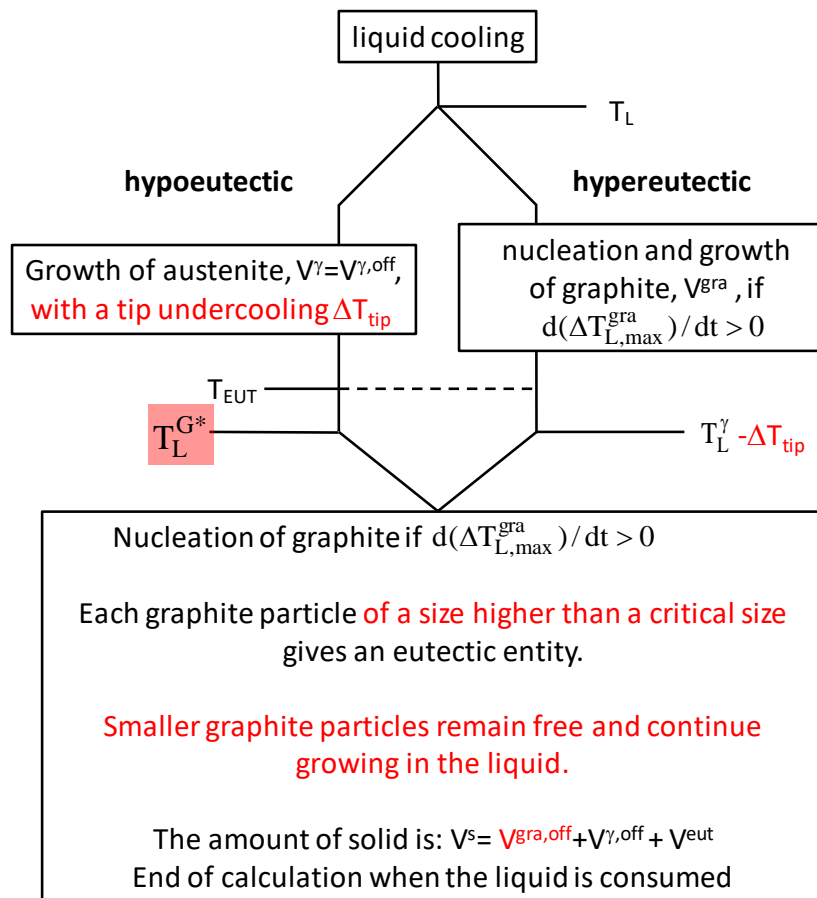


Figure 10.10. Same schematic as in Fig. 10.9 with in red indicated possible improvements of the modelling approach.

- Growth of primary graphite in hyper-eutectic alloys ends when the primary solidification path reaches the austenite liquidus shifted by  $\Delta T_{tip}$ . If nucleation of new austenite grains has to be taken into account, as done by Fras et al. [FRA97], both a nucleation stage and growth undercooling should be considered.

- Accounting for the possibility of graphite particles growing freely in the remaining liquid while the eutectic reaction has started implies to add a contribution  $V^{gra,off}$  to the volume of solid and thus to the mass balance (10.16) and the carbon balance (10.17). In this line, a first step has been recently (as for 2021) carried out to account for free growth of graphite between dendrites of hypoeutectic cast irons [TEW21]. The advantage of this addition is that it would allow relaxing the constraint of the liquid composition having to follow the austenite liquidus and would open new possibilities for describing the coupled zone in cast irons. It should be recalled that it has been reported that spheroids are only encapsulated in austenite once they have reached a diameter that varies between 7 and 15  $\mu\text{m}$  depending on the source, a value that is anyway well above the size of the nuclei.

### 10.7 Lamellar and compacted graphite eutectics

The simplest form for  $dr_i/dt$  to be introduced in Eq. (10.21) is that for eutectic cells of irregular eutectics, Eq. (6.6), with  $\phi$  the branching parameter:

$$\frac{dr_i}{dt} = \frac{\phi^2}{(1 + \phi^2)^2} \cdot a \cdot b \cdot \Delta T_{EUT}^2 \quad (10.24)$$

In addition to the volume increments, extending the derivation of Eq. (10.17) leads to the terms expressing the composition changes  $dw_C^{eutectic}$ ,  $dw_C^\gamma$  and  $dw_C^{liquid}$ . The two latter are constrained by the hypothesis that the liquid composition lies along the metastable extrapolation of the austenite liquidus and by the further assumption that carbon is homogeneous in austenite dendrites, i.e.  $dw_C^\gamma = k_C^{\gamma/1} \cdot dw_C^{liquid}$ . For LGI and CGI, one possibility to express  $d\bar{w}_C^{eutectic}$  is to consider that the two-phase eutectic has the same carbon content as the liquid from which it precipitates, leading to:

$$d(\bar{w}_C^{eutectic} \cdot V^{eutectic}) = w_C^{liquid} \cdot dV^{eutectic} \quad (10.25)$$

Numerical simulation can be simplified by considering an average cell size instead of a distribution. In case of continuous nucleation, the average size must be updated at each time step and this is made by writing that the volume of solid is preserved. The rate of latent heat release is not much affected by this procedure that has the advantages of easing computing and comparison to experimental results.

A first example is given in Fig. 10.11 that compares the predicted thermal records of a LGI and a CGI cast in a thermal cup. These calculations were performed with the same parameters (composition, nucleation law, etc.) for both alloys but  $\phi$  that was set to 2.5 for LGI and 10 for CGI. As expected, the undercooling and recalescence of the eutectic plateau for CGI is higher than for LGI.

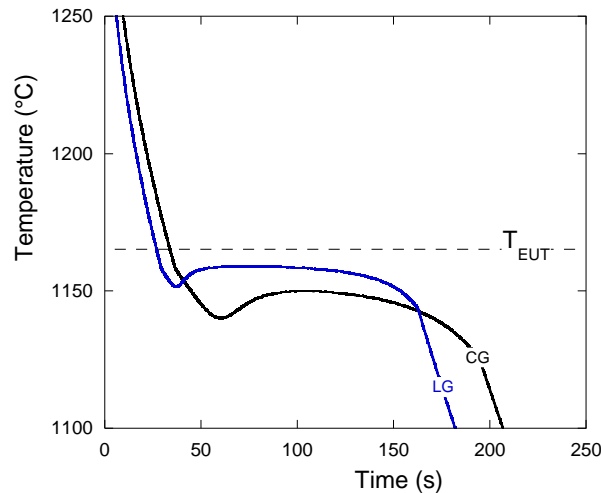


**Figure 10.11. Effect of the value of the branching parameter  $\phi$  on the predicted eutectic undercooling:  $\phi$  set to 2.5 for LG and 10 for CG.**

In a study on the transition between SG and CG that was carried out with a slightly hypereutectic alloy, a clear arrest associated with the formation of austenite was noticed when nucleation of graphite decreased and its shape turned to compacted [LAC21b]. An example of TA record is shown with the thin solid black curve in Fig. 10.12-a where are noticed the pre-eutectic arrest followed by a eutectic plateau with a marked recalescence. Setting  $\phi$  to 10, a first simulation was performed assuming austenite appears when the metastable extrapolation of the austenite liquidus is reached, which gave the dotted red curve in the graph. This simulation shows only a slope change when austenite appears, and also evidences that austenite does actually undergo a significant undercooling with respect to the extrapolated austenite liquidus. Fig. 10.12-b shows how the solidification path was modified in order to account for an austenite undercooling of  $10^{\circ}\text{C}$ . After primary graphite precipitation (along curve a), the point A was eventually reached at  $T_L^{\gamma} - \Delta T_{\text{tip}} = T_L^{\gamma} - 10^{\circ}\text{C}$ . Though the temperature is well below  $T_{\text{EUT}}$ , the growth rate of the CG cells is too low for the bulk eutectic reaction to take place and this is mostly off-eutectic austenite that can deposit. An intermediate stage was assumed to occur at constant temperature until the austenite liquidus was reached in B by rejection of carbon from austenite into the liquid. This somewhat expedient method allowed the simulation of a pre-eutectic plateau, as shown by the thick solid line in Fig. 10.12-a.

After this stage, solidification continued with the liquid composition following the austenite liquidus (along b) until the growth rate of the CG cells was high enough for the bulk eutectic reaction to take place. Note in Fig. 10.12-a that the simulated curves properly reproduce this reaction in terms of  $T_{\text{e,min}}$  and recalescence. The transition between stable and metastable eutectic was also introduced in this work [LAC21b] that allowed reproducing the decrease of recalescence in CGI when more and more of the solidification proceeds in the metastable system (along c).

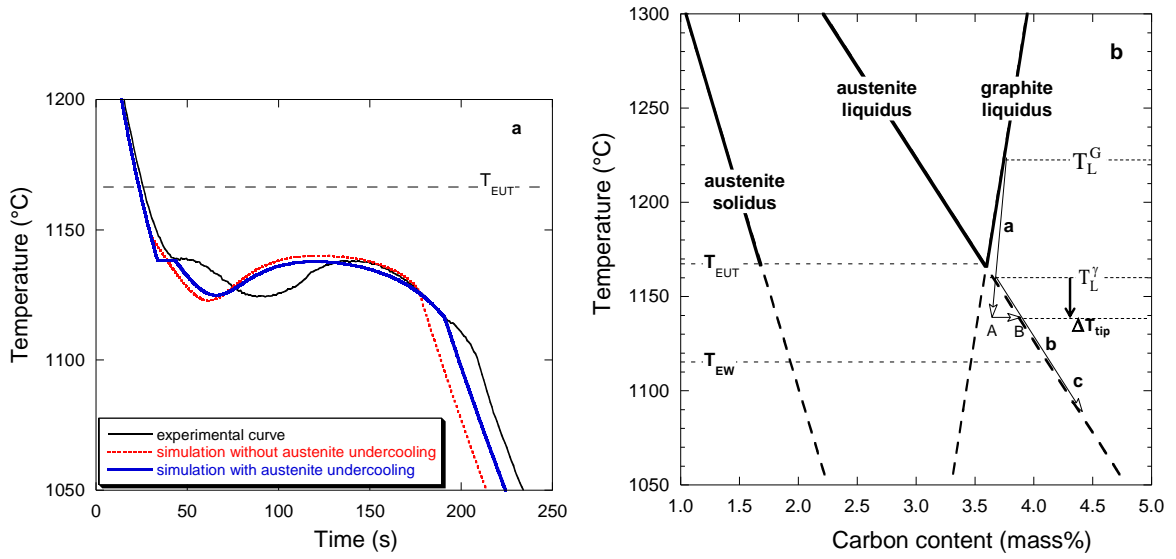


**Figure 10.12. Comparison of calculated and experimental TA curves of a slightly hypereutectic compacted graphite iron (a) and solidification path in the case where the formation of austenite occurs with an undercooling  $\Delta T_{tip}$  (b).**

### 10.8 Spheroidal graphite eutectic

In the case of SGI, the growth rate of a graphite spheroid of class  $i$  inside the austenite shell is given by Eq. (10.3) that was derived by Wetterfall et al.:

$$\frac{dr_i^{gra}}{dt} = D_C^\gamma \cdot \frac{\rho^\gamma}{\rho^{gra}} \cdot \frac{r_i^\gamma}{r_i^{gra} \cdot (r_i^\gamma - r_i^{gra})} \cdot \frac{w_C^{\gamma/1} - w_C^{\gamma/gra}}{w_C^{gra} - w_C^{\gamma/gra}} \quad (10.26)$$

The growth rate for the austenite shell is given as [LES98a]:

$$\frac{dr_i^\gamma}{dt} = D_C^\gamma \cdot \frac{\rho^{gra}}{\rho^\gamma} \cdot \frac{r_i^{gra}}{r_i^\gamma \cdot (r_i^\gamma - r_i^{gra})} \cdot \frac{w_C^{\gamma/1} - w_C^{\gamma/gra}}{(w_C^{1/\gamma} - w_C^{\gamma/1})} \cdot \left[ 1 + \frac{\rho^\gamma - \rho^{gra}}{\rho^{gra}} \cdot \frac{w_C^{\gamma/1} - w_C^{\gamma/gra}}{1 - w_C^{\gamma/gra}} \right] + \Delta(r_i^\gamma) \quad (10.27)$$

where it is seen that there are two more contributions compared to Eq. (10.4).

The first contribution is the second term inside the brackets and derives from the **graphite expansion** which pushes the austenite envelop. This term is easily evaluated assuming austenite is incompressible. The other contribution is the term  $\Delta(r_i^\gamma)$  that corresponds to the change in carbon content of the liquid and which may be expressed assuming the liquid is completely mixed. This term may be related to temperature change owing to the assumption that the composition of the liquid follows the austenite liquidus: upon cooling it will increase the rate of austenite precipitation while upon recalescence it will be negative and decrease that rate. Furthermore, it can be associated either to off-eutectic austenite or to the austenite shell. The former choice seems more realistic as it allows melting back of some of the off-eutectic dendrites which is effectively expected due to the fact that the curvature of dendrite arms is higher than the curvature of the austenite shells [EIK17]. If this latter choice is considered, then  $\Delta(r_i^\gamma)$  is set to zero in Eq. (10.27).



Due to impingement of SG eutectic entities, overlapping carbon diffusion fields at late solidification stage may affect the growth rate of graphite spheroids as given by Eq. (10.26). Quantitative information was provided by X-ray tomography which allowed following the individual growth of several hundreds of spheroids during solidification [BJE18] and evidenced the decrease of their growth rate as solidification proceeds. This suggested modifying Eq. (10.26) by multiplying it with an impingement factor that would allow describing the average decrease of graphite growth. This effect may be seen as corresponding to a decrease of the difference in the carbon content  $(w_C^{\gamma/1} - w_C^{\gamma/gra})$  that drives graphite growth [BJE18].

Contrary to LGI and CGI,  $d\bar{w}_C^{eutectic}$  is not explicitly calculated in the case of SGI and Eqs. (10.16) and (10.17) are combined to get a further relation between growth of the eutectic entities and change in liquid composition [LES98a].

Further, and similarly to the case of CGI illustrated above, it is quite possible to add the possibility of growth of metastable eutectic cell [SEL00]. Finally, there is no difficulty in writing mass balances as above for any substitutional solutes but the derivatives are at change with respect to the case of carbon as these solutes are expected to follow Scheil's redistribution [LAC99b]. This allowed simulating the built up of microsegregation as illustrated in the next section.

### 10.9 Description of microsegregation

Scheil's model can easily be extended to multiphase growth when the solid phases that precipitate are all in contact with the liquid [LAC86]. Applied to LGI, with a fraction  $f^{\gamma,eut}$  of austenite and  $f^{gra,eut}$  of graphite precipitating together in the eutectic, a straightforward extension of Eq. (10.11) gives the following mass balance for any substitutional solute  $i$ :

$$w_i^l \cdot \left[ (1 - k_i^{\gamma/1}) \cdot df^{\gamma,eut} + (1 - k_i^{gra/1}) \cdot df^{gra} \right] = \left[ 1 - (f^{\gamma,eut} + f^{gra,eut}) \right] \cdot dw_i^l \quad (10.28)$$

If graphite is pure carbon, then all  $k_i^{gra/1}$  are zero. Fredriksson et al. [FRE86] have derived a similar equation for treating eutectic solidification of LGI and accounting for the possibility of white solidification. They could show the influence of decreasing silicon content in the liquid during solidification (so-called negative segregation) on the shrinking of the temperature interval for stable solidification.

Scheil's equation has been applied by Boeri and Weinberg [BOE89] to SGI as is, i.e. without considering that the various phases of the eutectic show different partitioning behaviours. Nastac and Stefanescu [NAS93] applied a model developed for single phase spherical solidification to the growth of a SGI entity. The model describes redistribution of substitutional solutes at the austenite/liquid interface and their diffusion in both solid and liquid, but curiously does not converge to the Scheil's model when solid-state diffusion vanishes. As for the approach of Boeri and Weinberg, this latter model does not account for graphite expansion as it makes use of Eq. (10.4) for calculating the growth rate of the eutectic entities.

To deal with microsegregation build-up in multicomponent alloys, the most advanced modelling approach to date is certainly by phase field calculations coupled to a thermodynamic database [EIK10]. Such an approach has been applied to SGI after proper accounting for the molar volume of carbon, namely accounting for the pushing of the surrounding austenite during graphite precipitation [EIK20b]. In this work, prediction of silicon and manganese distribution (see Fig. 10.13) were satisfactorily compared to experimental ones.

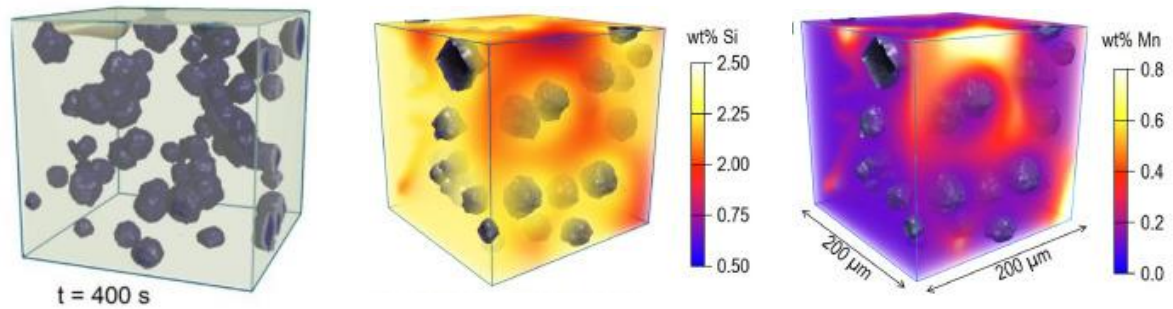


**Figure 10.13. Predicted distribution of nodules, silicon and manganese at the end of solidification of a small cubic block [EIK20b].**

Phase field modelling has confirmed that microsegregation of substitutional solutes in SGI is conveniently described with Scheil's model, but this approach presents the further interest to predict carbon distribution all along the solidification and cooling processes. However, though very powerful, phase field simulation needs high computer capabilities. In contrast, the physical models described in this chapter are not time consuming and allow easy check of the input parameters. As mentioned above, the mass balance Eq. (10.17) could be written for any solute and properly transformed following the Scheil's model for describing redistribution of substitutional solutes in any kind of cast iron. This has been carried out in the case of SGI and extended to describe the development of mottled structures [LAC99b].

The predicted solidification path is illustrated in Fig. 10.14-a in the  $w_{Si}$ - $w_C$  plane for a eutectic SGI at 2.6 wt.% Si. Two casting conditions were considered that differed by the casting thermal modulus, a large one at 0.01 m leading to solidification completing in the stable system and a small one at 0.0018 m leading to a switch from stable to metastable solidification. Solidification in the stable system corresponds to a continuous decrease of the silicon content in the liquid in agreement with the negative silicon segregation in cast iron (meaning that the partition coefficient between austenite and liquid is higher than one). By decreasing the thermal modulus, much less segregation occurs at first because much less solid deposits in the stable system. However, as soon as the metastable eutectic line has been reached, silicon microsegregation becomes positive because ledeburite rejects silicon in the liquid. This evolution is also illustrated in Fig. 10.14-b in the  $T$ - $w_{Si}$  plane. The predicted distributions of silicon and manganese in grey, mottled and white SGI have been compared successfully to experimental results [SEL00].

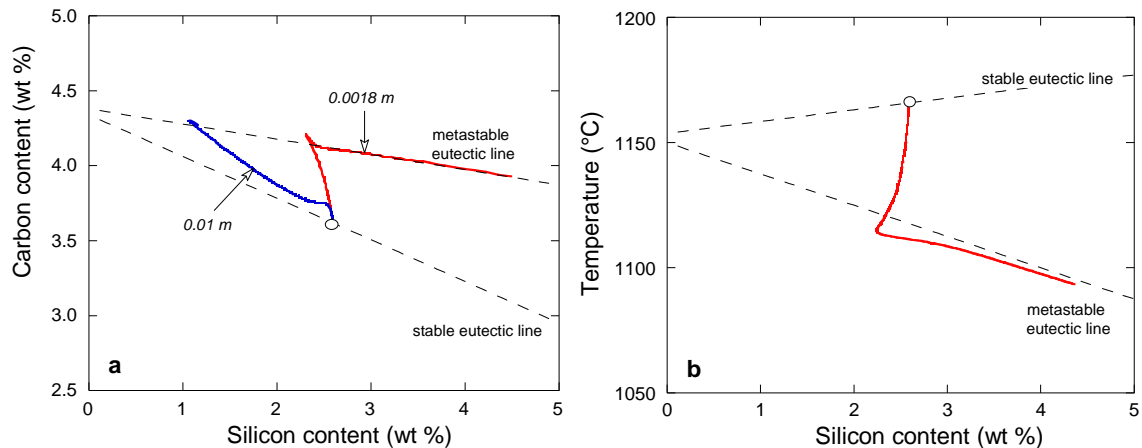


**Figure 10.14. Predicted solidification path of a eutectic SGI with 2.6 wt.% Si (open circle). a: plotted in the ( $w_{Si}$ ,  $w_C$ ) plane, solidification in the stable system (blue curve) when cast in large mould (0.01 m thermal modulus) or showing a transition to the metastable system (red curve) when cast in a small mould (thermal modulus of 0.0018 m). b: plotted in the ( $w_{Si}$ , T) plane to show the transition in the case of rapid solidification.**

### 10.10 Overall change of volume during solidification

With Eq. (10.16) and those following it, the **overall change of volume** during solidification was described but the RVE was considered as closed to exchange of matter. Accounting for the change in the mass balances that such exchange of matter leads to is possible, and this is the basis for the description of the development of **macrosegregation**, i.e. chemical heterogeneities at the scale of cast products, or for the description of microshrinkage in the case of cast irons.

At the beginning of solidification both liquid and solid can take part to mass flow, but above a critical volume fraction of solid,  $g_c^s$ , a continuous solid skeleton has formed and only liquid can move through the mushy zone. With further progress of solidification, the movement of the liquid is more and more difficult and is associated with a pressure drop which is described by Darcy's law. Coupled with a description of gas evolution in the liquid, this is the classical approach used to predict **porosity and shrinkage** formation in any alloys [RAP99, LES09] and in particular in cast irons [DIE86, KWE20]. The condition of gas bubble nucleation is written:

$$p^{gas} = p^l + \kappa \cdot \gamma^{l/gas} \quad (10.29)$$

where  $p^{gas}$  is the pressure of the gas,  $p^l$  the pressure of the liquid,  $\gamma^{l/gas}$  the surface tension of the liquid and  $\kappa$  the curvature of the surface of the bubble, respectively.

For hypoeutectic and mildly hypereutectic cast irons, solidification starts with a small contraction due to austenite precipitation corresponding to a flow of liquid from the riser to the casting. As eutectic solidification takes place, the average density of the solid that deposits is slightly lower than that of the liquid and a small and continuous expansion occurs with the extra liquid exuding to the riser. This second stage is the same for LGI and SGI until a continuous solid network has formed at the critical solid fraction. As a matter of fact,

once the solid skeleton has formed at  $g_c^s$ , it can expand or contract due to temperature changes and internal strains. The RVE may thus change in size and this can affect the mass balances. Further, in real castings, RVEs are open to exchange of matter and this has been applied to porosity formation in cast irons by Lesoult [LES85, LES09]. To describe the evolution of the system beyond this point, it is appropriate to define a RVE of volume  $V$  which is built on the solid framework and deforms with it. Considering that no solid can move out or enter into this RVE once the solid skeleton has formed, exchanges are limited to liquid flow through the mushy zone with  $v^{l/s}$  the relative speed of liquid with respect to solid. Using  $D$  to describe the derivative at the scale of this RVE, the divergence of the mass flow is such that:

$$V \cdot \text{div}(\rho^l \cdot g^l \cdot v^{l/s}) = -Dm/Dt \quad (10.30)$$

where  $m$  is the mass of matter in the RVE at time  $t$ .

With  $m^s$  and  $\rho^s$  the mass and density of solid, and  $V^{\text{pore}}$  the volume of voids, the change of the mass  $Dm/Dt$  of the RVE satisfies the following equation [LES09]:

$$\frac{1}{V} \cdot \frac{Dm}{Dt} = \rho^l \cdot \left\{ \frac{\rho^s - \rho^l}{\rho^s \cdot \rho^l} \frac{1}{V} \cdot \frac{Dm^s}{Dt} + \frac{1}{V} \cdot \frac{DV}{Dt} - \frac{1}{V} \cdot \frac{DV^{\text{pore}}}{Dt} \right\} \quad (10.31)$$

when neglecting the effect of temperature on the solid and liquid densities.

SGI is a very special case where graphite crystallization expands the already precipitated solid, which leads to bulging of the part when cast in too soft moulds. For illustration purpose, Fig. 10.15 compares the evolution of the solid packing at the end of solidification of LGI and SGI. In the case of LGI with both phases of the eutectic growing in contact with the liquid, the volume change is compensated by a related liquid movement during most of the solidification stage [HIL85]. Some very limited porosity may develop at the very end of solidification when the liquid cannot anymore move through the solid network. In contradistinction, crystallisation of graphite in the case of SGI expands each of the eutectic entities and this expansion is transferred to the neighbouring ones, leading eventually to bulging of the casting. A very rough geometrical model can give an idea of the expected bulging. If  $V_C$  is the volume of the RVE when the solid skeleton just formed, the volume change of the RVE,  $\Delta V_C$ , during the last solidification step is such that the piling up of solid entities remains self-similar. This can be written:

$$\frac{\Delta V_C}{V_C} \approx \frac{\Delta V^{\text{gra}}}{V_C \cdot g_c^s} \quad (10.32)$$

where  $\Delta V^{\text{gra}}$  is the increase of the volume of graphite fraction when the solid fraction changes from  $g_c^s$  to 1, and  $V_C \cdot g_c^s$  is the volume of solid in the RVE at  $g_c^s$ .

If the volume change cannot be compensated by liquid flowing from the riser, dispersed microporosity appears which is schematized as white curved triangles in the bottom right of Fig. 10.15. Ohnaka et al. [OHN03] have similarly accounted for expansion due to graphite precipitation for predicting porosity formation by means of a mechanical criterion.

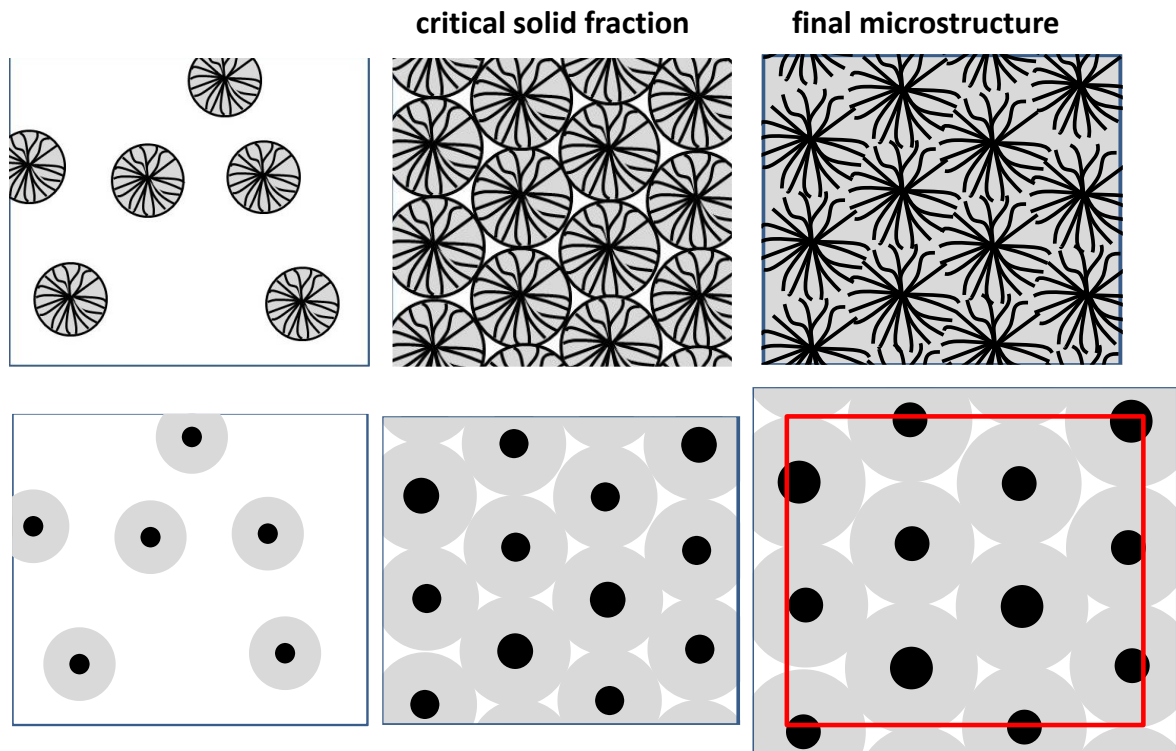


**Figure 10.15. Evolution during the progress of solidification of the packing of eutectic entities within a soft mould: comparison of LGI (top row) and SGI (bottom row). White areas in the bottom right scheme are porosities.**

Fig. 10.15 illustrates the fact that  $DV/Dt$  is negligible in the case of LGI while it may become significant in case of SGI. Calculation of the liquid pressure in a cast plate of 1 m long was carried out using Darcy's law and is illustrated in Fig. 10.16 for a eutectic SGI [LES85]. As the volume fraction of solid increases, the initial contraction leads to a small negative pressure, which then suddenly changes to a positive pressure when the eutectic reaction starts and increases until the critical value  $g_c^s$  is reached. In the case of a perfectly soft mould, the whole of the internal strains are transformed in expansion of the RVE and this leads to an immediate change in sign of the liquid pressure that takes large negative values as illustrated with  $g_c^s = g_{c,1}^s$  in Fig. 10.16. If the mould has some strength, creep of the austenite envelops may occur and the change in sign of the pressure is delayed until higher solid fraction, e.g.  $g_{c,2}^s$  in Fig. 10.16.

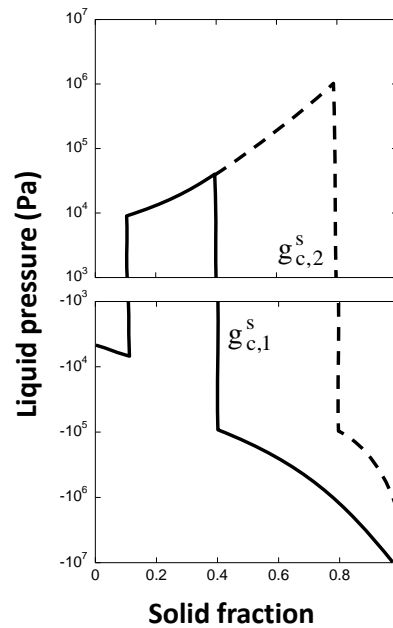


**Figure 10.16. Evolution of the dynamic pressure of the liquid during solidification of a eutectic SGI. Negative values correspond to a liquid sucked towards the mushy zone, positive values to a liquid exuding out of the mushy zone. The values  $g_{c,1}^s$  and  $g_{c,2}^s$  are critical values over which expansion of the mushy zone occurs.**

### 10.11 Solid-state transformation

The **final as-cast microstructure** of silicon cast irons results from the eutectoid decomposition of austenite. A few works have proposed a modelling approach accounting for the ferritic and pearlitic transformations that have been previously reviewed [LAC17e]. These works agree more or less with each other for the description of the ferritic reaction once ferrite has formed, but all of them assume that ferrite may appear at the upper temperature of the three-phase domain,  $T_{\alpha}^0$ , while it has been demonstrated in Chapter 9 that growth of ferrite can start only below the lower temperature of this three-phase domain,  $T_{\alpha}$ . This statement is valid regardless of the shape of the graphite, whereas the overall kinetics of the transformation is highly dependent on the type of graphite as already mentioned. The same drawback is observed in the works devoted to the pearlitic transformation, where it is considered that it can start at the upper limit,  $T_p^0$ , of the three-phase domain while it is the lower limit,  $T_p$ , that is the valid reference temperature.

As a matter of fact, the only paper that considered the appropriate temperatures for the ferritic and pearlitic reactions was dedicated to SGI [LAC98b]. Before the eutectoid reaction takes place, it has been emphasized in Chapter 9 that growth of graphite during cooling in the austenite field should be described. For a spherical geometry (SGI), this can be done as for growth of primary graphite from the liquid. If interfacial kinetics is not considered as already assumed for growth of spheroids encapsulated in austenite, the composition of austenite at the austenite/graphite interface follows the graphite solvus and the carbon mass balance at the graphite/austenite interface is:

$$\rho^{\text{gra}} \cdot (1 - w_C^{\gamma/\text{gra}}) \cdot \frac{dr^{\text{gra}}}{dt} = -\rho^\gamma \cdot D_C^\gamma \cdot \left. \frac{\partial w_C^\gamma}{\partial r} \right|_{r^{\text{gra}}} \quad (10.33)$$

Assuming further that the carbon gradient in austenite at the interface may be simply written as:

$$\left. \frac{\partial w_C^\gamma}{\partial r} \right|_{r^{\text{gra}}} = -\left( \bar{w}_C^\gamma - w_C^{\gamma/\text{gra}} \right) / r^{\text{gra}} \quad (10.34)$$

where  $\bar{w}_C^\gamma$  is the average carbon content in the remaining austenite that should be evaluated at each time step by an appropriate mass balance [LAC98b].

Combining Eqs. (10.33) and (10.34), the growth rate of the graphite spheroids is written:

$$\frac{dr^{\text{gra}}}{dt} = \frac{\rho^\gamma}{\rho^{\text{gra}}} \cdot \frac{D_C^\gamma}{r^{\text{gra}}} \cdot \frac{\left( \bar{w}_C^\gamma - w_C^{\gamma/\text{gra}} \right)}{\left( 1 - w_C^{\gamma/\text{gra}} \right)} \quad (10.35)$$

The process of carbon desaturation of austenite continues until the temperature reaches the lower limit of the austenite/ferrite/graphite three-phase field,  $T_\alpha$ . At that temperature, it is assumed that a ferrite shell forms immediately. The growth rate of the graphite spheroids is now given by the carbon mass balance at the graphite/ferrite interface:

$$\rho^{\text{gra}} \cdot (1 - w_C^{\alpha/\text{gra}}) \cdot \frac{dr^{\text{gra}}}{dt} = -\rho^\alpha \cdot D_C^\alpha \cdot \left. \frac{\partial w_C^\alpha}{\partial r} \right|_{r^{\text{gra}}} \quad (10.36)$$

Similarly, the growth rate of the ferrite/austenite interface results from the sum of the carbon fluxes to the spheroid (through the ferrite shell) and that from or to austenite:

$$\rho^\alpha \cdot (w_C^{\gamma/\alpha} - w_C^{\alpha/\gamma}) \cdot \frac{dr^\alpha}{dt} = \rho^\alpha \cdot D_C^\alpha \cdot \left. \frac{\partial w_C^\alpha}{\partial r} \right|_{r^\alpha} - \rho^\gamma \cdot D_C^\gamma \cdot \left. \frac{\partial w_C^\gamma}{\partial r} \right|_{r^\alpha} \quad (10.37)$$

With the same assumption of quasi steady-state diffusion of carbon in ferrite as already used for solidification, and writing the gradient of carbon ahead of the ferrite/austenite interface as:

$$\left. \frac{\partial w_C^\gamma}{\partial r} \right|_{r^\alpha} = -\left( \bar{w}_C^\gamma - w_C^{\gamma/\alpha} \right) / r^\alpha \quad (10.38)$$

the equations above are now written:

$$\frac{dr^{\text{gra}}}{dt} = \frac{\rho^\alpha}{\rho^{\text{gra}}} \cdot D_C^\alpha \cdot \frac{r^\alpha}{r^{\text{gra}} \cdot (r^\alpha - r^{\text{gra}})} \cdot \frac{\Delta w_C}{(1 - w_C^{\alpha/\text{gra}})} \quad (10.39)$$

$$\frac{dr^\alpha}{dt} = D_C^\alpha \cdot \frac{r^{\text{gra}}}{r^\alpha \cdot (r^\alpha - r^{\text{gra}})} \cdot \frac{\Delta w_C}{(w_C^{\gamma/\alpha} - w_C^{\alpha/\gamma})} + \frac{\rho^\gamma}{\rho^\alpha} \cdot D_C^\gamma \cdot \frac{1}{r^\alpha} \cdot \frac{\left( \bar{w}_C^\gamma - w_C^{\gamma/\alpha} \right)}{\left( w_C^{\gamma/\alpha} - w_C^{\alpha/\gamma} \right)} \quad (10.40)$$

where  $\Delta w_C = (w_C^{\alpha/\gamma} - w_C^{\alpha/\text{gra}})$  is the difference in carbon content defined in Chapter 9 (Fig. 9.8).

Note that the last term in Eq. (10.39) represents a flux of carbon atoms either to the ferrite/austenite interface or away from it depending on the location of the average carbon content in austenite with respect to the austenite/ferrite boundary.

Predictions were compared to experimental kinetics derived from DTA experiments on samples reheated from room temperature to the austenite field and then cooled at various rates. The overall agreement with the observed start temperature of the stable and metastable solid-state transformations was good but the kinetics of ferrite growth was too high when compared to those experimentally recorded. One possible explanation could be a decrease of the carbon diffusion coefficient as an effect of stresses. In this line, additional experiments were performed by dilatometry which showed that dissolution of graphite upon heating in the austenite field could be described using the standard value of  $D_C^\gamma$ , while re-precipitation of graphite upon cooling was much slower than predicted. Also, calculations of the stress field suggested this could hardly explain the difference [SIL03]. This led to the conclusion that this is the gap formed between graphite and the matrix upon reheating the samples from room temperature to the austenite field that could explain the discrepancy.

There is thus a clear interest to perform new experiments where the kinetics of solid-state transformation would be evaluated during cooling after solidification, without any reheating. This need extends to all graphite shapes. Accounting for microsegregation would lead to minor changes in the predictions (see Chapter 9) but could be of interest when ferritic-pearlitic structures are looked for. Finally, there is clearly a lack of knowledge on the partitioning between ferrite and cementite in the pearlite of cast irons which should reveal what is controlling pearlite growth kinetics.

### 10.12 Summary

The balance equations that are needed for a quantitative description of the microstructure development during solidification and solid-state transformation of silicon cast irons have been presented, together with some possible future improvements. Coupling of this microstructure modelling with heat-transfer, that is achieving a so-called micro-macro simulation, would greatly benefit to foundries, e.g. for getting the full capabilities of thermal analysis. This has been carried out by Mampaey for nucleation and growth of primary austenite [MAM01] while further achievements are still to be done.



# References A-I

- [AFS19] Metalcasting Forecast and Trends, AFS, 2019
- [ÅGR86] J. ÅGREN,  
A revised expression for the diffusivity of carbon in binary Fe-C austenite , Scr. Metall., 20, 1986, 1507-1510
- [AHM83] W.U. AHMED, L.J. GAWLICK,  
A technique for retaining graphite in cast irons during polishing,  
Modern Casting, January 1983, 20-21
- [AKA04] S. AKAMATSU, M. PLAPP, G. FAIVRE, A. KARMA,  
Overstability of lamellar eutectic growth below the minimum-undercooling spacing,  
Metall. Mater. Trans. A, 35A, 2004, 1815-1828
- [ALA84] A. ALAGARSAMY, F.W. JACOBS, G.R. STRONG, R.W. HEINE,  
Carbon equivalent vs. austenite liquidus: what is the correct relationship for cast irons?,  
AFS Trans., 1984, 871-88
- [ALO17] G. ALONSO, P. LARRAÑAGA, D.M. STEFANESCU, E. DE LA FUENTE, A. NATXIONDO, R. SUÁREZ,  
Kinetics of nucleation and growth of graphite at different stages of solidification for spheroidal graphite iron, Int. J. Metalcasting, 11, 2017, 14–26.
- [ALO18] G. ALONSO, D. STEFANESCU, E. DE LA FUENTE, P. LARRANAGA, R. SUAREZ,  
The Influence of Trace Elements on the Nature of the Nuclei of the Graphite in Ductile Iron,  
Materials Science Forum, 925, 2018, 78-85
- [AMI13] S. AMINI, R. ABBASCHIAN,  
Nucleation and growth kinetics of graphene layers from a molten phase,  
Carbon 51, 2013, 110-123. DOI: 10.1016/j.carbon.2012.08.019
- [ARA21] I. ARAGÃO DOS SANTOS,  
Rendas de ferro: uma doação pela memória civilizatória brasileira,  
Anais do Museu Paulista São Paulo, Nova Série, 29, 2021, 1-26
- [AUS67] S.B. AUSTERMAN, S.M.MYRON, J.W. WAGNER,  
Growth and characterization of graphite single crystals, Carbon, 5, 1967, 549
- [AZE18] M.A. AZEEM, M.K. BJERRE, R.C. ATWOOD, N. TIEDJE, P.D. LEE,  
Synchrotron quantification of graphite nodule evolution during the solidification of cast iron,  
Acta Materialia, 155, 2018, 393-401. DOI:10.1016/j.actamat.2018.06.007
- [BAE20] W. BAER,  
Chunky graphite in ferritic spheroidal graphite cast iron: formation, prevention, characterization, impact on properties: an overview,  
Int. J. Metalcasting, 14, 2020, 454-488. DOI: <https://doi.org/10.1007/s40962-019-00363-8>
- [BAR97] J.O. BARLOW, D.M. STEFANESCU,  
Computer-aided cooling curve analysis revisited, AFS Trans., 105, 1997, 349-354
- [BAS73] P.K. BASUTKAR, C.S. PARK, R.E. MILLER, C.R. LOPER,  
Formation of spiky graphite in high magnesium ductile iron castings, AFS Trans., 81, 1973, 180–184
- [BER98] V.M. BERMONT, J.A. SIKORA,  
Metallographic study on the influence of the morphology and distribution of graphite on the solid state transformations of grey and ductile cast iron, Int. J. Cast Metals Res., 11, 1998, 51-61
- [BIE98] BIELEK, M., P. GASSERE, S. GLEDHILL, R. STARAL  
Cost-effective iron inoculation: Four foundries' perspectives, *Modern casting* 88, 2, 1998, 45-48.

- [BJE18] M.K. BJERRE, M.A. AZEEM, N.S. TIEDJE, J. THORBORG, P.D. LEE, J.H. HATTEL,**  
A graphite nodule growth model validated by in situ synchrotron x-ray tomography,  
Modelling Simul. Mater. Sci. Eng., 26, 2018, 085012
- [BOB88] M. BOBADILLA, J. LACAZE, G. LESOULT,**  
Influence des conditions de solidification sur le déroulement de la solidification des aciers  
inoxydables austénitiques, J. Crystal Growth, 89, 1988), 531-544
- [BOE89] R. BOERI, F. WEINBERG,**  
Microsegregation in ductile iron, AFS Trans., 1989, 179-184
- [BOE18] R.E. BOERI, M.G. LOPEZ, N.E. TENAGLIA, J.M. MASSONE,**  
Solidification of ductile and compacted irons, macrostructure and shrinkage formation,  
Int. J. Metalcasting, 14, 2020, 1172–1182
- [BOL75] W. BOLLMANN, B. LUX,**  
Grain boundaries in graphite, The metallurgy of cast iron, Georgi Ed., 1975, 461-471
- [BOS74] W.P. BOSZE, R. TRIVEDI,**  
On the kinetic expression for the growth of precipitate plates, Metall. Trans., 5, 1974, 511-512.
- [BOU17] J. BOURDIE,**  
Sphéroïdisation du graphite - Cas de la fonte centrifugée  
PhD thesis, INP-Toulouse, France, 2017, <http://www.theses.fr/2017INPT0117>
- [BOU18] J. BOURDIE, F. BRUNESSEAU, P. DE PARSEVAL, S. GOUY, L. LAFFONT, J. LACAZE**  
Effect of cooling rate and aluminium addition on graphite growth  
during solidification and graphitization, Materials Science Forum, 925, 2018, 20-27
- [BOU20] J. BOURDIE, J. LACAZE, C. JOSSE, L. LAFFONT,**  
Growth of spheroidal graphite: light versus scanning and transmission electron microscopies,  
Int. J. Metalcasting, 14, 2020, 672-680
- [BRA70] B.L. BRAMFITT,**  
The effect of carbide and nitride additions on the heterogeneous nucleation behavior of liquid iron,  
Metall. Trans. 1, 1970, 1987–1995. <https://doi.org/10.1007/BF02642799>
- [BRO18] E. BRODU, E. BOUZY, J.J. FUNDENBERGER, B. BEAUSIR, L. LAFFONT, J. LACAZE,**  
Crystallography of growth blocks in spheroidal graphite,  
Science and Processing of Cast Iron, SPCI-XI, Materials Science Forum, 925, 2018, 54-61.
- [BUR12] A.A. BURBELKO, D. GURGUL, W. KAPTURKIEWICZ, J. POCZĄTEK, M. WRÓBEL**  
Stochastic nature of the casting solidification displayed by micro-modelling and cellular automata  
method, Solid State Phenomena, 197, 2013, 101-106, [doi:  
10.4028/www.scientific.net/SSP.197.101](https://doi.org/10.4028/www.scientific.net/SSP.197.101)
- [CAS91] M. J. CASTRO ROMAN,**  
Étude expérimentale et modélisation de la solidification des pièces coulées en fonte à graphite  
sphéroïdal: influence de la vitesse de refroidissement et de l'inoculation,  
PhD Thesis, 1991,. Vandoeuvre-les-Nancy, INPL, France.
- [CAS20] M.J. CASTRO-ROMAN, J. LACAZE, A. REGORDOSA, J. SERTUCHA, R. DEL CAMPO-CASTRO,**  
Revisiting thermal analysis of hypereutectic spheroidal graphite cast irons,  
Metall. Mater. Trans. A, <https://doi.org/10.1007/s11661-020-06005-7>
- [CAT96] A.V. CATALINA, D.M. STEFANESCU,**  
Lamellar growth of eutectic equiaxed grains,  
Metall. Mater. Trans., 27A, 1996, 4205-4210
- [CAT03] A.V. CATALINA, S. SEN, D.M. STEFANESCU,**  
A new analytical approach to predict spacing selection in lamellar and rod eutectic systems,  
Metall. Mater. Trans., 34A, 2003, 383-394
- [CAT15] A.V. CATALINA, P.W. VOORHEES, R.K. HUFF, A.L. GENAU,**  
A model for eutectic growth in multicomponent alloys,  
MCWASP, IOP Conf. Series: Mater. Sci. Eng., 84, 2015, 012085
- [CEN19] Census of word casting production, Modern Casting, December 2019, 22-25**

- [CHA74] M.D. CHAUDHARI, R.W. HEINE, C.R. LOPER,**  
Potential applications of cooling curves in ductile iron process control, AFS Trans., 82, 1974, 379-386
- [CHA75] M.D. CHAUDHARI, R.W. HEINE, C.R. LOPER,**  
Principles involved in the use of cooling curves in ductile iron process control, AFS Cast Metals Research J., June, 1975, 52-60
- [CHA92] S. CHANG, D. SHANGGUAN, D.M. STEFANESCU,**  
Modeling of the liquid/solid and the eutectoid phase transformations in spheroidal graphite cast iron, Metall. Trans., 23A, 1992, 1333-1346
- [CHA13] D. CHAKRABORTY, G.N. PATEY,**  
Evidence that crystal nucleation in aqueous NaCl solution occurs by the two-step mechanism, Chem. Phys. Lett. 587, 2013, 25–29. <https://doi.org/10.1016/j.cplett.2013.09.054>
- [CHE84] I.G. CHEN, D.M. STEFANESCU,**  
Computer-aided differential thermal analysis of spheroidal and compacted graphite cast irons, AFS Trans., 92, 1984, 947-964
- [CHU15] C. CHUANG, D. SINGH, P. KENESEI, J. ALMER, J. HRYN, R. HUFF,**  
3D quantitative analysis of graphite morphology in high strength cast iron by high-energy X-ray tomography, Scripta Mater., 106, 2015, 5-8; and <https://www.anl.gov/article/highenergy-xrays-give-industry-affordable-way-to-optimize-cast-iron>.
- [CIB49] A. CIBULA,**  
The mechanism of grain refinement of sand castings in aluminium alloys, J. Inst. Met. 76, 1949, 321.
- [CIN00] E. CINI, B. VINET, P.J. DESRÉ,**  
A thermodynamic approach to homogeneous nucleation via fluctuations of concentration in binary liquid alloys. Philos. Mag. A 80, 2000, 955–966. <https://doi.org/10.1080/01418610008212092>
- [COZ00] J. LE COZE,**  
Purification of iron and steels, a continuous effort from 2000 BC to AD 2000, Materials Transactions, JIM, 41, 2000, 219-232
- [COZ17] J. LE COZE,**  
Récits sidérurgiques d'hier et d'aujourd'hui, fers, fontes, aciers: 4000 ans d'affinage et de purification, EDP Sciences, Les Ulis, 2017
- [COW81] N. COWLAM, G.E. BACON, L. GILLOTT, D.H. KIRKWOOD,**  
Diffraction measurements of graphite nodules in ferritic steels, Acta Metall., 29, 1981, 6511981
- [CRE21] J. CREE ET AL.,**  
Statistical Comparisons of Four (4) Different Thermal Analysis Sample Cup Types for Chemistry Control of Ductile Base Iron, International Journal of Metalcasting, 15, 2021, 729–746
- [DAN09] J.A. DANTZIG, M. RAPPAZ,**  
Solidification, CRC Press, first edition, 2009
- [DAW01] S. DAWSON,**  
A brief history of ... foundry, see appendix A
- [DAW02] Microstructure and Porosity Control, Sintercast datasheet, [www.sintercast.com](http://www.sintercast.com)**
- [DAW03] S. DAWSON,**  
Cast iron alloy and method making the same, US Patent 6,613,274 B2
- [DAW13] S. DAWSON, P. POPELAR,**  
Thermal analysis and process control for compacted graphite iron and ductile iron, Keith Millis symposium, 2013, 32-39
- [DEK20] L. DEKKER, B. TONN, G. LILIENKAMP,**  
Effect of antimony on graphite growth in ductile iron, Int. J. Metalcasting, DOI: 10.1007/s40962-020-00434-1.

- [DIE96] P. DIERICKX, C. VERDU, A. REYNAUD, R. FOUÈRES,**  
A study of physico-chemical mechanisms responsible for damage of heat-treated and as-cast ferritic spheroidal graphite cast irons, *Scr. Mater.* 34 (1996) 261-268.
- [DIE86] P. DIETRICH, G. LESOULT,**  
Simulation of heat transfer and capillary feeding during solidification of sand mold S.G. iron castings,  
State of the art of computer simulation of casting and advanced solidification processes, Les éditions de Physique, les Ulis, France, 1986, 225-235
- [DIO04] A. DIOSZEGI, J. HATTEL,**  
Inverse thermal analysis method to study solidification in cast iron,  
*Int. J. Cast Metals Res.*, 17, 2004, 311-318
- [DIO05] A. DIOSZEGI, I.L. SVENSSON,**  
Inverse kinetic analysis method to study eutectic growth, *Int. J. Cast Metals Res.*, 18, 2005, 41-46
- [DIO07] A. DIÓSZEGI, K.Z. LIU, I.L. SVENSSON,**  
Inoculation of primary austenite in grey cast iron,  
*Int. J. Cast Met. Res.* 20, 2007, 68–72. <https://doi.org/10.1179/174313307X216633>
- [DIN80] B. DHINDAW, J.D. VERHOEVEN,**  
Nodular graphite formation in vacuum melted high purity Fe-C-Si alloys,  
*Metall. Trans.*, 11A, 1980, 1049-1057
- [DOM21] B. DOMENGÈS, M. MARTINEZ CELIS, F. MOISY, J. LACAZE, B. TONN,**  
On the role of impurities on spheroidal graphite degeneracy in cast irons,  
*Carbon*, 172, 2021, 532-541. DOI: 10.1016/j.carbon.2020.10.030
- [DON68] L.F. DONAGHEY, W.A. TILLER,**  
On the diffusion of solute during eutectoid and eutectic transformations. Part 1,  
*Mater. Sci Eng.* 3, 1968/69, 231-239
- [DOU69] D.D. DOUBLE, A. HELLAWELL,**  
The structure of flake graphite in Ni-C eutectic alloy, *Acta metall.*, 17, 1969, 1071-1083
- [DOU71] D.D. DOUBLE, A. HELLAWELL,**  
Defects in eutectic flake graphite, *Acta metall.*, 19, 1971, 1303-1306
- [DOU74] D.D. DOUBLE, A. HELLAWELL,**  
Cone-helix growth forms of graphite, *Acta Metall.*, 22, 1974, 481-487
- [DOU75] D.D. DOUBLE, A. HELLAWELL,**  
Growth structure of various forms of graphite,  
The metallurgy of cast iron, Georgi Ed., 1975, 509-525
- [EBE20] A. EBEL, M. ALVES PEGORARO, B. MALARD, C. TENAILLEAU, J. LACAZE,**  
Coarsening and dendritic instability of spheroidal graphite in high silicon cast iron under thermal cycling in the ferritic domain, *Scripta mater.*, 178, 2020, 86-89,
- [EIK10] J. EIKEN**  
A phase field model for technical alloy solidification, PhD thesis, Shaker Verlag, 2010
- [EIK15] J. EIKEN, M. APPEL, SONG-MAO LIANG, R. SCHMID-FETZER,**  
Impact of P and Sr on solidification sequence and morphology of hypoeutectic Al-Si alloys: combined thermodynamic computation and phase-field simulation, *Acta Mater.* 98, 2015, 152-163
- [EIK17] J. EIKEN,**  
private communication
- [EIK20A] J. EIKEN,**  
Calphad-based phase-field study of the interplay between spheroidal graphite growth and chemical segregation in ductile cast iron,  
*IOP Conf. Series: Materials Science and Engineering*, **861**, 2020, 012055
- [EIK20B] J. EIKEN, E. SUBASIC, J. LACAZE,**  
3D phase-field computations of microsegregation in nodular cast iron compared to experimental data and CalPhad-based Scheil-prediction, *Materialia*, 9, 2020, 100538

- [EKP78] U. EKPOOM, R.W. HEINE,**  
Austenite transformation temperature range in cast irons, AFS Trans., 86, 1978, 281-286
- [EKP81] U. EKPOOM, R.W. HEINE,**  
Thermal analysis by differential heat analysis (DHA) of cast iron, AFS Trans., 89, 1981, 27-38
- [ELL88] R. ELLIOTT,**  
Cast iron technology, Butterworths, 1988
- [ELM10] L. ELMQUIST, S. SALERA, A. DIÓSZEGI,**  
Inoculation and its effect on primary solidification structure of hypoeutectic grey cast iron,  
Int. J. Cast Met. Res. 23, 2010, 124–129. <https://doi.org/10.1179/136404609X12490478029317>
- [EUS88] N. EUSTATHOPOULOS, D. CAMEL, J.J. FAVIER,**  
La solidification à l'échelle de l'interface, in F. Durand (Ed.) , Solidification des Alliages-du Procédé à la Microstructure, Les Editions de Physique, 1988, 133-146
- [FEE83] E.A. FEEST, G. MCHUGH, D.O. MORTON, L.S. WELCH, I.A. COOK,**  
Inoculation of grey cast iron,  
in "Solidification in the foundry and casthouse", The Metals Society, 1983, 232-239
- [FID82] H. FIDOS,**  
Structural analysis of a graphite nodule and surrounding halo in ductile iron, FWP Journal, 22, 1982, 43-62
- [FLE58] N.H. FLETCHER,**  
Size effect in heterogeneous nucleation. J. Chem. Phys. 29, 1958, 573–576.
- [FOU05] J. FOURMANN,**  
Preconditioning Effect of Barium in Ductile Iron Production,  
AFS Cast Iron Inoculation Conference, 2005, p. 1-15
- [FRA79] B. FRANCIS,**  
Heterogeneous nuclei and graphite chemistry in flake and nodular cast irons,  
Metallurgical Transactions, 10, 1979, 21-31
- [FRA84] S.E. FRANKLIN, R.A. STARK,**  
Application of secondary ion mass spectrometry to study of graphite morphology in cast iron,  
Metal Science, 18, 1984, 187-200
- [FRA85A] S.E. FRANKLIN, R.A. STARK,**  
Further use of secondary ion mass spectrometry in the study of graphite morphology control in cast irons,  
E-MRS Symp Proc., 34, 1985, 25-35
- [FRA85B] E. FRAS,**  
A computer-aided simulation of the kinetics of solidification of the eutectic ductile cast iron,  
in The Physical Metallurgy of Cast Iron, MRS symposia proceedings, 34, 1985, 191-199
- [FRA93] E. FRAS, H. F. LOPEZ,**  
A theoretical analysis of the chilling susceptibility of hypoeutectic Fe-C alloys,  
Acta metallurgica et materialia 41.12 (1993): 3575-3583.
- [FRA95] E. FRAS, W. KAPTURKIEWICZ, A.A. BURBIELKO,**  
Micro-macro modeling of casting solidification controlled by transient diffusion and undercooling,  
MCWASP, 1995, 679-686
- [FRA97] E. FRAS, W. KAPTURKIEWICZ, A.A. BURBIELKO, H.F. LOPEZ,**  
Numerical simulation and Fourier thermal analysis of solidification kinetics in high-carbon Fe-C alloys, Metallurgical and Materials Transactions B, 28, 1997, 115-123
- [FRA19] D. FRANZEN, P. WEISS, B. PUSTAL, A. BÜHRIG-POLACZEK,**  
Influence of aluminium on silicon microsegregation in solution strengthened ductile iron,  
Materials Science and Technology, 35, 2019, 687-694
- [FRE75A] H. FREDRIKSSON, S.E. WETTERFALL,**  
A study of transition from undercooled to flake graphite in cast iron,  
The metallurgy of cast iron, Georgi Ed., 1975, 277-289

- [FRE75B] H. FREDRIKSSON,**  
The coupled zone in grey cast iron, *Metall. Trans.*, 6A, 1975, 1658-1660
- [FRE84] H. FREDRIKSSON,**  
Inoculation of iron-base alloys,  
*Mater. Sci. Eng.*, 65, 1984, 137–144. [https://doi.org/10.1016/0025-5416\(84\)90207-6](https://doi.org/10.1016/0025-5416(84)90207-6)
- [FRE85] H. FREDRIKSSON, I.L. SVENSSON,**  
Computer simulation of the structure formed during solidification of cast iron,  
in *The Physical Metallurgy of Cast Iron*, MRS symposia proceedings, 34, 1985, 273-284
- [FRE86] H. FREDRIKSSON, J.T. THORGRIMSSON, I.L. SVENSSON,**  
Computer simulation of structure formation and segregation during the solidification of cast iron,  
*State of the art of computer simulation of casting and advanced solidification processes*,  
Les éditions de Physique, les Ulis, France, 1986, 267-275
- [FRI70] J. FRIDBERG, M. HILLERT,**  
Ortho-pearlite in silicon steels, *Acta metal.*, 18, 1970, 1253-1260
- [FRU98] R.J. FRUEHAN,**  
The making, shaping and treating of steel: steelmaking and refining,  
1998, AISE steel Foundation.
- [FUJ99] T. FUJIKAWA, K. NAKAMURA, H. SUMIMOTO, S. KIGUCHI,**  
Effects of tertiary elements on the critical solidification rate of the flake-undercooled graphite  
transition of Fe-C alloys, *Int. J. cast Metals Res.*, 11, 1999, 313-318
- [FUL79] A.G. FULLER,**  
Fading of inoculants,  
AFS Conference on Modern Inoculating Practices for Gray and Ductile Iron, 1979, 141-183.
- [GAD85] M.A. GADD, G.H.J. BENNETT,**  
The physical chemistry of Inoculation of cast Iron,  
in "The Physical Metallurgy of Cast Iron", *Materials Research Society Symposium*, 34, 1985, 99-  
108.
- [GAR19] L.N. GARCIA, A.J. TOLLEY, F.D. CARAZO, R.E. BOERI**  
Identification of Cu-rich precipitates in pearlitic spheroidal graphite cast irons,  
*Materials Science and Technology*, 35, 2019, 2252-2258
- [GER97] V. GERVAL, J. LACAZE,**  
Effect of the solidification path on the eutectoid transformation of spheroidal graphite cast iron,  
*Proc. SP97*, Sheffield, 1997, 506-510
- [GER00] V. GERVAL, J. LACAZE,**  
Critical temperatures of spheroidal graphite cast irons: a review of literature data,  
*ISIJ International* 40, 2000, 386-392
- [GHA19] E. GHASSEMALI, J.C. HERNANDO, D.M. STEFANESCU, A. DIOSZEGI, A.E.W. JARFORS,  
J. DLUHOŠ, M. PETRENEC,**  
Revisiting the graphite nodule in ductile iron, *Scripta Mater.*, 161, 2019, 66-69
- [GHE14] R. GHERGU, L. MAGNUSSON-ABERG, J. LACAZE,**  
A possible mechanism for the formation of exploded graphite in nodular cast irons,  
*Mater. Sci. Forum*, 790-791, 2014, 435-440
- [GOR18] M. GORNY, M. KAWALEC, G. SIKORA, E. OLEJNIK, H. LOPEZ**  
Primary structure and graphite nodules in thin-walled high-nickel ductile iron castings,  
*Metals*, 8, 2018, 649; [doi: 10.3390/met8080649](https://doi.org/10.3390/met8080649)
- [GOS86] A. GHOSH, G. V. R. MURTHY,**  
An assessment of thermodynamic parameters for deoxidation of molten iron by Cr, V, Al, Zr and Ti  
*Transactions of the Iron and Steel Institute of Japan*, 26, 1986, 629-637.
- [GRA20]** Granta Edupack 2020, Ansys/Granta Inc.
- [GRU75] J.E. GRUZLESKI,**  
On the growth of spherulitic graphite in nodular cast iron, *Carbon*, 13, 1975, 167-173

- [GUE19] W.L. GUESSER,**  
personal communication
- [GUI71] P.J. GUICHELAAR, P.K. TROJAN, T. MCLUHAN, R.A. FLINN,**  
A new technique for vapor pressure measurement applied to the Fe-Si-Mg system,  
Metall. Trans., 2, 1971, 3305-3313
- [GUS85] P. GUSTAFSSON,**  
A thermodynamic evaluation of the Fe-C system, Scand. J. Metall., 14, 1985, 259-267
- [GUT77] M. GUTTMANN,**  
Grain boundary segregation, two dimensional compound formation, and precipitation,  
Metallurgical Transactions A, 8A, 1977, 1383-1401
- [GUZ06] E. GUZIK, D. KOPYCINSKI,**  
Modeling structure parameters of irregular eutectic growth : modification of Magnin-Kurz theory,  
Metallurgical and Materials Transactions A, 37, 2006, 3057-3067
- [HAR98] R.A. HARDING, N. J. SAUNDERS,**  
Theory and practice of computer modeling of phase diagrams for cast irons  
AFS Trans., 1998, 451-458.
- [HEC00] M. HECHT,**  
Influence du titane sur les fontes GS largement ferritiques : structures et caractéristiques en  
traction usuelles, Fonderie Fondateur d'aujourd'hui, 200, 2000, 24-41
- [HEI71] R.W. HEINE,**  
The carbon equivalent, Fe-C-Si solidification diagram and its application to cast irons,  
AFS Cast Metals Research J., June 1971, 49-54
- [HEI77] R.W. HEINE,**  
Liquidus and eutectic temperatures and solidification of white cast irons, AFS Trans., 85, 1977,  
537-544
- [HEI86] R.W. HEINE,**  
The Fe-C-Si solidification diagram for cast irons, AFS Trans., 94, 1986, 391-402
- [HEI95] R.W. HEINE,**  
Austenite liquidus, carbide eutectic and undercooling in process control of ductile base iron,  
AFS Trans., 103, 1995, 199-206
- [HER64] K. HERFURTH,** cited and commented by Lux [LUX70b]
- [HER66] K. HERFURTH,**  
Investigations into the influence of various additions on the surface tension of liquid cast iron with  
the aim of finding relationships between the surface tension and the occurrence of various forms of  
graphite.  
Freiberger Forschungshefte 105, 1966, pp. 267-309.
- [HER98] M. HERRERA-TREJO, M.R. CASTRO, J.N. MENDEZ, H.T. SOLIS, J.M. TENA, E. GUZMAN,**  
Evolution of inclusion nature during the EAF-LF-CC process, Scand. J. Metall. 27, 1998, 233–239
- [HER19] J.C. HERNANDO, J. ELFSBERG, A.K. DAHLE , A. DIÓSZEGI,**  
Evolution of primary austenite during coarsening and impact on eutectic microstructure in Fe–C–Si  
alloys, Materialia 7, 2019, 100391. DOI: 10.1016/j.mtla.2019.100391
- [HIL54] M. HILLERT, Y. LINDBLOM,**  
The growth of nodular graphite, J. Iron Steel Inst., 148, 1954, 388-390
- [HIL64] M. HILLERT,**  
Some theoretical considerations in nucleation and growth during solidification of graphitic and white  
cast iron, In Recent Research on Cast Iron, 1964, 101-127
- [HIL68] M. HILLERT, V.V. SUBBA RAO,**  
Grey and white solidification of cast iron, ISI Publ. 110, The Iron and Steel Institute, 1968, 204-212

- [HIL71] M. HILLERT,**  
Diffusion controlled growth of lamellar eutectics and eutectoids in binary and ternary systems,  
Acta Metallurgica, 19, 1971, 769-778
- [HIL78] M. HILLERT,**  
Fundamental aspects of aligned growth,  
TITRA-MAC-0146, Materials Center, Royal inst. Techn., Stockholm, 1978
- [HIL81] M. HILLERT,**  
An analysis of the effect of alloying elements on the pearlite reaction,  
Proc. Int. Conf. "Solid/solid phase transformations", 1981, 789-806
- [HIL85] M. HILLERT,**  
The relation between porosity and solidification mechanism in grey cast iron,  
in "The Physical Metallurgy of Cast Iron", Mat. Res. Soc. Symp. Proc., 34, 1985, 233-237
- [HIL98] M. HILLERT,**  
Phase equilibria, phase diagrams and phase transformations, Cambridge University Press, 1998
- [HIL02] M. HILLERT,**  
Nature of local equilibrium at the interface in the growth of ferrite from alloyed austenite,  
Scripta materialia, 46, 2002, 447-453
- [HIL04] M. HILLERT, J. ÅGREN,**  
On the definition of paraequilibrium and orthoequilibrium,  
Scripta materialia, 50, 2004, 697-699  
the discussion of it by Speer et al.: 52, 2005, 83-85; and the reply: 52, 2005, 87-88
- [HOF72] D.W. HOFFMAN, J.W. CAHN,**  
A vector thermodynamics for anisotropic surfaces: I. Fundamentals and application to plane  
surface junctions, Surface Science, 31, 1972, 368-388
- [HOG71] L.M. HOGAN, R.W. KRAFT, F.D. LEMKEY**  
Eutectic grains, Advances in materials research, 1971.
- [HOL07] D. HOLMGREN, R. KÄLLBOM, I.L. SVENSSON,**  
Influences of the graphite growth direction on the thermal conductivity of cast iron,  
Metall. Mater. Trans. A, 38, 2007, 268-275
- [HUN84] J.D. HUNT,**  
Steady state columnar and equiaxed growth of dendrites and eutectic,  
Mater. Sci. Eng., 65, 1984, 75-83. [https://doi.org/10.1016/0025-5416\(84\)90201-5](https://doi.org/10.1016/0025-5416(84)90201-5)
- [IGA98] Y. IGARASHI, S. OKADA,**  
Observation and analysis of the nucleus of spheroidal graphite in magnesium-treated ductile iron,  
Int. J. Cast Met. Res. 11, 1998, 83-88. <https://doi.org/10.1080/13640461.1998.11819261>

## References J-Z

- [JAC66] K.A. JACKSON, J.D. HUNT,**  
Lamellar and rod eutectic growth, Trans. Met. Soc. AIME, 236, 1966, 1129-1142
- [JAN82] J.F. JANOWAK, R.B. GUNDLACH,**  
A modern approach to alloying gray iron, AFS Trans. 90, 1982, 847.
- [JAS94] J. A. JASZCZAK,**  
The Picking Table, 35, 1994, 6
- [JAV95] A. JAVAID, C.R. LOPER,**  
Quality control of heavy-section ductile cast irons. AFS Trans., 103, 1995, 119-134



- [JHA17] K. JHAVERI, G. M. LEWIS, J. L. SULLIVAN, G. A. KEOLEIAN,**  
Life cycle assessment of thin-wall ductile cast iron for automotive lightweighting applications, Sustainable Materials and Technologies 15, 2018, 1–8
- [JOH74] W.C. JOHNSON, B.V. KOVACS, J.A. CLUM,**  
Interfacial chemistry in magnesium modified nodular iron, Scripta metallurgica, 8, 1974, 1309-1316
- [JOH75] W.C. JOHNSON, H.B. SMARTT,**  
Confirmation of impurity adsorption at flake/iron interfaces in gray cast iron, Scripta metallurgica, 9, 1975, 1205-1210
- [JOH78] W.C. JOHNSON, B.V. KOVACS,**  
The effect of additives on the eutectoid transformation of ductile iron, Metallurgical Transactions A, 9, 1978, 219-229
- [JOL17] M.R. JOLLY, K. SALONITIS,**  
Primary Manufacturing, Engine Production and on-the-road CO<sub>2</sub>: How can the Automotive Industry Best Contribute to Environmental Sustainability?, Vienna motor symposium, 2017
- [JON80] H. JONES, W. KURZ,**  
Growth temperatures and the limits of coupled growth in unidirectional solidification of Fe-C eutectic alloys, Metall. Trans., 11A, 1980, 1265-1273
- [JON81] H. JONES, W. KURZ,**  
Relation of interphase spacing and growth temperature to growth velocity in Fe-C and Fe-Fe<sub>3</sub>C eutectic alloys, Z. Metallkde., 72, 1981, 792-797
- [JUN08] S. JUNG, T. ISHIKAWA, H. NAKAE,**  
Critical conditions for formation of spheroidal graphite, Materials Science and Engineering A, 476, 2008, 350-356
- [KAN18] S. KANTE, A. LEINWEBER,**  
EBSD characterization of the eutectic microstructure in hypoeutectic Fe-C and Fe-C-Si alloys, Mater. Charac. 138, 2018, 274-283
- [KAR1816] C.J.B. KARSTEN,**  
1816, Translation in French by F.J. Culmann, 1820: Manuel de la métallurgie du fer, tome 2, <https://gallica.bnf.fr/ark:/12148/bpt6k98189063/f142.image.r=silice>
- [KEE88] B.J. KEENE,**  
Review of data for the surface tension of iron and its binary alloys, Int. Materials Rev., 33, 1988, 1-37
- [KEV57] J. KEVERIAN, H.F. TAYLOR,**  
Effects of gaseous and solid addition elements on surface tension and contact angle (on graphite) of various iron-carbon alloys, Trans. AFS, 65, 1957, 212-221
- [KOV80] B.V. KOVACS,**  
Pearlite stabilization in cast irons, AFS Trans. 89, 1980, 79-96
- [KOZ61] P. KOZAKEVITCH, G. URBAIN,**  
Tension superficielle du fer liquide et de ses alliages, Mémoires Scientifiques Rev. Métallurg., 58, 1961, pp. 401-413, pp. 531-534 and pp. 931-947
- [KUR79] W. KURZ, D.J. FISHER,**  
Dendritic growth in eutectic alloys: the coupled zone, Int. Mat. Rev. 244, 1979, 177-204
- [KUR98] W. KURZ, D.J. FISHER,**  
Fundamentals of Solidification, Fourth. ed., 1998, Trans Tech Publications LTD.
- [KWE20] E.S. KWEON, D.H. ROH, S.B. KIM, D.M. STEFANESCU,**  
Computational modelling of shrinkage porosity formation in spheroidal graphite iron: a proof of concept and experimental validation, Int. J. Metalcasting, 14, 2020, 601-609
- [LAC86] J. LACAZE, G. LESOULT,**  
Microsegregation and precipitation of minor phases during the solidification of Al-Cu-Mg-Si alloys, in State of the art of computer simulation of casting and solidification processes, E-MRS symposia proceedings, 14, 1986, 119-127

- [LAC89] J. LACAZE, M. CASTRO, N. AICHOUN, G. LESOULT,**  
Influence de la vitesse de refroidissement sur la microstructure et la cinétique de solidification de fontes G.S.: expérience et simulation numérique de solidification dirigée,  
Mémoires et Etudes Scientifiques de la Revue de Métallurgie, 1989, 85-97
- [LAC90] J. LACAZE, M. CASTRO, G. LESOULT,**  
Nucleation of Graphite Particles in Grey and Nodular Iron.  
EUROMAT'89, DGM Informationsgesellschaft. Verlag, 1990, 147-152
- [LAC91] J. LACAZE, B. SUNDMAN,**  
An assessment of the Fe-C-Si system, Metall. Trans. A, 22A, 1991, 2211-2223
- [LAC94] J. LACAZE, C. WILSON, C. BAK**  
Experimental study of the eutectoid transformation in spheroidal graphite cast iron  
Scandinavian Journal of Metallurgy 23 (1994) 151-163
- [LAC98A] J. LACAZE, M. CASTRO, G. LESOULT,**  
Solidification of spheroidal graphite cast irons - II. Numerical simulation,  
Acta Mater. 46, 1998, 997–1010.
- [LAC98B] J. LACAZE, V. GERVAL,**  
Modelling the eutectoid reaction of spheroidal graphite Fe-C-Si alloys,  
ISIJ International 38 (1998) 714-722
- [LAC99A] J. LACAZE,**  
Pearlite growth in cast irons : a review of literature data,  
Int. J. Cast Metals Research 11 (1999) 431-436
- [LAC99B] J. LACAZE**  
Solidification of spheroidal graphite cast irons. Part III : microsegregation related effects,  
Acta materialia 47 (1999) 3779-3792
- [LAC13A] J. LACAZE, N. VALLE, K. THEUWISSEN, J. SERTUCHA, B. EL ADIB, L. LAFFONT**  
Redistribution and effect of various elements on the morphology of primary graphite growth in cast iron, Advances in Materials Science and Engineering, 2013, 638451
- [LAC13B] J. LACAZE, L. MAGNUSSON-ÅBERG, J. SERTUCHA,**  
Review of microstructural features of chunky graphite in ductile cast irons,  
Proc. Keith Millis symposium, AFS, 2013, 232-240
- [LAC16] J. LACAZE, J. SERTUCHA, L. MAGNUSSON ÅBERG**  
Microstructure of as-Cast Ferritic-Pearlitic Nodular Cast Irons, ISIJ Int., 56, 2016, 1606-1615
- [LAC17A] J. LACAZE, J. BOURDIE, M.J. CASTRO ROMAN,**  
A 2-D nucleation-growth model of spheroidal graphite,  
Acta mater., 134, 2017, 230-235, DOI : <https://doi.org/10.1016/j.actamat.2017.05.032>
- [LAC17B] J. LACAZE**  
Trace elements and graphite shape degeneracy in nodular graphite cast irons,  
Int. J. Metalcasting, 11, 2017, 44-51
- [LAC17C] J. LACAZE,**  
Discussion on “Stable eutectoid transformation in nodular cast iron: modeling and validation”,  
Metallurgical and Materials transactions A, 48, 2017, 5146-5148.
- [LAC17D] J. LACAZE, J. SERTUCHA,**  
Effect of tin on the phase transformation of cast irons  
Journal of phase equilibria and diffusion, 38, 2017, 743-749.
- [LAC17E] J. LACAZE,**  
The austenite to Pearlite/ferrite transformation,  
ASM Handbook, Vol. 1A, Cast Iron Science and Technology, 2017, pp. 106-113
- [LAC18] J. LACAZE, J. SERTUCHA,**  
Some paradoxical observations about spheroidal graphite degeneracy,  
China Foundry, 15, 2018, 457-463

- [LAC19] J. LACAZE, D. CONNÉTABLE, M.J. CASTRO DE ROMAN,**  
Effects of impurities on graphite shape during solidification of spheroidal graphite cast irons,  
Materialia, 8, 2019, 100471
- [LAC21A] J. LACAZE, S. DAWSON, A. HAZOTTE**  
Cast irons: a historically green material worthy of continuous research,  
Inter. J. Technology, 12, 2021, 167-181. DOI: 10.14716/ijtech.v12i6.5235
- [LAC21B] J. LACAZE, A. REGORDOSA, J. SERTUCHA, U. DE LA TORRE,**  
Quantitative analysis of solidification of compacted graphite irons – A modelling approach,  
ISIJ Int., 61, 2021, 1539-1549. DOI: 10.2355/isijinternational.ISIJINT-2020-476
- [LAC22A] J. LACAZE, O. DEZELLUS,**  
Surface tension, interfacial segregation and graphite shape in cast irons,  
Metall. Mater. Trans. B, 53, 2022, 161-177. DOI: 10.1007/s11663-021-02352-x
- [LAC22B] J. LACAZE**  
On the role of interfacial segregation on graphite shape in cast irons,  
proceedings of the ICASP conference, 2022
- [LAF18] L. LAFFONT, R. JDAY, J. LACAZE,**  
An electron microscopy study of graphite growth in nodular cast irons,  
Metall. Mater. Trans., 49A, 2018, 1287-1294.
- [LAF20] L. LAFFONT, A. PUGLIARA, T. HUNGRIA, J. LACAZE,**  
3D-STEM observation of a multiphase nucleus of spheroidal graphite,  
J. Mater. Res. Technol., 9, 2020, 4665–4671.
- [LAK68] K.D. LAKELAND, L.M. HOGAN,**  
The coupled zone concept applied to solidification of cast irons,  
ISI Pub. 110, The Iron and Steel Institute, 1968, 213-223
- [LAL73] M.J. LALICH, C.R. LOPER,**  
Effects of pearlite-promoting elements on the kinetics of the eutectoid transformation in ductile cast  
irons, AFS Trans. 79, 1973, 217-228
- [LEK03] S. LEKAKH, C.R. LOPER,**  
Improving inoculation of ductile iron. AFS Trans. 111, 2003, 885–894.
- [LEK06] S.N. LEKAKH, D.G.C. ROBERTSON, C.R. LOPER,**  
Thermochemistry and kinetics of iron melt treatment, WFC06, paper 68
- [LEK09] S. LEKAKH, V. RICHARDS, K. PEASLEE,**  
Thermo-Chemistry of Non-Metallic Inclusions in Ductile Iron,  
Int. J. Metalcasting, 3, 2009, 25–37. <https://doi.org/10.1007/BF03355456>
- [LEK17] S.N. LEKAKH, JUN GE, V. RICHARDS, R. O'MALLEY, J.R. TERBUSH,**  
Optimization of melt treatment for austenitic steel grain refinement,  
Metall. Mater. Trans. B, 48, 2017, 406-419
- [LEK18] S. LEKAKH,**  
Effect of Non-metallic Inclusions on Solidification of Inoculated Spheroidal Graphite Iron,  
AFS Trans., 2018, 129–138.
- [LES75] G. LESOULT, M. TURPIN,**  
Le couplage de croissance du graphite et de l'austénite pendant la solidification dirigée des fontes  
grises,  
The metallurgy of cast iron, Georgi Ed., 1975, 255-275
- [LES84] G. LESOULT, R. BELLOCCI, M. GRANDPIERRE,**  
Les fontes à Pont-à-Mousson, CR PAM, 1984
- [LES85] G. LESOULT, P. DIETRICH, F. ARNOULD, J.M. THÉRET,**  
Formation of internal defects in G.G. cast irons in relation to the solidification process,  
in "The Physical Metallurgy of Cast Iron", Mat. Res. Soc. Symp. Proc., 34, 1985, 223-232

- [LES98A] G. LESOULT, M. CASTRO, J. LACAZE,**  
Solidification of spheroidal graphite cast iron. Part I : physical modelling,  
Acta materialia, 46, 1998, 983-995
- [LES98B] G. LESOULT, M. CASTRO ROMAN, J. LACAZE**  
Physical modelling of the solidification of spheroidal graphite cast irons : revisitation of the coupled zone concept, Proc. Modelling of Casting, Welding and Advanced Solidification Processes - VIII,  
B.G. Thomas and C. Beckerman neds., TMS, 1998, 479-486
- [LES09] G. LESOULT,**  
Microporosity in cast alloys: simple considerations on its formation,  
Int. J. Cast Metals Research, 22, 2009, 2-7
- [LIE97] LIETAERT F.,**  
The austenite decomposition reaction kinetics as affected by surface active elements in graphite cast irons, Giessereiforschung, 49, 1997, 106-122
- [LIU83] P.C. LIU, C.L. LI, D.H. WU, C.R. LOPER,**  
SEM study of chunky graphite in heavy section ductile iron, AFS Trans., 91, 1983, 119-126
- [LIU89] Z.K. LIU, J. ÅGREN,**  
On the transition from local equilibrium to paraequilibrium during the growth of ferrite in Fe-Mn-C Austenite, Acta Metallurgica, **37**, 1989, 3157-3163
- [LIU90A] S. LIU, C.R. LOPER,**  
Morphology of kish graphite, AFS Trans., 1990, 385-394
- [LIU90B] B.C. LIU, T.X. LI, Z.J. RUE, X.Y. YANG, E.Q. HUO, C.R. LOPER,**  
The role of antimony in heavy-section ductile iron, AFS Trans., 1990, 753-757.
- [LIU91] S. LIU, C.R. LOPER,**  
The formation of kish graphite, Carbon, 29, 1991, 547-555
- [LOP85] C.R. LOPER, S. SHIRVANIS, T.H. WITTER,**  
Graphite Inoculants for Gray Cast Iron,  
in The Physical Metallurgy of Cast Iron, MRS, 34, 1985, 89-99.
- [LOP98] C.R. LOPER,**  
Inoculation of cast iron--summary of current understanding, AFS Trans., 1998, 523-528.
- [LOP99] C.R. LOPER,**  
Inoculation of cast iron--summary of current understanding,  
103rd Annual Meeting of the American Foundrymen's Society. 1998.
- [LOP20] M.C. LOPEZ, J.M. MASSONE, R.E. BOERI,**  
Examination of the size and morphology of austenite grains in lamellar graphite cast iron,  
Int. J. Metalcasting, 14, 2020, 689-695
- [LUP83] C.H.P. LUPIS,**  
Chemical thermodynamics of materials, New York, North Holland, 1983.
- [LUX68] B. LUX, W. KURZ,**  
Eutectic growth of iron-carbon-silicon and iron-carbon-silicon-sulphur alloys,  
ISI Pub. 110, The Iron and Steel Institute, 1968, 193-203
- [LUX69] B. LUX, W. BOLLMANN, M. GRAGES,**  
On the structure of graphite in pure Fe-C-Si alloys, Practical Metallography, 6, 1969, 530-535
- [LUX70A] B. LUX,**  
On the theory of nodular graphite formation in cast iron- Part I : experimental observations of nodular graphite formation during the solidification of cast iron melts.  
Giesserei Forschung in English, 22, 1970, 65-81, and also AFS cast metals research journal, 1972
- [LUX70B] B. LUX,**  
On the theory of nodular graphite formation in cast iron- Part II : theoretical interpretation of the experimental observations,  
Giesserei Forschung in English, 22, 1970, 158-177, and also AFS cast metals research journal, 1972

- [LYU63] A.P. LYUBCHENKO, D.G. SHERMAN, G.S. KUZ'MINOV,**  
Iron self-diffusion in dependence on its cerium content, *Phys. Met. Metallogr.*, 15, 1963, 151-153
- [MAC80] D.G. MCCARTNEY, J.D. HUNT, R.M. JORDAN,**  
The structures expected in a simple ternary eutectic system: Part I. Theory, *Metall. Trans.*, 11A, 1980, 1243-1249
- [MAG87] P. MAGNIN, W. KURZ,**  
An analytical model of irregular eutectic growth and its application to Fe-C, *Acta metal.*, 35, 1987, 1119-1128
- [MAM83] F. MAMPAEY,**  
A quantitative study on the solidification morphology of cast iron, *La Fonderie Belge*, 1983, pp. 3-15 of issue 1 and pp. 4-16 of issue 3.
- [MAM98A] F. MAMPAEY,**  
Application of austenite dendrite growth model to analyse liquidus temperature measurements in cups, *AFS Trans.* 106, 1998, 461-467
- [MAM98B] F. MAMPAEY,**  
Modeling and experimental validation of austenite dendrite growth, *AFS Trans.* 106, 1998, 469-476
- [MAM00] F. MAMPAEY,**  
Influence of compacted graphite on solidification morphology of cast iron, *AFS Trans.*, 2000, 11-17
- [MAM01] F. MAMPAEY,**  
Practical examples using the finite volume method for simulating the casting process, *AFS proceedings*, 2001, paper 01-075
- [MAT53] E. MATUYAMA**  
Inhomogeneity of crystal structure within graphite grain in cast iron, *J. Japan Inst. Metals Materials*, 1953, 17-20
- [MAT15] T. MATSUSHITA, E. GHASSEMALI, A. GÓMEZ SARO, L. ELMQUIST, A.E.W. JARFORS,**  
On thermal expansion and density of CGI and SGI cast irons, *Metals* 2015, 5, 1000-1019
- [MCS74] R.H. McSWAIN, C.E. BATES, W.D. SCOTT,**  
Iron-graphite surface phenomena and their effects on iron solidification, *AFS Cast Metals Research J.*, 10, 1974, 181-190
- [MER68] H.D. MERCHANT,**  
Solidification of cast iron – A review of literature, *Recent research on cast iron*, Gordon and Breach, 1968, 1-100
- [MIA94] BAIHE MIAO, D.O. NORTHWOOD, WEIMIN BIAN, KEMING FANG, MINZ HENG FAN,**  
Structure and growth of platelets in graphite spherulites in cast iron, *J. Mater. Sci.*, 29, 1994, 255-261
- [MIL49] K.D. MILLIS, A. P. GAGNEBIN, N. B. PILLING,**  
Cast ferrous alloy, patent 2,485,760
- [MIL76] B.S. MIL'MAN, N.N. ALEKSANDROV, V.T. SOLENKOV, L.V. IL'ICHEVA**  
Interfacial tension and the type of graphite formed in molten iron, *Russian Casting Production*, 1976, pp. 179-182.
- [MIN83] I. MINKOFF,**  
The physical metallurgy of cast iron, John Wiley and sons, 1983
- [MIT17] J. MITTERPACH, E. HRONCOV, J. LADOMERSKÝ, K. BALCO,**  
Environmental evaluation of grey cast iron via life cycle assessment, *Journal of Cleaner Production* 148 (2017) 324e335
- [MIY98] H. MIYAKE, A. OKADA,**  
Nucleation and growth of primary Austenite in hypoeutectic cast iron, *AFS Trans.*, 1998, 581–587.
- [MOH20] S. MOHAGHEGI, S. BOTTIN-ROUSSEAU, S. AKAMATSU, M. SEREFOGLU,**  
Decoupled versus coupled growth dynamics of an irregular eutectic alloy, *Scripta Mater.*, 189, 2020, 11-15

- [MOO72] A. MOORE,**  
Carbon equivalent of white cast irons, AFS Cast Metals Research J., March 1972, 15-19
- [MON01] J.P. MONCHOUX, C. VERDU, G. THOLLET, R. FOUGÈRES, A. REYNAUD,**  
Morphological changes of graphite spheroids during heat treatment of ductile cast irons, Acta mater. 49, 2001, 4355-4362
- [MUH13] H.M. MUHMOND, H. FREDRIKSSON,**  
Relationship between inoculants and the morphologies of MnS and graphite in gray cast iron, Metall. Mater. Trans. B, 44, 2013, 283–298.
- [MUH15] H.M. MUHMOND, H. FREDRIKSSON,**  
Graphite growth morphologies in high Al cast iron, in "Advances in the science and Engineering of Casting Solidification", TMS, 2015, 323-330
- [MUN78] A. MUNITZ, I. MINKOFF,**  
Determination of the structure of graphite in cast iron from melt analysis, Proc. of the 45<sup>th</sup> Int. Foundry Congress, Budapest, 1978, paper 32
- [MUN82] A. MUNITZ, S. NADIV,**  
Effect of doping elements on the morphology of graphite grown from Ni-C melts, J. of Materials Science, 17, 1982, 3409-3422
- [NAK02] H. NAKAE, Y. IGARASHI**  
Influence of sulfur on heterogeneous nucleus of spheroidal graphite Mater Trans, 43, 2002, 2826-2831
- [NAK16] I. NAKAE, Y. ZOU, Y. SATO,**  
Influence of graphite morphology, thermal history and S and Cu on ferrite/pearlite formation in cast iron, Proceedings of the 72nd world foundry congress, Nagoya, paper SL-2
- [NAS93] L. NASTAC, D.M. STEFANESCU,**  
Modeling of microsegregation in SG cast iron, AFS Trans., 134, 1993, 933-938
- [NEC82] E. NECHTELBERGER, H. PUHR, J.B. VON NESSELRODE, A. NAKAYASU,**  
Cast iron with vermicular graphite – State of the art. Development, production, properties, applications, Int. Foundry Congress, CIATF, 1982, 1-39
- [NEU68] F. NEUMANN,**  
The Influence of additional elements on the physico-chemical behavior of carbon in carbon saturated molten iron, Recent Research on Cast Iron, Gordon and Breach, 1968, 659-705
- [NG21] KOK LONG NG, H. SASAKI, H. KIMURA, T. YOSHIKAWA, M. MAEDA,**  
Effects of high-concentration Cu and Sn on the nucleation and growth behavior of graphite on rare-earth compounds during the solidification of cast iron, Metall. Mater. Trans. A, 52, 2021, 902-913
- [NIE75] H. NIESWAAG, A.J. ZUITHOFF,**  
The effect of S, P, Si and Al on the morphology and graphite structure of directionally solidified cast iron, in "The Metallurgy of Cast Iron", Georgi Ed., 1975, 327-351
- [OHN03] I. OHNAKA, J. IWANE, H. YASUDA, J. ZHU,**  
Prediction of porosity defect in spheroidal graphite iron castings, Int. J. Cast Metals Research, 16, 2003, 293-299
- [OLD62A] W. OLDFIELD, J.G. HUMPHREYS,**  
Formation of nodular graphite in hypo-eutectic irons, BCIRA J., 10, 1962, 315-324
- [OLD62B] W. OLDFIELD,**  
The chill-reducing mechanism of silicon in cast iron, BCIRA J., 10, 1962, 17-27
- [OLD66] W. OLDFIELD,**  
A quantitative approach to casting solidification: freezing of cast iron, Trans ASM 59, 1966, 945-961.
- [OWA77] T. OWADANO, K. YAMADA, K. TORIGOE,**  
Quantitative metallographic study of the solidification of spheroidal graphite cast iron, Trans. JIM, 18, 1977, 871-878

- [PAN82] E.N. PAN, K. OGI, C.R. LOPER,**  
Analysis of the solidification process of compacted/vermicular graphite cast iron,  
AFS Trans., 90, 1982, 509-527.
- [PAN86] E.N. PAN, C.R. LOPER,**  
Matrix development in graphitic cast irons, AFS Trans. 94, 1986, 545-556
- [PAN87] E.N. PAN, M.S. LOU, C.R. LOPER**  
Effects of copper, tin, and manganese on the eutectoid transformation of graphitic cast irons,  
AFS. Trans. 95, 1987, 819-840
- [PAR96] J.S. PARK, J.D. VERHOEVEN,**  
Transitions between type A flake, type D flake, and coral graphite eutectic structures in cast irons,  
Metall. Mater. Trans. A, 27A, 1996, 2740-2753
- [PEN11] I. PENCEA, D.M. STEFANESCU, R. RUXANDA, F.V. ANGHELINA,**  
New aspects regarding the structure of spheroidal cast iron carbon inclusions revealed by WAXD  
investigations, Key Eng. Materials, 457, 2011, 120-125
- [PER84] J.H. PEREPEZKO,**  
Nucleation in undercooled liquids,  
Mater. Sci. Eng., 65, 1984, 125–135, [https://doi.org/10.1016/0025-5416\(84\)90206-4](https://doi.org/10.1016/0025-5416(84)90206-4)
- [PER13] M. PERRUT, S. BOTTIN-ROUSSEAU, G. FAIVRE, S. AKAMATSU**  
Dynamic instabilities of rod-like eutectic growth patterns: a real-time study,  
Acta mater., 61, 2013, 6802-6808
- [PERRE] W. VAN DER PERRE**  
Thermal analysis of cast iron, Heraeus,  
[https://www.heraeus.com/media/media/hen/media\\_hen/products\\_hen/iron/thermal\\_analysis\\_of\\_cast\\_iron.pdf](https://www.heraeus.com/media/media/hen/media_hen/products_hen/iron/thermal_analysis_of_cast_iron.pdf), accessed March 4, 2020
- [PUG19] A. PUGLIARA, T. HUNGRIA-HERNANDEZ, L. LAFFONT, J. LACAZE,**  
3D-STEM observation of a multiphase nucleus of spheroidal graphite,  
2<sup>nd</sup> Carl Loper Cast Iron Symposium, Bilbao, September 2019
- [QIN17] J. QING, V.L. RICHARDS, D.C. VAN AKEN,**  
Growth stages and hexagonal-rhombohedral structural arrangements in spheroidal graphite  
observed in ductile iron, Carbon 116, 2017, 456-469
- [QIN20] J. QING, M. XU, V. PIKHOVICH,**  
Why is graphite spherical in ductile iron? A study of elemental distribution at interfaces in ductile  
iron using atom probe tomography and transmission electron microscopy,  
Int. J. Metalcasting, 14, 2020, 1115-1122
- [QIN21] J. QING, S. LEKAKH, SIMON LEKAKH, M. XU, D. FIELD**  
Formation of complex nuclei in graphite nodules of cast iron, Carbon 171, 2021, 276-288
- [RAP86] M. RAPPAZ, P. THEVOZ, Z. JIE, J.P. GABATHULER, H. LINDSCHEID,**  
Micro-macroscopic modelling of equiaxed solidification, State of the Art of Computer Simulation of  
Casting and Solidification Processes, Les éditions de Physique, les Ulis, France, 1986, 277-284.
- [RAP89] M. RAPPAZ,**  
Modeling of microstructure formation in solidification processes  
Int. Mater. Rev., 34, 1989, 93-124
- [RAP90] M. RAPPAZ, S.A. DAVID, J.M. VITEK, L.A. BOATNER,**  
Analysis of solidification microstructures in Fe-Ni-Cr single-crystal welds,  
Metallurgical Transactions, 21A, 1990, 1767-1782
- [RAP99] M. RAPPAZ, J.M. DREZET, M. GREMAUD,**  
A new hot-tearing criterion, Metall. Mater. Trans, 30A, 1999, 449-455
- [REG20] A. REGORDOSA, U. DE LA TORRE, J. SERTUCHA, J. LACAZE,**  
Quantitative analysis of the effect of inoculation and magnesium content on compacted graphite  
irons – Experimental approach, J. Materials Processing and Technology, 9, 2020, 11332-11343

- [REG21] A. REGORDOSA, J. SERTUCHA, J.R. OLAIZOLA, J. LACAZE,**  
When is a cast iron eutectic?, International Journal of Metalcasting, DOI: 10.1007/s40962-021-00587-7
- [REG22] A. REGORDOSA, J. LACAZE, J. SERTUCHA, M.J. CASTRO-ROMAN, U. DE LA TORRE, O. DEZELLUS**  
Is thermal analysis able to provide carbon and silicon contents of cast irons?, work in progress
- [REY05] A. REYNAUD ,**  
Oligo-éléments et fontes, éditions ETIF, 2005
- [RID71] A. RIDING, J.E. GRUZLESKI,**  
Effects of freezing rate on graphite morphology in ductile iron,  
AFS Cast Metals Research J., June 1971, 67-69
- [RIP03] I. RIPOSAN, M. CHISAMERA, S. STAN, T. SKALAND,**  
Graphite nucleant (microinclusion) characterization in Ca/Sr inoculated grey irons,  
Int. J. Cast Met. Res. 16, 2003, 105–111. <https://doi.org/10.1080/13640461.2003.11819567>
- [RIV02] G. RIVERA, R. BOERI, J. SIKORA,**  
Revealing and characterising solidification structure of ductile cast iron,  
Mater. Sci. Techn., 18, 2002, 691-697. DOI: [10.1179/026708302225003668](https://doi.org/10.1179/026708302225003668)
- [RIV04] G.L. RIVERA, R.E. BOERI, J.A. SIKORA,**  
Solidification of gray cast iron, Scripta mater., 50, 2004, 331-335
- [RIV11] G.L. RIVERA, R.E. BOERI, J.A. SIKORA,**  
Growth of eutectic austenite in free graphite cast irons,  
Key Engineering Materials, 457, 2011, 67-72
- [ROB18] C. ROBION-BRUNNER,**  
L'Afrique des métaux, in "L'Afrique ancienne, de l'Acacus au Zimbabwe, 20000 avant notre ère – XVIIème siècle", F.X. Fauvelle ed., Belin, chap. XVIII, 519-543
- [ROH79] K. RÖHRIG, W. FAIRHURST,**  
Heat treatment of nodular cast iron, Giesserei-Verlag GmbH, Düsseldorf, 1979
- [ROS71] C. ROSCOE, D. NAGLE.,S.B. AUSTERMAN,**  
Growth of graphite single crystals from iron-carbon solutions, J. Materials Science, 6, 1971, 998-1006
- [ROV94] A. ROVIGLIONE, J.D. HERMIDA,**  
X-ray diffraction characterization of flake and compacted graphite in cast iron,  
Mater. Charac. 32, 1994, 127-137
- [RUN97] K.B. RUNDMAN,**  
Segregation of alloying elements in ductile cast iron: the use of chemical, thermal, and mechanical processing to control the effects of segregation in austempered ductile iron,  
101st casting congress, AFS, 1997, paper 97-117
- [SAD75] J.P. SADOCHA, J.E. GRUZLESKI,**  
The mechanism of graphite spheroid formation in pure Fe-C-Si alloys,  
The metallurgy of cast iron, Georgi Ed., 1975, 443-459
- [SAL19] K. SALONITIS, M. JOLLY, E. PAGONE M. PAPANIKOLAOU,**  
Life-Cycle and Energy Assessment of Automotive Component Manufacturing: The Dilemma Between Aluminum and Cast Iron, Energies 12, 2019, 2557-2580
- [SAR59] D.D. SARATOVKIN,**  
Dendritic crystallization. Consultants bureau, 1959. <https://www.nature.com/articles/187093b0>
- [SAW68] J.C. SAWYER, J.F. WALLACE, W.L. HALLERBERG,**  
Effects and neutralization of trace elements in gray, ductile and malleable iron,  
AFS Trans., 1968, part 1: 2-20; part 2: 21-32.
- [SEA75] M.P. SEAH, C. LEA,**  
Surface segregation and its relation to grain boundary segregation,  
Philosophical Magazine, 31, 1975, 627-645



- [SEL94] C. SELIG,**  
Développement des microstructures et microségrégations lors de la solidification des fontes : transition de l'eutectique graphitique vers l'eutectique cémentitique,  
PhD thesis, Nancy, France, 1994
- [SEL00] C. SELIG, J. LACAZE**  
Study of microsegregation buildup during solidification of spheroidal graphite cast iron,  
Metallurgical and Materials Transactions 31B (2000) 827-836
- [SER10] J. SERTUCHA, P. LARRAÑAGA, J. LACAZE, M. INSAUSTI,**  
Experimental investigation on the effect of copper upon the eutectoid transformation of as-cast and austenitized spheroidal graphite cast iron, International Journal of Metalcasting, 4, 2010, 51-58
- [SER21] J. SERTUCHA, G. ARTOLA, U. DE LA TORRE, J. LACAZE,**  
Chunky Graphite in Low and High Silicon Spheroidal Graphite Cast Irons—Occurrence, Control and Effect on Mechanical Properties, Materials 2020, 13, 5402. DOI: 10.3390/ma13235402
- [SHA16] A.J. SHAHANI, XIANGHUI XIAO, P.W. VOORHES,**  
The mechanism of eutectic growth in highly anisotropic materials,  
Nature Communications, 7, 2016, 12953
- [SHI08] D. SHI, D. LI, G. GAO, L. WANG,**  
Relation between surface tension and graphite shape in cast iron, Mater. Trans., 49, 2008, 2163-2165
- [SHI20] G.Q. SHI, Z. YANG, J.P. LI, D. TAO, Z.J. MA,**  
Investigation on the graphite nucleation and growth mechanism of the compacted graphite iron,  
J. Materials Research and Technology, 9, 2020, 8186-8196
- [SIL03] R. J. C. SILVA, A. HAZOTTE, H.M.C.M. SANTOS, A. M.P. PINTO, J. LACAZE, M. BRAZ FERNANDES, F. HELLAL,** Carbon diffusion and compatibility stresses generated by temperature cycling of spheroidal graphite cast irons in the austenitic field, Int. J. Cast Metals Research, 16, 2003, 149-153
- [SIR93] N. SIREDEY, J. LACAZE,**  
Growth conditions at the solidification front of multicomponent alloys,  
Scripta Metallurgica et Materialia 29, 1993, 759-764.
- [SKA93] T. SKALAND, Ø. GRONG, T. GRONG,**  
A model for the graphite formation,  
Metall. Trans. A 24, 1993, 2321–2345. <https://doi.org/10.1007/BF02648605>
- [SMI99] SMITHELLS METALS REFERENCE BOOK,**  
E.A. Brandes and G.B. Brook eds., Butterworth and Heinmann, 1999
- [SOL01] J.K. SOLBERG, M.I. ONSOIEN**  
Nuclei for heterogeneous formation of graphite spheroids in ductile cast iron  
Mater Sci Tech, 17, 2001, 1238-1242
- [SPE72] M.C. SPEER, N.A.D. PARLEE,**  
Dissolution and desulfurization reactions of magnesium vapor in liquid iron alloys,  
AFS Cast Metals Res., 1972, 122
- [STE90] D.M. STEFANESCU, D.K. BANDYOPADHYAY**  
On the solidification kinetics of spheroidal graphite cast iron  
in "Physical Metallurgy of Cast Iron IV", MRS, 1990, 15-26
- [STE05] D.M. STEFANESCU,**  
Solidification and modeling of cast iron - A short history of the defining moments,  
Mater. Sci. Eng., 413-414, 2002, 322-333
- [STE15] D.M. STEFANESCU,**  
Thermal analysis – Theory and applications in metalcasting, Int. J. Metalcasting, 9, 2015, 7-22
- [STE16] D.M. STEFANESCU, R. HUFF, G. ALONSO, P. LARRANAGA, E. DE LA FUENTE, R. SUAREZ,**  
On the crystallization of compacted and chunky graphite from liquid multicomponent iron-carbon-silicon-based melts, Metall. Mater. Trans. A, 47, 2016, 4012-4023

- [STE17A] D.M. STEFANESCU,**  
A history of cast iron, ASM Handbook, Volume 1A, Cast Iron Science and Technology, 2017, 3-11
- [STE17B] D.M. STEFANESCU, G. ALONSO, P. LARRANAGA, E. DE LA FUENTE, R. SUAREZ,**  
Reexamination of crystal growth theory of graphite in iron-carbon alloys,  
Acta mater, 139, 2017, 109-121
- [STE18] D.M. STEFANESCU, G. ALONSO, P. LARRANAGA, E. DE LA FUENTE, R. SUAREZ,**  
A comparative study of graphite growth in cast iron and in analogous systems,  
Int. J. Metalcasting, 12, 2018, 722-752
- [STE19A] D.M. STEFANESCU, A. CRISAN, G. ALONSO, P. LARRANAGA, R. SUAREZ,**  
Growth of spheroidal graphite on nitride nuclei: disregistry and crystallinity during early growth,  
Metall. Mater. Trans. A, 50, 2019, 1763-1772
- [STE19B] E. STEFANA , P. COCCA , F. MARCIANO , D. ROSSI, G. TOMASONI,**  
A Review of Energy and Environmental Management Practices in Cast Iron Foundries to Increase Sustainability, Sustainability 2019, 11, 7245-7263
- [STE20] D.M. STEFANESCU, R. SUAREZ, SUNG BIN KIM,**  
90 years of thermal analysis as a control tool in the melting of cast iron,  
China Foundry, 17, 2020, 69-84
- [SU85] K.C SU, I. OHNAKA, I. YAMAUCHI, T. FUKUSAKO,**  
Computer simulation of solidification of nodular cast iron,  
in The Physical Metallurgy of Cast Iron, MRS symposia proceedings, 34, 1985, 181-189
- [SUA16] R. SUÁREZ, J. SERTUCHA, P. LARRAÑAGA, J. LACAZE**  
Active Mg estimation using thermal analysis: a rapid method to control nodularity in ductile cast iron production, Metall. Mater. Trans. B, 47B, 2016, 2744-2753, [10.1007/s11663-016-0750-6](https://doi.org/10.1007/s11663-016-0750-6)
- [SUB80] S.V. SUBRAMANIAN, D. GOSH, D.A.R. KAY, G.R. PURDY,**  
Graphite morphology control in cast iron, Iron and Steelmaking, March 1980, 18-25
- [SUB82] S.V. SUBRAMANIAN, D.A.R. KAY, G.R. PURDY,**  
Compacted graphite morphology control, AFS Trans., 1982, 582-603
- [SUN83A] G.X. SUN, C.R. LOPER,**  
Influence of hypereutectic graphite on the solidification of gray cast iron,  
AFS Trans., 91, 1983, 217-224
- [SUN83B] G.X. SUN, C.R. LOPER,**  
Graphite flotation in cast iron, AFS Trans., 91, 1983, 841-854
- [SVE03] I.L. SVENSSON, A. MILLBERG, A. DIÓSZEGI,**  
A study of eutectic inoculation in grey iron by addition of Fe-Si-Ca-Al-, Sr, Ba, Zr, Ti, RE and C,  
Int. J. Cast Met. Res. 16, 2003, 29–34. <https://doi.org/10.1080/13640461.2003.11819554>
- [TAN10] TAN DERUI, LIAN HAIPING,**  
The Chinese traditional casting technique, Proc. 69<sup>th</sup> World Foundry Congress, 54-65 and  
An illustrated history of ancient Chinese casting, edited by the organization committee of the 69<sup>th</sup>  
World Foundry Congress, 2010
- [TEW21] U. TEWARI ET AL.,**  
An integrated multi-scale model for graphite growth mechanism in industrial cast iron,  
Metallurgical and Materials Transactions, B, 2021, published on line January 2021
- [TCFE8] Calculations performed with the THERMOCALC software and the TCFE-8 database,**  
<https://www.thermocalc.com/>
- [THE79] J.M. THERET,**  
Etude du déroulement de la solidification des fontes G.S. Conséquences prévisibles pour  
l'alimentation des pièces en fonderie, PhD thesis, E.N.S. des Mines de Paris, 1979.
- [THE12] K. THEUWISSEN, M.C. LAFONT, L. LAFFONT, B. VIGUIER, J. LACAZE,**  
Microstructural characterization of graphite spheroids in ductile iron,  
Trans. Indian Inst. Met., 65, 2012, 627-631

- [THE13] K. THEUWISSEN,**  
Etude de l'influence des impuretés et des éléments à l'état de traces sur les mécanismes de croissance du graphite dans les fontes,  
PhD thesis, INP-Toulouse, France, 2013, <http://ethesis.inp-toulouse.fr/archive/00002393/>.
- [THE14] K. THEUWISSEN, J. LACAZE, M. VÉRON, L. LAFFONT,**  
Nano-scale orientation mapping of graphite in cast irons, Mater. Characterization, 95, 2014, 187-195
- [THE16] K. THEUWISSEN, J. LACAZE, L. LAFFONT,**  
Structure of graphite precipitates in cast iron, Carbon, 96, 2016, 1120-1128
- [THI70] T. THIELEMANN,**  
Zur Wirkung von Spurenelementen im GuBeisen mit Kugelgraphit, Giesereitechnik, 16, 1970, 16-24.
- [THO86] J.T. THORGRIMSSON,**  
Effect of cooling rate on structure formation in cast iron castings,  
The Royal Institute of Technology, Stockholm, Sweden, thesis, 1986
- [TIL68] W.A. TILLER,**  
isothermal solidification of Fe-C and Fe-C-Si alloys,  
In Recent Research on Cast Iron, 1968, 129-171
- [TON18] B. TONN, J. LACAZE, S. DUWE,**  
Degenerated Graphite Growth in Ductile Iron, Materials Science Forum, 925, 2018, 62-69
- [TOR16] U. DE LA TORRE, J. LACAZE, J. SERTUCHA,**  
Chunky graphite formation in ductile cast irons: effect of silicon, carbon and rare earths,  
Int. J. Mater. Res. (previously Zeitschrift für Metallkunde), 107, 2016, 1041-1050.
- [TRO64] P.K. TROJAN, R.A. FLINN,**  
Fundamentals of magnesium addition to ductile iron, SAE, January 1964
- [TUR50A] D. TURNBULL, R.E. CECH,**  
Microscopic observation of the solidification of small metal droplets,  
J. Appl. Phys. 21, 1950, 804–810. <https://doi.org/10.1063/1.1699763>
- [TUR50B] D. TURNBULL,**  
Kinetics of Heterogeneous Nucleation, J. Chem. Phys. 18, 1950, 198–203.
- [TUR52] D. TURNBULL, B. VONNEGUT,**  
Nucleation Catalysis, Ind. Eng. Chem. 44, 1952, 1292–1298.
- [UHR77] B. URHENIUS**  
Optimization of parameters describing the interaction between carbon and alloying elements in ternary austenite, Scand. J. Metall., 6, 1977, 83-89
- [VEN90] D. VENUGOPALAN,**  
Decomposition of multicomponent austenite in spheroidal graphite cast iron  
in "Fundamentals and applications of ternary diffusion", 1990, 173-183
- [VER1665] <https://en.chateauversailles.fr/discover/estate/gardens>**
- [VER89] J.D. VERHOEVEN, A.J. BEVOLO, J.S. PARK,**  
Effect of Te on morphological transitions in Fe-C-Si alloys: Part II. Auger analysis,  
Metall. Trans. A, 20A, 1989, 1875-1881
- [VIG73] B. VIGNERON,**  
Contribution à l'étude de la dissolution d'alliages fer-silicium dans les alliages fer-carbone et fer-carbone-silicium (modèle des procédés d'inoculation des fontes), Thesis, 1973, University of Nancy, France
- [VIN02] B. VINET, L. MAGNUSSON, H. FREDRIKSSON, P.J. DESRÉ,**  
Correlations between surface and interface energies with respect to crystal nucleation,  
J. Colloid Interface Science, 255, 2002, 363-374

- [VON47] B. VONNEGUT,**  
The nucleation of ice formation by silver iodide,  
J. Appl. Phys. 18, 1947, 593–595. <https://doi.org/10.1063/1.1697813>
- [WAD80] N. WADE, Y. UEDA,**  
Continuous heating transformation of spheroidal graphite cast iron, Trans. ISIJ, 20, 1980, 857-861
- [WAL13] A.F. WALLACE, L.O. HEDGES, A. FERNANDEZ-MARTINEZ, P. RAITERI, J.D. GALE, G.A. WAYCHUNAS, S. WHITELAM, J.F. BANFIELD, J.J.D. YOREO,**  
Microscopic evidence for liquid-liquid separation in supersaturated CaCO<sub>3</sub> solutions,  
Science 341, 2013, 885–889. <https://doi.org/10.1126/science.1230915>
- [WES96] M. WESSEN, I.L. SVENSSON,**  
Modeling of ferrite growth in nodular cast iron, Metall. Mater. Trans. A, 27, 1996, 2209-2220
- [WET72] S.E. WETTERFALL, H. FREDRIKSSON, M. HILLERT,**  
Solidification process of nodular cast iron, J. Iron Steel Inst., May 1972, 323-333.
- [WHI83] C.V. WHITE, R.A. FLINN, P.K. TROJAN**  
Correlation of percent nodularity with Mg-Ce content – Section thickness and mechanical properties of ductile iron, AFS Trans. 91 (1983) 549-558
- [WIG21] T. WIGGER, T. ANDRIOLLO, C. XU, S.J. CLARK, Z. GONG, R.C. ATWOOD, J.H. HATTEL, N.S. TIEDJE, P.D. LEE, M.A. AZEEM**  
*In situ* synchrotron investigation of degenerate graphite nodule evolution in ductile cast iron, Acta materialia, 221, 2021, 117367
- [WIL05] J. DE WILDE, L. FROYEN, V. T. WITUSIEWICZ, U. HECHT,**  
Two-phase planar and regular lamellar coupled growth along the univariant eutectic reaction in ternary alloys: An analytical approach and application to the Al–Cu–Ag system, Journal of Applied Physics 97, 2005, 113515
- [WIT59] A. WITTMOSER,**  
Ein halbes Jahrhundert Giessereitechnik in Deutschland, Giesserei, 22, 1959, 630-639
- [WYN06] P. WYNBLATT, D. CHATAIN,**  
Anisotropy of segregation at grain boundaries and surfaces, Metall. Mater. Trans. A, 37, 2006, 2595-2620
- [ZHA97] Y. ZHANG, S.V. SUBRAMANIAN, G.R. PURDY,**  
Graphite growth in S.G. Irons: simulation vs. experiment, Advanced Mater. Research, 4-5, 1997, 461-468
- [ZHO09] ZHOU JIYANG,**  
Colour metallography of cast iron, China Foundry, 6, 2009, 57-69; 152-163; 255-267; and 366-374
- [ZHO10] ZHOU JIYANG,**  
Colour metallography of cast iron, China Foundry, 7, 2010, 76-88; 183-198; 292-307; and 470-478
- [ZHO11] ZHOU JIYANG,**  
Colour metallography of cast iron, China Foundry, 8, 2011, 154-164; 239-26; 337-349; and 447-462
- [ZHU15] MINGFANG ZHU, LEI ZHANG, HONGLEI ZHAO, D.M. STEFANESCU,**  
Modeling of microstructural evolution during divorced eutectic solidification of spheroidal graphite irons, Acta mater., 84, 2015, 413-425
- [ZOU89] ZOU JIE,**  
Simulation de la solidification eutectique équiaxe,  
Ph.D thesis, Ecole Polytechnique Fédérale de Lausanne, Switzerland, 1989.
- [ZOU12] Y. ZOU, M. OGAWA, H. NAKAE**  
Interaction of boron with copper and its influence on matrix of spheroidal graphite cast iron, ISIJ Int., 52, 2012, 505-509



# Glossary

- ACOM: automatic crystal orientation mapping is a technique implemented on TEM
- CCT: continuous cooling transformation. CCT diagrams are used to illustrate the effect of cooling rate on solid-state phase transformations.
- CE;  $CE_{EUT}$ : carbon equivalent which is calculated in the literature with various formulae; value of the carbon equivalent corresponding to the eutectic (4.26 to 4.34 wt.% depending on the source)
- CET: columnar to equiaxed transition
- DAS: dendrite arm spacing
- DAAS: direct austempering after solidification
- CGI: compacted graphite iron.
- DIS: ductile iron society.
- DS: directionally solidified, directional solidification. This relates to solidification against a chill in casting, but is also used in laboratories where it is often associated with a quenching device.
- DTA: differential thermal analysis. This technique measures the temperature difference between a sample and a reference located in the same furnace. It should not be confused with derivative thermal analysis which simply consists in using the time derivative of a cooling curve.
- EBS: electron back-scattered diffraction. This technique uses the formation of Kikuchi lines when an electron beam is made to diffract on a surface. The position and the distance between the lines depends on the crystallographic structure of the analysed area, so that EBS images may be analysed to characterize / differentiate phases based on their crystallography, but also to map grain crystallographic orientation of a polycrystalline structure up to the submicron scale. It is sometimes combined with chemical analysis with EDX for improving phase identification.
- EDX: Energy dispersive Spectrometer (called also EDXS, EDS, EDS-X). This technique uses the characteristic X-ray photons resulting from a sample exposed to an electron beam and allows the chemical characterization of a region of interest for qualitative and quantitative analysis. Modern software packages allow obtaining elements distribution maps and line profiles.
- ECI: European Cast Iron. Used to name an informal group of European academics and industrialists which was created in 2008 and has a yearly spring meeting since 2009.
- FIB: field ion beam is used to mill a sample with a beam of a vaporized heavy element. In materials science, it is primarily used to investigate particular features in a microstructure up to a nanometre scale. It allows preparing thin foils (100 nm or so in thickness) for TEM observation. FIB ion column is commonly associated with a SEM electron beam column, known as DUAL-BEAM FIB-SEM.
- Keel-block: standardized casting for laboratory investigation, with various sizes (Y2, Y3, etc., where the number is the thickness of the leg in inches).
- LGI: lamellar graphite iron.
- Mottled: said of a microstructure mixing stable and metastable eutectics
- QDS: a laboratory set-up designed for quenching during directional solidification

RE: rare earth. Most of the time, these are cerium and lanthanum which are used in cast irons, while mischmetal seems to be disregarded because of the presence of impurities.

RT: room temperature.

RVE: representative volume element, defines the elementary volume for numerical calculations in which every quantity is constant

SAED: selected area electron diffraction. When the crystalline lattice diffracts the electron beam in a TEM, it gives rise to an image made of diffraction spots that relate to the reciprocal space.

SEM: A variety of scanning electron microscopes (SEM) are available depending on the type of electron beam gun and the operational pressure. The most usual detectors use the secondary electron (SE) and the back scattered electron (BSE) modes that are sensitive to topography and atomic mass respectively. In the last decades, many other types of detectors have been developed.

SGL: spheroidal graphite iron. Ductile iron is often used as well but should be restricted to SGI having a fully ferritic matrix.

SIMS: secondary ion mass spectroscopy uses a beam of ionized particles to erode a surface. The extracted ions are then analysed by a mass spectrometer. This powerful technique asks for complex analysis when there is a risk of mass interferences, which is most often the case.

Solidification path: change with temperature of the composition of the remaining liquid during solidification of an alloy.

T,  $T_K$ : temperature, in Celsius and Kelvin respectively

TEM and HR-TEM: transmission and high-resolution transmission electron microscopes allow microstructure investigation at the nanometre and sub-nanometre scales. This includes imaging, e.g. of grains and dislocations, but also electron diffraction (SAED) for analysis of crystallographic structures. Combined with the EELS techniques, it allows also chemical analysis at atomic scale.

Tilting, twisting: defines the types of change in orientation of a plate-like precipitate, either by rotation around an axis in the plane of the plate (tilting, giving out-of-plane rotation/branching) or around an axis perpendicular to this plane (twisting, giving a rotation/branching parallel to the plate)

TKD: transmission Kikuchi diffraction. Much alike EBSD but with images obtained with a detector located on the opposite side of the thin foil sample with respect to the beam.

TTT: temperature-time-transformation. TTT diagrams are used to illustrate the effect of time on solid-state phase transformations.

# Index of terms and values of the parameters

*Note: the values given here are indicative and were used for the calculations performed in the main text. They should be checked and modified as appropriate when necessary.*

$\alpha$  stands for ferrite and  $\gamma$  for austenite when dealing with phases

$\alpha_{Th} = \lambda_{Th} / (\rho \cdot C_p)$ : thermal diffusivity

$\lambda_{Th}$ : thermal conductivity [ $J \cdot s^{-1} \cdot m^{-1} \cdot K^{-1}$ ], 80 for liquid and 30 for solid cast iron

$\lambda_.$ : inter-lamellar spacing

$\lambda_{min}$ ,  $\lambda_0$ ,  $\lambda_{br}$ : minimum, optimum and branching inter-lamellar spacing

$\rho$ : density

$\rho^\alpha$ , ferrite density:  $7870 \text{ kg} \cdot \text{m}^{-3}$  at RT for pure iron, thermal coefficient of expansion of iron from RT to  $800^\circ\text{C}$ :  $14.6 \cdot 10^{-6}$  [SMI99]

$\rho^\gamma$ , austenite density [ $\text{kg} \cdot \text{m}^{-3}$ ]

$$\rho^\gamma = 10^3 \cdot \left( 0.1193 + 9.7 \cdot 10^{-6} \cdot T + 4.0 \cdot 10^{-3} \cdot w_C^\gamma - 2.2 \cdot 10^{-4} \cdot (w_C^\gamma)^2 + 1.3 \cdot 10^{-3} \cdot w_{Si}^\gamma \right)^{-1} \quad [\text{DIE86}]$$

$\rho^l$ : density of liquid cast iron,  $6800 \text{ kg} \cdot \text{m}^{-3}$

$\rho^{gra}$ : density of graphite,  $2200 \text{ kg} \cdot \text{m}^{-3}$

$\Delta H$ ,  $\Delta H_{EUT}$ ,  $\Delta H^{gra}$ : latent heat of melting (positive), of the eutectic

$\Delta H^{gra}$ : latent heat of dissolution (positive) of graphite

$\sigma$ : surface or interface tension

$C_p$ : specific heat [ $J \cdot \text{kg}^{-1} \cdot K^{-1}$ ], 920 for liquid and 750 for solid cast iron

$$D_C^\alpha = 2 \cdot 10^{-6} \cdot \exp\left(-\frac{10115}{T_K}\right) \cdot \exp\left\{0.5898 \cdot \left[1 + \frac{2}{\pi} \cdot \arctan\left(\frac{15629}{T_{Curie} + 273} - \frac{15309}{T_K}\right)\right]\right\} \quad \text{diffusion}$$

coefficient of carbon in ferrite [ $\text{m}^2 \cdot \text{s}^{-1}$ ], where  $T_{Curie}$  ( $^\circ\text{C}$ ) is the Curie temperature of ferrite [AGR86]

$$D_C^\gamma = 2.343 \cdot 10^{-5} \cdot \exp\left(-\frac{17767}{T_K}\right) \quad \text{diffusion coefficient of carbon in austenite (m}^2 \cdot \text{s}^{-1}) \quad [\text{LIU89}]$$

$f^\varphi$ : mass fraction of phase  $\varphi$ , e.g.  $f^{gra}$ : mass fraction of graphite

$g^\varphi$ : volume fraction of phase  $\varphi$ , e.g.  $g^{gra}$ : volume fraction of graphite

$k_i^{s/l}$ : partition coefficient of element  $i$  between solid (s) and liquid (l)

$T$ ,  $T_K$ : temperature, temperature in Kelvin

$T_{EUT}$ : temperature of the stable eutectic

$T_{EW}$ : temperature of the metastable eutectic

$\Delta T$ : eutectic undercooling



$\Delta T_{EUT} = T_{EUT} - T$ : undercooling with respect to the stable eutectic

$\Delta T_{EW} = T_{EW} - T$ : undercooling with respect to the metastable eutectic

$T_L$ : liquidus temperature

$T_L^\gamma$ : austenite liquidus temperature according to the phase diagram

$T_{AL}$  or  $T_{LA}$ : austenite liquidus estimate from thermal analysis records

$T_L^{gra}$ : graphite liquidus temperature according to the phase diagram

$\Delta T_{tip}$ : growth undercooling of austenite

$\Delta T_L^{gra} = T_L^{gra} - T$ : undercooling with respect to the graphite liquidus

$T_\alpha^0$  and  $T_\alpha$ : upper and lower temperatures of the stable austenite/ferrite/graphite three phase field

$\Delta T_\alpha = T_\alpha - T$ : undercooling below  $T_\alpha$

$T_p^0$  and  $T_p$ : upper and lower temperatures of the metastable austenite/ferrite/cementite three phase field

$\Delta T_p = T_p - T$ : undercooling below  $T_p$

$V_m^{gra}$ : molar volume of graphite

$w_i^0$ : nominal weight fraction of solute i

$w_i^\phi$ : weight fraction of solute i in phase  $\phi$  ( $\phi$ = liquid, l, austenite,  $\gamma$ , graphite, gra)

## Appendix A

### A Brief History of ... Foundry

Based on an article published by S. Dawson in the December 2001 issue of Engine Technology

#### Basic Foundry Practice

1. Make a hole in sand
2. Melt some iron
3. Pour iron into sand

To the end-user, today's cast iron production may seem as simple as 1-2-3. However, behind the grey walls, dusty air and amine odours, foundrymen routinely control the behaviour of atoms at temperatures in excess of 1500°C. It's not always as simple as it looks, and neither was the path along the way.

#### The First Cupola

Approximately 4,000 years BC, in Egypt and China, scientists and sages commissioned the first iron cupolas. These early metallurgists placed a curious metal-like substance, which we now know as iron ore, in the hollow of a burnt out tree trunk. The charred inner surface of the trunk provided fuel for the fires and thermal insulation, while random holes that burned through the trunk allowed the ambient winds to enter and feed the charcoal. With the right combination of wind, rich ores and extra charcoal, the charge was reduced to a metallic iron sponge that could be rolled, using rocks, into decorative beads. It was 6000 years ago, and iron was more highly valued than gold.

Production techniques and raw materials were gradually refined as the Iron Age evolved. Iron implements and weapons began to appear in approximately 3000 BC, and the comparatively advanced technique of hardening iron weapons by heat treatment was known to the Greeks by about 1000 BC. Unfortunately for their slaves, the Greek metallurgists found that the most effective way to harden a sword was to plunge the glowing red blade into a human body. More than 2000 years later, the Scots quenched their swords in the urine of red haired boys. A new industry was borne as barrels of 'red-hair' urine were shipped across large distances. Presumably, the Tier II supply industry for red hair dye also flourished. The common link between the Greeks and the Scots: both realised that brine solutions had superior thermal conductivity to water.

#### The Iron Revolution

By the mid 1800's, liquid cast iron was routinely being produced in four continents to provide components such as pots, pans and woodstoves. However, because of the high carbon content of the iron (approximately 3.5% carbon, derived from the charcoal fuel), the solidified iron contained graphite particles. These particles, which were in the form of elongated flakes, made the iron weak and brittle and therefore unsuitable for demanding applications such as horseshoes.

While the majority of the liquid cast iron of 1850 was poured directly into sand moulds, some was poured into bar stock for further processing. The liquid iron was tapped from a Cupola furnace into a trough made in the sand floor of the foundry and flowed into impressions made by the foundryman's foot on either side of the trough. Because the orientation of the foot-sized ingots along the trough resembled piglets feeding at a sow, the small ingots became known as pig iron. The availability of individual pigs was a key for the early expansion of the iron industry. Each village could now have a blacksmith without needing a cupola.

Despite the advances, the iron masters of 1850 were not able to produce a strong and ductile iron. When they re-melted the pig iron in clay ovens in order to oxidise the graphite, the iron became thick and 'pasty'. They did not understand that the melting temperature of iron increases as the carbon content decreases, and their furnaces could



*The First Cupola?*

not achieve the temperatures required to keep the low-carbon steel in a molten state. When their 50 kg batches of iron became pasty, they removed them from the furnace and hammered, rolled or squeezed them into usable shapes. The hammering process forced the carbon to fly out of the iron as sparks. This process of 'stealing' the carbon away from the iron ultimately gave rise to the name steel, as opposed to iron. One of the first applications of this new steel was in ploughshares produced by a young entrepreneur named John Deere.

The new steel was in high demand, but the processing was slow, and every three tonnes of steel consumed a football pitch of virgin forest. Over the next thirty years, men like Bessemer, Siemens, Krupp, Mushet and Carnegie transformed the industry. However, the single most significant revelation belongs to Bessemer. Bessemer found that the sparks and droplets of molten pig iron that splashed out of his experimental furnace were malleable. He thereby deduced that air could decarburise iron and he decided to insert a lance into his clay crucible to blow air onto the surface of the iron. Bessemer's contemporaries must have scoffed. Surely, the solution to pasty iron was to provide more heat and, like blowing on a bowl of soup to make it colder, the air injection could only make things worse. Nonetheless, Bessemer persisted and in his first trial he converted a pasty 20 lb melt into "a beautiful fluid condition" in a few minutes. Although the metallurgy was not understood, and Bessemer wrongly concluded that air was fuel, the breakthrough was realised. Steelmaking could leap from kilograms per day to tonnes per hour. The patent was filed on 12 February 1856 and, although Bessemer died in 1898, he would still recognise the process used in modern steel mills for converting blast furnace pig iron into steel.

### The Modern Era

Until about 1940, the standard cast iron with flake-type graphite was sufficient for most applications. However, the onset of the Second World War significantly increased the demand for stronger cast materials. Iron metallurgists, who now had the benefit of chemical analysis and microscopes, realised that the relative weakness and brittleness of cast iron was caused by cracks that initiated at the edge of the graphite flakes and travelled along their flat surfaces. In fact, it is the fracture along the graphite flakes which gives cast iron its grey rather than metallic colour, and its name. In order to improve the strength and stiffness of cast iron, metallurgists turned their attention to the shape of the graphite flakes. Surely, if they could alter the sharp edges and the flat surfaces of the graphite flakes they could improve the mechanical properties. Cast iron was about to become the first engineered composite material.



*Bessemer's Bright Spark?*

Following the Second World War, researchers in England and America were both making progress on the new, ductile, iron. The British (BCIRA) found that additions of less than 0.1% cerium were sufficient to cause the graphite to grow in the form of individual spheroids instead of flakes. The Americans (at Inco) found that additions of approximately 0.05% magnesium would do the same thing. The commercial angle for Inco, the largest nickel supplier in the world, was that the magnesium would be sold as a nickel-magnesium alloy. According to Keith Millis, the lead researcher at Inco, "the British published first and forced our hand, we had to go public". Although Inco had intended to develop and commercialise a complete production process, the BCIRA publication by Morrrough and Williams in the March 1948 issue of the *Journal of Iron and Steel Institute* prompted Inco to file its patent application on 20 March 1948. The Inco magnesium process eventually won the battle on technical grounds and the annual worldwide production of ductile (aka: nodular, spheroidal graphite, SG) iron has since grown to approximately 13 million tonnes. Keith Millis was only 29 years old when the Inco patent was filed.

The modification of the graphite shape from flakes to nodules had a profound affect on the properties and the market potential of cast iron. In comparison to grey iron, the tensile strength tripled, the stiffness increased by 50% and ductility or elongation changed from 0% to more than 5%. Although another 20 years would be required to establish confidence in the production process, the next quantum step in cast iron technology had been realised.

### Atomic Engineering

With the aid of a microscope, we can see that the diameter of a typical graphite nodule is approximately 50µm (0.05 mm) and, depending on the cooling rate, a casting may have approximately 300 nodules per square millimetre of surface area. Even a simple test bar used for determining mechanical properties (25 mm diameter and 150 mm in length) will contain approximately  $1.3 \times 10^8$  (130 million) graphite nodules.

Each of the graphite nodules is comprised of individual carbon atoms that bond together in a hexagonal pattern similar to that of oranges on a supermarket shelf. If we add extra oranges to the ends of the display we obtain a long thin row, with smooth top and bottom surfaces, similar to a graphite flake. If we stack the oranges in a reasonably

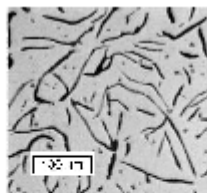
equal manner around all sides we will develop a spheroidal display, similar to a graphite nodule. In the case of our 50µm diameter graphite nodule, approximately  $10^{16}$  (ten million billion) carbon atoms must join together to make each nodule.

Our simple test bar will solidify in approximately two minutes as the iron cools from about 1150°C to 1120°C. During these two minutes,  $10^{24}$  (one million billion billion) carbon atoms will race through a liquid sea of larger iron atoms to find each other and join together in groups of  $10^{16}$  atoms to produce a total of 130 million well-formed graphite nodules. And this unimaginable choreography is routinely done, behind the grey foundry walls, three shifts per day, for each of the 13 million tonnes of ductile iron produced annually. In the perspective of our supermarket display, if each man, woman and child on earth could stack 1,000 oranges per hour, we could make the equivalent of a single 500g test bar in just 100 million years.

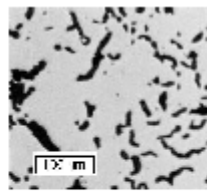
## The Newest Iron

In October 1998, the world foundry industry gathered in South Carolina to celebrate the 50 year anniversary of ductile iron and all of the remarkable progress that had been made. Relatively few of the delegates knew that Millis and his Inco co-workers filed a patent application for compacted graphite iron (CGI) on the exact same date in 1948.

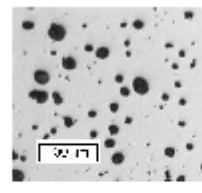
It is logical that the initial development efforts focused on ductile iron. It is stronger than CGI and its stable production range is five times larger. Although stronger and easier to produce, the choice between gray and ductile iron forced designers to select from either end of the cast iron spectrum: grey iron with good castability, machinability, damping capacity and thermal conductivity; or, ductile iron with good strength and stiffness. Every decision required compromise.



Grey Iron



CGI



Ductile Iron

In response to the increasing demands on engineered materials over the past 25 years, foundrymen have made several attempts to introduce CGI to high volume production applications. However, until recently, the stable range for CGI production was too small to provide risk-free high volume production of CGI. An addition of just 0.001% magnesium, or 10 grams of magnesium in a one tonne ladle of molten iron, is sufficient to convert a casting containing a combination of CGI and grey iron into a perfect CGI structure. The burden is for foundrymen to measure their additions in grams, rather than shovels, and for metallurgists to be able to measure and control the iron before, rather than after, it is poured into the moulds. Although several control strategies were proposed in the 1970's and 1980's, the ability to measure and analyse such small variations had to await the development of modern high-speed, large memory computers. Today, in the third millennium, we have the necessary equipment and understanding to reliably control CGI, and the first volume production commitments have been made. Fifty years on, CGI is ready for production.

## The Next Irons

"Great material, too bad about the image". While we teach our children not to judge a book by its cover, we continue to judge the iron foundry by its grey walls. The real image should be the atoms, not the walls. Cast iron is the first composite material, and it remains to be one of the most versatile composites available today. In the future, iron foundries will produce castings with different graphite shapes in different areas of the component to optimise specific properties where they are needed. While the iron foundry world may struggle for image, our present-day ability to control alloy additions to within 10 grams per tonne will seem as rudimentary to our great-grandchildren as Bessemer's cold bowl of soup seems to us. The real Iron Age is only just beginning.



## Appendix B

### Comparison of nucleation and growth rates of graphite and cementite

Let us consider a hypoeutectic alloy that started solidifying with precipitation of austenite  $\gamma$  and undercools to the temperature at which the graphite and cementite liquidus intersect each other. Fig. B.1 shows schematically the plot of molar Gibbs energy of the liquid, cementite and graphite phases in the Fe-C diagram [HIL64, HIL98 page 154] at this particular temperature. Please, note the use of molar fraction here. The Gibbs energy curves of the three phases (liquid,  $\text{Fe}_3\text{C}$  and graphite) possess a common tangent. As there is also an equilibrium between austenite and the undercooled liquid, the common tangent between their Gibbs energy curves indicates by how much the curves for graphite and cementite fall below it. The driving force for precipitation of cementite  $\Delta G_m^{\text{cem}}$  and graphite  $\Delta G_m^{\text{gra}}$  are shown. It is clearly seen that for a liquid composition  $x_C^1$  close to the eutectic composition at  $x_C^{\text{EUT}} = 0.175$ ,  $\Delta G_m^{\text{gra}}$  is  $(1 - x_C^1)/(0.25 - x_C^1) = 11$  times larger than  $\Delta G_m^{\text{cem}}$  indicating nucleation of graphite has a **higher driving force** and thus is much more favoured than that of cementite.

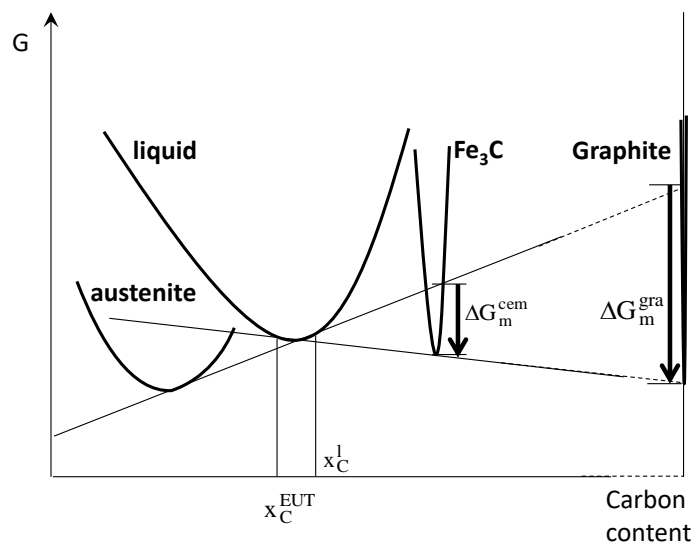


**Figure B.1. Molar diagram of the Fe-C system showing the Gibbs energy of the liquid, cementite and graphite phases at the temperature T for which the graphite and cementite liquidus intersect.**

Assuming that pro-eutectic graphite and cementite grow as plate with a thickness proportional to the critical width of the respective nuclei shows that the ratio of the growth rate of cementite plate,  $V_{\text{growth}}^{\text{cem}}$ , to the growth rate of graphite plate,  $V_{\text{growth}}^{\text{gra}}$ , is such that:  $V_{\text{growth}}^{\text{cem}} / V_{\text{growth}}^{\text{gra}} = \Delta G_m^{\text{gra}} / \Delta G_m^{\text{cem}}$  [HIL64]. Growth of cementite plate is thus much easier than growth of graphite plate. Similarly, assuming diffusion controls the growth of austenite/graphite and of austenite/cementite eutectics, growth of ledeburite will be made easier than that of the stable eutectic because much less carbon has to redistribute at the solidification front of the metastable eutectic as compared to the stable eutectic (see Chapter 6).

### **Authorisations for re-use.**

A number of illustrations which were prepared in the original text of the monograph have been withdrawn because fees were asked for their re-use. This is quite unfortunate as this certainly inhibits appropriate dissemination of knowledge. In turn, obtaining the possibility for re-use without any condition was greatly appreciated.

### **Courtesy of AFS**

- Figure 5.6-b: figure 14c of S. Liu, C.R. Loper, Morphology of kish graphite, AFS Trans., 1990, 385-394
- Figure 5.9-a: figure 11 of S. Liu, C.R. Loper, Morphology of kish graphite, AFS Trans., 1990, 385-394
- Figure 10.4: H. Miyake, A. Okada, Nucleation and growth of primary austenite in hypoeutectic cast iron, AFS Trans., 106, 1998, 581-587

### **Courtesy of DIS**

- Figure 5.16-b: figure 9 of J. Qing, M. Xu, V. Pikhovich, Why is Graphite Spherical in Ductile Iron? A Study of Elements in the Spheroidal Graphite Using Atom Probe Tomography and Transmission Electron Microscopy, Keith Millis symposium, 2018.
- Figure 7.10: figure 6 of J. Bourdie, J. Lacaze, C. Josse, L. Laffont, Growth of spheroidal graphite: light versus scanning and transmission electron microscopies. Keith Millis symposium, 2018.

### **From the Iron and Steel Institute of Japan**

Figure 9.3 is Figure 3 of, V. GERVAL, J. LACAZE, Critical temperatures of spheroidal graphite cast irons: a review of literature data, ISIJ International, 40, 2000, 386-392

### **From TMS**

- Figure 3.12-a –Figure 3 of. FRAS, W. KAPTURKIEWICZ, A.A. BURBIELKO, H.F. LOPEZ, Numerical simulation and Fourier analysis of solidification kinetics in high-carbon Fe-C alloys, Metall. Mater. Trans. B, 28, 1997, 115-123. Copyright 1997 by The Minerals, Metals & Materials Society and ASM International. Used with permission.
- Figure 5.16-a: figure 5 of D.M. STEFANESCU, A. CRISAN, G. ALONSO, P. LARRANAGA, R. SUAREZ, Growth of spheroidal graphite on nitride nuclei: disregistry and crystallinity during early growth, Metall. Mater. Trans. A, 50, 2019, 1763-1772. Copyright 2019 by The Minerals, Metals & Materials Society and ASM International. Used with permission.
- Figure 6.11-a: figure 8 of D. HOLMGREN, R. KÄLLBOM, I.L. SVENSSON, Influences of the graphite growth direction on the thermal conductivity of cast iron, Metall. Mater. Trans. A, 38, 2007, 268-275.  
Copyright 2007 by The Minerals, Metals & Materials Society and ASM International. Used with permission.

### **From Elsevier**

- Figure 6.10: figure 1 of J. LACAZE, D. CONNÉTABLE, M.J. CASTRO DE ROMAN, Effects of impurities on graphite shape during solidification of spheroidal graphite cast irons, Materialia, 8, 2019, 100471. Copyright (2019), with permission from Elsevier
- Figures 5.10-a: figure 9 of K. THEUWISSEN, J. LACAZE, L. LAFFONT, Structure of graphite precipitates in cast iron, Carbon 96, 2016, 1120-1128. Copyright (2015), with permission from Elsevier.
- Figures 5.10-b: figure 10 of K. THEUWISSEN, J. LACAZE, L. LAFFONT, Structure of graphite precipitates in cast iron, Carbon 96, 2016, 1120-1128. Copyright (2015), with permission from Elsevier.
- figures 5.11-a: figure 5b of K. THEUWISSEN, J. LACAZE, L. LAFFONT, Structure of graphite precipitates in cast iron, Carbon 96, 2016, 1120-1128. Copyright (2015), with permission from Elsevier.